University of Southampton

Chemical Applications of Fourier-transform Raman spectroscopy

A thesis submitted by

Christopher David Dyer, B.Sc. CChem. MRSC

for the degree

Doctor of Philosophy

Department of Chemistry

February 1995

UNIVERSITY OF SOUTHAMPTON

ABSTRACT

FACULTY OF SCIENCE

CHEMISTRY

Doctor of Philosophy

Chemical Applications of Fourier transform Raman Spectroscopy

by Christopher David Dyer

Details are presented of five studies in the application of Fourier transform (FT) Raman spectroscopy. The studies encompass a diverse range of chemical species, and indicate the wide applicability of FT-Raman methods.

A series of coloured sulphur-containing organic compounds based on the thione ring structure were analysed. Characteristic group frequencies were determined, enabling the thione ring structure to be easily identified. Spectral changes on reaction of thiones or related oxones to yield tetrathiafulvalenes (TTFs) were discovered, whilst the differentiation of thione and oxone species was shown to be straightforward.

The novel allenylketenimine-tetracyanoethylene (TCNE) system was investigated, in order to provide the first vibrational assignment of these compounds. Characteristic frequencies of the underlying cyclic structure were determined. The extremely weak IR absorption of the nitrile (-CN) group was noted, contrasted against the reliable Raman signature, and discussed.

The first study of the hydrated γ-alumina surface was undertaken in a combined FT-IR/FT-Raman study, that unambiguously determined the surface to comprise the bayeritic polymorph of aluminium hydroxide. The temperature and pH-dependency of the formation of the hydroxide were studied. The role of phenylphosphate in the suppression of hydration was discussed.

Near-IR excitation was shown to produce anomalous luminescence from a series of calcium silicate cement minerals. Investigations using near-IR diffuse reflectance suggested a connection with the presence of metal ions impurities (especially manganese) and calcium hydroxide. Calcium oxide and hydroxide were shown to display similar anomalous behaviour. The application of conventional Raman spectroscopy in this area was appraised as an alternative, and shown to be successful.

A method for obtaining rotational and vibrational spectra of gases on a commercial FT-Raman spectrometer using multiple-reflection cells was designed, developed, and appraised. The technique was then applied to a previously-intractable system (NO_2/N_2O_4) to record the first vapour-phase spectrum of the dimer. In addition, the data suggests that the NO minority species scattering may be strongly-enhanced, and that NO_2 may be unenhanced at this wavelength.

Contents

Acknowledgements

I thoroughly enjoyed taking the opportunity given to me by Patrick Hendra to work in his group for three years. During that period, many people made greatly-valued contributions to that enjoyment. My heartfelt thanks to them all.

Firstly, Professor Patrick Hendra - for his supervision, support, many good evenings in Crawley, and wine seminars.

Professor Willis Forsling, for being a superb host during my exchange to Sweden, and providing cross-country skiing opportunities on frozen lakes.

Dr Bill Maddams, for his sound input and ever-willing advisory role.

Dr Jeremy Kilburn and Dr Richard Whitby, for allowing collaborations within their research groups.

Mrs Jill Allen, for secretarial services above and beyond the call of duty.

My current employers, Renishaw PLC, for the time to conclude the thesis preparation.

The US Office of Naval Research, for funding.

My parents - for even more funding - and quiet, patient support.

Of course, the horde of past and present members of the Hendra group, a supporting cast of undergraduates, postgraduates, Graham from t' PCL, assorted house-mates (special thanks to Andy Wright & Dave Pegg), Southampton publicans (especially John and Mo at the New Inn), my bank manager Sarah, Dr Ross & diverse night-clubs, assorted cricket teams, and the (semi-)human members of the Phys Chem group. Oh - and Zog. Because he's never been mentioned in a thesis before. Nor will be ever again. What larks, eh ?

Lastly, Sarah. Thanks for the support; still want to marry me ?

Chapter 1:

The application of Raman scattering techniques in chemistry.

1.1 Overview

For nearly seventy years chemists have used Raman spectroscopy in both fundamental research and analytical roles. The huge literature on the technique bears testament to its applicability, and the number of researchers who find it an invaluable tool.

The work presented in this thesis represents a critical appraisal of one such new technique - Fourier transform (FT-) Raman spectroscopy - for applications of chemical interest.

In order to introduce the concepts of Raman scattering and vibrational spectroscopy, a brief and by no means exhaustive review of relevant theory is presented - followed by a description of the experimental procedures and instrumentation employed in the FT-Raman technique.

1.2 Theoretical background of the Raman effect.

When intense monochromatic light is shone into a vessel containing a liquid or gas, secondary radiation may be detected emanating from the vessel to shorter and longer wavelength of the exciting light, in addition to a strong component at the same wavelength. Predicted in the early 1920s, although first observed and reported experimentally by Sir C.V. Raman[1], this secondary radiation comes about by the inelastic scattering of the incident light by the irradiated molecules. The simple demonstration that scattered light is detected at right-angles to the direction of propagation of the exciting beam shows that the scattered beam is not simply due to reflection within the vessel.

Molecules can be considered to consist of relatively heavy positively-charged nuclei interacting with a number of negatively-charged lighter electrons. The distribution of the electrons depends on the configuration of the nuclei - as the configuration determines the inter-electron, inter-nuclear, and electron-nuclear interactions.

The mechanism by which the light is scattered involves the polarisation of the electron distribution by the incident light. A molecule in field-free space irradiated by a beam of visible light experiences an electric field which is time-varying but not significantly varying over the length of the molecule. The electric field of the light displaces the electrons more readily than the more massive nuclei, resulting in a periodic distortion of the electron cloud*. This periodic movement of electrical charge constitutes an induced dipole at the frequency of the incident light. The magnitude of the induced dipole** moment (Cm) can be related to the polarisability ($J^{-1}C^2m^2$) and the electric field strength (V/m):

$$\mu = \alpha \, . \, E$$

According to classical mechanics, dipoles are the source of electromagnetic radiation. The dipole induced by the incident light radiates at the same frequency of the incident light, and is radiated into a full 4π steradian solid angle. The endothermic transferral of energy to the molecule on interaction by polarisation of the electron cloud results in the tendency of the system to re-equilibrate by re-radiation as quickly as possible. This scattering at the same frequency of the incident light is called Rayleigh scattering, after its discoverer. It is of course elastic scattering.

Scattering at shifted wavelengths - both shorter and longer - occurs because the polarisability function may be modulated by the motion of the nuclei, as the exact and instantaneous molecular configuration determines the polarisability.

1.2.1 Molecular structure

If the predominantly-electrostatic forces in operation between the nuclei and the electrons result in a nuclear configuration where the species is stable - such that small deviations away from this configuration result in a force being generated to restore it - then the system can be thought of as having formed a stable chemical bond.

It can be seen immediately that changing the chemistry - simply "changing the atoms" - alters the balance of the net forces acting on the nuclei, and therefore also the polarisability, a concept related to the "deformability" of the electron distribution.

---

* The magnetic field of the light has a much weaker interaction with the charge distribution, and may be ignored.

** This treatment deliberately ignores higher-order terms in the expansion, as these are only important where extremely high electric fields are generated - as in pulsed laser applications.

The potential energy function which governs the bond may be derived from basic principles:

- Firstly, the function must reflect the fact that molecules dissociate if enough energy is supplied
- Secondly, that realistic atomic displacements will not result in the nuclei coalescing
- Thirdly, that if the nuclei are separated by large distances then the conditions for stability will not be met
- Fourthly, a restoring force must operate for deviations about the stable, equilibrium, nuclear configuration.

A suitable function to describe the potential energy for the stable bonding case as described above is given below. This is the well-known Morse curve:

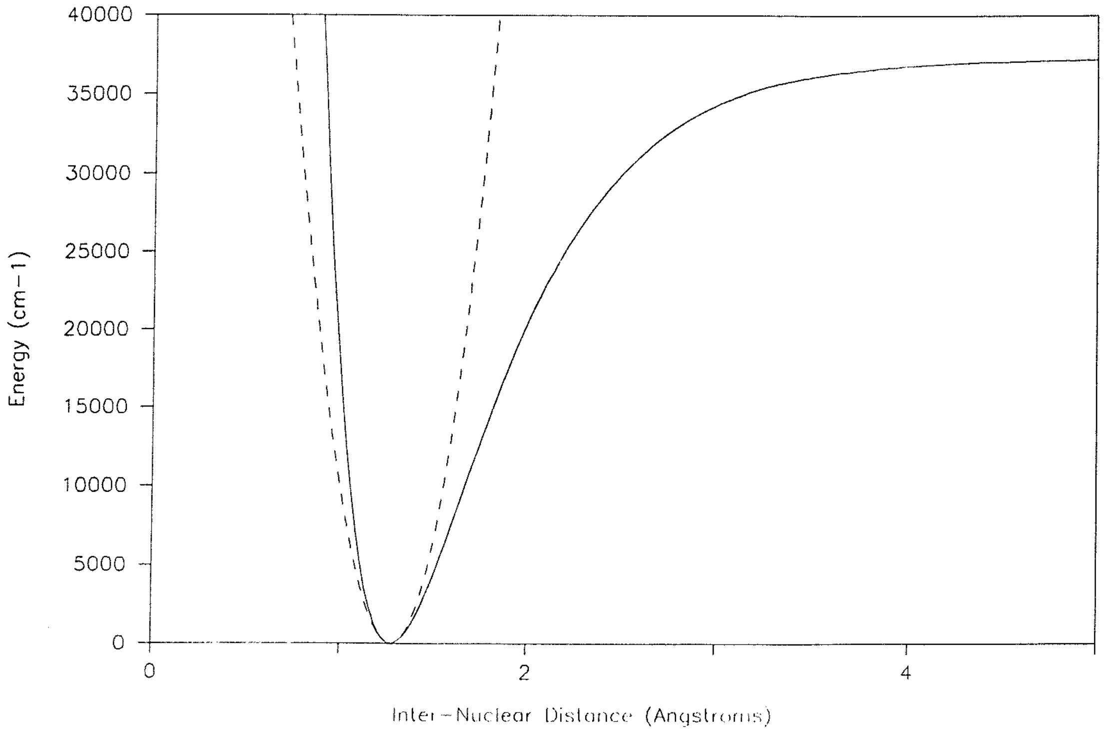

Figure 1.1 The Morse potential (dotted curve is a quadratic potential)

The Morse curve can be described as:

$$V(x) = D_e(1-e^{-ax})^2$$

where a is a constant (m^{-1}) for a given potential well. The difference in potential energy between the equilibrium configuration and infinite atomic separation is called the depth of the potential well (D_e) and is identified with the energy required to break the bond. It is a measure of the strength - not the stiffness - of the bond.

The existence of a restoring force leads ***directly*** to the existence of molecular vibrations. The Morse function can be described close to the equilibrium position as a quadratic function of the bond extension (defined as x = bond length-equilibrium bond length). In this approximation - the simple harmonic oscillator (SHO) approximation - the bond force constant k_{vib} is associated with the Young's modulus of a spring (the bond), whilst the nuclei are associated with point masses. The restoring force is given by:

$$F = -k_{vib}.x$$

A solution to the problem is found by rewriting this as:

$$d^2x/dt^2 = -(k_{vib}/\mu_{ab}).x$$

Using $x = A.\cos(\omega t)$ as a trial solution, we see:

$$d^2x/dt^2 = -A.\omega^2.\cos(\omega t) = -\omega^2.x$$

So that by inspection

$$x = A.\cos(\omega t)$$

with

$$\omega = 2\pi\nu_{vib} = \sqrt{(k_{vib}/\mu_{ab})}$$

This shows that for a classical model the nuclei in a stable bond undergo periodic motion about their equilibrium position in response to the net force acting on them.

Note that the reduced mass, $\mu_{ab} = (m_a.m_b)/(m_a+m_b)$ where m_a is the mass of atom a is used in the derivation above. In general a molecule undergoes a complex combination of vibration, rotation, and translation which to reasonable approximation can be considered independent. Vibrational motion concerns the relative motion of the nuclei about the molecular centre of mass, not changes of orientation, or in translation through space; given these conditions, mechanics suggests the reduced mass as the correct mass parameter.

Note also that the bond stretching force constant (k_{vib}) is a function *only* of the curvature of the potential well - and not of the depth of the potential well, or of the nuclear mass. Although the above derivation only applies strictly to the (non-realistic) SHO potential, its approximates the Morse curve and similar potential functions quite well at small bond extension; the deviation of the Morse curve at higher values identifies it as an anharmonic oscillator (AO) potential function.

1.2.2 Raman scattering

The appearance of Stokes-shifted scattering to longer wavelength and anti-Stokes scattering to shorter wavelength constitutes Raman-scattered light (also known as inelastic scattering). As indicated above, it arises due to the periodic modulation of the polarisability consequent upon molecular motion, and can be derived straightforwardly.

Firstly the polarisability as a function of the bond extension is expressed as a Taylor series about the equilibrium configuration. Secondly, all term higher than the second are disregarded, which interprets polarisability as a linear function of bond extension for small extensions about the equilibrium position. Thirdly, the vibrationally-unmodulated polarisability* α_0 is associated with the first term of the expansion, whilst the second term $\delta\alpha/\delta x$ is associated with the change in polarisability due to vibration.

Let ν_v be the vibrational frequency of the bond, whilst ν_i is the frequency of the incident light.

Then:

$$\mu_{induced} = [\alpha_0 + \delta\alpha/\delta x.\cos(2\pi\nu_v t)][E\cos(2\pi\nu_i t)]$$

$$\mu_{induced} = \alpha_0.E\cos(2\pi\nu_i t) + \delta\alpha/\delta x.\cos(2\pi\nu_v t)E\cos(2\pi\nu_i t)$$

Using the relationship $\cos(A+B) + \cos(A-B) = 2\cos A.\cos B$,

---

* Notice that this is not static polarisability - that term refers to polarisability under static electric fields. Note that polarisability is properly a function of incident frequency, as well as field strength; to good approximation, this functional dependence is weak when $\omega_{incident}$ is far from strong resonance in the system.

$$\mu_{induced} = \alpha_0.E\cos(2\pi\nu_i t) + \delta\alpha/\delta x.E/2.[\cos2\pi(\nu_i+\nu_v)t] + \delta\alpha/\delta x.E/2[\cos2\pi(\nu_i-\nu_v)t]$$

Therefore, $\mu_{induced}$ scatters light ν_s at ν_i with sidebands at $(\nu_i-\nu_v)$ and $(\nu_i+\nu_v)$. This expression also shows that ν_v may be obtained by measuring ν_s and subtracting ν_i. Note the symmetric disposition of the sidebands with respect to ν_i.

The above derivation shows the same features even when a small change is made to the notation. Rather than writing the polarisability as a function of bond displacement, it is possible to describe the polarisability as a function of progress through the vibration, q. This has advantages when considering complex vibrational motions, where a simple extension of a single bond is not the only contortion that needs to be described; q varies between $\pm\pi$.

Modulation of the polarisability by molecular vibration is one method by which Raman scattering may occur. As discussed briefly in chapter 6, rotation about the centre of gravity may also modulate the polarisability and give rise to Raman scattering.

Using the classical theory of light scattering, it is possible to relate the intensity of light radiated by a dipole to the frequency of the dipole oscillation. This is usually given as the intensity ratio of scattered light per unit solid angle to incident light, and is proportional to the fourth power of the *scattered* frequency. This implies anti-Stokes scattering should be stronger than Stokes scattering, by the ratio:

$$I_{anti\text{-}Stokes} / I_{Stokes} = [(\omega_i + \omega_v) / (\omega_i - \omega_v)]^4$$

However, the shifted-wavelength scattering may be many orders of magnitude *weaker* in intensity than the Rayleigh scattering; the ratio depends on the magnitude of the modulation term $\delta\alpha/\delta x$ relative to the static term α_0 in this model. Obviously, $\delta\alpha/\delta x < \alpha_0$; however, $\delta\alpha/\delta x << \alpha_0$ in many cases.

Even though the shifted wavelengths borrow their titles from fluorescence spectroscopy, the spectra are *not* due a luminescence process. The absorption of light, followed by the possible re-arrangement of the electronic and nuclear configurations, with subsequent re-emission of radiation, *does not describe the Raman effect*.

Several factors allow scattering to be separated from spontaneous emission - several are given below:

- Firstly, measurements of the timescale of fluorescence show that it is slow in comparison with Raman scattering, which has a timescale typically around 10^{-15} seconds.

- Secondly, if the wavelength of the exciting radiation is varied, the Raman scattering also varies in wavelength - *such that the scattered light maintains its frequency (or inverse wavelength) shift from the incident light; fluorescence is fixed in absolute wavelength*.
- Thirdly, the intensity of fluorescence emission is usually several orders of magnitude stronger than Raman scattering.
- Fourthly, Stokes and anti-Stokes Raman spectra in principle contain the same data; anti-Stokes fluorescence spectra arise from transitions from an electronic excited state with a different set of vibrational parameters, such that Stokes and anti-Stokes shifts are often different.

1.2.3 Anisotropic polarisability

The net binding force acting on the electron cloud differs at different points in the molecule, reflecting the observed directional nature of chemical bonding. This results in anisotropic polarisability, as the electron distribution is easier to polarise in certain sections of a molecule where the net electron binding force is weaker than elsewhere. Anisotropy in the polarisabiliy function can be described by an ellipsoid:

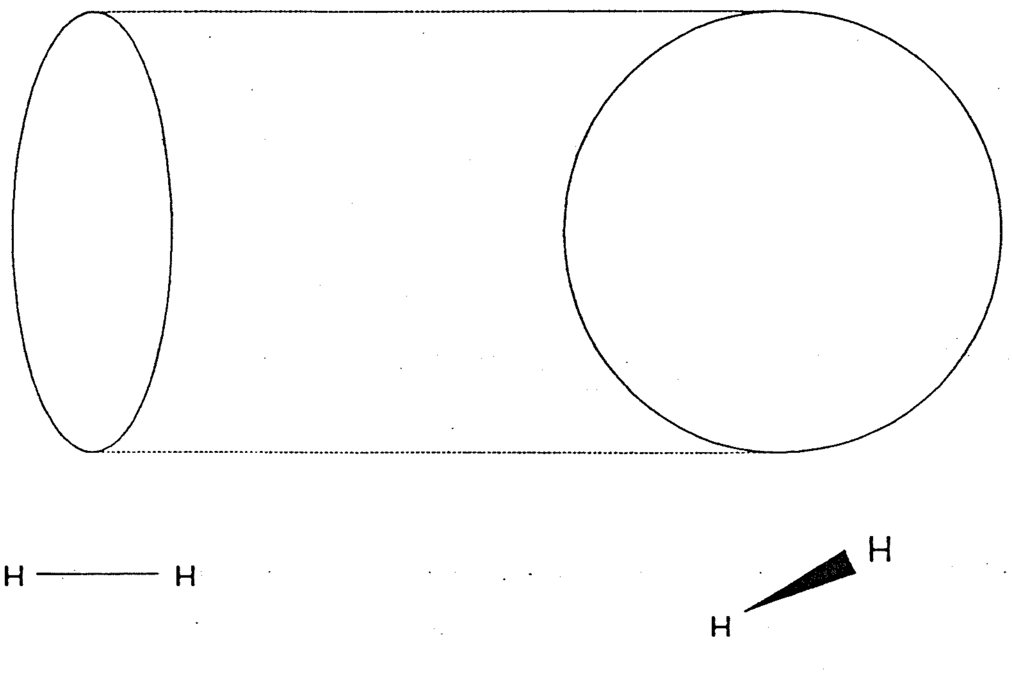

Figure 1.2 Polarisability of the hydrogen molecule

The ellipsoid is plotted as surface from the electrical centre of the molecule, with length in *a given direction* proportional to the inverse square root of the polarisability *in that direction*. In the above example, the distance from the centre of the ellipsoid is shortest along the internuclear axis. Therefore, the polarisability along the axis between the nuclei in the bonding region is *highest* - interpreted as meaning the electron density is highest along the bond, and therefore easiest to deform. This simple interpretation must be used with caution, however.

This anisotropy is present in nearly all molecules, except those with very high intrinsic symmetry, brought about by symmetric disposition of identical bonds. In these molecules - $C^{35}Cl_4$, for instance - the ellipsoid takes on higher symmetry, that of a sphere.

It is also apparent that polarisability is a tensor property - since it is possible systems to induce a dipole (a vector quantity, having direction and magnitude defined) that is not collinear with the exciting dipole (again, a vector). The description of a tensor quantity is quite straightforward in matrix notation:

$$\begin{vmatrix} \mu_x \\ \mu_y \\ \mu_z \end{vmatrix} = \begin{vmatrix} \alpha_{xx} & \alpha_{xy} & \alpha_{xz} \\ \alpha_{xy} & \alpha_{yy} & \alpha_{zz} \\ \alpha_{zx} & \alpha_{zy} & \alpha_{zz} \end{vmatrix} \times \begin{vmatrix} E_x \\ E_y \\ E_z \end{vmatrix}$$

If a single molecule is fixed in space and excited with a polarised monochromatic beam of light, the exact directional properties of the scattered dipole radiation depend on elements of the scattering tensor.

Off-axis tensor entries give rise to the scattering which is not co-linear with the exciting beam. By reversal symmetry*, we can see that the entry α_{ij} for $i \neq j$ must be equal to α_{ji}. In addition, a spherical polarisability ellipsoid is derived from a totally symmetric tensor with all α_{ij} equal for $i=j$ and zero for $i \neq j$. Of course, it is vital to remember that in discussing Raman scattering, the derived polarisability tensor $\delta\alpha_{ij}/\delta q$ is required, not the polarisability tensor α_{ij}.

---

* These simple arguments break down for more complex scattering processes such as resonant Raman scattering.

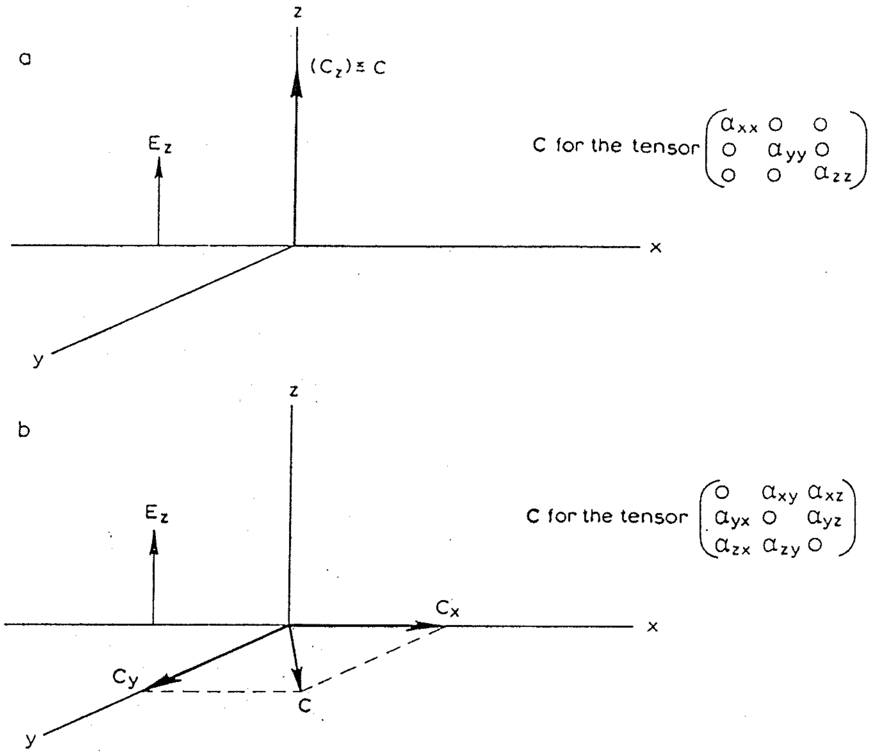

Figure 1.3 Examples of 2 different scattering tensors

1.2.4 Mechanism of interaction

The frequency of vibration for a simple diatomic molecule can be estimated to lie around 600 Terahertz (10^{12} Hz). Using the relationship $\lambda\nu = c$, it can be seen that this frequency corresponds to light of wavelength in the mid-infrared (mid-IR) region. Therefore one method of exciting molecular vibrations is to bathe the molecule in IR radiation; at frequencies that correspond to molecular vibrations, strong absorption of radiation will be noted.

The absorption can be considered to be due to the resonant transfer of energy from the beam to the molecule. For IR absorption, variation of bond dipole moment during the vibration is required - $(\delta\mu/\delta q)_{eqm}$ must be non-zero, where the dipole moment is evaluated as a Taylor series expansion about the equilibrium position.

A separation of charges constitutes a dipole - characterised by its dipole moment, the product of charge difference and distance between the centres of positive and negative charge. Typically, bond dipole moments have magnitude 3×10^{-30} Cm -around 1 Debye unit. Heteronuclear diatomic molecules all have a permanent dipole, as the electronegativity of each atom is different, resulting in non-coincidence of the centres of positive and negative charge for the molecule. In the simplest models, the partial charges are assumed to be resident on and to move with the nuclei*. Dipole moments are vectors, so the position and magnitude of the dipole moment can be expressed as the sum of three orthogonal components; in general, the dipole moment of a complex molecule can be then treated as the vector sum of all the individual bond dipole moments.

IR radiation does work on the dipole - the force exerted being proportional to the charge imbalance and directed in the same direction as the electric field. Hence as the electric field direction alternates, contraction and expansion of the bond is induced. Solving the more-complex vibrational equation** with a field-induced driving term, the transfer of energy to the bond is strongest when the frequency of the bond and the frequency of the light are closest - *in resonance*.

Homonuclear diatomics do not exhibit a change in dipole during vibration, so homonuclear diatomic molecules do not absorb infrared radiation. However, their vibrational spectrum may still be deduced via the Raman effect.

All molecules have a finite polarisability; this is most easily expressed in units of $Å^3$ when defined as a polarisability volume ($\alpha'=4\pi\alpha/\varepsilon_0$) with magnitude around 1 $Å^3$.

Variation of polarisability with bond length is required for Raman scattering; unless $(\delta\alpha/\delta q)_{eqm}$ is finite the shifted-frequency scattering is not allowed. Another way of viewing the interaction is that light deforms the electron cloud on interaction, which perturbs the electron/nuclei interaction; this results in a mechanism for the energy of the irradiating light which acts on the electrons to be transferred into nuclear motion. This sees $(\delta\alpha/\delta q)_{eqm}$ as a coupling function between nuclear and electronic motions; if $(\delta\alpha/\delta q)_{eqm}$ is zero, there is little coupling, and therefore little Raman scattering.

The diagram below gives examples of vibrations with zero and finite $(\delta\mu/\delta q)_{eqm}$ and $(\delta\alpha/\delta q)_{eqm}$ for a simple molecule.

---

* Certain higher-order terms sometimes need to be included to reflect charge redistribution on bond-stretching.

** Damping terms leading to finite lifetimes and line widths can also be included if needed.

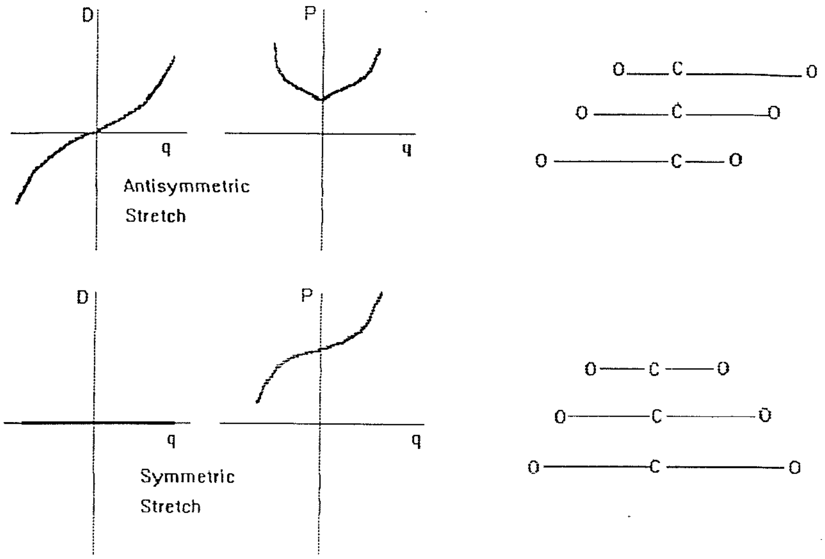

Figure 1.4 Change in dipole moment (D) and polarisability (P) as a function of progress through vibration (q) for the symmetric and antisymmetric stretching modes of CO_2.

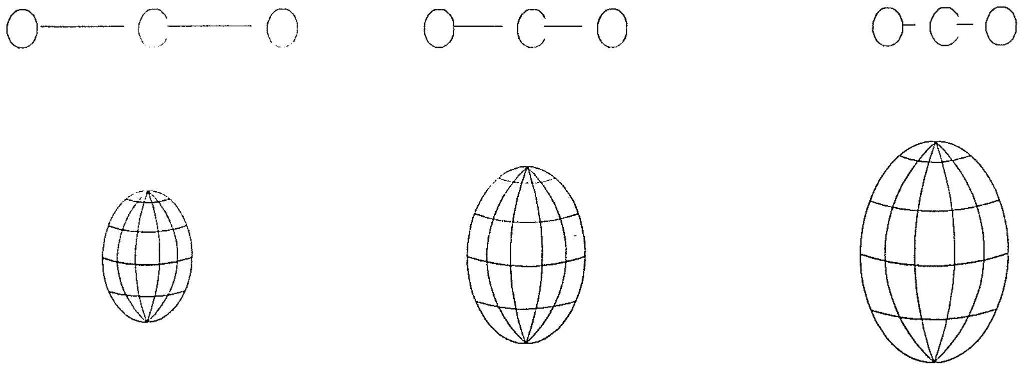

Figure 1.5 Change in polarisability ellipsoid during symmetric stretch of CO_2

The change in polarisability is reflected by the deformation of the polarisability ellipsoid during vibration. Of special interest is the case where the ellipsoid is in fact spherical, since the ellipsoid remains spherical during totally symmetric vibrations.

1.2.5 Extension to multi-atom problems - normal modes

Many features of molecular vibrations may be deduced from simple mechanical models*. In multi-atom systems, the molecular contortion is a complex superposition of motions; two very important points are apparent:

- Firstly, no change in the position or orientation of the molecule occur during the contortion - the centre of mass does not translate and the molecule does not rotate.
- Secondly, all atoms move through their equilibrium configurations at the same time (in phase) and oscillate with the same frequency - although individual amplitudes and speeds vary depending on the mass of the nuclei and stiffness of the bonds involved.

In complex systems, the problem is often cast in terms of normal modes - certain combinations of the individual nuclear displacements chosen such that excitation of one normal mode leaves all other modes unexcited - so the complex vibrational motion is described by a linear superposition of the normal modes[2]. This is equivalent to choosing a set of co-ordinates such that the kinetic and potential energy functions for each normal mode are independent of all other normal modes. The effect is that each normal mode can be excited individually *without* starting motion in any other mode.

The number of such vibrations is simple to calculate. If the species under consideration has N nuclei, 3N independent ways of combining the 3 mutually-orthogonal nuclear displacement vectors on each atom are possible. However, 3 of these represent translatory motion, not inter-nuclear motion; whilst a further 3 (in the case of a non-linear molecule) describe rotation about the centre of mass, again with no relative nuclear motion. Hence for a 5-atom non-linear molecule, there are 9 molecular motions that correspond to molecular vibrations, and therefore 9 normal modes of vibration.

---

* The effects of damping terms are ignored in most treatments, as they lead to more complexity.

The effect of realistic potential energy functions like the Morse potential described above is that a "decoupled" approach can not be taken, since there are no descriptions which separate the normal modes. This is due to cubic and quartic terms in the potential energy function. Simple "ball and stick" models eventually fail because they cease to accurately describe complex molecules.

1.2.6 Breakdown of the simple theory

Several unpredicted features occur when observing Raman spectra. The most obvious peculiarity is the intensity of the anti-Stokes scattering relative to the Stokes scattering. For any exciting wavelength, the simple theory predicts a stronger anti-Stokes band. For any real system, *exactly the opposite is observed* - for instance, the intensity ratio of Stokes-to-anti-Stokes scattering from silicon is about 10:1 with 632.8 nm excitation, whereas simple theory predicted the anti-Stokes band to be about 30% more intense than the Stokes.

Classical theories of electromagnetism and mechanics which serve to describe (phenomenologically) the basic interactions break down at the molecular level. The modern mechanics of quantum theory is required to describe these events*.

For systems such as the SHO potential, exact analytical solutions to the equations of motion exist^3. The imposition of quantum mechanical rules result in the total energy being quantised - that is, the sum of kinetic and potential energies can only have specified discrete values. These values are given by:

$$E_{SHO} = h\nu_{vib}(v+½)$$

The allowed states are equally spaced, whilst the quantum number (v) describes which allowed energy state is being discussed. The appearance of zero-point energy ($½h\nu_{vib}$) reflects the impossibility of localising the vibrational motion exactly**. Note that due to the existence of zero-point energy, the bond dissociation energy D_0 is related to the depth of the potential well D_e by $D_e = D_0+(½h\nu_{vib})$.

For the Morse potential analytical solutions also exist^3, with the expression for the energy of the oscillator:

---

* The justification simply being that it produces more accurate answers more often than classical mechanics.

** This may be interpreted by application of the Heisenberg Uncertainty Principle, a postulate of quantum mechanics.

$$E_{AO} = h\upsilon_{vib}(v+\tfrac{1}{2}) - h\upsilon_{vib}\chi_{vib}(v+\tfrac{1}{2})^2$$

χ_{vib} is the so-called anharmonicity constant for the vibration, and may be related to the depth of the potential well (D_e) by $\chi_{vib} = h\nu_{vib}/4D_e$. The effect is a lowering of all energy levels with respect to the SHO, and also a reduction in separation between adjacent levels as v increases. In addition, $D_e = D_0+(\tfrac{1}{2}h\nu_{vib}-\tfrac{1}{4}h\upsilon_{vib}\chi_{vib})$.

The following diagram shows the effect of quantisation on the Morse function:

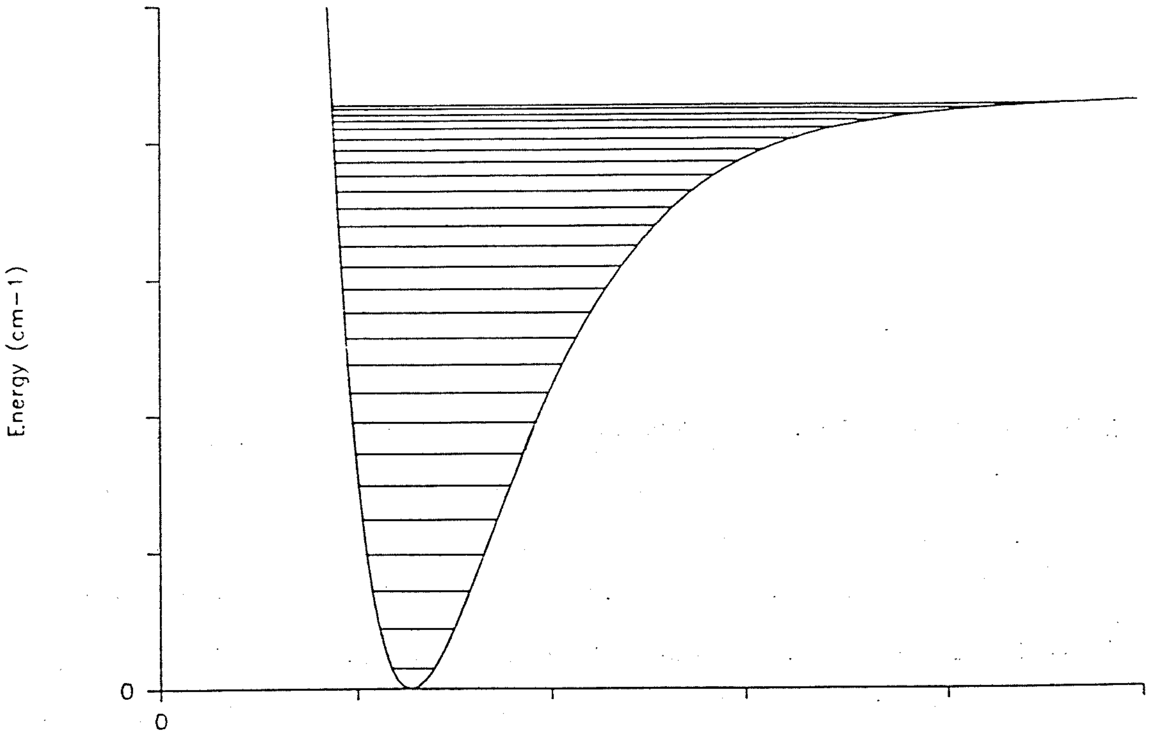

Figure 1.6 Quantisation of the Morse function.

The dashed lines represent the intersection of the quantised *total* energy on a diagram showing *potential* energy - the intersections with the curve are the classical turning points of the motion.

The occupancy of the energy levels can be described by a simplified Boltzmann equation:

$$n_{upper}/n_{lower} = e^{-(h\nu/kT)}$$

where the fundamental constants h and k take their usual meaning, T is the absolute temperature measured in Kelvin and ν the vibrational frequency in Hertz. The error in the classical approach was the assumption that an equal population of Stokes and anti-Stokes vibrations existed. Upon applying this equation for silicon at room temperature, the ratio n_{upper}/n_{lower} is only around 8 %. Taking account of the increase in scattering efficiency at shorter wavelength of about 30 %, this implies the overall intensity ratio of Stokes to anti-Stokes scattering should be about 10:1 - as observed experimentally*.

1.2.7 Selection rules

The *gross* selection rule for Raman scattering has already been discussed in some detail - during the molecular motion, the polarisability must be modulated. For vibrations, $(\delta\alpha/\delta q)_{eqm}$ must be non-zero. In addition, the gross selection rule for IR absorption has been discussed - $(\delta\mu/\delta q)_{eqm}$ must be non-zero.

However, the *specific* selection rules governing transitions between the different quantised energy states are regulated by quantum mechanics. The SHO may change quantum number (v) by $\Delta v = \pm 1$. This implies that the change in vibrational energy is:

$$\therefore \Delta E_{SHO} = h\upsilon_{vib}$$

The (v=0) to (v=1) transition abbreviated $v_{1 \leftarrow 0}$ and is called the fundamental - whereas other allowed transitions with $\Delta v = +1$ starting from v>0 are called "hot bands". In this approximation, they appear at the same transition energy, but have lower intensity as the population of higher states depends on the temperature.

Although somewhat tenuous, the classically-derived reasoning for $\Delta v = \pm 1$ is that the dipole moment (IR) and polarisability (Raman scattering) functions go through one complete cycle per vibration; however, the Morse AO potential can change by $\Delta v = \pm n$ where n is an integer, and this can only be fully explained by quantum mechanics. Manipulating the expression for E_{AO} yields:

$$\Delta E_{AO} = h\upsilon_{vib}[1 - \chi_{vib}(2v+2)] \quad \text{for } \Delta v = +1$$

---

* This derivation is not intended to demonstrate the subtleties of temperature measurement with Raman techniques, as it is too simplistic.

Notice that the fundamental does not occur at the same transition energy as in the SHO; similarly, hot-bands no longer lie exactly under the fundamental.

Overtone transitions - $\Delta v > 1$ - occur in the AO case through cubic and higher terms in the potential function and non-linearity in the dipole moment and polarisability functions:

$$\Delta E_{AO} = 2h\upsilon_{vib}[1 - \chi_{vib}(4v+6)] \quad \text{for } \Delta v = +2$$

As can be seen, $\Delta v = +2$ transitions (first overtones) do not have exactly twice the fundamental transition energy.

1.2.8 Details in the quantum mechanical picture

In the quantum mechanical derivation, the transitions between the energy states are facilitated by absorption or emission of quantised units of energy. When this energy is supplied by electromagnetic radiation, the unit is termed the photon. The energy of the photon is easily related to the frequency of light:

$$E = h\upsilon \text{ [Joules]}$$

The wavenumber unit is *proportional* to the energy of the photon in the following way:

$$E = hc'\upsilon \text{ [Joules]}$$

where c' is the speed of light in cm/s and υ has wavenumber units (cm^{-1}).

It is therefore acceptable to speak of wavenumbers *as if they described* an energy scale*. The various interaction processes can be summarised in figure 1.7. This diagram helps reinforce the hypothesis that the IR experiment is direct absorption of infrared radiation (2500-25000 nm), whereas Raman scattering is indirect, in that it involves the scattering of light. An intermediate state - usually not a true solution to the steady-state equations for the electronic structure - is produced instantaneously on interaction with the excitation beam, and a photon destroyed in the process; the "virtual" state radiates its energy into creation of a Rayleigh-scattered photon or a Raman-scattered photon plus vibrational (de-)excitation in the latter case. Both the

---

* The wavenumber is better represented as a unit of momentum.

exciting and scattered light usually fall in the ultraviolet (UV) to near-IR regions (250-2500 nm).

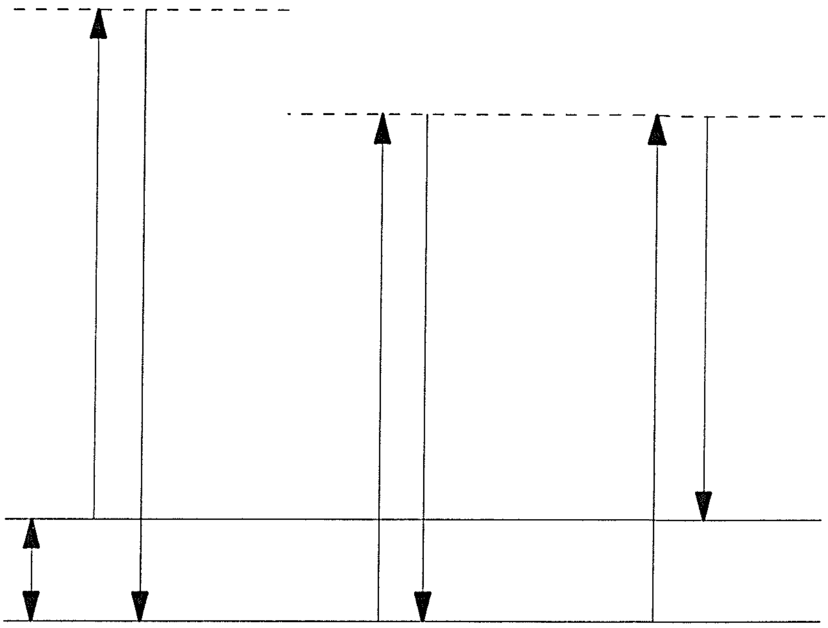

Figure 1.7 Mid-IR absorption, anti-Stokes Raman, Rayleigh, and Stokes Raman scattering (left to right)

1.2.9 Polarisation measurements

If polarised light is shone into a sample of gas and care taken to record the *depolarisation ratio, ρ_l* (defined as the ratio of light intensity transmitted with a polarisation analyser perpendicular to the excitation electric field vector to the intensity transmitted with the analyser parallel) a simple fact is evident: ρ_l is zero - the Rayleigh scattering is completely polarised. In fact, very careful investigation[4] shows that the depolarisation is actually finite - the smallest values being observed for molecules such as isotopically-pure CCl_4 and SF_6.

However - when the depolarisation ratios of the vibrational Raman bands are measured, it is immediately apparent that some of the bands are polarised - giving $\rho_l = 0$ - whilst several others are depolarised - that is, they have finite transmission, ρ_l being about 0.75.

Both these observations can be rationalised in terms of anisotropic polarisability. During a gas or liquid phase experiment, where molecules are rapidly tumbling and free to change their orientation*, the instantaneous polarisability and derived polarisability of the molecule vary - since the scattering occurs almost instantaneously, any real experiment detects a superposition of scattering from the various orientations.

Consider the experiment below:

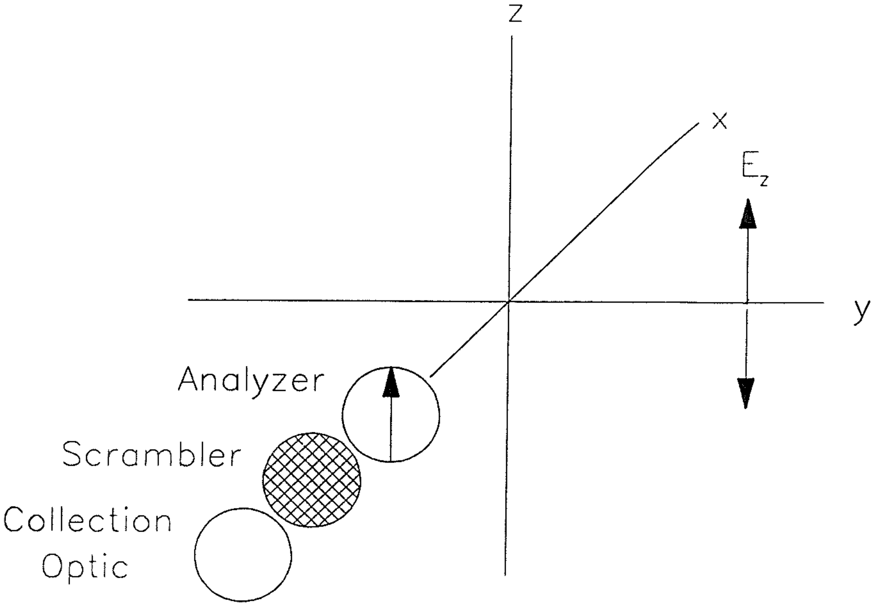

Figure 1.8 Experimental determination of the polarisation of the Raman scattering

Linearly polarised light is incident onto a fixed-orientation molecule, oriented such that its polarisability ellipsoid axes are oriented with respect to the laboratory axes. The scattered light is detected at 90° to the incident beam, and passed through an analyser which is rotated to be either parallel to the incident electric field vector or perpendicular to it.

With the analyser parallel to the incident vector, scattering will be detected due to the α_{zz} tensor component, since:

$$I_{\text{scattered}} \propto |\mu_{\text{induced}}|^2$$

$$= |\alpha_{zz} E_{\text{incident}}|^2$$

---

* Strong inter-molecular interaction in non-ideal solutions and vapours may affect these results.

$$\propto |\alpha_{zz}|^2 I_{incident}$$

When the polariser is rotated to be perpendicular, scattering due to α_{zx} will be detected. The depolarisation ratio ρ_l gives the ratio $I_{perpendicular}/I_{parallel}$.

If the molecule rotates freely, the molecule-fixed properties α_{zz} and α_{zx} must be averaged. The result for a tensor (unlike a vector) is that there are two invariants under free rotation, related to the trace and anisotropic components of the molecular tensor:

$$\alpha^2 = 1/9(\alpha_{xx} + \alpha_{yy} + \alpha_{zz})^2$$

$$\beta^2 = 1/2[(\alpha_{xx} - \alpha_{yy})^2 + (\alpha_{xx} - \alpha_{zz})^2 + (\alpha_{zz} - \alpha_{xx})^2 + 6(\alpha_{xy}^2+\alpha_{yz}^2+\alpha_{zx}^2)]$$

The depolarisation ratio may be written to take advantage of these invariants[5], the result being:

$$\rho_l = 3\beta^2 / (45\alpha^2 + 4\beta^2)$$

ρ_l clearly depends on *which components* of the polarisability (for Rayleigh scattering) and derived polarisability (for Raman scattering) tensors are involved.

Since Rayleigh scattering is very highly polarised, the β^2 term must approach zero. Since the polarisability can not vanish the trace of the tensor can not disappear, and so this implies that the anisotropic components are zero and that the trace components are almost equal in magnitude ($\alpha_{ij} = 0$ for $i \neq j$, $\alpha_{ii}-\alpha_{jj} \approx 0$ for all i,j). The smallest values are noted for molecules with spherical tensors - like $C^{35}Cl_4$ - where the trace components are indeed equal.

The fact that some Raman bands in this highly-symmetrical molecule are depolarised indicates that the *Raman* effect allows anisotropic terms in the derived polarisability tensor; in CCl_4 certain bands have a ρ_l value of 0.75. The value $\rho_l = 3/4$ can only be derived if all trace terms are exactly equal - they cancel out of the expression for β^2.

1.2.10 Applications of group theory to Raman spectroscopy

The prediction of which vibrations will be Raman active through which derived tensor components can be greatly expedited by the application of group theory. Since a small part of this thesis involves determining the number, classification and activity of normal vibrations in a simple species, the basics will be briefly reviewed here.

Group theory allows use of the concept of symmetry in molecular spectroscopy. Symmetry operations are those combinations of symmetry elements (rotations about axes, inversions, and the like) which move an object such that its orientation in space is absolutely indistinguishable from the original position*. The collection of possible symmetry operations for a molecule define the molecular point group.

Certain combinations of symmetry operations exist that can not be broken down into simpler combinations; and when taken together, any complex combination of symmetry operations can be described by a linear combination of these basis functions. Each of these basis functions are labelled with a certain symmetry species; any more complex combination can be labelled with a linear combination of the symmetry species.

Each of the completely-independent symmetry species may be described by a representation. A representation in group theory has the meaning that any set of functions - matrices, for instance - may represent the actions of the symmetry operations, if the group of functions has the same combination properties (group table) as the group of symmetry operations. Since the representations describe the basis symmetry species, they can be called irreducible representations.

If matrices are used, a very convenient way of expressing the irreducible representation becomes apparent, as the sum of the diagonal elements of the matrix (the trace) may be either zero or an integer. The sign of the integer is helpful in labelling the symmetry species; if the irreducible representation is itself a linear combination of N functions (because no transformation could be applied to all the matrix representations and still generate an equivalent representation of the group), then the representation is said to be N-fold degenerate and the irreducible representation will have character N.

The characters of the irreducible representations are inserted into the character table of the point group under the generating symmetry operation. The symmetry species of the irreducible representations is decided by using a set of rules which briefly mentioned in order of application are:

- Degeneracy - N=1 gives A or B, N=2 gives E, N=3 gives T

---

* Assuming field-free space.

- Rotational symmetry - If N=1, rotation about the axis of highest symmetry is labelled A if the character is +1, and B if the character is -1.
- Inversion - if the group includes the inversion operation, character +1 implies symmetric with respect to inversion and is labelled g, and -1 if antisymmetric, labelled u.

The normal vibrational modes of a molecule can be shown to constitute a representation of the group. In addition, the nuclear displacement co-ordinates can be generated from a linear combination of the normal co-ordinates, which can be shown to have no effect on the outcome of the reduction procedure, since the normal modes are an orthogonal set.

This is extremely useful; a reducible representation of the molecule can be formed by considering the nuclear displacement co-ordinates as the basis, and using standard reduction equations to arrive at the combination of irreducible representations that describe the normal modes of the molecules.

The example below indicates the principle of the method - in essence, one probes the reducible representation with the basis functions to determine the number contained in the reducible representation derived from the nuclear displacement co-ordinates.

For water, the group of symmetry operations that apply fall under the C_{2V} point group. The diagram below shows the positioning of the rotation axis in the molecule - the x axis is normal to the page:

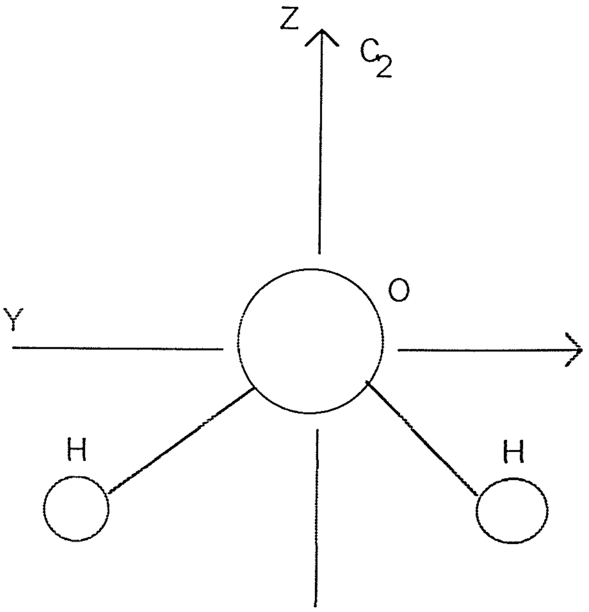

Figure 1.9 The water molecule.

A table is then drawn up:

Sym. Ops.	E	C_2	σ_{xz}	σ_{yz}	
RR (NDCs)	9	-1	1	3	
IR (A_1)	1	1	1	1	z, α_{ii}(x,y,z)
IR (A_2)	1	1	-1	-1	R_z, α_{xy}
IR (B_1)	1	-1	1	-1	x, R_y, α_{xz}
IR (B_2)	1	-1	-1	1	y, R_x α_{yz}

The "Sym. Ops." are the different classes of symmetry operation in point group C_{2V}. The "RR (NDCs)" is the reducible representation derived from considering whether each nuclear displacement co-ordinate (NDC) vector is left in the same orientation after an operation (+1), whether it reverses (-1), or whether it is shifted to another (identical) position (0) - summed over all the NDCs. The "IR ( )" entries are the characters of the irreducible representations (IRs) from the character group table. The extra column shows which vector components (x, y, z), tensor components (xx, etc.) and rotations (R_x) transform under that IR.

A reduction equation is then applied to the data set for each IR:

$$N = \frac{1}{n}\sum_R g\chi\chi'$$

Where N = number of times that IR appears in the RR

n = number of symmetry elements (number of classes × operations per class)

g = number of operations in a given class R

χ = character in class R in the RR

χ' = character in class R in the IR

This yields the result $N_{tot} = 3A_1 + A_2 + 2B_1 + 3B_2$. Hence there are 9 molecular motions, none degenerate. Of these, $A_2 + B_1 + B_2$ describe rotations, whilst $A_1 + B_1 + B_2$ describe translations. Hence the vibrations of water can be characterised as $2A_1 + B_2$.

Another particularly useful application of group theory arises because vector (dipole moment) and tensor (polarisability) elements have well-defined behaviour under symmetry operations of the point group. For a fundamental vibration to be Raman active, it must belong to a symmetry species which also contains one or more of the tensor components' irreducible representation. Similarly, the vibration will be IR-active if it is of the same symmetry species as a component of the vector representation. For the example above, all modes are IR and Raman active.

This selection rule is complementary to the gross selection rule discussed earlier. Certain vibrations may be neither IR- nor Raman-active, whilst others may have dual activity. In molecules with a centre of inversion symmetry, vibrations may be either IR or Raman active - or neither - but not both.

The final point that needs to be made concerns the use group theory. The intensity of the Raman effect - discussed below - can only be predicted, insofar as group theory predicts which modes will NOT be Raman active; it says nothing about the observed intensity of allowed bands. This is because the magnitude of the change in polarisability - which governs the overall intensity - is not predicted by group theory.

1.2.11 Intensity of the Raman effect

The intensity of Raman scattered light is usually very low. Typically, around 10^{-9}-10^{-12} Watts are scattered into a full 4π solid angle with approximately 1 Watt excitation power. Of this, only a fraction (about 5 % for f/1 collection optics) is collected - and of this, perhaps 5-10% reaches the detector.

The intensity of the Raman effect may be derived in a number of ways, from classical through to relativistic quantum mechanical methods. A useful derivation is the semi-classical derivation of Placzek[6], where the problem is treated as quantised matter in contact with a classical radiation field.

The result of this approach is that the total (or integrated) scattered intensity into a full 4π solid angle due to a vibrational transition from state l to state u may be expressed for linearly-polarised excitation with collection at 90° as:

$$I_{ul} = N.f_l.I_0.\sigma_{ul}$$

N represents the number of scattering species illuminated, and f_l the fraction of this number in the lower state, l, whilst I_0 is the incident intensity (W/cm^2). The scattering cross section σ_{ul} (cm^2) for a given vibrational normal mode m of degeneracy n under the above conditions is:

$$\sigma_{ul} = [2^7.\pi^5/3^2.(\nu_0-\nu_m)^4.n.(b_m)^2.(3\alpha_m{}^2 + 2/3\beta_m{}^2)] \,/\, [1-e^{\{-\Delta E/kT\}}]$$

where ν_0 = the excitation wavenumber, ν_m is the vibrational wavenumber (positive for Stokes scattering), $\Delta E = h\nu_m c$, the fundamental constants take their usual meaning, $(b_m)^2 = h/(8\pi^2 c\nu_m)$, and $\alpha_m{}^2$ and $\beta_m{}^2$ take on their meaning as the rotational invariants of the derived polarisability tensor for normal mode m. Notice the dependence of the intensity on the square of the derived polarisability components through the rotational invariants.

Also, simply focusing the light to produce a higher intensity spot will not produce more Raman scattering; the area of the focused beam decreases, so fewer molecules are irradiated within the field of view of the spectrometer. The sampling volume of the spectrometer remains the same; more photons are simply incident on a smaller area of the sample.

Since in general collection is made over a finite solid angle, at a fixed angle with respect to the excitation direction, with a given polarisation state, on a material with refractive index different from the surrounding air, corrections must be applied to even this most basic of formulae. In addition, the effect of absorption of both laser beam and Raman scattering on scattered intensity is ignored, along with heating effects on the partition functions.

In general, calculations of this quantity have been very complex, and are barely reliable; in addition, the predicted dependency on excitation frequency is often not observed, deviations being due to the occurrence of resonance effects between the excitation wavelength and electronic transitions of the molecule. The effects of these resonance processes is to significantly increase the intensity of the scattering, whilst depolarisation ratios and selection rules are also changed. Nevertheless, the idea of the cross-section is still discussed with respect to scattering efficiency calculations and relative intensity measurements.

1.3 Implementation of the Raman experiment

Chemical structure may be inferred by measuring the spectrum of Raman shifts, and correlating band positions to bond characteristics. Put simply, *a given Raman shift often signifies a certain bond*. Better than this, each molecule has a *unique* spectrum which greatly aids identification.

The Raman shift is usually presented as $\Delta\nu$ (cm^{-1}) = $\nu_{laser} - \nu_{scatter} = \nu_{vib}$ where $\nu_{scatter}$ is experimentally determined. Raman spectra usually range from between 0-4000 cm^{-1} shift, zero shift representing the Rayleigh line position, a negative value indicating anti-Stokes scattering.

In essence, the Raman experiment requires that the sample - solid, liquid, or gas - be irradiated with intense monochromatic light, and that the Raman scattered wavelengths generated are efficiently collected and separated from the intense component at the laser wavelength, followed by determination of the wavelengths of the scattering.

1.3.1 Classical techniques

Many excellent reviews of the classical Raman scattering experiment exist in the literature[8] - only the general points will be raised here*. Rayleigh line rejection and wavelength-analysis are usually accomplished using devices based on diffraction gratings to spatially disperse the collected light. Such devices are generally termed spectrographs (if many wavelengths are simultaneously measured using a multi-element detector) or spectrometers (if the scattered wavelengths are sequentially scanned across a single-element detector).

The requirement for strong attenuation of the laser beam leads to the use of double or triple grating devices - usually double grating spectrometers operated in additive dispersion, or triple-stage spectrographs comprising a single dispersive grating after a double-subtractive filter. Single spectrographs may also be used, providing the attenuation of the laser line with additional filtering is strong enough.

The intrinsic weakness of the Raman effect leads to the requirement for very sensitive detectors - until recently, either the cooled photomultiplier tube operated in photon counting mode, or multichannel devices such as the linear photodiode array with electron multiplier plate - along with powerful excitation sources, typically the argon ion (Ar^+) gas laser at around 488.0 nm (blue) or 514.5 nm (green) providing around 1-2 Watts at the sample maximum. Much of the above equipment is complex, expensive, difficult for the non-expert to align or maintain, and requires several specialist facilities - cooling water and 3-phase supplies for lasers; for certain detectors, liquid nitrogen for cooling.

Given the complexity of the experimental apparatus, optical efficiencies are small - and therefore exposure times long if high resolution or low laser power density (to avoid sample damage) are required. This places constraints on stability and means calibration becomes a significant issue; this presents difficulties for repeatable analyses. In general, a controlled environment is required. At the very minimum, the

---

* Prism-based systems with arc-lamp excitation and photographic analysis are excluded from this summary.

experiment requires black-out facilities and a reasonably clean environment; air-conditioned rooms with anti-vibration tables are not uncommon for complex experiments.

The chances of such equipment finding major applicability may seem slim, yet prior to 1940-1950 the Raman effect was very widely used because of the major advantages over the competing technology for vibrational spectroscopy, dispersive mid-IR absorption spectroscopy.

1.3.2 Advantages of Raman scattering over mid-IR absorption

Apart from fundamental considerations involving the inherent weakness or non-activity of certain species' vibrations in the IR, practical considerations include:

- Water is an excellent solvent for Raman analyses, since its Raman spectrum is very weak. Hence aqueous solution studies are facile, providing the species' concentrations and scattering cross-sections are suitably large.
- Glass is an excellent vessel for sample cells, as it too exhibits weak scattering; in contrast, glass is opaque in the IR, with other materials being unsuitable on grounds of solubility, mechanical strength, toxicity, or cost.
- High temperature studies are facile, since the blackbody radiation emitted by the sample is far too long in wavelength to appreciably affect the visible Raman spectrum.
- The sample need not be specially prepared to collect a spectrum - resulting in a fast analysis, without spectral interference from mulling or solvent features.
- No contact is necessary - this means many diverse shapes and sizes may be studies, including sampling in low-temperature or high-pressure cells, increasing the versatility of the experiment.
- Since no contact or preparation are required, many samples can be studied non-destructively - important for scarce or precious samples.
- In addition, small samples may be studied far more easily with optical microscopes, which also yield a higher spatial resolution, that with indirect-view IR microscopes.
- Also, fibre-optics operate far better in the visible - low-loss material is far cheaper/km in the visible than in the IR, plus materials are non-toxic.

1.3.3 The rise of IR interferometry

In the mid-1960s the development of the interferometric far-IR experiment meant that the much-improved throughput of the interferometer plus attendant multiplex detection advantages made it the technique of choice for the far-IR. Simplicity, reliability, sensitivity, and accuracy attracted other potential users in stellar and very-high-resolution IR spectroscopy. This meant that large instrument companies became interested, at first in research markets, then in analysis - eventually the cost reduced significantly. Especially beneficial to the technique were developments in electronics (FFT firmware) and the development of low-cost amplitude-dividing Michelson interferometers and derivatives.

1.3.4 Problems with visible excitation in analytical Raman studies

However, these factors alone would still not have resulted in Raman spectroscopy falling behind in analytical usage. The Raman experiment using visible excitation suffers extremely badly from one very major drawback - fluorescence.

It has been estimated[9] that fluorescence results in 90-95% of all visibly-excited applications of industrial interest being significantly hampered, whether the fluorescence is intrinsic to the analyte or due to impurity. The effect of fluorescence is usually to superimpose a strong and featureless broad continuum over the Raman scattering, effectively obliterating it.

It is unsurprising that many different methods have been examined, attempting the reduction or elimination of fluorescence. It has long been assumed - with good reason - that the number of systems that exhibit fluorescence increase as the excitation wavelength shortens. This can be viewed as reflecting that more molecular species have electronic absorption bands in the blue/near-UV than in red/near-IR, therefore the likelihood of exciting fluorescence should be reduced with red excitation.

This is undoubtedly true - indeed, early applications of the Raman effect soon identified red lines from arc lamps as useful in reducing the effect of fluorescence interference from darkly-coloured materials[10]; later applications of red/near-IR laser lines confirmed this. However, attempts to improve overall performance of long-wavelength spectrometers were hampered by poor red performance of detectors, low laser output - but most importantly: the fact that the reduction in fluorescence was simply not high enough.

1.3.5 The inception of the FT-Raman technique

Only with the introduction of the FT-Raman experiment[11] and its recent developments[12] has the aim of fluorescence reduction been truly successful. FT-Raman spectroscopy utilises a long-wavelength near-IR laser source *beyond 1 μm* and a near-IR optimised interferometer/detector combination. This approach combines many of the advantages of interferometry (high throughput, good resolving power, excellent precision, simplicity, and cost), Raman spectroscopy (ease and versatility of sampling), and near-IR excitation for fluorescence avoidance.

Although a very recent application, the interferometric Raman experiment had been considered[13] - and even tried[14] - in the 1960s. Several problems figured strongly in the results - these were due to problems rejecting the wavelength component at the laser frequency, and the issue of how noise affects multiplex techniques using detectors where the noise is correlated to the signal, an issue which limits the usefulness of multiplex techniques with shot-noise-limited detectors in many applications. However, visible FT spectroscopy is used in some very high resolution atomic emission experiments, and in some stellar observation telescope devices. It generally requires expensive interferometers with high-performance optics to provide the necessary tolerances for operation right through to the near-UV (below 400 nm). In addition, the Nyquist limit must be suitable to cover the wavelength range of interest. The use of visible FTS in the Raman experiment is not restricted by cost or by theoretical and experimental difficulties - *but by fluorescence*, the same problem as dispersive spectroscopy. However, several quite successful visible FT-Raman studies of gases have been undertaken, and will be commented on in chapter 6.

1.4 Instrumentation

The *major* advance of FT-Raman spectroscopy is the use of near-IR excitation on a near-IR interferometer to avoid fluorescence. So successful has this been, that only 15-20% of all industrial analyses are now estimated to be unsuccessful[9]. This situation would not have arisen without reliable interferometers, lasers, and detectors in the near-IR. To appreciate why near-IR Raman is dependant on FT-spectrometry, the interferometer needs to be considered in some detail.

1.4.1 Basic layout of a near-IR Michelson-type interferometer

The necessary features of the basic interferometer can be reduced to the diagram in figure 1.10. Assume the light incident on the beamsplitter is monochromatic and perfectly parallel to the optic axis. Light incident on the beamsplitter is divided in amplitude. The reflected beam falls onto a moving mirror. The transmitted component reflects from a stationary mirror. The beams traverse the same path on return to the beamsplitter - the two return beams are themselves split, where the interference takes place, and yield resultant beams towards both detector (I_d) and source (I_s).

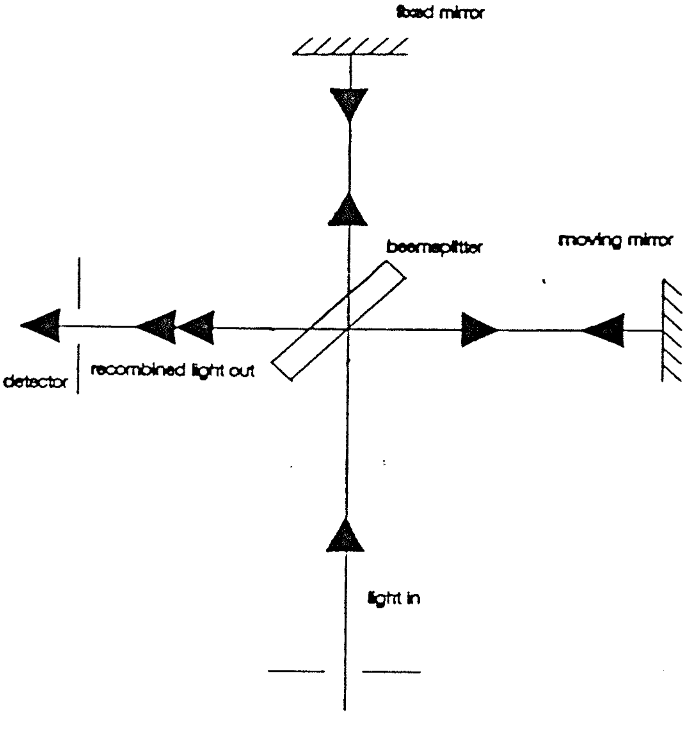

Figure 1.10 Simple representation of the Michelson interferometer.

I_d and I_s depend on the optical path difference (OPD) introduced by varying the position of the moving mirror. The function $I(\Delta)$ is the *interferogram*, the intensity as a function of the OPD, Δ. In terms of the incident intensity I_0 the intensity falling onto the detector is:

$$I_d(\Delta) = I_0/2[1 + \cos(2\pi\Delta/\lambda)]$$

I_d varies as a function of the OPD *and* of the incident wavelength. At zero OPD, the signal is a maximum - going through a further maximum every time the OPD equals an integer multiple of λ. Note that the OPD is twice the mirror displacement, and that the actual frequency of modulation depends on the velocity of the moving mirror[*]. For radiation around 1 µm, this equals 1 KHz at scan speed 1 mm/s. Note also that the interferogram is the sum of OPD-invariant ("d.c.") and cosinusoidally-varying ("a.c.") terms.

The beam returning to the source is also cosinusoidally-modulated at the same frequency. Conservation of energy demands that the sum of optical power in the output beams equal the input power in this simple case. Since both the beams returning to the source experience one more reflection than the beams travelling towards the detector, this results in the interference term being 180° out-of-phase:

$$I_s(\Delta) = I_0/2[1 - \cos(2\pi\Delta/\lambda)]$$

The exact balance of optical power in each "arm" of the interferometer depends on the beamsplitter characteristics. If the beamsplitter has reflectivity R and transmissivity T:

$$I_d = (2RT)I_0[1 + \cos(2\pi\Delta/\lambda)]$$

$$I_s = (R^2+T^2)I_0[1 - \cos(2\pi\Delta/\lambda)]$$

Hence the ideal beamsplitter has R=T=0.5, and the maximum signal attainable towards the detector is $I_0/2$. This is difficult to achieve in practice; R and T vary with wavelength, so that when collimated polychromatic light - continuum or line spectrum - is incident on the beamsplitter, the efficiency varies with wavelength.

In fact, the interferogram with many wavelengths is a sum of the cosinusoids of the individual wavelengths. This function is strongest at zero optical path difference (centreburst), and decays towards the wings - the rate of decay depending on the number of wavelengths in the sum. Raman interferograms tend to appear more "periodic" at first glance, since there are few terms in the sum if the background is negligible. Since the IR experiment relies on absorption, the IR interferogram decays very quickly because many wavelengths contribute to the signal.

---

[*] Different scan speed required for different detector response times.

It should be noted that the individual intensities of each component wavelength add; since the OPD is longer than the coherence length of the radiation (related to source optical bandwidth) the signal at the detector is not due to superposition of individual fields integrated to obtain intensity, but the superposition of intensities:

$$I_D(\Delta) \propto \sum_{\lambda} I \cos(\frac{2\pi\Delta}{\lambda})$$

At the centreburst, all the intensities add together - as infinite OPD is approached, the intensity tends to a limiting value. For polychromatic interferograms, the value at infinite OPD is flat and in a perfect interferometer, would be equal to $I_0/2$. This is important, because it suggests (correctly) that the efficiency of the ideal interferometer is 50%, as the average energy in each arm of the interferometer is half the input power. Providing the intensity does not vary during the collection of an interferogram, stray light will only contribute a zero offset, and will affect the untransformed "d.c." term only; noise from the stray light will, however, be present on the observed signal so the exclusion of stray light is still desirable.

The model above is unrealistic for several reasons - for instance, it ignores the effect of absorption and dispersion of polychromatic light in the beamsplitter. Dispersion results in each wavelength experiencing a slightly different delay in phase; since the initially-reflected beam in the detector arm only traverses the beamsplitter once whilst the initially-transmitted beam traverses it three times, resulting in an imbalance. To compensate for the imbalance in absorption and dispersion, a compensator plate (made of the same material as the beamsplitter) is incorporated in the simple design above between the beamsplitter and the moving mirror.

The effect of a wavelength-dependant phase delay on the interferogram is to introduce components that are not maximal at zero OPD*. The signal can not then be wholly described as a sum of cosines, but must be related to a sum of sines and cosines. This can present great problems in the analysis stage as band shape and intensity may become distorted, and data may be completely lost; therefore, several methods have been devised to correct the phase of the interferogram to be described accurately by a sum of cosines. These corrections are applied automatically to the data, and are not consider further here.

If data is collected on both sides of the centreburst, the interferogram is said to be double-sided; if the data is collected on mirror travel to and from the position of

---

* Many phase errors accrue from processing electronics and not optics.

zero OPD the data is said to be collected bi-directional. It is equally possible to have one-sided, uni-directional sampling. The exact method depends on the chosen method of phase correction and scan speed, amongst other considerations.

The efficiency of the interferometer is obviously affected by the optical constants R and T and by the component quality - especially of mirror surfaces and beamsplitter plates and coatings. In the near-IR (800 nm - 2500 nm) several solutions exist - popular mirror coatings being protected silver, enhanced aluminium, and over-coated gold. Quartz is the beamsplitter of choice, although carefully-prepared KBr is adequate. Overall, the efficiency of a good near-IR interferometer will be around 25-35% - about the same as for a single diffraction grating spectrograph operating in first order dispersion close to the grating blaze angle.

1.4.2 Analysing the data - the Fourier transform

The signal from the detector is a function with periodic components. To work backwards towards its spectrum by "harmonic analysis" as did Michelson would be wholly inappropriate for modern analytical techniques - especially since the mathematics of Joseph Fourier[15] give a a powerful method to analyse the data.

Essentially, the Fourier transform (FT) maps data from one functional domain into the inverse domain - for instance, time⇔frequency (s⇔s^{-1}), and optical path length difference⇔ wavenumbers (cm⇔cm^{-1}). In doing so it produces the spectrum of the starting function.

For our purposes, the periodic interferogram is decomposed, and represented as a histogram of its constituent frequencies at the correct intensity ratio. The OPD-invariant term of the interferogram can be ignored, as this "d.c." terms simply represents a biasing about the x-axis. Hence the "a.c." term is often represented as symmetrically disposed about the x-axis*.

The analysis relies on a very useful property of cosine functions. If a cosine is multiplied by another cosine and the result integrated, the integral must be zero for all cases where the phase and frequency of the cosinusoids differ. If phase and frequency match, the resulting integral is proportional to the product of the amplitude of the two cosines.

This is exploited in FT spectrometry in the following way. The interferogram is sequentially "probed" by multiplication with a cosine function of unit amplitude.

---

* It should be noted that for a perfect cosinusoid. this results in two crossings of the x-axis ("zero-crossings") per period.

The orthogonality of cosines "filters out" the component at that frequency in the interferogram, and the magnitude is given by the amplitude of the integral.

Problems arise from the sheer volume of calculation required. The only sensible manner to carry out the computation is using a digital computer or dedicated firmware. The calculation was greatly facilitated by the introduction of the fast Fourier Transform (FFT) algorithm, by Cooley and Tukey[16]. This reduces the number of computations requited to carry out the FT hugely, and so considerably speeds the calculation*.

1.4.3 Resolution in FT spectroscopy

It is patently obvious that the interferogram can not be recorded to infinite path difference - the maximum OPD usually attained even in very-high-resolution (VHR) spectrometers is around 2 m. This affects the FT process, as basic Fourier mathematics operates by integrating over infinite limits. The effect of the truncation of the data set is to introduce strong oscillatory sidebands onto the spectral lines. This "ringing" can be smoothed in a process known as apodisation. The apodisation process amounts to truncating the interferogram with gently-varying functions, instead of imposing a rectangular "box-car" function on the interferogram. Unfortunately, no single best function to cover every experiment exists. Since the degree of apodisation affects the resolution a suite of apodisation functions are usually made available, chosen before data acquisition, and applied without further user-input.

The resolution attainable depends on the optical path difference. In order to resolve two closely-overlapped features, a suitable length of interferogram must be recorded. To show this, consider the interferogram of two monochromatic lines of equal intensity, and wavelength λ_x and λ_y:

$$I_d = I/2[1+\cos(2\pi\Delta/\lambda_x)] + I/2[1+\cos(2\pi\Delta/\lambda_y)]$$

This may be rewritten, using a simple trigonometric identity, as:

$$I_d = I + I[\cos(2\pi\Delta\{\lambda_x+\lambda_y\}/2\lambda_x\lambda_y)\cos(2\pi\Delta\{\lambda_x-\lambda_y\}/2\lambda_x\lambda_y)]$$

---

* The number of calculations reduces from n^2 to (n)log(n) for an n-point data set. Typically, n is ca. 4000

This shows that there is a carrier wave term, $\{\lambda_x+\lambda_y\}$ and a modulation term, $\{\lambda_x-\lambda_y\}$. In order to determine the periodicity of the modulation simply by observation of the interferogram, one complete period of the modulation must be observed. The *period* of the modulation is *inversely* proportional to the *difference* in line position, so *closely-spaced lines require more interferogram to be recorded to resolve them.* Hence the resolution attained is inversely proportional to the optical path difference, $\delta\upsilon = 1/\Delta$.

1.4.4 Sampled data

In actuality, the data collected is not continuous, as continuous data simply is not required. Discrete data may be used, providing the effects of a discrete data set are taken into account. A well-known theory in communication engineering called the Nyquist theorem[16] shows that the frequency of a continuous periodic function may be truthfully determined from discrete data if the function is sampled *at least twice per period* - that is, two samples are needed to solve the coupled equations for amplitude and frequency of an arbitrary cosine function. The Nyquist limit is the frequency above which data is no longer sampled twice per period. Above this limit, data becomes more difficult to interpret; a phenomenon known as aliasing occurs, where the spectrum derived by the FT process is "folded" about the Nyquist frequency, and may overlay the spectrum below the Nyquist limit.

Sampling intervals are derived from a reference Helium-Neon (HeNe) laser source within the interferometer, which follows a near-identical beampath to the source radiation through the interferometer, also experiences interference as a function of OPD, but is detected at separate photodiodes. Every time the HeNe signal zero-crosses, corresponding to one signal per 316.4 nm OPD, a timing signal is generated. Since there are two zero-crossings per cycle of the HeNe fringes, we have a Nyquist limit of 15803 cm^{-1}. Electronic filters are often used to remove components around the Nyquist limit to avoid aliasing. The HeNe signal may be processed to yield extra zero-crossings, and these used to push the Nyquist limit into the near-UV.

The discrete data set requires the use of a discrete (DFT) and not continuous (CFT) Fourier transform. This is a well-understood method; however, the spectral data available from the DFT is limited in the sense that data is "missing" from the digitised interferogram. In passing, an example of a problem is the consideration of what happens to data at spectral positions that do not correspond exactly to sampled frequencies. Although beyond this simple introduction, the data from such frequencies is weighted into the nearest two data points.

For the most faithful representation of band shape, many data points must be used to define the band - a large number of frequency-domain data points must be determined. In the FT technique, this means a long interferogram must be recorded. The resolution attainable for a given OPD can be rewritten as $\delta\upsilon.N.I = 1$. Here, the OPD is given by the number of data points (N) multiplied by the interval between them (I). Hence, twice the number of data points must be collected and processed for a given interferogram sampling rate in order to achieve twice the resolution.

Note that increasing the interferogram sampling rate *whilst leaving the number of samples taken the same* can NOT increase spectral resolution. In the above equation, as the sampling rate increases, *the interferogram sampling interval goes down*. The fallacy of the opposite claim can also be seen by considering behaviour at abstract limits - what occurs on continuously sampling a data set of zero length. Put another way, increasing the sampling rate on the interferogram is *only* required if higher maximum spectral frequencies need to be studied.

1.4.5 J-stop effects

Resolution is not governed only by the length of interferogram collected - but also by the finite source required for finite optical throughput. Finite source size means that there are off-axis rays propagating through the interferometer. A beam stop is placed at the image of the detector, to limit the cone angle of the source radiation to try to minimise the effect of the off-axis rays; this beam stop is known as the Jacquinot stop, or J-stop.

Consider an interferometer, uniformly illuminated with monochromatic light, so that the rays falling onto the beamsplitter define a cone of half-angle α to the optical axis. The central ray, lying on and therefore parallel to the optical axis, experiences an optical path difference Δ equal to twice l, the moving mirror retardation.

$$I_{on}(\Delta) = 2RTI_0(1+\cos\{2\pi\Delta / \lambda\})$$

However, the extreme ray that lies at an angle α to the optical axis experiences a *shorter* difference in optical path, for the same mirror displacement. The optical path difference is given by:

$$\Delta_{ext} = 2l.(1 - \alpha^2/2)$$

Hence

$$I_{off}(\Delta) = 2RT(1+\cos\{2\pi\Delta[1 - \alpha^2/2] / \lambda\})$$

The interferogram recorded from this ray will have a characteristic periodicity *longer* than that of the on-axis ray. The FT process *can not discriminate* between on- and off-axis beams; it simply operates on signal produced by the detector. In order for a given maximum OPD to yield the desired resolution, the half cone angle of the source must be kept below a limiting value. This can be estimates as follows. The half-angle α is related to the radius of the entrance aperture and the focal length of the collimating optic (both in mm):

$$\tan \alpha = r / f$$

The paraxial approximation is assumed to hold, so that $\tan \alpha \approx \alpha \approx r / f$

$$\therefore\ 1 - (\alpha^2) / 2 = 1 - (r / f)^2 / 2$$

However, this is also the ratio of the wavenumber difference ν_{off} / ν_{on} - which is a measure of the degradation in resolution for a given J-stop size. For r = 4 mm and f = 125 mm as for a Perkin Elmer 1700 series interferometer, $\nu_{off} / \nu_{on} = 0.9995$. That is, at 10,000 cm^{-1}, there is no point in attempting to achieve 4 cm^{-1} resolution with a 4 mm radius J-stop as the divergence of light limits the resolution to about 5 cm^{-1}. Hence for high-resolution spectra, the number of data points collected must be high enough to define the bands' profile adequately and the J-stop must be small enough to limit the off-axis cone angle in order to give a broadening less than the desired resolution.

Another effect of finite source size is that the *measured* wavelength is *greater* than the *true* wavelength. As the interferogram is recorded each component ray in the cone of light illuminating the beamsplitter produces a cosinusoid of characteristic period. The on-axis ray has periodicity λ, and the FT correctly interprets this as indicating the input wavelength was λ. Therefore, on-axis ray gives rise to no error in the measured wavelength. On the other hand, for a given value of mirror displacement l (=Δ/2) an off-axis ray observes - as shown above - a *shorter* optical path difference, so that the characteristic periodicity in the interferogram is $\lambda / [1-\alpha^2/2]$. In other words, *longer* than the on-axis. The FT process incorrectly interprets the wavelength as indicating a longer wavelength input signal.

The effect is to shift every band in a recorded spectrum to *lower wavenumber*:

$$\upsilon_{recorded} / \upsilon_{true} = 1 - \alpha^2/2$$

When the weighting of off-axis rays in the ray-bundle entering the interferometer is taken into account, a smaller shift is actually seen. The effect can be dealt with simply by averaging the shift experienced for an on-axis ray - zero, of course, so $\alpha = 0$ - and extreme off-axis ray, at $\alpha = r / f$:

$$\upsilon_{recorded} / \upsilon_{true} = [(1) + (1 - \{r / f\}^2 / 2)] / 2$$

$$\therefore \upsilon_{recorded} / \upsilon_{true} = 1 - (r / f)^2 / 4$$

Using a small J-stop reduces the apparent error in band positions *no matter what the OPD-determined spectral resolution*. The OPD-determined resolution defines the number of points collected; the J-stop width may be usually selected independently. Of course, smaller J-stop size means smaller energy throughput, and lower signal-to-noise ratios for given exposure time and source brightness.

Conversely, if band shape needs to be well-defined for frequency measurement but the linewidth is such that high resolution in not required the OPD-defined resolution may be increased, to over-sample the data, whilst leaving the J-stop open, to give good throughput.

1.4.6 Advantages of FT spectrometry

The optical advantages of the interferometer are very well-known. Briefly summarised, they are presented below:

The Jacquinot (or throughput) advantage- for spectrometers operating at equal spectral resolution and covering the same spectral range, interferometers have higher optical light-gathering power (expressed as étendue or luminosity) than grating- or prism-based spectrometers[17]. Throughput may be defined at any point in an optical system as the product of solid angle with cross-sectional area:

$$\Theta = \Omega.A$$

This wavelength-independent property is a constant of the system, being conserved throughout a well-designed optical system. In a Raman experiment, the throughput should be source-limited - that is, limited by the collection optics' solid angle times the area of the spectrometer entrance aperture. For near-IR interferometers, the improvement in comparison with a grating system has been estimated to be around a factor of 100-200; this comes the derivation:

$$\Theta_{\text{Interferometer}} / \Theta_{\text{Grating}} = 2\pi.F / l'$$

where F = focal length of collimating optic and l' = height of slit. This ratio may be around 20-30, for well-designed systems, therefore the advantage simply on light-gathering grounds of an interferometer is about 2 orders of magnitude. Hence their use in low-light-level applications.

The Fellgett (or multiplex) advantage - every point in the interferogram is a superposition of the individual interferences from each wavelength, hence each point contains information on each wavelength. FT spectroscopy is a multiplex technique - many signal channels are mixed together and detected at a single detector. Each wavelength is "coded" by the interferometer; each has a unique modulation frequency below the Nyquist limit. The FT reproduces the spectrum of the signal as a unique solution, because the "code" used was orthogonal - remembering that each component can be represented as a cosine function, and the orthogonality of cosines.

The advantage of multiplex detection can be stated in several ways, although the outcome depends on the dominant noise process of the experiment. In the case of FT-Raman spectroscopy, this means the detector. Detector-noise-limited experiments show no correlation between signal flux and noise level - that is, if the signal is increased, the noise remains the same.

The most common rendering of the Fellgett advantage[18] is as follows. If the total number of wavenumber increments to be detected *in a given time* is N, a true multiplex method views the signal from each wavenumber increment N times longer than the equivalent sequential scanning experiment. During this effective integration, noise also builds up - except there is no correlation with total signal level, so that this tends to average to $\sqrt{N}$. Hence the advantage in SNR of multiplex versus sequential detection in a detector-noise-limited experiment is $N / \sqrt{N} = \sqrt{N}$. It must be emphasised that the equivalent experimental conditions for both spectrometer and interferometer encompass spectral range, resolution, optical efficiency, and signal flux.

For N=100, we would predict a gain in SNR of 10 from this simple approach. However, many subtleties are ignored in the above derivation; in reality, the SNR gain is a complex function to derive, and may yield a (significantly) lower result than the simple model.

The Connes advantage - Wavelength precision is absolutely critical for co-adding many spectra to derive gains in SNR. The gain in SNR on co-adding N data sets is $\sqrt{N}$, to good approximation - although chapter 6 contains additional comments on the validity of this approach for very large co-added data sets. The Connes advantage describes using a monochromatic reference source[19] to achieve good relative frequency precision, which expedites this. Co-addition is a very common way to achieve good SNR in many experimental techniques; it is *not* a property only of interferometric spectrometers[*] .

However, since the HeNe laser used for generating timing pulses is extremely stable in frequency, it is an excellent internal calibration for wavelength precision, which may in turn be related to absolute accuracy, with care - since angular misalignment of the HeNe causes wavelength-dependant frequency shift.

Spectral subtraction studies are straightforward using FT spectrometry as a result of the Connes advantage. Spectra must overlay exactly for meaningful results in low-concentration systems. However, this must be treated with some care. If the J-stop is unevenly illuminated, then spectral shifts arise. These effect may be present using powders; for liquids, the J-stop is more evenly illuminated - and sample cells may be filed *in situ* to so that alignment errors due to sample placement remain approximately constant.

It should be noted that the concepts of throughput and efficiency refer to different aspects of an optical system - the light-gathering power and the wavelength-response, respectively. They are not interchangeable - the former is wavelength-independent, the latter obviously not. Intuitively, it is possible to design a low-efficiency, high-throughput device and get the same performance as a low-throughput, high-efficiency optic. Signal flux must also be taken into account when determining the amount of light incident on the detector - whilst the signal-to-noise ratio (SNR) in turn depends on the noise characteristics of the detector, and the length of time available for the experiment. Describing a spectroscopic experiment analytically using these four parameters is, in general, very difficult, and rarely undertaken in practice.

---

[*] It must also not be confused with the Fellgett advantage.

1.4.7 FT-Raman instrumentation at Southampton

The advantages of FTS discussed above hold the key to understanding why FT-Raman is the method of choice for near-IR excited Raman spectrometry beyond 1 μm:

- The theory section showed that the intensity of linear Raman scattering drops dramatically for equal excitation powers on moving from 488 nm to 1064 nm excitation; a decrease of about 23-fold, for a band close to the Rayleigh line.
- More seriously, the detectors available are 100 - 1000 times less sensitive than those available in the visible region.

The layout of the Perkin Elmer 1700 series instrument is given below. Most of the work in this thesis was carried out on the second development prototype or the first commercial 1700 series interferometer:

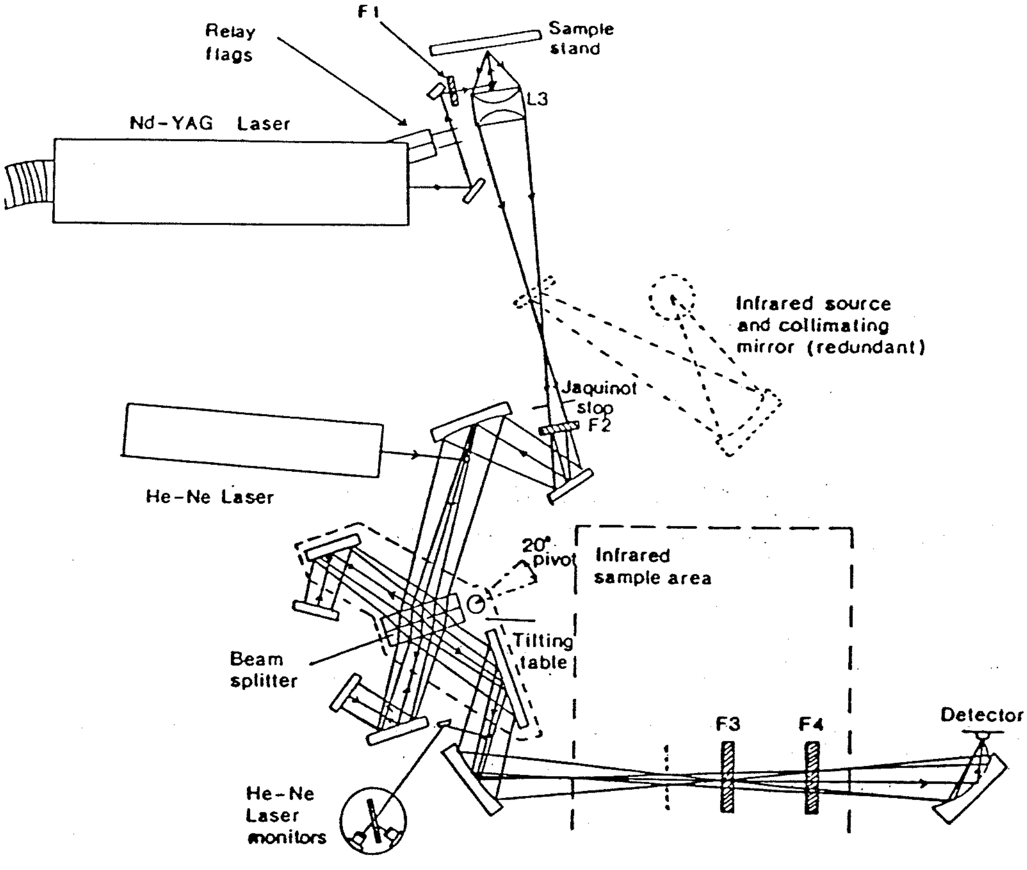

Figure 1.11 The PE 1700 series FT-Raman spectrometer optical layout

A near-IR laser is focused onto the sample. The scattering, along with luminescence and reflected light, is collected and focused into the interferometer. The component at the Rayleigh wavelength is rejected, the light modulated by the interferometer, and focused to the near-IR detector.

Notice that the interferometer must come after the sample, as this is the source for our experiment. In IR experiments, the sample may come before or after the interferometer. It does not matter whether the sample is placed in modulated light - the most important aspect is that the interferometer acts to code each wavelength, so that the FFT determines the absorption spectrum; in the Raman experiment, the scattering must be modulated and therefore must come before the interferometer.

The laser is usually a lamp-pumped (on 1700 series) or diode-laser-pumped (on 2000 series) Neodymium-doped Yttrium Aluminium garnet (Nd^{3+}:YAG) device, operating in continuous-wave emission at 1064.1 nm (9398 cm^{-1}) in air. The laser should not limit the experiment - thus a maximum power around 2-3 Watts, linewidth less than 0.1 cm^{-1}, and high output stability are demanded. Stability is critical to the optimisation of the experiment - and resulted in active-feedback stabilisation being fitted to all the lamp-pumped systems. This is discussed later as part of chapter 6, during the gas-phase experiments. The diode-based systems are very new and extremely convenient, requiring no cooling and having low power consumption. The lamp-pumped systems require both cooling water and 415 volt 3-phase a/c supplies.

In addition to the laser, a plasma-line rejection filter is required. This has a very high transmission at the laser wavelength, and very high blocking elsewhere - it should also have a passband width that complements the Stokes/anti-Stokes performance of the Rayleigh line filters. Non-ideality can be tolerated, providing the low-shift plasma lines* do not mask out any low-frequency Raman shifts of the sample.

The removal of the laser line from the collected scattering is absolutely critical. Its sheer intensity (Rayleigh scattering plus reflection) causes the interferogram to be dominated by a huge component at the laser wavelength, with the Raman sidebands appearing almost as "noise". Since the laser line at 0 cm^{-1} shift is far more intense than the Raman signal, "ringing" extends hundreds of wavenumbers into the spectrum, dwarfing the Raman spectrum. Worse still, the FT process redistributes noise; although not important to report in depth, the effect is that noise

---

* Plasma lines can be recognised as they appear more strongly when the sample is replaced by a mirror.

at each wavelength is weighted into all other wavelengths during FFT. The "ringing" and Rayleigh line noise simply obliterates the Raman spectrum.

The intensity also often saturates the near-IR detector, and can even "blind" the HeNe fringe detectors, crashing the interferometer - although this can be avoided by placing HeNe bandpass filters in front of the fringe diodes. The least that happens is that the detector may exhibit non-linear response, which gives erroneous spectral positions and intensities.

Rayleigh rejection on the 1700 series instruments was achieved by use of multilayer dielectric filters, which are so designed to be extremely reflective at the laser wavelength. Their performance parameters (optical density at the laser wavelength, spectral bandwidth of blocking region, transmission in pass bands, variation in profile) developed astonishingly quickly. In order to achieve suitable blocking, four filters were usually employed, installed at the J-stop and in the redundant IR sampling compartment. Since the performance of these filters depends on angle of incidence, the positioning was not ideal, since the light passing through them was diverging - however, the first development filters were small and required installation at a beam waist, easily accessible for replacement.

System 2000 spectrometers operate with larger filters in collimated light, away from focus points. However, the major change is that laser rejection is achieved by holographic notch filters - an alternative method to selectively reflect light. This is one of many alternative technologies available; others are based on transmission, scattering, or absorption.

The detectors used for the near-IR experiment need to be sensitive over the wavelength range 1-1.8 μm, as the Raman scattering excited at about 1 μm falls out to around 1.7 μm. The only two commercially-available detectors with good enough performance are the Germanium photoconductive and the InGaAs photovoltaic devices. In routine applications, InGaAs is more suitable, because Ge requires cooling to liquid nitrogen temperature to operate. The performance of near-IR detectors needs to improve markedly before scanning spectrometric or spectrographic applications beyond 1000 nm become routinely advisable; a few researchers have tried other techniques beyond 1 μm, with little prospect to challenge the interferometric experiment for most tasks.

1.4.8 Sampling problems in FT-Raman spectroscopy

FT-Raman has greatly alleviated the number of analyses fatally compromised by fluorescence. Although FT-Raman offers many advantages to sampling over mid-

IR methods, over the last years at Southampton certain features have come to light that need to be kept in mind:

- Black or very darkly-coloured materials - these give very poor spectra. The reason is usually strong laser absorption, followed by fluorescence, thermal emission, or pyrolysis. In general, FT-Raman uses high laser powers - 200-800 mW - so that heating material always causes problem.
- Elevated temperatures - thermal emission is problematic as the region of interest (1-2 μm) is significantly affected by emission from samples above 150-200°C. Thermal emission may be approximated in certain cases with the blackbody model - which shows objects at 150°C have a maximum emission at around 6 μm. The edge of the emission profile is strong enough to cause saturation of the detector. Methods to avoid thermal background interference include pulsed laser/gated detection and long-wave-blocking filters, as well as sample cooling.
- Aqueous solutions - these can present difficulties, as the first overtone of water is broad and strong enough to significantly attenuate the Raman scattering from the 2000-2500 cm^{-1} shift area. Deuterated solutions are a somewhat expensive and non-trivial solution; if -CN, CO, triple CC, certain SH or SiH vibrations need to be probed in aqueous media, care must be exercised.
- Self-absorption in organic species - many organic species re-absorb Raman scattering generated in the sample in the overtone and combination region. This can significantly attenuate relative intensity, and is a complex function of pathlength, optical coefficients, and sampling geometry. It may make the use of standard intensity scales and internal standards untenable. Although the overtone of CH is relatively quite weak in absorption, the effect on the Raman spectrum may be profound.
- Glass - some glasses are not suitable for sample vessels, as they contain high levels of either transition metals or rare earths, which fluoresce weakly. Quartz is ideal, if free from ferric iron.

1.4.9 Optical constants and correction functions

The most obvious conclusion to draw is that time spent determining either the reflectance or transmission near-IR spectrum from 800-2500 nm is always worthwhile; the knowledge of the optical constants (refractive index, n, and absorption coefficient, k) as a function of wavelength is very useful when planning an experimental approach. Although well-used in visible Raman spectroscopy, this idea is only slowly being accepted by near-IR Raman spectroscopists. In chapter 5, near-IR diffuse reflectance is used as a method to probe the absorptions of cement minerals; it is hoped that more owners of near-IR-optimised FT spectrometers will start to use this profitable method to aid their FT-Raman studies.

Unfortunately, few also appreciate the need to routinely correct single-beam spectra for instrument response as a function of wavelength[20].

$$\Psi_{\text{recorded}} = \Psi_{\text{response}} \times \Psi_{\text{true}}$$

so that

$$\Psi_{\text{true}} = \Psi_{\text{recorded}} \times \Psi_{\text{correction}}$$

where

$$\Psi_{\text{correction}} = \Psi^{\text{known}}{}_{\text{theoretical}} \;/\; \Psi^{\text{known}}{}_{\text{experimental}}$$

This is well-reviewed elsewhere - all spectra in this thesis are corrected by the method of Petty *et al* developed at Southampton[20] or by a modified method based on the output of a quartz halogen tungsten (QTH) strip lamp. Although promising, care must be taken to carefully correct the blackbody equation to reflect the emissivity of tungsten as a function of wavelength (linear from 0.9-1.9 μm) and temperature (measured with difficulty and uncertainty with an optical pyrometer). Alignment was found to be critical - if the lamp were placed off-axis, quite large spectral changes could be brought about. Since the QTH lamp filament is not a suitable shape to image in the J-stop evenly, a piece of spectrally-grey scattering glass was used to produce a diffuse image. It must be remembered that while not sensitive to individual photons, photodiodes are photon-detectors, not energy-integrating detectors; therefore, the Planck curve has to be cast in terms of photons, and not intensity, to calculate the correction function from the blackbody equation.

1.4.10 Polarisation measurements

The simple introduction given earlier in this chapter is adequate to describe the polarisation of Raman scattering. However, the angular dependency of the scattered light was not considered - hence an important result was overlooked: depolarisation ratios can vary, depending on the sampling geometry used. Most common are the 90° and 180° geometries - the latter prevalent on FT-Raman spectrometers, as it is far easier for non-experts to align and obtain reproducible results. Fortuitously, the expression for ρ_l in both geometries is the same*. Care must therefore be taken to ascertain the polarisation state of the excitation laser, and also whether the pre-sample optics rotate this polarisation or introduce significant depolarisation.

During the work in chapter 2, depolarisation ratios were measured for a simple melt-phase species. As described therein, the experiment involved setting a linear polariser in the J-stop, and using vertically-polarised excitation. Before the results could be interpreted, a calibration was required. Since CCl_4 has perfect tetrahedral symmetry (molecular point group T_d) the totally symmetric vibration near 460 cm^{-1} should have been almost completely polarised - nearly complete extinction should have been seen under crossed polarisers whilst the other bands should have been depolarised, with ratio equal to 0.75. The values obtained (<0.1 for near 460 cm^{-1}, 0.74-0.76 for the others) showed the experiment to be imperfect, but not fatally flawed; the reasons are discussed below.

Problems with near-IR depolarisation ratio measurements are due to well-known optical considerations. It has been shown recently that interferometry offers an advantage over grating or prism spectrometry for the routine recording of depolarisation ratios[21]. Orthogonal linear polarisations are transmitted through near-IR Michelson interferometers with almost equal efficiency - expressed as a ratio, 80-90% compared to 10-20% for conventional spectrometers and spectrographs. The reason for this improvement is the absence of strongly polarising optical components. Diffraction gratings are particularly poor in this respect, necessitating the use of polarisation scrambling optics before the entrance slit, "fixing" the polarisation admitted to the spectrometer (several different configurations possible), or the application of a correction to the derived ratio of intensities. The near-equity of polarisation response for interferometers circumvents the requirement to correct for the spectrometer, or the use of expensive polarisation scramblers, for qualitative analytical work.

The errors in the method as a whole are assumed to be:

- Finite transmission of the desired polarisation through the polariser
- Finite extinction of the undesired polarisation through the polariser
- Wavenumber-dependency of these two functions
- Angular misalignment of the analyser

---

* The same is not true for ρ_n, the depolarisation ratio obtained using unpolarised excitation, where no depolarisation may be recorded in the backscattering geometry.

- Divergence of the incident beam at the analyser
- Large solid acceptance angle
- Polarisation response of the spectrometer.

Of course, for the highest accuracy, correction of interferometrically-derived data should be carried out, especially since the accuracy of the depolarisation ratio has a dependency on spectrometer fore optic *f*-number. This tends to be low (less than unity in some cases) to allow high optical throughput. This high angular acceptance aperture introduces a source of error[22]. A particular problem of the near-IR is that the Raman scattering falls over a long wavelength range (1-1.7 μm) and it is difficult to fabricate optical components to have equal polarisation transmittance/extinction over such a range. The problems of dichroic measurements on polymers highlight these problems[23].

1.5 References:

1.) C.V. Raman and K.S. Krishnan, Nature, 121, 619 (1928)

2.) G. Herzberg, "Molecular spectra and molecular structure. II. Infrared and Raman spectra of polyatomic molecules", Van Nostrand (1945)

3.) See, for instance, P.W. Atkins, "Molecular Quantum Mechanics", 2nd Ed., Oxford University Press (1983)

4.) N.J. Bridge and A.J. Buckingham, Proc. Roy. Soc. Lon., 295A, 334 (1966)

5.) E.B. Wilson, J.C. Decius, and P.C. Cross, "Molecular Vibrations", McGraw-Hill (1977)

6.) G. Placzek, Handbuch der Radiologie VI, Part 2 (Akademische Verlagsgesellschaft, 1934); URCL Translation 526 (L)

7.) H.W. Schrötter and H.W. Klöckner, Chapter 4 in "Raman spectroscopy of gases and liquids" Ed. A. Weber (Springer, 1979)

8.) See, for instance, C.E. Hathaway, Chapter 4 in "The Raman Effect" Vol.1, Ed. A. Anderson (Marcel Dekker, 1970)

9.) B. Schrader, A. Hoffmann, and S. Keller, Spectrochim. Acta 47A(9/10) 1135 (1991)

10.) H. Stammreich, Spectrochim. Acta 8, 41 (1956)

11.) T. Hirschfeld and B. Chase, Appl. Spectrosc. 40(2), 133 (1986)

12.) See, for instance, the special editions of Spectrochim. Acta 46A, 47A, 49A, and 50A devoted to FT-Raman techniques and applications, edited by P.J. Hendra.

13.) E.R. Schildkraut and T.B. Hirschfeld, in "Laser Raman Gas Diagnostics" Eds. Lapp and Penney, page 379 (Plenum, 1974)

14.) G.W. Chantry, H.A. Gebbie, and C. Hilsum, Nature 203, 1052 (1964)

15.) J.B.J. Fourier, "Theorie Analytique de la Chaleur", Firmin Didcot, Paris (1822)

16.) J.W. Cooley and J.W. Tukey, Mathematics of Computation 19, 297 (1965)

17.) P. Jacquinot, Rep. Prog. Phys. 23, 267 (1960)

18.) P. Fellgett, J. De Phys. et de la Rad. 19 187 (1958)

19.) J. Connes, Rev. Theor. Opt. Instrum. 40, 45 (1961)

20.) C.J. Petty, G.M. Warnes, P.J. Hendra, and M. Judkins, Spectrochim. Acta 47A(9/10), 1179 (1991)

21.) A. Hoffman, S. Keller, B. Schrader, R. Ferwerda, and J. Van Der Maas, J. Raman Spectrosc., 22, 497 (1991)

22.) N.J. Bridge and A.D. Buckingham, Proc. Roy. Soc. (London), 295A, 334 (1966)

23.) D.I. Green and D.I. Bower, Spectrochim. Acta, 49, 1191 (1993)

Chapter 2:

1,3-dithiole-2-thione and related compounds

2.1 Introduction

Workers in Southampton have been engaged in tetrathiafulvalene (TTF) chemistry for several years, progressing from basic cyclic thione syntheses towards complex TTF species. Cyclic thiones and their oxygenated analogues oxones are precursors in TTF synthesis; TTFs are of considerable interest because their cation radical salts form molecular conductors and superconductors$^{1-3}$. The general structure of cyclic thiones, oxones, and TTFs are shown below in figure 2.1:

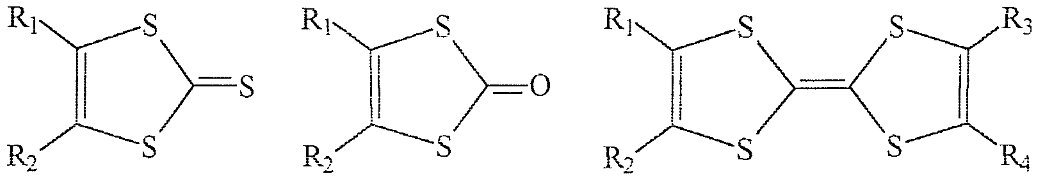

Figure 2.1 Structures of thione (left), oxone (centre), TTF (right).

Validating each new synthetic product at the bench is a major concern, and presents problems. Mid-IR absorption spectra of synthetic intermediates and final products often prove difficult - if not impossible - to obtain. Many thiones are difficult to mull adequately, whilst pressed into KBr discs poor quality spectra result.

For simple thiones, oxones, and TTFs these problems are surmountable by experience, given enough time and quantity of analyte to optimise each sample. These three factors (experience, time, quantity) are often *not* available. A fast, reliable, and robust method would be greatly beneficial, especially a technique that removed the sample preparation need for IR analyses.

The need for a routine, bench-top analysis method becomes even more pressing when TTF salts are considered. Since the properties of interest in these materials are only present in the solid state, data can not be gained from *most typical* organic characterisation methods, since these usually require the preparation of a solution*. Quite often, elemental analysis is the only technique regularly used by

---

* In some cases, reflectance IR and solid-state NMR show promise.

synthetic chemists for characterising TTF salts after synthesis - which is a wholly destructive technique.

FT-Raman techniques could greatly beneficial in this area. The basis for this hope is that *conventional* Raman spectroscopy has proved rather successful *in the area of fundamental research.* A very large research effort has been made - not only have the vibrational spectra of simple TTFs been accurately assigned[4], but theories developed to explain the bandshifts seen on the formation of the TTF salt complexes[5-8] in terms of the degree of partial charge-transfer that takes place between donor and acceptor. Many TTF salts are highly-coloured, and fluorescence and pyrolysis figure strongly as disadvantages in the routine use of conventional Raman spectroscopy.

For these reasons, an evaluation of FT-Raman spectroscopy was undertaken. The work presented in this chapter began with the objective to evaluate the technique in an analytical context. The intended development of the project was to use the knowledge gained during the initial thione study, together with the considerable conventional Raman literature, to survey the analytical applications for TTF salt synthesis.

2.2 Experimental

All the synthetic work was carried out by Dr. Jeremy Kilburn and co-workers in the Departments of Chemistry in the Universities of Southampton and Bangor. Compounds were purified by recrystallisation or by column chromatography, whilst novel compounds were additionally characterised by proton nuclear magnetic resonance (^{1}H-NMR), mass spectroscopy (MS), and elemental analysis (EA).

For FT-Raman studies, simple powder cells for solids and bulb cells for oils proved sufficient. The colour and physical state of the samples varied considerably, as did the amount of sample available, the minimum being ca. 25 milligrams, although this presented no problem.

2.3 Results & Discussion

In general, the spectra obtained by the FT-Raman technique are of good quality. Excitation power levels varied between 10 mW and 1 W. The spectra are the result of 50-250 co-added scans, recorded at either 3 or 4 cm^{-1} resolution, from 350-3500 cm^{-1}, and then corrected for instrumental sensitivity versus wavelength[9].

The only serious difficulties encountered, albeit in a small number of cases (<10% of all samples studied), were the decomposition of some samples in the laser beam, and the fluorescence from others.

- Fluorescence - Although only severe in a few cases, fluorescence was problematical, since it proved unpredictable. It was detected from some very dark samples, and from those that recrystallised poorly. However, some of the lightly-coloured high-purity samples also fluoresced badly. Deep coloration usually indicates long-wavelength absorption bands, the tail of which might well reach into the near-IR, and poorly recrystallised samples are likely still to contain by-products from synthetic "work-up". Such impurities are notorious in conventional Raman spectroscopy for causing fluorescence. Although a great advance over the extreme precautions needed in conventional Raman spectroscopy, it is quite plain that good sample purity is still a requisite for near-IR Raman spectroscopy.

As an example, the zinc-containing bis-dithiolene **H** (shown later in figure 2.10) fluoresced strongly and decomposed at very low laser powers. The reason for this is probably the occurrence of an electronic absorption bands near 1 μm; transition metal dithiolenes are known[12] to have low-lying electronic transitions around 0.8-1 μ m, depending on the metal centre and the nature of the TTF. These are most likely to be metal-based *d-d* transitions.

- Pyrolysis - Decreasing the power and defocusing the beam had limited success in reducing the cases of pyrolysis. One of the effects of sample pyrolysis was to produce a thermal emission background which obscured nearly all other spectral features. Pyrolysis was especially severe for dark red or dark brown samples.

It should be noted that the high noise level at low Raman shift in figure 2.10 was caused by multiplication with an unmodified instrument response correction function. The correction function could not be smoothed, as the shape is critical to a good correction[9], whilst smoothing the spectrum sufficiently rendered the band near 1450 cm^{-1} impossible to resolve.

The first ten thiones and derivatives considered in this study are labelled **A-J** in order to simplify identification. Spectra are presented, followed by the chemical structure. **A-H** are thiones, **I** an oxone, and **J** a TTF. Subsequent batches of thiones and derivatives were compared and contrasted with these original compounds, providing a check on the original conclusions, and refining the data.

2.3.1.1 The Raman spectrum of 1,3-dithiole-2-thione

In the case of the simplest structure (1,3-dithiole-2-thione, **A**) several authors had previously attempted vibrational analyses. Gayathri Devi, Sathyanarayana and Engler[11] reported IR spectra and the results of a normal co-ordinate analysis, whilst Iqbal and Owen[12] provided IR spectra and Raman band position data together with a normal co-ordinate analysis.

Unfortunately, there are significant differences between the two sets of results, whilst the Raman data collected during this study contradicted both previous analyses - consequently the assignments in these analyses must be open to doubt. Consequently, a further aim of this work became the re-assignment of the vibrational description of **A** by group frequency methods.

The Raman spectrum of **A** is shown in figure 2.2. This material was recrystallised from 20% EtOH:80% MeOMe to leave light yellow needle-like crystals.

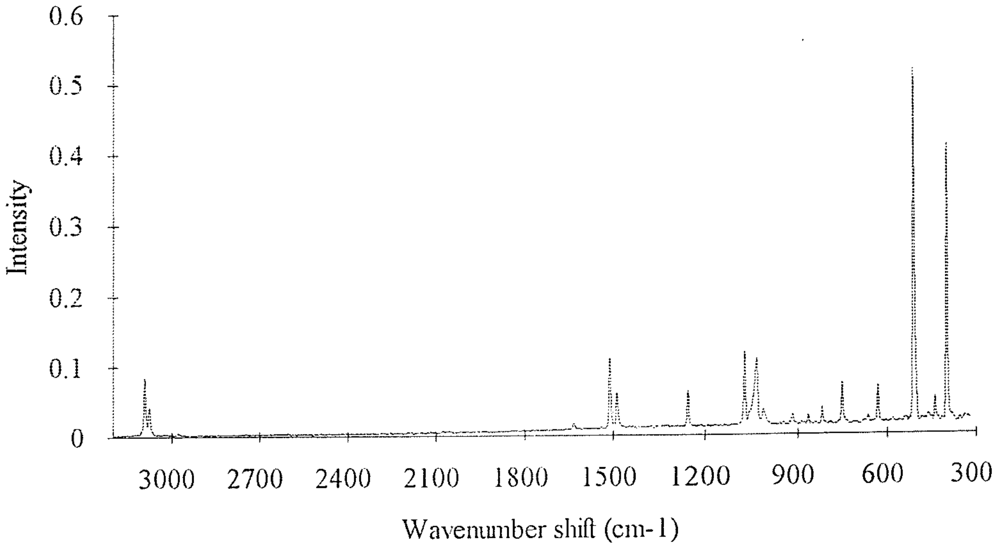

Figure 2.2a The FT-Raman spectrum of **A**.

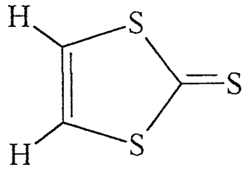

Figure 2.2b Structure of **A**.

An experimental crystal structure of **A** is not available. However, since analogues and derivatives of **A** have been shown to contain planar or near-planar thione rings by X-ray crystallography[13] the convention established in previous work assuming **A** is planar is followed.

According to basic group theory, the molecule has C_{2v} symmetry, and has 18 fundamental modes of vibration ($7A_1$, $2A_2$, $6B_1$, and $3B_2$). All but the two A_2 modes are expected to be jointly Raman and IR active, the A_2 modes only possessing Raman activity.

Before rushing to assign all bands in figure 2.2 as fundamentals, it must be remembered that although group theory predicts those bands which *will* have non-zero intensity, it says nothing about the *actual* intensity. Although all the fundamental vibrations of **A** are Raman-active, it is *very* dangerous to proceed only on the basis of the Raman spectrum, because some Raman bands may be very weak.

Even if IR and Raman data are combined, care must still be exercised when using mode-counting as a method of assigning vibrational spectra. Most FT-IR spectrometers are fitted with KBr optics - hence the lowest frequency attainable is ca. 400 cm^{-1}. Most FT-Raman spectrometers struggle to approach shifts under ca. 150 cm^{-1}. Any IR-active fundamentals lying below 400 cm^{-1} and Raman bands below ca. 150 cm^{-1} shift could be overlooked - the effect on a detailed assignment would be disastrous. In addition, some of the weaker bands may be due to overtone and combination modes. Care is always needed when mode counting[a].

Table 2.1 below lists the Raman shift, approximate description, and tentative assignment of the bands. From group frequency arguments the following Raman bands would be expected:

- (C-H) around 3100-3000 cm^{-1}
- (C=C) between 1680-1600 cm^{-1}
- (C=S) about 1200-1050 cm^{-1}
- (C-S) at 650-500 cm^{-1}

Bending motions of the C=S and C-H groups, as well as modes associated with ring deformations, would also be expected, in the region below ca. 1500 cm^{-1}.

---

[a] Sometimes vibrational models can help, but since these are often in largest error in the low-frequency domain, their use must be well-considered.

2.3.1.2 Vibrational assignment of 1,3-dithiole-2-thione

Depolarisation ratio measurements were made on **A,** since its low melting point allowed a simple heating accessory to be used. The solid was packed into a bulb cell, fitted into a hot-cell, then heated to just above the melting point (near 55°C).

As described in chapter 1, the polarised Raman experiment involved setting a near-IR linear polariser (an iodine-doped polyvinyl acetate sheet from Oriel Corp.) at the image position of the Jacquinot stop (in the redundant IR sampling compartment) on a stand capable of rotation through 90 degrees.

Band position (cm^{-1})	**Approximate Description**	**Tentative Assignment**
3092	Medium, sharp	C-H stretch
3076	(as above)	(as above)
1634	Weak, broad	Overtone ?
1512	Medium, sharp	C=C stretch
1488	Medium-weak, sharp	Fermi-enhanced combination ?
1252	(as above)	C-H in-plane
1077	Medium, sharp	C=S/C-S-C
1038	Medium, broad, asymmetric	(as above)
1015	Weak, broad, asymmetric	(as above)
919	Weak, broad	Ring ?
867	Weak & broad	?
820	Weak, sharp	Ring ?
753	Medium-weak, sharp	C-C stretch
666	Very weak & broad	?
633	Medium-weak, sharp	Ring ?
512	Very strong, sharp	Thione ring (C-S)
440	Weak, sharp	?
400	Very strong, sharp	Thione ring (C-S)

Table 2.1 Assignment of major bands in A.

The Raman scattering with excited as usual with a (fixed) vertical linear polarisation. Calibration of the experiment was by reference to carbon tetrachloride (CCl_4), and comparison against accepted values[14].

For totally symmetric vibrations, the depolarisation ratio ρ_l should lie between 0-0.75, whereas all other vibrations should be depolarised, such that ρ_l should be exactly 3/4. Most totally symmetric vibrational modes of compound **A** have ρ_l values between 0.15 and 0.23 (one at 0.4) - the values 0.70-0.74 are taken to indicate depolarised bands. These values were obtained by integrating the areas under the bands, and then taking the ratio of the value obtained with the analyser perpendicular to the incident polarisation vector to that obtained with the analyser parallel to the polarisation vector.

The values of the depolarisation ratios, without correction for polarisation response, are given table 2.2. Some bands shifted position slightly on melting, but this did not prove problematical, as their origin was quite clear.

Band position (cm^{-1})	**Depolarisation ratio (ρ_l)**
3081	0.23
3066	?
1634	0.22
1510	0.23
1485	0.22
1262	0.74
1090	0.22
1046	0.21
1018	0.20
920	0.15
819	0.71
751	0.19
625	0.71
510	0.17
440	?
400	0.42

Table 2.2 Depolarisation ratios of the melt-phase of A

The depolarisation ratio for some bands was difficult to determine, since a certain amount of band broadening occurred on heating, which resulted in appreciable overlap - such bands have been omitted from the analysis. The same is obviously true of bands which were so weak in the solid state that they were unobservable in the melt.

The C=C bond stretching motion in the thione structure has A_1 character in the point group C_{2v}, and should lead to a polarised Raman band. Symmetric stretching of the carbon-carbon double bond in an aromatic compound is expected to produce a reasonably strong Raman band towards the lower end of the ν(C=C) range. The depolarisation ratio (ρ_l=0.2) and the relative intensity of the band at 1512 cm^{-1} suggest this band as a candidate. The depolarisation ratios of the various bands for the melt of **A** at 50-55°C are given below in table 2.2.

The rather low ν(C=C) frequency represents a downshift of more than 100 cm^{-1}, but several features support its assignment. The C-H stretching modes appear as strong sharp features at 3092 and 3075 cm^{-1}. Their appearance above 3000 cm^{-1} might simply be due to their ethylenic position, but also might indicate aromaticity; there is likely to be appreciable π-orbital overlap between the carbon and sulphur atoms in the thione ring, leading to conjugation throughout the cyclic structure, and a reduction in C=C bond-order - with a consequent decrease in C=C bond stretching force constant. This reduction would lead to a low C=C stretching frequency.

The previous work on 1,3-dithiole-2-thione is not in agreement with these observations. From IR data and a normal co-ordinate analysis, Gayathri Devi et al assign a reasonably strong band at 1396 cm^{-1} to be the C=C stretch. Although additionally reporting Raman band positions, Iqbal and Owen neither publish the Raman spectra nor comment upon their quality. Their band intensity assignments seem quite similar to those derived in this work from near-IR excitation, although the C-H stretching modes were apparently not resolved with their equipment - the reason for this is not mentioned. The spectra were obtained by Ar^+ laser excitation, although which wavelength was not reported.

Iqbal and Owen claim that the 1514 cm^{-1} band in their Raman data is due to C-H bending, whilst that at 1630 cm^{-1} band in the IR is due to the C=C stretch. This is curious. The most damning evidence is provided by the FT-Raman depolarisation study of this work - see table 2.2. The 1634, 1512, and 1488 cm^{-1} bands are all strongly polarised (ρ_l ca. 0.2). This is expected only if the modes of vibration are of A_1 symmetry. Since Iqbal and Owen describe the mode near 1500 cm^{-1} as mostly out-of-plane C-H bending, with consequent A_2 symmetry, their assignment must be wrong.

In addition, if the band at 1634 cm^{-1} were the C=C stretch it would be reasonable to anticipate such a band throughout the thione series, probably shifted down in frequency by the combined mass and bonding effects of four sulphur atoms instead of two sulphur and two hydrogen around the double bond - if previous assignments were correct, this would suggest a band at around 1600 cm^{-1} shift in other members of the thione series. Such a band was not observed. Taken with the depolarisation ratio data of this work, and the aromaticity in the structure, the assignment of the C=C stretching mode of **A** to the band at 1512 cm^{-1} seems firm. Comparison against known data for the central and ring C=C bonds of TTF[4] consolidates this.

Since the 1634 cm^{-1} band can not also be the symmetric C=C stretch, an assignment must be found. To aid in the interpretation, the KBr disc IR transmission spectra of **A** was obtained. This involved much more effort than obtaining an FT-Raman spectrum. To compare:

- Firstly, drying and grinding KBr to minimise water absorption and scattering of the incident IR beam.
- Secondly, determining the correct ratio of **A** to KBr in the sample disc - 1:200 proved adequate (0.5 mgs **A** in 100 mgs KBr) avoided derivative band shapes and low transmission.
- Thirdly, further grinding to achieve intimate mixing.
- Then the spectrometer carefully purged with dry N_2 gas, a background blank KBr pressed, a spectrum obtained of both background and sample by co-adding 200 scans at 2 cm^{-1} resolution, each requiring ca. 30 minutes.

The spectrum shown below in figure 2.3 is very good quality by KBr disc standards. There is little evidence of water absorption, minimal scattering, and few anomalous band shapes. The assignment of the weak 1634 cm^{-1} Raman band is immediately suggested as the overtone of the strong IR band at 817 cm^{-1}.

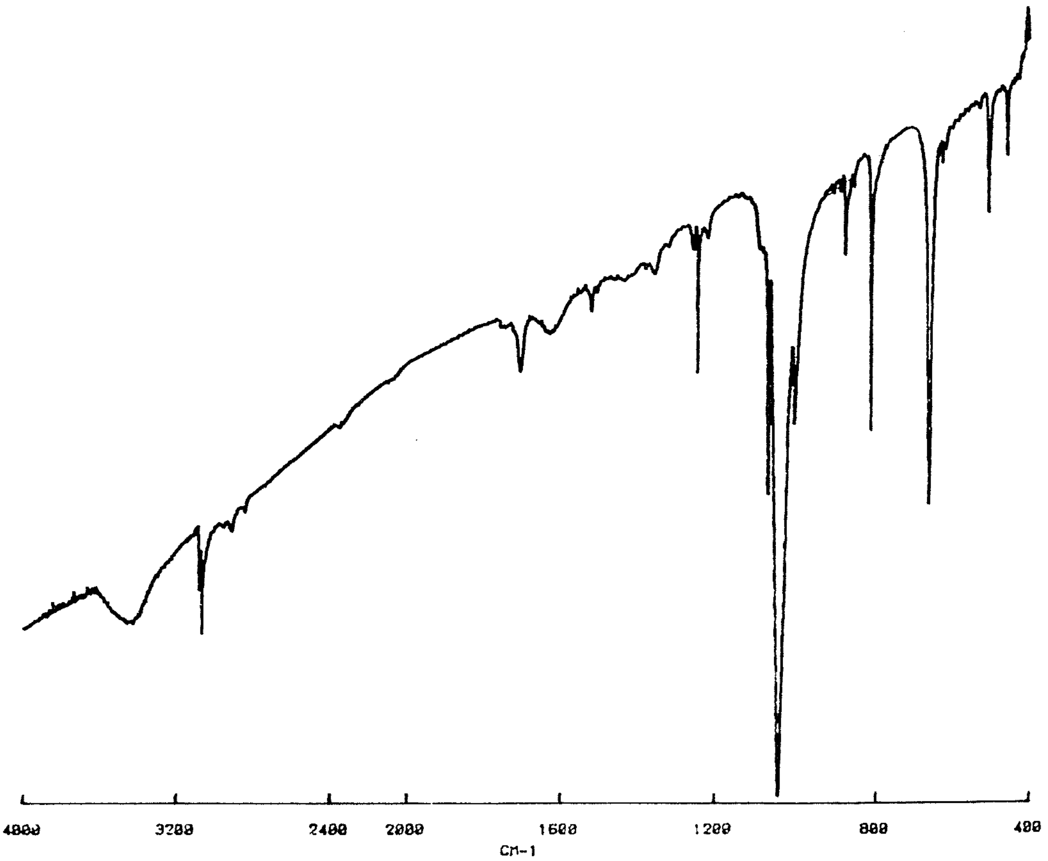

Figure 2.3. The mid-IR transmission spectrum of A dispersed in KBr.

The 1488 cm^{-1} band in the Raman spectrum of A is more difficult to assign. It may well be a combination mode, the most likely candidates being the strong IR bands at 817 cm^{-1} and 664 cm^{-1} (Σ=1487 cm^{-1}), or the strong Raman bands at 1077 cm^{-1} and 400 cm^{-1} (Σ=1477 cm^{-1}). It is unlikely to be a C-H deformation mode, as C-H bonds in this environment usually have lower frequency in-plane C-H bending modes, whilst out-of-plane bending is generally lower still. Additionally, neither of the analyses carried out by the previous authors derived a fundamental mode near this frequency.

The band is very much more intense than the 1634 cm^{-1} overtone; in fact, it is around 50% of the height of the 1512 cm^{-1} fundamental. This may well imply that it is in Fermi resonance with the C=C stretching mode.

Fermi resonance is a process whereby transitions with very similar energy of the same symmetry species may interact, the result being a mutual "repulsion" from the unperturbed wavenumber positions, and a change in the relative intensity of the bands, such that the weaker is enhanced at the expense of the stronger. If the weaker in the Fermi pair is an overtone or combination, the degree of enhancement can be striking.

The C=C stretch in this compound is not as strong as that in the other thiones studied, where it is often the strongest Raman feature. This lack in strength is consistent with "intensity-borrowing" by the weaker band (1488 cm^{-1}) in the resonance pair. However, this speculation is better reserved for further study.

The depolarised 1252 cm^{-1} band, which disappears upon substitution of -SMe and similar groups for the hydrogen atoms, is likely to involve C-H in-plane bending modes - compare to the assignment bands around 1250 cm^{-1} in ethylene, alkyl-substituted ethylenes, and of dialkyl-substituted cis-alkenes. The band is also seen in the IR spectrum, at 1249 cm^{-1}.

The bands at 1077, 1038, and 1015 cm^{-1} are associated with the C=S stretching motion and its coupling to S-C-S motions, although the exact assignment is unclear. Bellamy[15] comments that C=S is prone to shifts in frequency, coupling easily and significantly to other modes. All of these modes are polarised, whilst appearing very strongly in the IR at 1074, 1047, and 1014 cm^{-1} respectively. Indeed, the 1047 cm^{-1} band is the strongest IR absorption seen, confirming its C=S stretching nature. Given the number of A_g fundamental modes should be seven, it may well be that one or other of these modes is a combination or overtone mode; maybe the weak 1015 cm^{-1} band is the first overtone of extremely strong band Raman band at 512 cm^{-1}.

The assignment of bands below 1000 cm^{-1} becomes more complex; "mode-mixing" (the interaction of vibrations) becomes more likely, so the unequivocal assignment of IR and Raman bands to modes of vibration is problematic. Modes such as C=S bending and C=C torsion lie in this region, as will C-S stretch and numerous ring-related modes.

There are several plausible explanations for the intense Raman band at 512 cm^{-1}. It is possibly due to a stretching mode associated with the C-S bond in the -S-(C=S)-S- unit. A similar assignment is possible for the 400 cm^{-1} Raman band, this time as a stretching motion of the C-S bond in the -S-(C=C)-S- region. There is little reason to assume that the C-S stretching vibrations in the -S-(C=S)-S- and -S-(C=C)-S- units will occur at the same frequency. The C-S stretch is not normally seen as low as 400 cm^{-1}, however; so assignment as a ring-related mode is possible. The two previous papers are in considerable disagreement in this region.

The depolarisation ratio measurements show that the 512 cm^{-1} band of **A** is highly polarised, with a ρ_l value of ca. 0.1, and must be due to an A_1 mode. For such a strong low-frequency mode, this would seem to indicate a symmetric ring-breathing motion. Thus the 512 cm^{-1} band seems quite characteristic of the thione ring itself. The ρ_l value of the 400 cm^{-1} band is 0.4, indicating a polarised band. The assignment of the 512 and 400 cm^{-1} bands is commented on later, after consideration of several more thione structures.

The IR spectrum shows strong bands at 817, 664, and 509 cm^{-1}. The first two of these are depolarised in the Raman spectrum, the last being strongly polarised as discussed above. Also in evidence are a large number of weaker bands; obviously some are combinations and overtones of lower-frequency modes. Since the IR and Raman data cut off at 350-400 cm^{-1}, it is inappropriate to assign these bands. It is also noticeable that a shift occurs on pressing into disc form, affecting some bands more than others, as revealed by the non-coincidence of the IR and Raman data. In order to extract the maximum information from the vibrational spectra, further studies are required.

2.3.2 Thiones **B-H**

The Raman spectra of these species are presented through the next portion of the text, in figures 2.4-2.10. The aim is to illustrate the validity of the assumptions made on group frequency bases for **A**, and to highlight useful group frequencies for analysis. Throughout the series the expected positions of the C-H modes are observed. **B-E** all contain aliphatic C-H, whose band position falls in the 2900-3000 cm^{-1} range, whereas bands due to aromatic C-H occur between 3000-3100 cm^{-1}.

A good example is **E**, where there are two groups of shifts, one characterising each kind of C-H bond:

- aliphatic at 2965, 2937, and 2917 cm^{-1}
- aromatic at 3068, 3053, and 3039 cm^{-1}.

A strong band is in evidence in nearly all spectra near 1470 cm^{-1} which is assigned as the C=C stretch. This is quite characteristic of the series. Even in **H** a peak is discernible in the 1450 cm^{-1} area, despite the fluorescence commented upon before. This is in reasonable agreement with previously-reported solution-phase resonance Raman spectroscopy of this species[16]. In **A** the band occurs at 1512 cm^{-1}. The downshift of 30-40 cm^{-1} probably results from the change in mass [from -$S_2(C{=}C)H_2$ to -$S_2(C{=}C)S_2$] attached to the double bond.

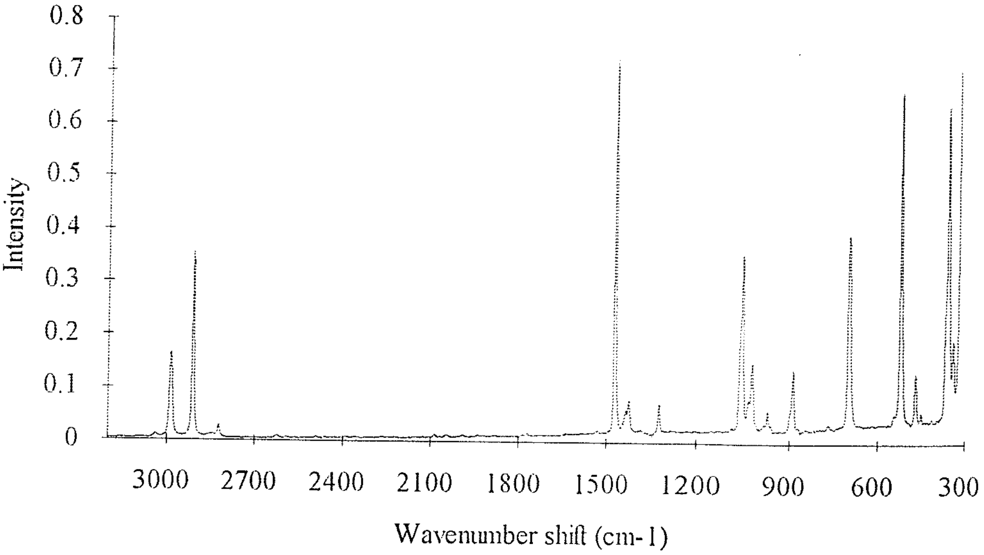

Figure 2.4a FT-Raman spectrum of **B**.

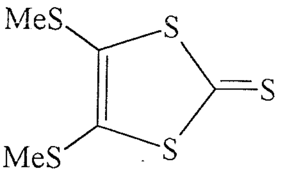

Figure 2.4b Structure of **B** - **C** (below) has EtS- groups in place of MeS-.

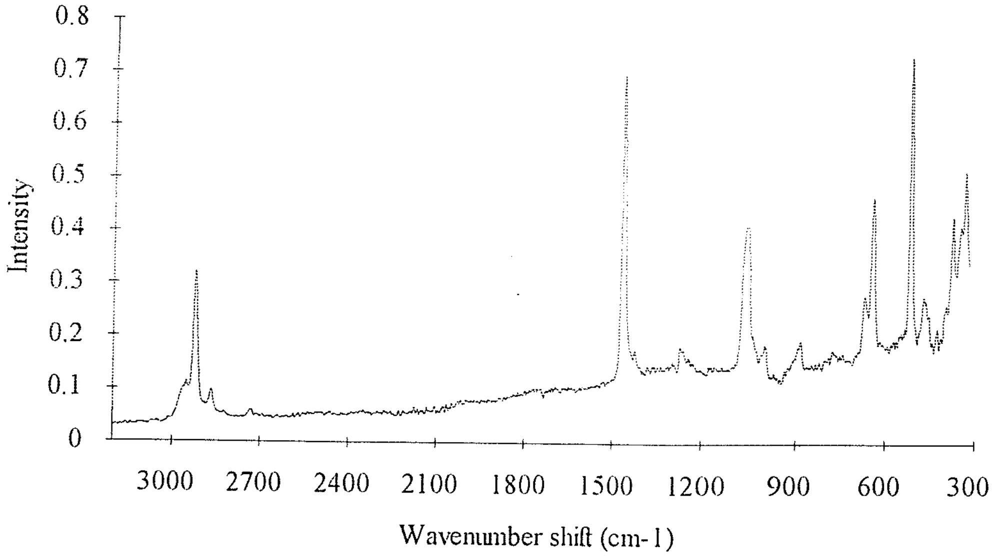

Figure 2.5 The FT-Raman spectrum of **C**.

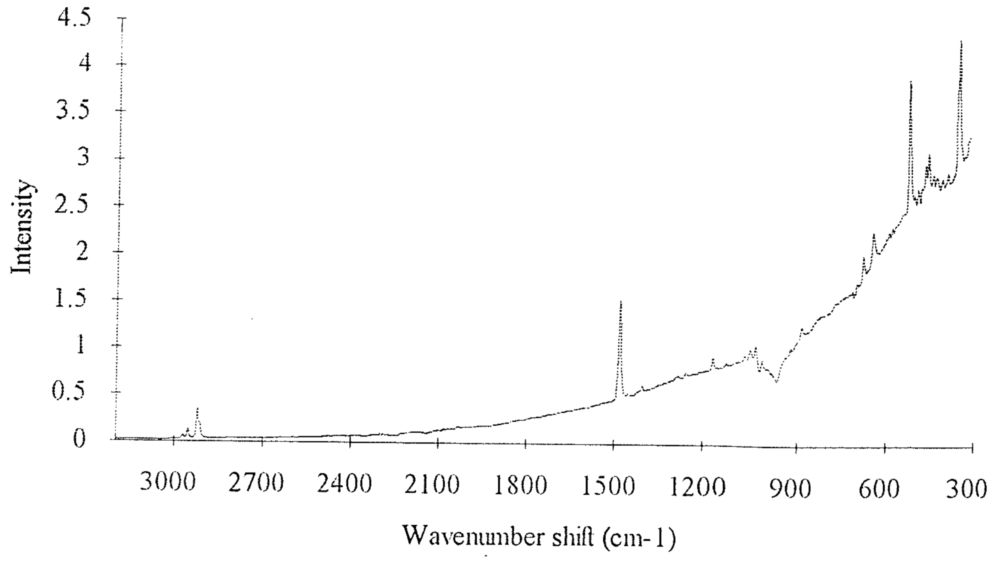

Figure 2.6a The FT-Raman spectrum of **D**.

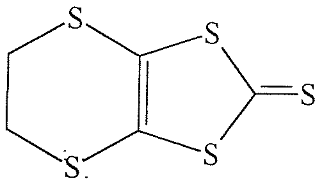

Figure 2.6b Structure of **D**.

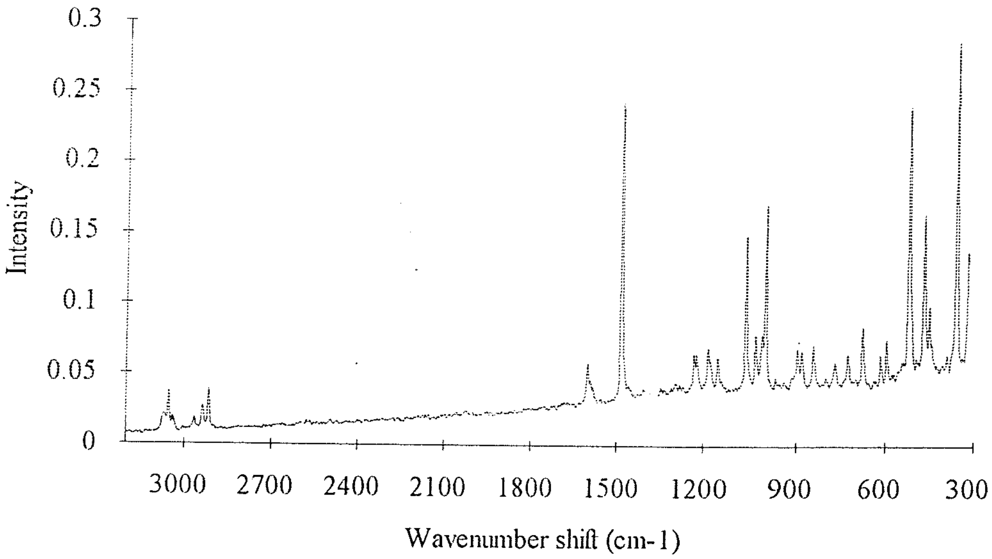

Figure 2.7a The FT-Raman spectrum of **E**.

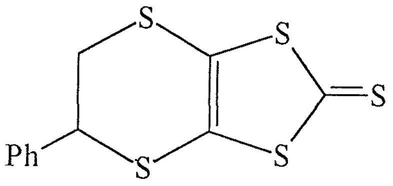

Figure 2.7b Structure of **E**.

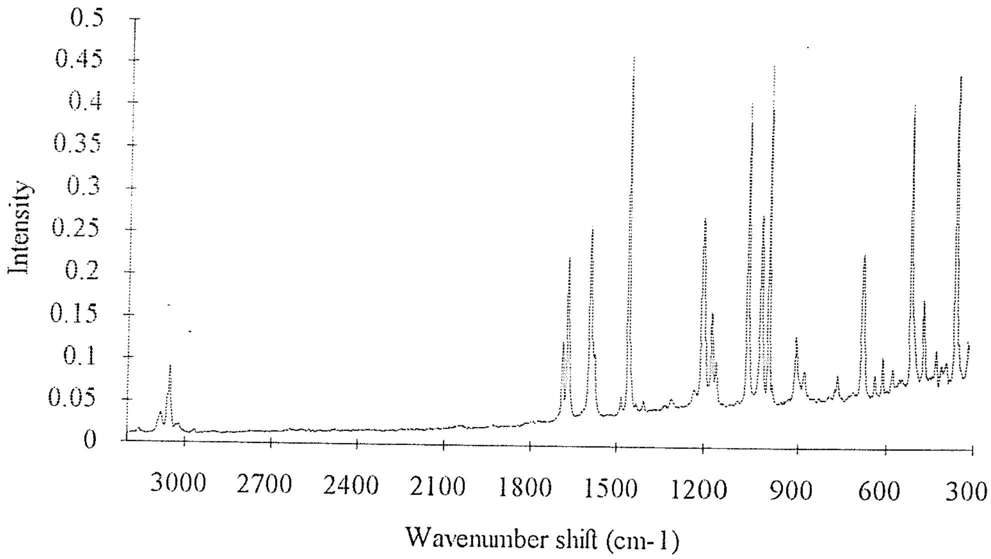

Figure 2.8a The FT-Raman spectrum of **F**.

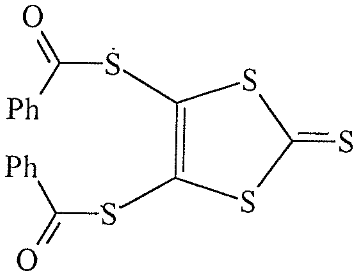

Figure 2.8b Structure of **F**.

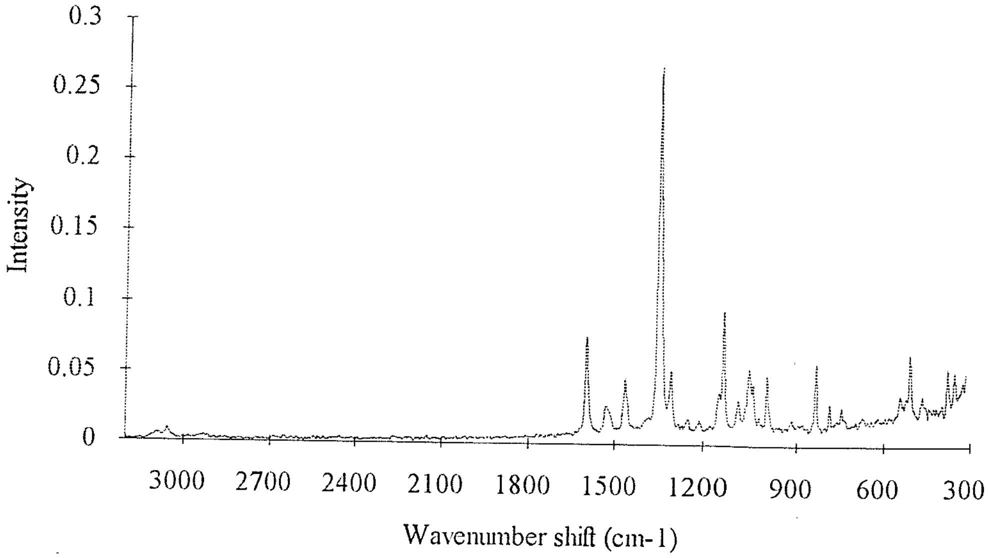

Figure 2.9a The FT-Raman spectrum of **G**.

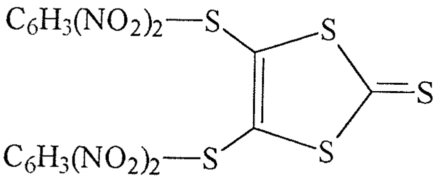

Figure 2.9b Structure of **G**.

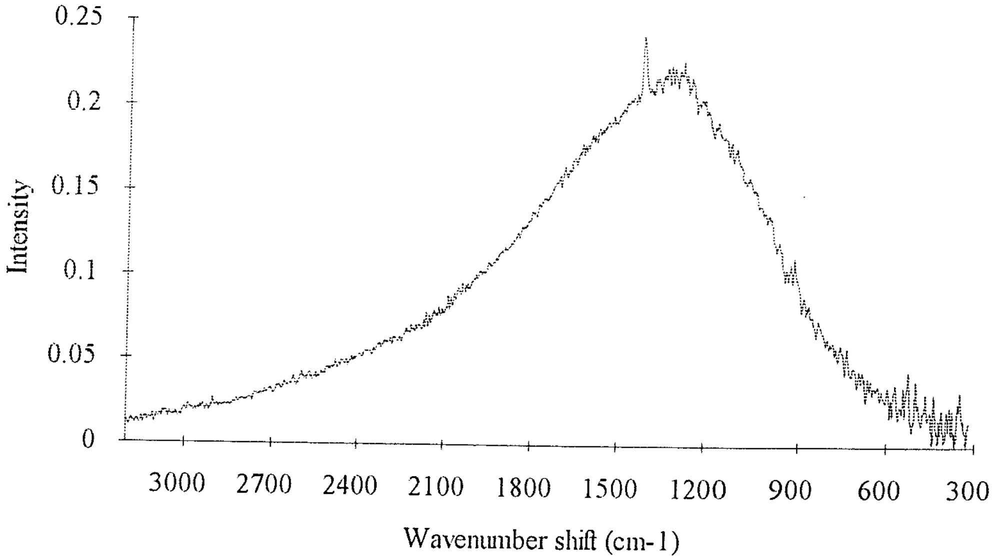

Figure 2.10a The FT-Raman spectrum of **H**.

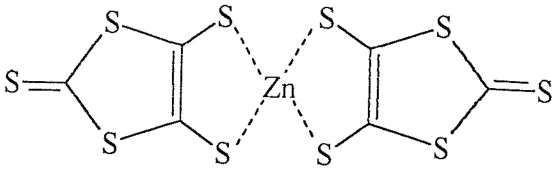

Figure 2.10b Structure of **H**.

In **G** the relative intensity of the C=C stretching band is low. **G** also has weak C-H bands, relative to the other compounds containing "aromatic" hydrogen. 2,4-dinitrobenzene shows similar behaviour, implying that the presence of nitro-groups on the benzene ring reduce the intensity of the aromatic C-H bands. The presence of dinitrophenyl groups seems to dominate other strongly-scattering groups, such as C=C.

The first point to be made about the other bands around 1400 cm^{-1} shift is the disappearance of those near 1488 and 1252 cm^{-1} in **A** which are C-H related. C-H deformation modes (in-plane and out-of-plane methylene and methyl bends) in those species with methyl groups would lie in this region - for instance, the spectra of **B** and **C** exhibit these bands, albeit weakly.

The second point concerns those compounds which have functional groups with group-frequencies between 1800-1000 cm^{-1}, including (-C=O), (C_6H_5-), and (-NO_2). These features appear at shifts predicted by group frequency arguments, and seem little affected by the cyclic thione structure. In cases where the assignment is difficult due to lack of specific information on a given side group, comparison with spectra of closely related species is of help - comparing **G** with 2,4-dinitrobenzene, for instance, helps identify the bands due to the -$S(C_6H_3(NO)_2)$ side group.

Comparison against similar species aids in the interpretation of the region around 1070 cm^{-1}. Ethylene trithiocarbonate has υ(C=S) at 1074 cm^{-1} in the IR[15]. Considering the similarity of the thione ring structure and the fact that C=S stretch generally falls into the 1200-1050 cm^{-1} region, the assignment of a band around 1070-1060 cm^{-1} to the stretching mode of the exocyclic C=S bond seems convincing - and supported by the FT-Raman spectrum of ethylene trithiocarbonate.

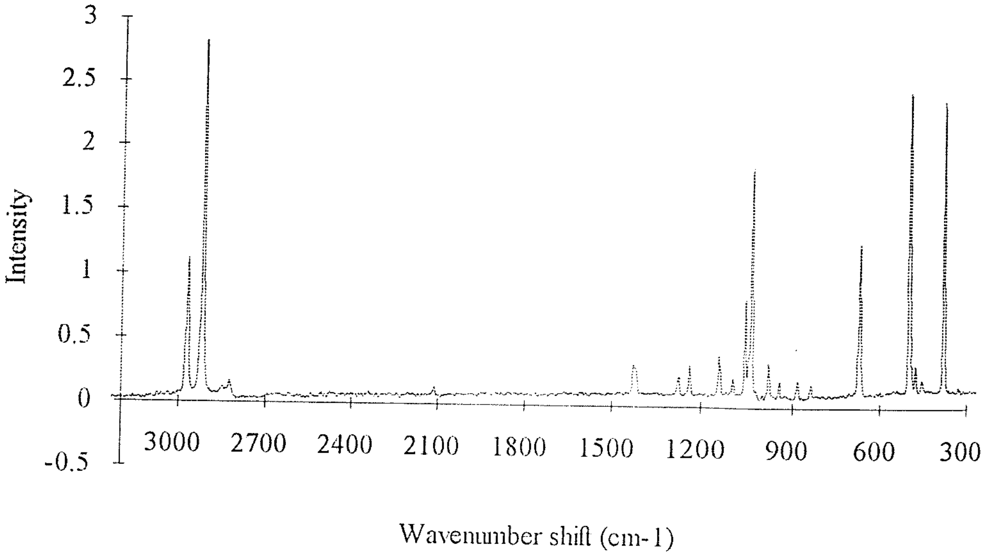

Figure 11a FT-Raman spectrum of ethylene trithiocarbonate.

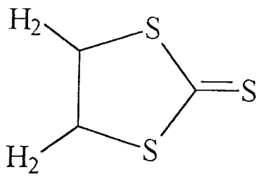

Figure 11b Structure of ethylene trithiocarbonate.

Two strong bands in the C=S stretching region at 1046 cm^{-1} and 1068 cm^{-1} are prominent in this spectrum. Two more strong bands appear at 506 cm^{-1} and 386 cm^{-1}. These are clearly ring-related, involving primarily C=S motion, since they are reasonably insensitive to the substitution of a single for a double carbon-carbon bond. The strongest band in the spectrum is at 2919 cm^{-1}, a C-H stretching mode. A slightly weaker C-H stretch appears near 2971 cm^{-1}, both bands having prominent shoulders to higher shift. The downshift of the C-H frequencies is clearly related to the change from double to single C-C bonding with subsequent decrease in aromaticity. The C-H deformation modes near 1425 cm^{-1} are plainly visible, although not so in the spectra of the thione **A**.

An intriguing feature of the comparison between the "saturated" ethylene trithiocarbonate (figure 2.11b) and the "unsaturated" vinylene trithiocarbonate (figure 2.2a) is the higher intensity scattering from the *saturated* species. Indeed, the scattering from the former is ca. 5-fold greater than that of the latter, the comparison being made by summing the area under the bands near 500 and 400 cm^{-1}, which are indicative of the trithiocarbonate ring. This differs from the empirical rule that aromatic systems are more strongly Raman active than saturated systems, resonance Raman effects notwithstanding.

The thiones studied all show several peaks in the C=S stretch region. This may imply that coupling of the C=S stretch occurs to other modes, as Bellamy suggests, or that combination modes are involved.

Iqbal and Owen report three Raman bands for **A**:

- 1076(w) - C=S stretch
- 1038(m) - combination of -S-(CS)- stretch and -S-(CS)- in-plane bend
- 1008(w) - -S-(CS)- stretch

Devi and Sathyanarayana report three IR bands:

- 1079 - out-of-plane C-H bend with C=S stretch
- 1050 - C=S stretch with -S-(CS)- stretch and ring deformation
- 1015 - unassigned

These disagreements underline the difficulty in making unambiguous assignments, and the ambiguity that can arise using models with many possible solutions. Nevertheless, the 1070-1000 cm^{-1} region is indicative of the C=S stretch and modes unassigned concerning the ring, and is therefore useful in fingerprinting each of the series.

It would perhaps be better to call the C-S stretching region the true fingerprint region of the spectrum, because apart from a strongly Raman active band at 510-530 cm^{-1} in all compounds there is strikingly little in common between the spectra. On examination of the series, the assignment of the band at around 500 cm^{-1} to a mode involving -S-(C=S)-S- and not to -S-(C=C)-S- is proposed purely on simple mechanical arguments - and is suggested by the stability of this band's position with respect to substitution on the C=C bond; it is quite characteristic of the thione ring structure. In a similar way, the band that appears in **A** near 400 cm^{-1} may be identified with a mode involving -S-(C=C)-S- because this band appears greatly dependant on the exact substitution at the C=C bond.

The methodology to assign the low-shift region is to look for correlation in intensity, position, and band shape between compounds of similar structure, such as **B** and **C**, and **D** and **E**. Certain features are shared:

i. 890 cm^{-1} (w) - apparent as a weak single peak, split into a weak doublet in **E**.
ii. 700-670 cm^{-1} (mw) - in **B**: sharp close doublet, in **C**: two peaks of different intensity separated by 28 cm^{-1}; in **D**: two peaks of equal intensity separated by 32 cm^{-1}, in **E**: only one peak.
iii. 510-530 cm^{-1} (mw-ms) - always a sharp single peak.

iv. 380-320 cm^{-1} (mw) - closely replicated between the two pairs.

A further characteristic of this region is a weak feature at around 470 cm^{-1}, possibly combined with a very weak feature at lower shifts, around 430 cm^{-1}. In some spectra this feature is not well-resolved and very weak.

It may prove possible after further study to predict the whereabouts of the C-S stretching modes for the side groups by analogy to the thiol series, R-SH. As a simple example, consideration of the mercaptans MeSH and EtSH suggests S-Me should be near 700 cm^{-1} and S-Et near 650 cm^{-1}. Bands are indeed observed in these positions, the former in **B**, the latter in **C**.

2.3.3 Comparison of thione B, oxone I, and TTF J

In general*, oxones are prepared from thiones by treating the thione with mercuric acetate, $Hg(OAc)_2$, whereas TTFs are prepared from either thione or oxone by coupling with triethylphosphite, $P(OEt)_3$. The most obvious question to ask is whether Raman spectroscopy can easily differentiate between the three forms - oxone, thione, and TTF. To provide a starting point, the first set of comparisons to be made involved **B**, the symmetric SMe- analogue of thione **A** (figure 2.4); **I**, the symmetric SMe analogue of the oxone 1,3-dithiole-2-one (figure 2.12); and **J**, the symmetric SMe- analogue of TTF (figure 2.13).

Several features are immediately obvious on comparison:

- Substituting (C=O) for (C=S) decreases the C-H stretching frequencies by only 2 - 5 cm^{-1}. Since the C-H bonds are well-removed mechanically from the C=X bond (X=O,S), the implication that the shift is due to higher aromaticity in -SMe-thione than in -SMe-oxone.

- The C=C stretching frequency in **B** (C=S) is 14 cm^{-1} lower than in **I** (C=O); however, this could also imply that **I** has is less aromatic than **J**, although the C=C mode will also be influenced by the change in mass.

- The TTF **J** has two more peaks than **B** in the C=C stretching region, at 1554 and 1542 cm^{-1}. Following the assignments previously made[4], the bridging C=C bond is probably the lowest of the three. The doubling of the higher-shift band is possibly caused by Fermi resonance with a combination band.

---

* Synthetic details kindly supplied by Dr. J.D. Kilburn

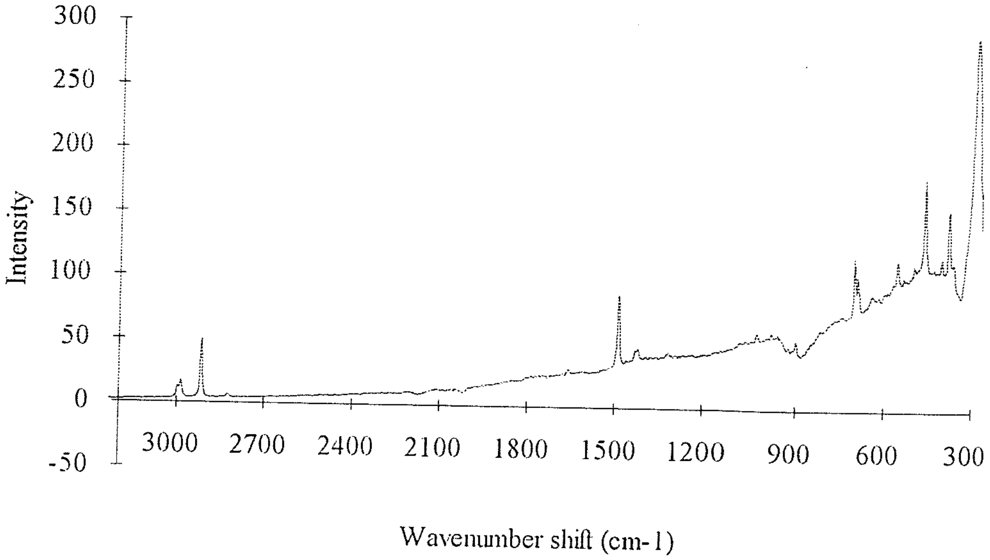

Figure 2.12a FT-Raman spectrum of **I**.

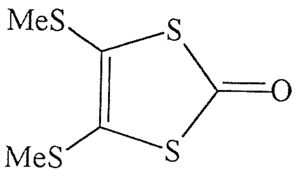

Figure 2.12b Structure of **I**.

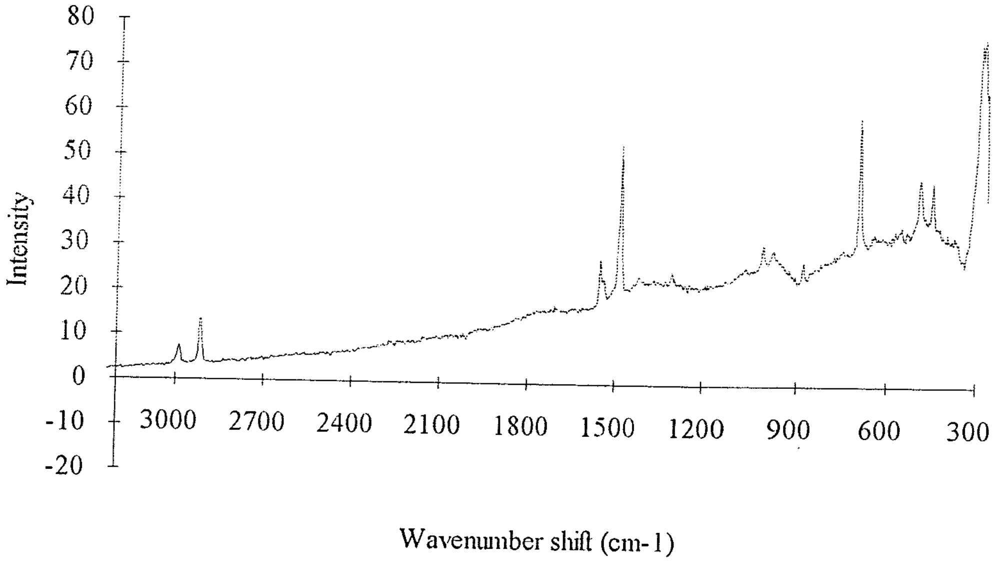

Figure 2.13a FT-Raman spectrum of **J**.

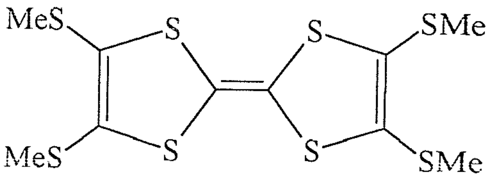

Figure 2.13b Structure of J.

- A band is visible in the -SMe-oxone at 1658 cm^{-1}. This is probably the weak C=O stretching mode, as an upshift of ca. 600 cm^{-1} is in order for the change from C=S to C=O.

- Features present in **B** around 1420 cm^{-1} and 1320 cm^{-1} are still visible in both **J** and **I**. This suggests they are concerned with the -SMe groups, probably due to -CH_3 deformation motions.

Obviously, the C=S stretching region is significantly different in **J** and **I** - in the latter the sulphur is exchanged for oxygen, whereas the former is a TTF. The bands near 700 cm^{-1} in all three spectra are probably due to C-S stretching in the SMe side groups, as indicated above by comparison to the C-S stretch of methyl mercaptan (MeSH).

The most striking difference between the spectra is the disappearance of the characteristic thione ring-related 510 cm^{-1} band in **B**. In **J** bands appear at 495 and 450 cm^{-1} - in **I**, at 465 and 381 cm^{-1} - but none in either case around 510 cm^{-1}. The disappearance of this thione ring mode could therefore be the basis of a technique for determining the success of TTF syntheses from thione precursors.

To summarise the conclusions from the first ten compounds to be studied - the number of differences between the spectra allows for facile discrimination between thione, oxone, and TTF - exactly as required for a routine analytical test.

2.3.4 Further comparisons - thiones

Over the course of the year (1992) following the initial study, many further compounds were synthesised. Some of these proved intractable due to fluorescence or pyrolysis. However, the vast majority (>90%) of the new compounds were amenable to study. A selection of these results are presented and discussed below, to illustrate the points made above and test them further.

In addition to the simple thiones in the first batch, several thiones with large aromatic side groups were synthesised - **K**, **L**, and **M** in figures 2.14-2.16 below.

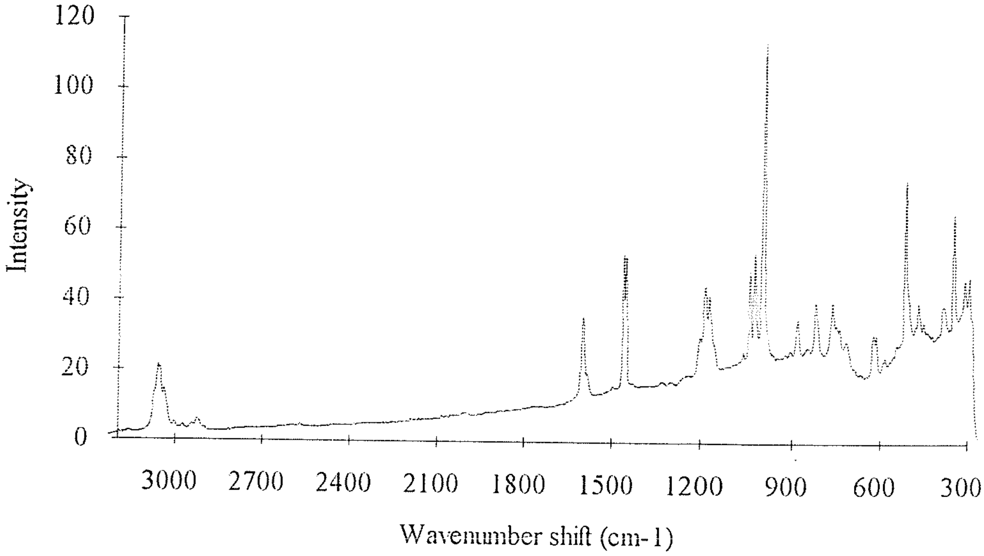

Figure 2.14a FT-Raman spectrum of **K**.

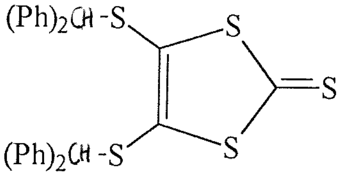

Figure 2.14b Structure of **K**.

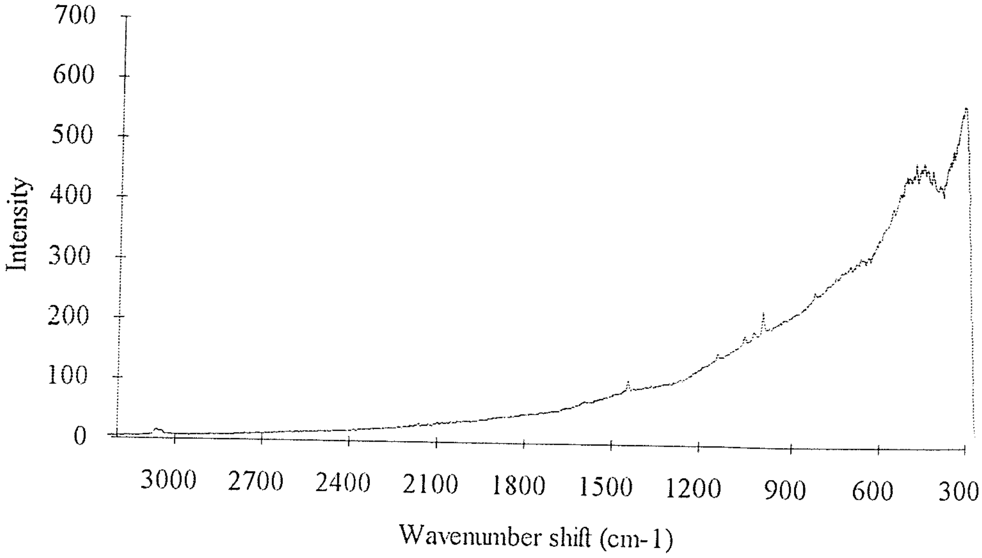

Figure 2.15a FT-Raman spectrum of **L**.

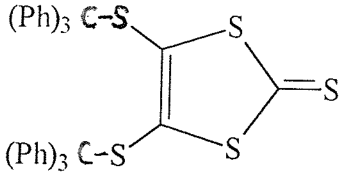

Figure 2.15b Structure of **L**.

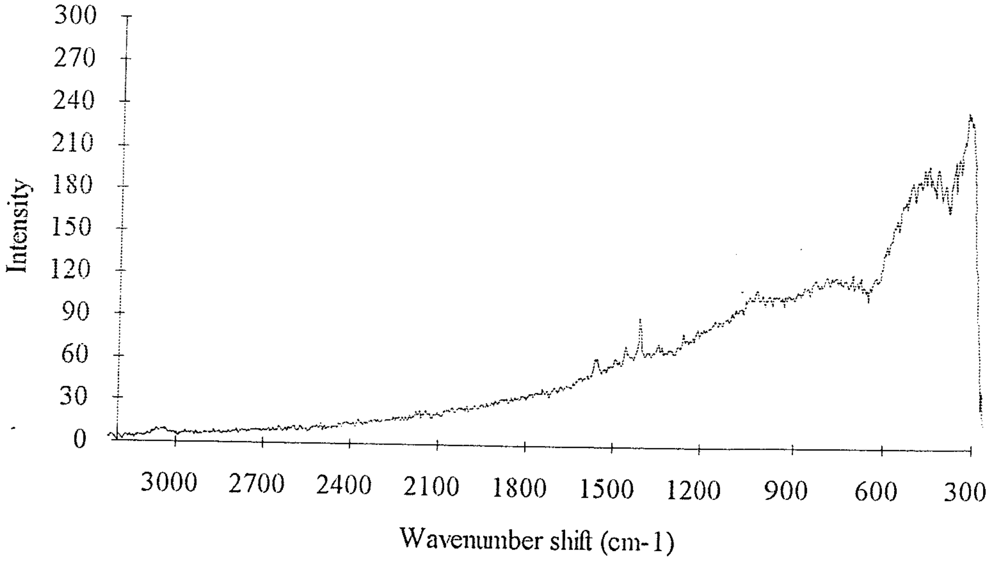

Figure 2.16a. FT-Raman spectrum of **M**.

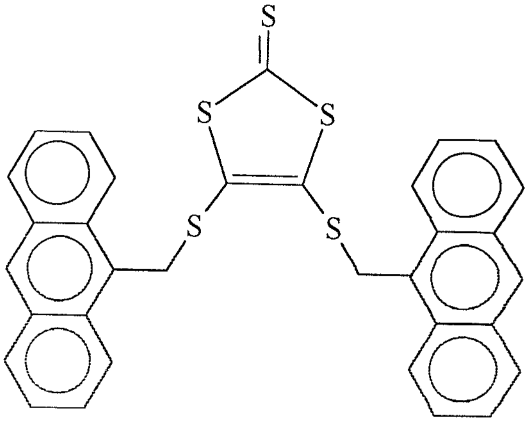

Figure 2.16b Structure of **M**.

The first of these three new compounds - **K**, with $(Ph)_2CHS$- sidegroups - scattered reasonably strongly, with many peaks clearly resolvable. Phenyl groups are quite definitely indicated by:

- Ring breathing at 1006 cm^{-1}
- C-H deformations around 1188 cm^{-1}
- Fermi-coupled ring stretches at 1605 and 1583 cm^{-1}
- Aromatic C-H stretch at 3060 cm^{-1}

Without having to resort to finding the characteristic frequencies of the $(Ph)_2CH$- group, this compound can be differentiated from the other thiones studied by the apparently symmetric doublet at 1463 and 1455 cm^{-1} shift - the first example of such a splitting in the series studied. Thione character is confirmed by the presence of a strong band at 520 cm^{-1}. It should be noted that despite the large mass of the side groups, the C=C mode of the thione ring still occurs around 1470 cm^{-1} shift.

L and **M** do not give such clear spectra - although the same colour and crystallinity as **K**, the two samples fluoresced strongly. Nevertheless, weak bands are still discernible. However, the 1445 cm^{-1} band is now difficult to assign *definitely* to thione ring C=C, since no other thione-specific bands are in evidence, such as the 510 cm^{-1} ring mode; the 1445 cm^{-1} feature may be due to a side group mode. The spectrum of **M** is little help; it seems to be dominated by side group bands exclusively - the strongest Raman band of the anthracene-derived side group is barely in evidence at 1413 cm^{-1} shift, yet is the strongest Raman band. The fluorescence may well be associated with real long wavelength absorption in these materials rather than due to impurity; this may in turn imply that the little Raman scattering seen is in fact pre-resonantly enhanced scattering from sidegroup modes.

A much simpler thione, **N**, is shown together with its Raman spectrum in figure 2.17. Again, this sample shows a strong fluorescence. However, the side groups do not dominate the Raman spectrum, with thione-indicative modes at:

- 1468 cm^{-1} (C=C stretch)
- 1061 & 1051 cm^{-1} (C=S stretch)
- 516 cm^{-1} (thione ring)
- 623 cm^{-1} (S-Et)

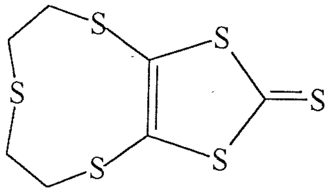

Figure 2.17a. Structure of **N**.

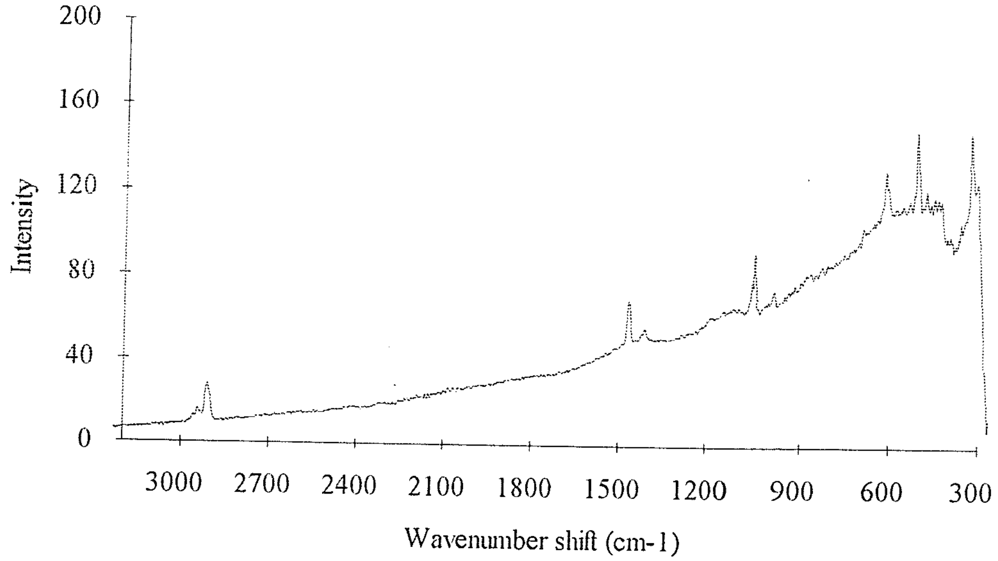

Figure 2.17b FT-Raman spectrum of **N**.

In this case, the absence of phenyl groups is obvious from the lack of bands at 1000 cm^{-1} and 1600 cm^{-1} shift. The methylene C-H stretch (at 2913 cm^{-1}) is the strongest high-shift mode. The cyclic side group is difficult to distinguish, the band at 1414 cm^{-1} shift possibly due to the methylene C-H deformation vibration of the -(CH_2-CH_2)- linkages between the sulphur atoms of the side group.

Continuing the theme of cyclic side groups, the two crown thiones **O** and **P** shown in figures 2.18 and 2.19 represent the next step in complexity.

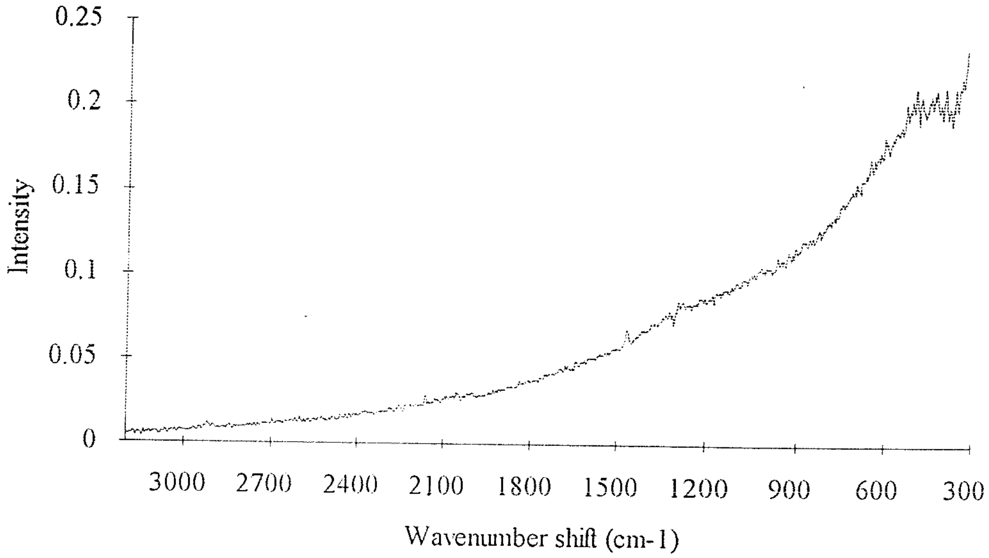

Figure 2.18a FT-Raman spectrum of **O**.

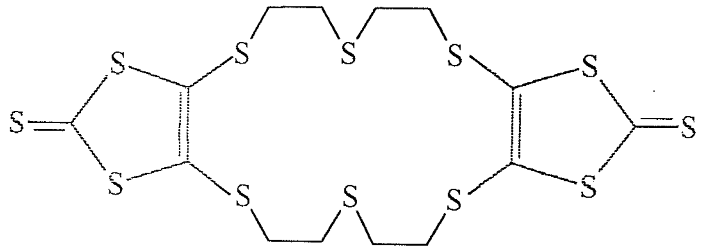

Figure 2.18b Structure of **O**.

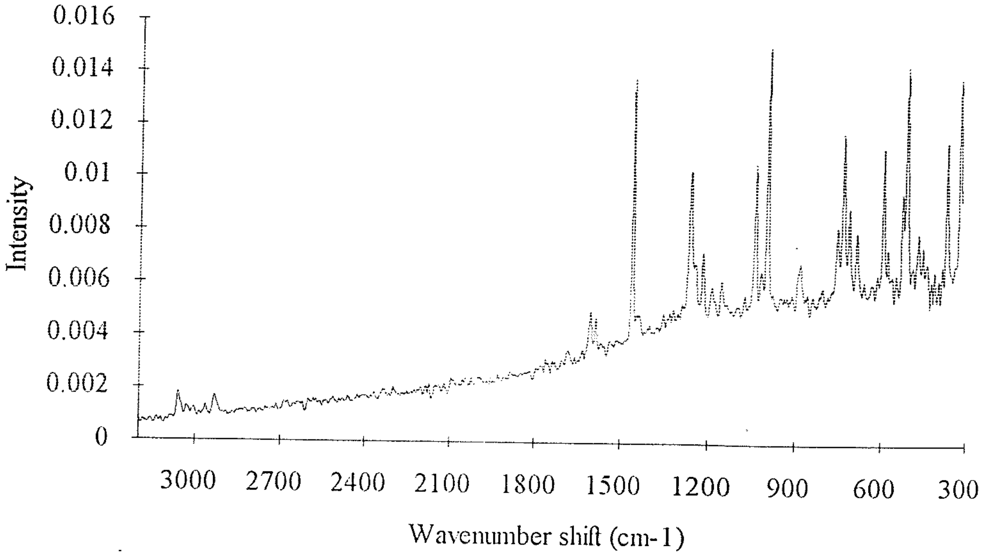

Figure 2.19a FT-Raman spectrum of **P**.

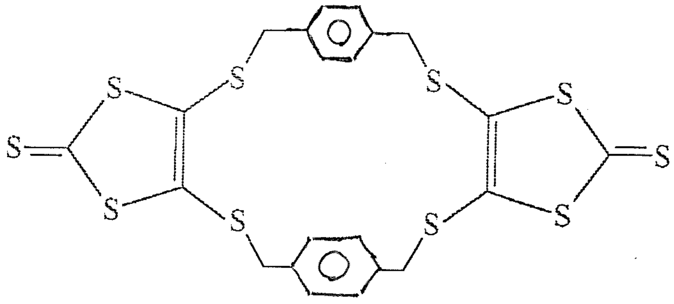

Figure 2.19b Structure of **P**.

Despite many recrystallisations **O** always showed strong fluorescence. The tricks of "burning out" and "bleaching" the fluorescence often used in conventional Raman methods were tried unsuccessfully. Still in evidence, albeit weakly, is the C=C stretch of the thione ring - quite characteristically at 1468 cm^{-1}. **P**, on the other hand, has a far clearer Raman spectrum. Using the rules developed so far:

- The phenyl ring in the crown is confirmed by 3061, 1605 & 1583, and 1006 cm^{-1}
- The thione ring structure is confirmed by 888, 514, and 372 cm^{-1}
- Other bands of note: C=C appears at 1461 cm^{-1}, C=S appears at 1046 cm^{-1}.

The last example of a thione to be considered is **Q**, shown in figure 2.20. This is another simple symmetric thione, without cyclic or bridging side groups. Once again:

- Thione-indicative bands at 1462, 893, 327 and 523 cm^{-1} are quite plain

- C=S stretching region is a little confused, with several bands in the area around 1050 cm^{-1}
- The expected phenyl ring modes are in evidence
- C-H stretch modes attributable to methylene asymmetric modes near 2921 cm^{-1}

There are still many bands left in the spectrum unassigned that makes differentiation between this and the other thiones quick, simple, and quite unambiguous.

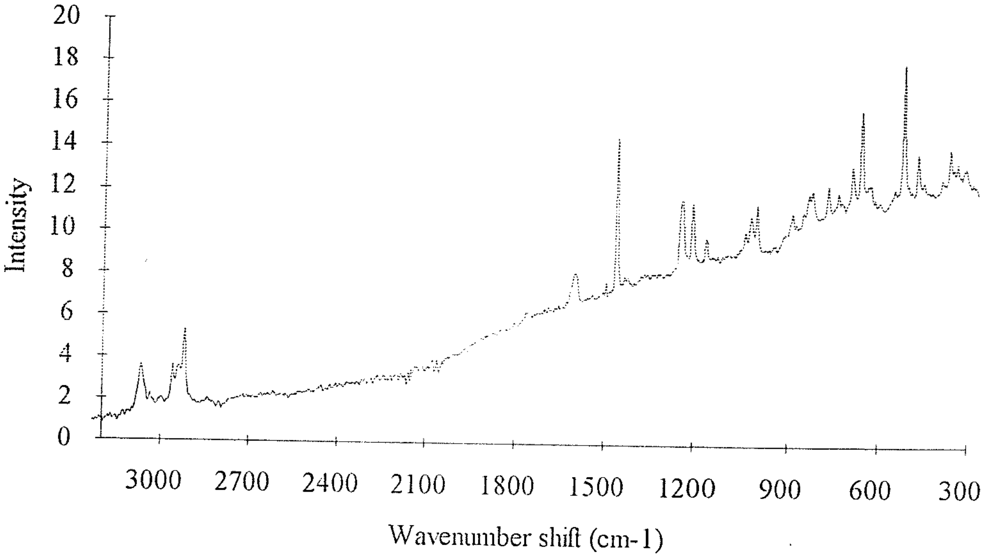

Figure 2.20a FT-Raman spectrum of **Q**.

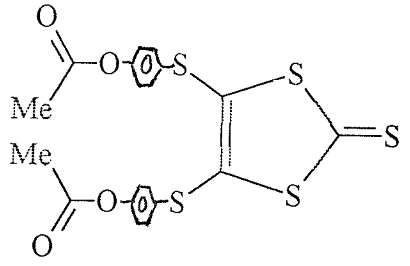

Figure 2.20b Structure of **Q**.

2.3.5 Further comparisons - oxones

The structure of the oxone **R** (shown below in figure 2.21) is the oxygenated analogue of the thione **F** from original group of ten (shown in figure 2.8). **R** was synthesised as part of a scheme to produce the corresponding TTF. Comparing the spectrum of **R** with that of **I** (figure 2.12), the oxone analogue of thione **B** (figure

2.4), it seems apparent that oxones give a larger fluorescence background than the corresponding thione.

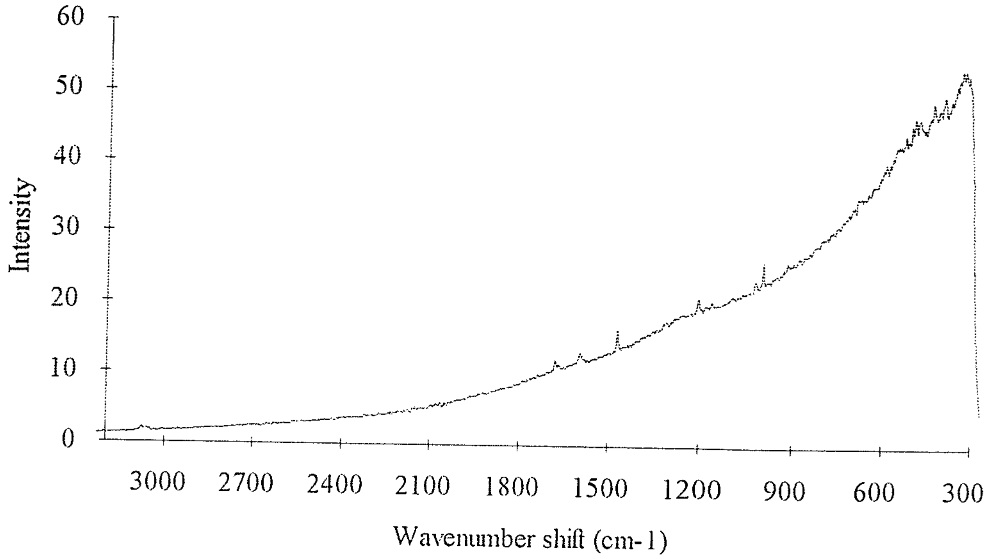

Figure 2.21a FT-Raman spectrum of **R**.

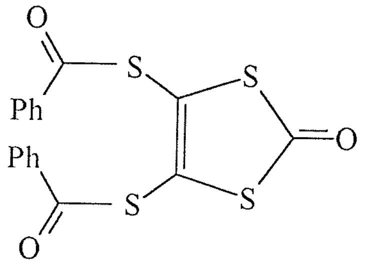

Figure 2.21b Structure of **R**.

This fluorescence might be intrinsic to oxones, or may be due to residue from the mercuric acetate conversion. Near-IR Raman spectroscopy of inorganic species is not always straightforward, since many compounds containing heavy metals have metal-based intra-valence orbital transitions (*'d-d'* or *'f-f'* transitions) that lead to near-IR absorption bands around 1μm - perhaps a similar effect is being seen in the case of mercuric-coupled oxones.

As noted on converting **B** to **I**, the thione ring C=C stretch rises in frequency - from 1464 cm^{-1} to 1470 cm^{-1}, although the upshift (6 cm^{-1}) is less than in the previous case. This is the most analytically-relevant change on converting C=S to C=O, since fluorescence obscures the low-shift region so the disappearance of the 512 cm $^{-1}$ ring mode cannot be used to indicate successful conversion.

The next strongest indicator is the absence of the C=S mode around 1069 cm^{-1}, which is fortunately not obscured by the oxone fluorescence. This *redundancy* - the availability of more than one band to indicator a change in the system - is very attractive, since it makes the analytical method more robust.

The C=O stretching region remains confusing. Two bands are in evidence in both the thione (**F**) and oxone (**R**) spectra, where the thione only has one C=O environment. As noted in the analysis of thione **A**, this region requires more data for assignment purposes; but for analysis, such idiosyncrasies are a godsend, making identification each analogue quite unambiguous.

2.3.6 Alternative comparisons of thiones and oxones

The thione S and oxone T (Raman spectra and structures shown below in figures 22 and 23) provide another check on the assignments made, but in a different way. In both the previous comparisons of oxone against thione (**B** with **I**, and **F** with **R**) the thione had been a member of the original group. In this case, *both* thione and oxone were previously unstudied.

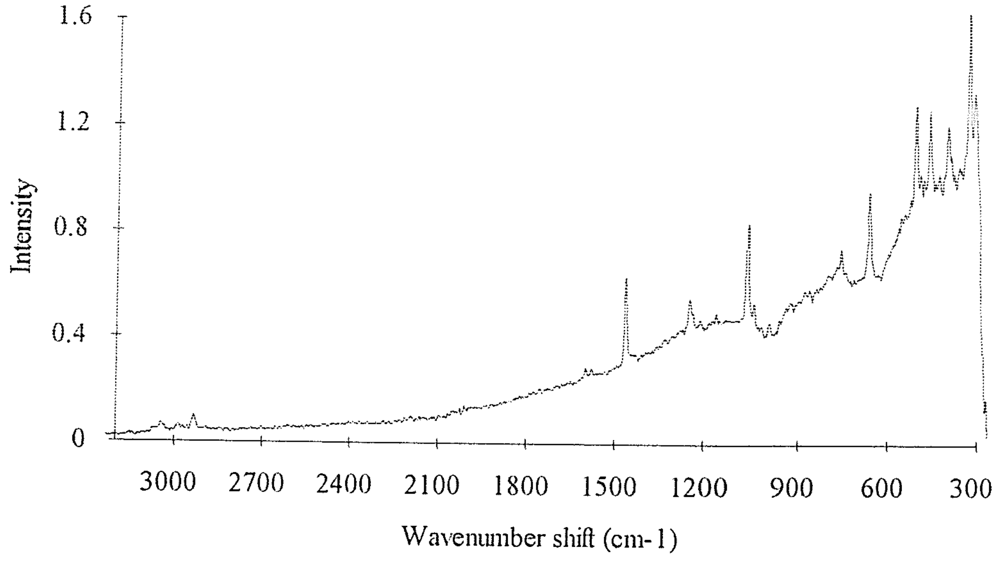

Figure 2.22a FT-Raman spectrum of S.

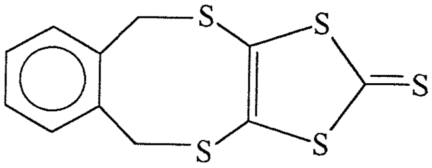

Figure 2.22b Structure of **S**.

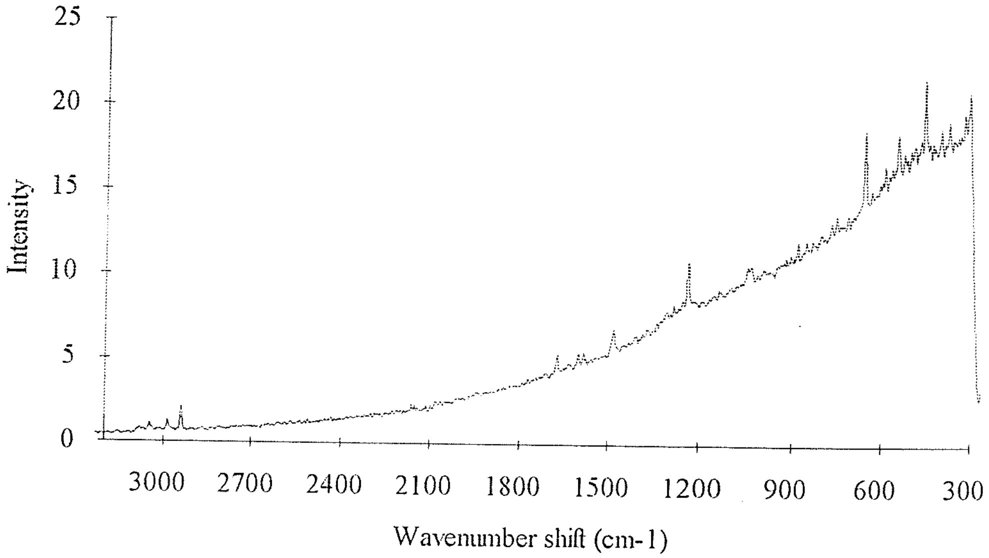

Figure 2.23a FT-Raman spectrum of **T**.

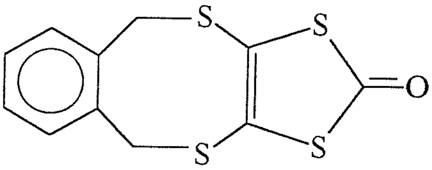

Figure 2.23b Structure of **T**.

It has been shown that the band near 510 cm^{-1} peculiar to the thione ring disappears on conversion to the oxone. This is consistent with the 514 cm^{-1} band in S not being evident in **T**. In place of the prominent thione band at 1070 cm^{-1} shift, one appears in the oxone at 1674 cm^{-1}. This confirms the change of exocyclic substitution from (C=S) to (C=O). The thione ring bands at 668 and 468 cm^{-1} change very little on conversion to the oxone, appearing at 665 and 463 cm^{-1}, indicating that they involve little motion of the exocyclic bond, and are possibly localised around the C=C double bond. Although very weak, the phenyl-associated modes at around 1600 cm^{-1} shift are just resolvable in both spectra

A reduction of aromaticity was proposed as a consequence of conversion, based upon a shift in C=C stretching frequency. This is consistent, the 1466 cm^{-1} band in **S** moving upwards to 1488 cm^{-1} in **T**. The C-H stretching region provides an indication of aromaticity, with the phenyl (C-H) stretching bands at 3046 and 3047 cm^{-1} shift respectively. These two analogues do indicate, however, that the assessment of aromaticity on the basis of C-H band position needs extra study; the three bands in the thione at 3047, 2985, and 2934 cm^{-1} all shift up in frequency to 3047, 2987, and 2941 cm^{-1}. The C=C mode around 1480 cm^{-1} must be a better indicator of change in electronic structure than the C-H stretching region.

2.4 Postscript

The program to synthesise TTF salts was significantly delayed, so the expansion of the project was not possible. At the time of writing (1994), the first TTF-acceptor salts are being produced in Southampton. Recently published results have borne out the predicted success of FT-Raman in the TTF field. In the course of the initial phase of this study (1990-1) Fourier transform surface-enhanced Raman spectroscopy (FT-SERS)[17] was successfully applied to the study of tetrathiafulvanene during electrochemical oxidation\reduction. Also, viability was proven with a combined FT-IR/FT-Raman study of a TTF[18], and a FT-Raman study of a TTF complex with an inorganic salt acceptor[19]. In addition, studies using long-wavelength visible excitation and CCD detection has proved very useful as an analysis method for microscopic quantities of TTF-acceptor materials, with a publication pending[20].

2.5 References

1. G. Schukat, A. M. Richter, and E. Fanghanel, Sulphur Reports 7 155 (1987)
2. J.M. Williams, H.H. Wang, T.J. Emge, U. Geiser, M.A. Ben, P.C.W. Leung, K.D.Carlson, R.J. Thorn, and A.J. Schultz, Prog. Inorg. Chem. 35 51 (1987)
3. K. Kikuchi, K. Murata, Y. Honda, T. Namiki, K. Saito, K. Kobayashi, T. Ishiguro, and I. Ikemoto, J. Phys. Soc. Jpn. 56 4241 (1987)
4. R. Bozio, I. Zanon, A. Girlando, and C. Pecile, J.Chem. Phys. 71 (5) 2282 (1979)

5. R. Zamboni, D. Schweitzer, and H.J. Keller, "Lower-dimensional systems and molecular electronics" Ed. R.M. Metzger et al, p.239 (Plenum Press, 1991)
6. J.R. Ferraro and J.M. Williams, Appl. Spectrosc. 44 (2), 200 (1990)
7. M. Tanaka, M. Shimizu, Y. Saito, and J. Tanaka, Chem. Phys. Lett., 125, 594 (1986)
8. S. Matsuzaki, T. Moriyama, and K. Toyoda, Solid State Commun. 34, 857 (1980)
9. C.J. Petty, G.M. Warnes, P.J. Hendra, and M. Judkins, Spectrochim. Acta 47A (9/10), 1179 (1991)
10. E.M. Engler, N. Martinez-Rivera, and R.R. Schumaker, IBM research reports
11. K.R. Gayathri Devi, D.N. Sathyanarayana, and E.M. Engler, J. Mol. Struct. 71 15 (1981)
12. K. Iqbal and N.L. Owen, J. Mol. Struct. 71 91-5 (1981)
13. B. Girmay, J. Kilburn, A. Underhill, K. Varma, M. Hursthouse, M. Harman, J. Becher, and G. Bojesen, J. Chem. Soc. Chem. Comm. 1406 (1989)
14. W. Kiefer and J.A. Topp, Appl. Spectrosc. 28, 26 (1974)
15. L.J. Bellamy, "The Infrared Spectra Of Complex Molecules, Vol.2: Advances in Infrared Group Frequencies", 2nd edition, p.356 (Chapman and Hall, 1960)
16. W.J. Barreto, M.C.C. Ribeiro, and P.S. Santos, J. Mol. Struct. 269, 75 (1992)
17. S. Nie, and N-T. Yu, J. Raman Spectrosc. 22, 489 (1991)
18. J.R. Ferraro, A.M. Kini, J.M. Williams, and P. Stout, Appl. Spectrosc. 48(4), 531-534 (1994)
19. R. Zamboni, D. Schweitzer, and H.J. Keller, Synth. Metals 41-43, 2241 (1991)
20. J.M. Williams, private communication.

Chapter 3:

Allenylketenimine-Tetracyanoethylene Diels-Alder reaction products

3.1 Introduction

The series of compounds known as allenylketenimines constitute a new development in structural organic chemistry, with many developments pioneered by researchers at the University of Southampton. During 1991, Dennehy and co-workers succeeded in synthesising these compounds by the reaction of certain titanium metallacycles with tertiary butylisonitrile[1] - see figure 3.1:

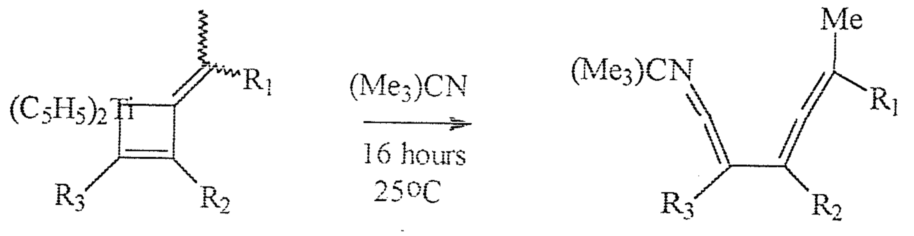

Figure 3.1 The reaction scheme to form the allenylketenimines.

A comprehensive structural analysis was required on this class of compounds. A combination of ^{13}C and ^{1}H nuclear magnetic resonance (NMR) spectroscopies are usually employed for such studies; however, the number of adjacent quaternary carbon centres made unambiguous determination of the structure difficult by ^{13}C NMR - whilst the species also proved to be rather reactive, which made sample preparation difficult.

Methods were clearly required to produce a more stable structure, amenable to structural analysis. Derivatisation (reaction to produce a more stable adduct) had previously been successfully applied to the characterisation of structurally-related vinylketenimines[2]. Tetracyanoethylene (TCNE) derivatives of the allenylketenimines were produced successfully (a brief reaction scheme given in figure 3.2) and ^{13}C NMR successfully employed[3], enabling the structure of the parent allenylketenimine to be inferred.

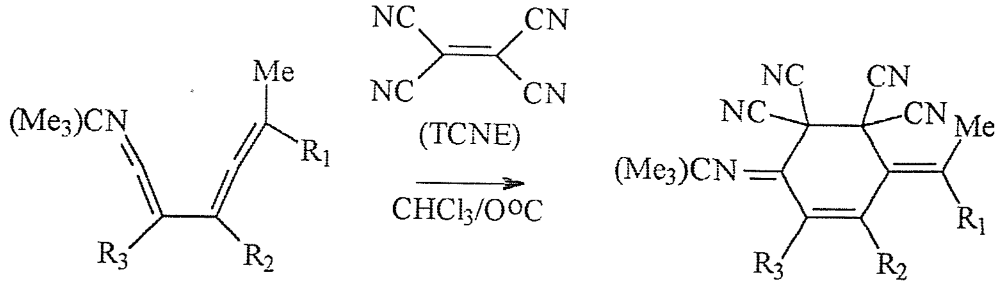

Figure 3.2 Reaction scheme for the derivatisation process, showing production of major isomer.

Mid-IR absorption spectroscopy was employed to monitor the progress and success of the derivatisation - previous work had shown that the intense cumulene stretch near 2000 cm^{-1} disappeared upon reaction with TCNE[1]. However, the IR data was not always straightforward to interpret, as the extreme weakness or complete absence of the nitrile (CN) stretching band often confused the interpretation.

Although curious, this is actually not without precedent[4]. In an attempt to clarify the situation, FT-Raman spectroscopy was employed. The study described in this chapter was carried out with the basic aim of identifying characteristic spectral features of the major functional groups, as well as prominent features of the underlying cyclic framework. From this, an *unambiguous* and *reliable* assignment of any given adduct should be possible. In addition, the study aimed to clarify the reason for the absence of appreciable IR activity for the nitrile bands.

Since direct application to bench chemistry was held in mind throughout the study, group-frequency correlation was employed to assign the spectra. This is the analysis method most often employed for complex vibrational spectra. The basis is simple - on examination of a series of closely-related compounds, common *spectral* features are evident that can be ascribed either to common *structural* features, or to specific functional groups[5].

Group-frequency methods have a sound theoretical basis[6] and an excellent track record[7]. Very often, it is possible to make very good assignments of spectral bands to vibrational modes by this method, without recourse to unreliable, inaccurate, and over-simplistic models. In large, complex, and novel systems with little intrinsic symmetry and very little literature data it is often the *only* viable way to proceed.

The synthetic details of the allenylketenimine-TCNE adducts are well outlined in reference 1. The full IUPAC names for the adducts are cumbersome in the extreme for a discussion where frequent comparisons must be made. Therefore, the numbering scheme of reference 1 has been adopted. The functionalities R_1, R_2, and R_3 are listed in table 3.1.

Adduct	**R_1**	**R_2**	**R_3**	**Yield ratio**
a	Ph-	C_3H_7-	C_3H_7-	6:1
b	Ph-	H-	$SiMe_3$-	Major only
c	Ph-	C_5H_{11}-	$SiMe_3$-	Major only
d	C_5H_{11}-	H-	Ph-	1.4:1
e	C_5H_{11}-	Ph-	Ph-	3:1
f	C_3H_7-	C_3H_7-	C_3H_7-	3:1

Table 3.1 Nomenclature used to describe the allenylketenimine-TCNE adducts. (**1a-f** refer to major isomeric form. **2a-f** refer to minor form.)

The ratio of yield refers to the amount of the major isomer formed with respect to the minor. The reason for the existence of two isomers for most of the series is explained in reference 1. Briefly, the major isomers (denoted **1a-f** in table 3.1) formed in the cycloaddition of the TCNE to the dienophile have the methyl group 'syn' to the nitrile (CN-) groups; this reflects the approach of the dienophile from the side away from the larger terminal group on the parent allene. The structure of the allene is such that the terminal groups lie perpendicular to the plane of the diene, and hence directly on the line of approach of the alkene.

The structural backbone of the series may be described as an essentially-planar, slightly-distorted 6-member ring. Single-crystal X-ray diffraction (XRD) studies on one of the series which crystallised well (**1b**) revealed the tertiary butylimino- ($^tBuN=$) group tilted upwards out of the ring plane, and the R_1 phenyl (Ph-) group twisted at an angle to the plane[8]. These features are primarily due to the steric interactions of the imino group and the trimethylsilyl functional group (Me_3Si-), and the clash of the Ph- group with the vinylic proton at R_2. This results in a loss of conjugation, since a truly planar compound would have considerably more π-orbital overlap, involving the imino group through to the R_1 Ph- group. The two π-bonds in the ring do, however, remain conjugated.

3.2 Experimental

The FT-Raman spectrometer used in this study was the second PE 1700 series Southampton prototype. The spectral range covered was 300 - 3300 cm^{-1} Stokes shift. All Raman spectra are the result of 100 accumulated scans of 4 cm^{-1} resolution, and were excited with 200-400 mW of laser power. The Raman spectra were corrected for wavelength-dependant instrumental response by the method of Petty et al[9]. As usual, the most important point is that relative peak heights may be discussed more meaningfully than for uncorrected spectra.

All the samples studied were off-white, aggregated solids. Although much less reactive than the parent allenylketenimines, the adducts were kept under refrigeration in the dark when not being examined, since their long-term stability was still suspect. For this reason large numbers of co-added scans and high laser powers were avoided. Most of the adducts were available in good yield, except **2f**, which was only available in very low yield. Since **f** was also thought to be quite unstable, the spectra had to be collected without removing the sample from the glass container. This was not ideal for collecting spectra, yet it proved possible to obtain quite adequate results. *In situ* sampling is required for many toxic or air-sensitive compounds; it is far simpler to implement using FT-Raman spectroscopy than with mid-IR techniques.

The mid-IR transmission-absorption spectra were recorded in either CCl_4 or $CDCl_3$ solution using a standard potassium bromide (KBr) window cell on a Perkin Elmer 1600 series FT-IR spectrometer. The spectra presented here are the result of 4 scans at 4 cm^{-1} resolution, and reproduced from reference 1 with the author's kind permission. Only two spectra are displayed, over the range 3500-1000 cm^{-1}, since all the features pertinent to this discussion are clearly demonstrated.

3.3 Results

Figure 3.3 shows the IR spectrum of **1a**, obtained from CCl_4 solution. The IR spectra of the rest of the series were obtained in $CDCl_3$ solutions, since this proved to be the solvent of choice for ^1H NMR spectroscopy. With low-yield products, taking both IR and visible-region absorption spectra from previously-prepared NMR solutions is not uncommon practice; the product made up into solution is put to the best possible use, whilst conserving the remaining product for further syntheses. However, C-D stretching vibration of the solvent appeared around 2250 cm^{-1}, obscuring the nitrile region - as is shown in figure 3.4, the IR spectrum of **1b**, making the collection of mid-IR spectra in this way rather limited in value for these species.

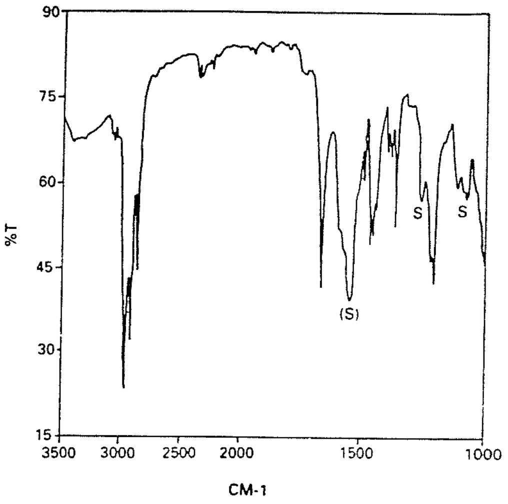

Figure 3.3 Mid-IR spectrum of **1a** in CCl$_4$. S marks solvent peaks.

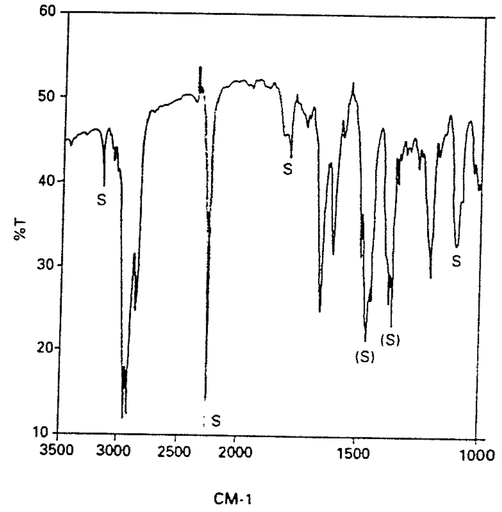

Figure 3.4 Mid-IR spectrum of **1b** in CDCl$_3$. S marks solvent peaks.

However, no interferences are present in the Raman spectra, which are presented along with structures in figures 3.5-3.14. These spectra illustrate elegantly one of the major advantages of Raman spectroscopy over IR for analytical work - because the scattered light is collected directly from the sample without preparation or contact, solvent or mulling agent bands do not complicate the observed spectra, or obscure vibrational detail.

All the Raman spectra are composed of sharp bands superimposed on either a flat or gently-sloping baseline. **2f** constitutes a special case, because the background

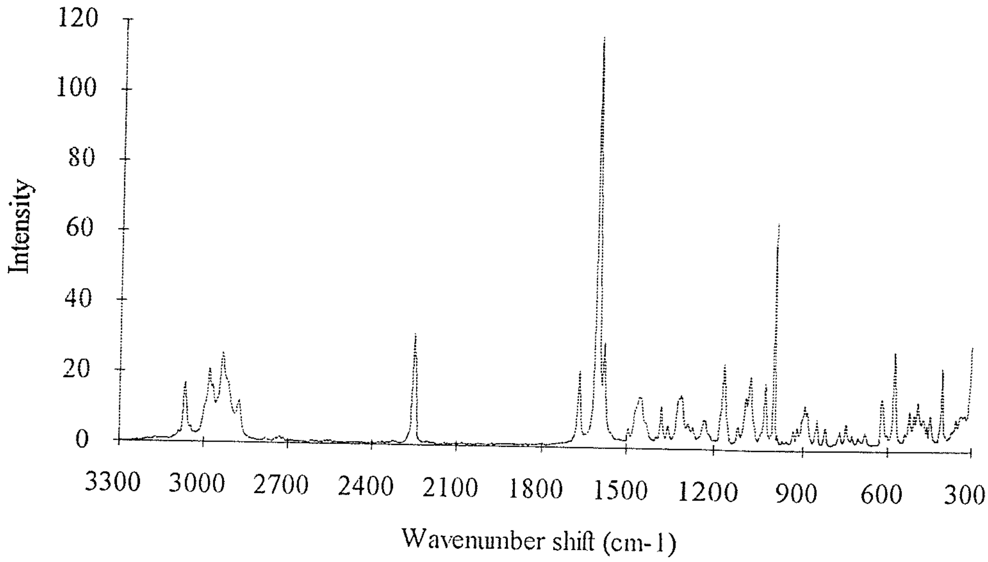

Figure 3.5a FT-Raman spectrum of **1a** (major isomer).

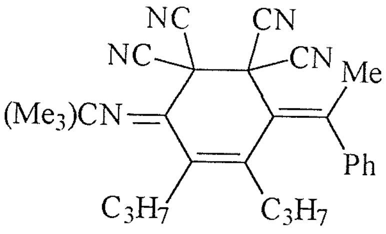

Figure 3.5b Structure of **1a**. Ph group at R_1 is 'syn' to CN in **2a** below.

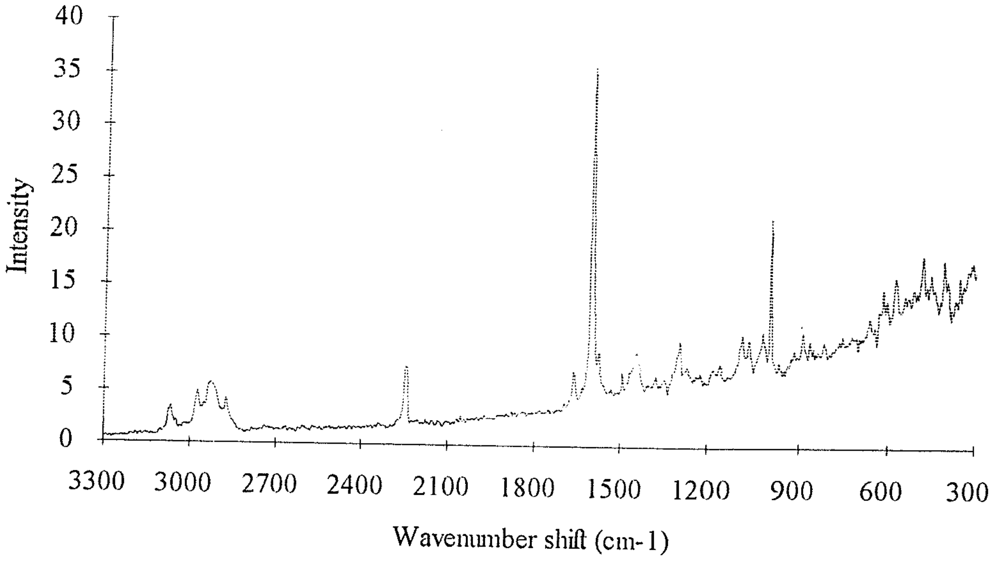

Figure 3.6 FT-Raman spectrum of **2a** (minor isomer).

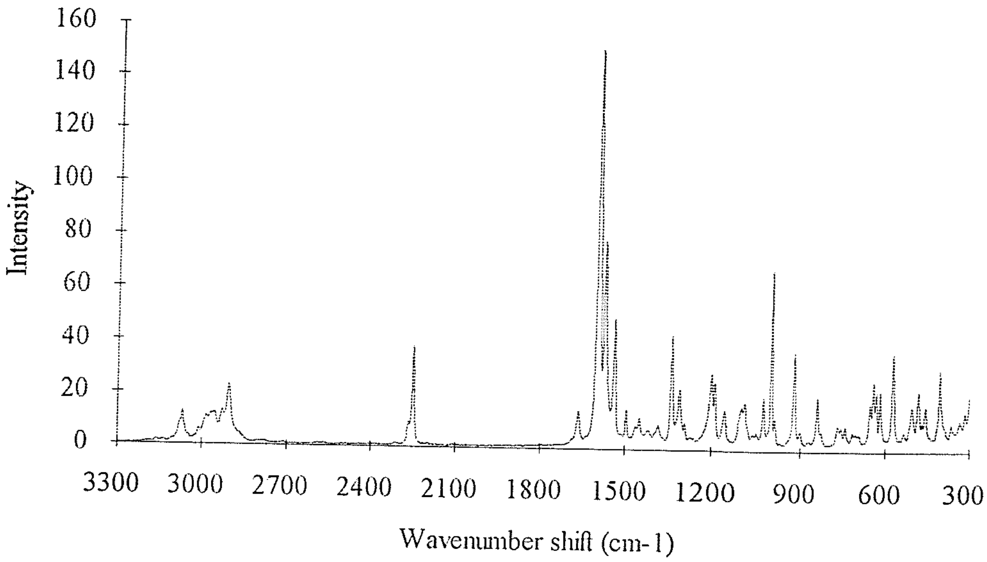

Figure 3.7a FT-Raman spectrum of **1b** (single isomer).

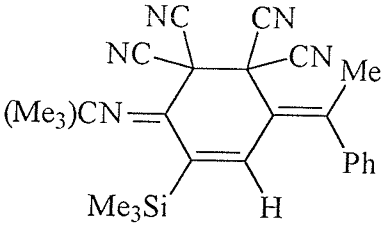

Figure 3.7b Structure of **1b**. H group at position R_2 replaced by C_5H_{11} in **1c**.

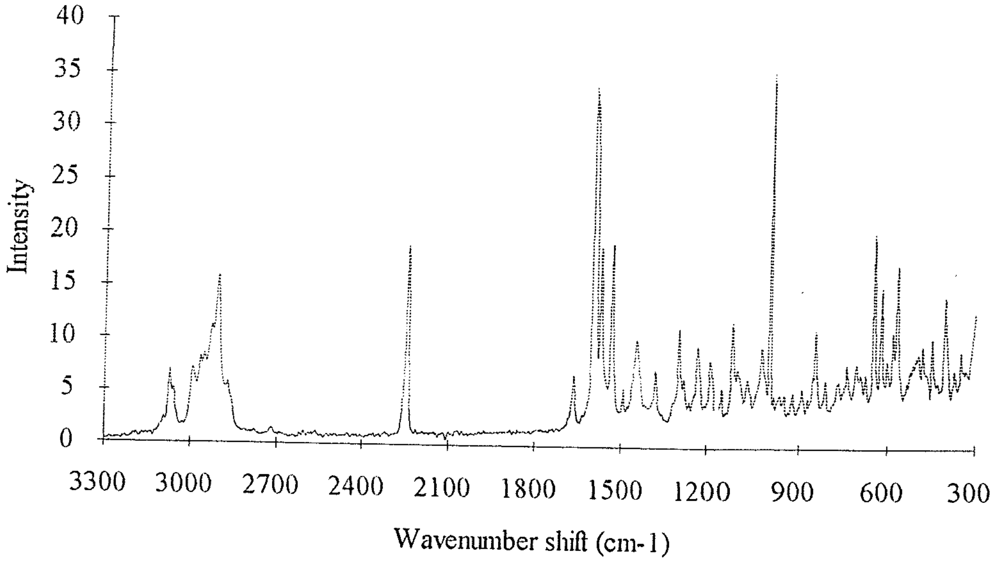

Figure 3.8 FT-Raman spectrum of **1c** (single isomer).

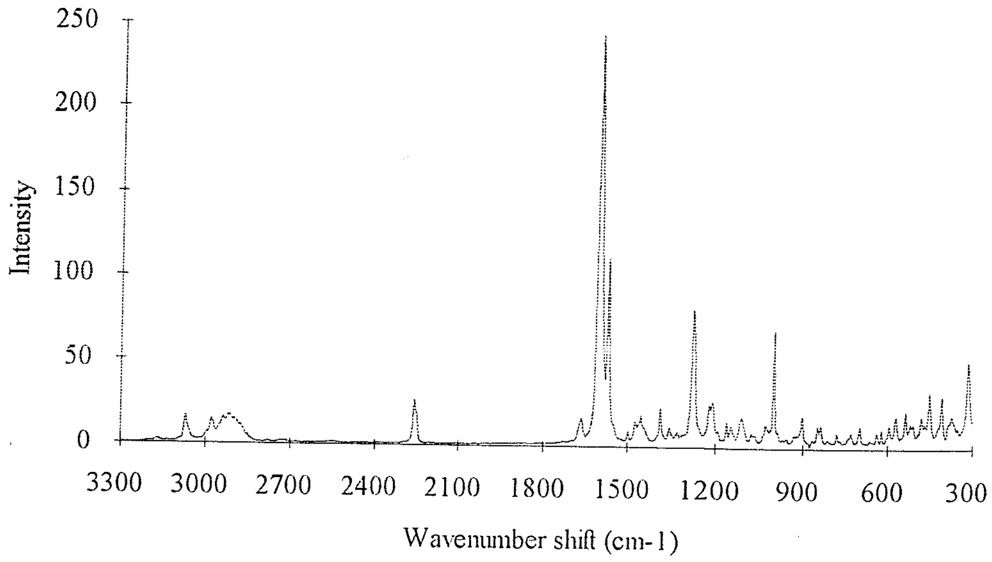

Figure 3.9a FT-Raman spectrum of **1d** (major isomer).

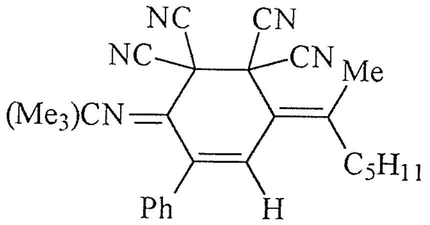

Figure 3.9b Structure of **1d**. C_5H_{11} group at R_1 is 'syn' to CN in **2d** below.

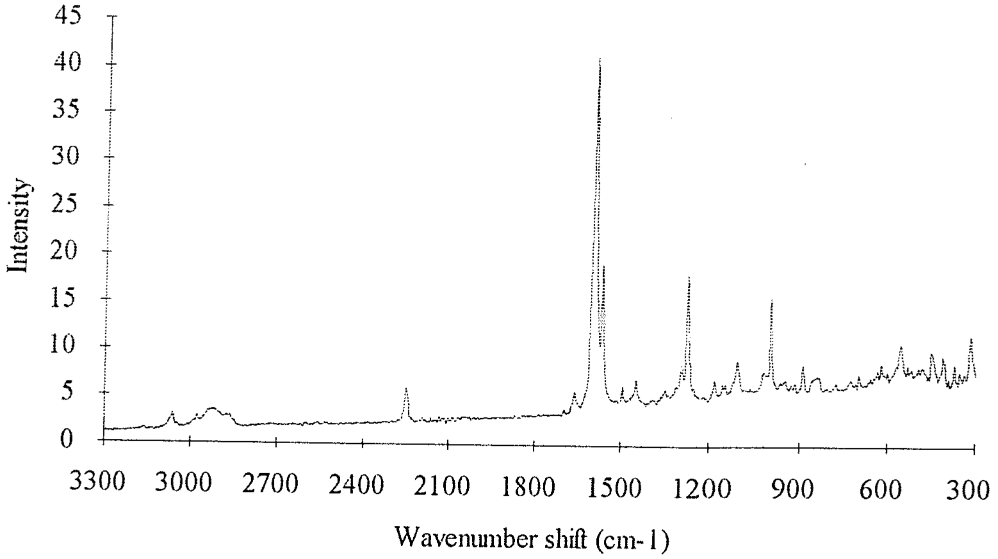

Figure 3.10 FT-Raman spectrum of **2d** (minor isomer).

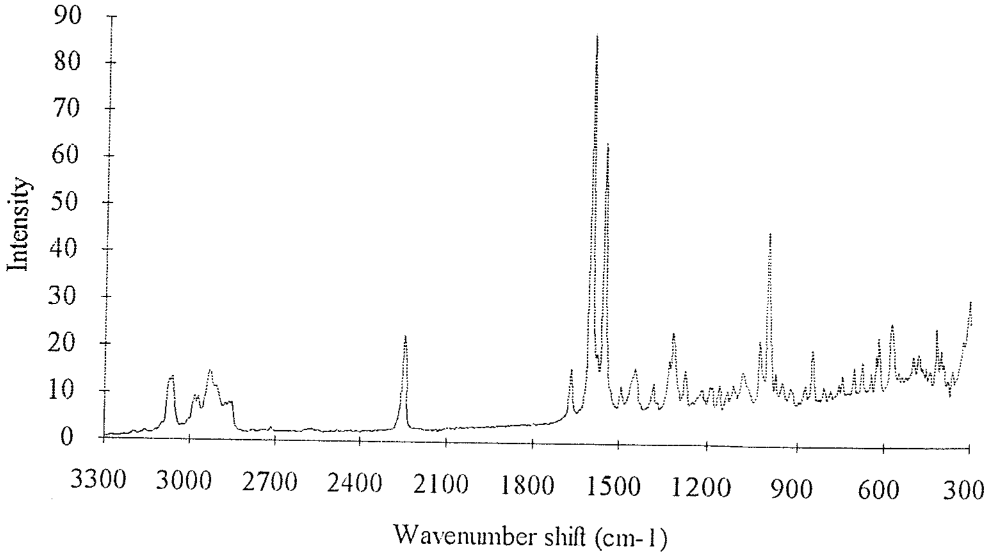

Figure 3.11a FT-Raman spectrum of **1e** (major isomer).

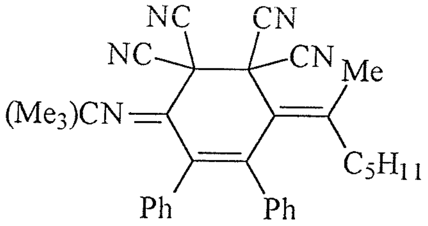

Figure 3.11b Structure of **1e**. C_5H_{11} group at R_1 is 'syn' to CN in **2e** below.

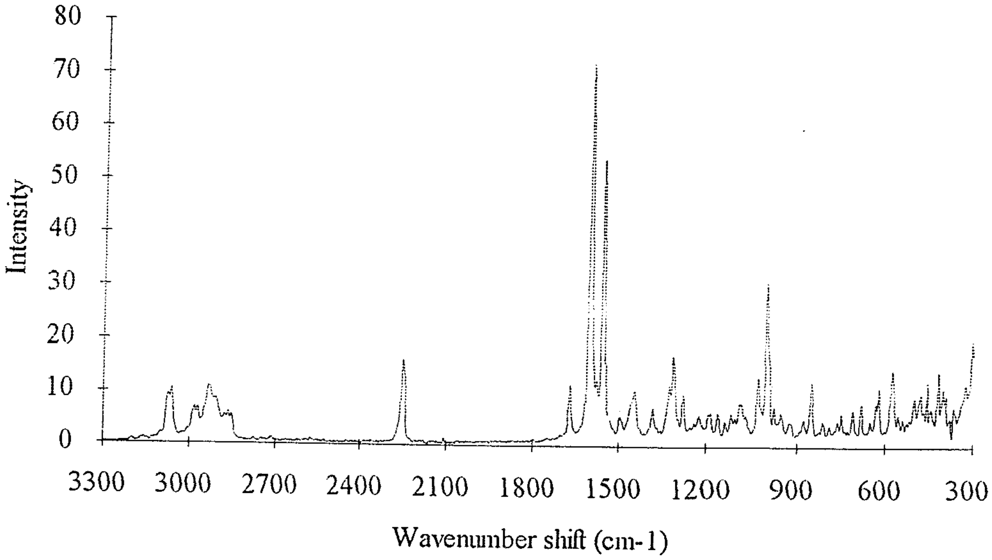

Figure 3.12 FT-Raman spectrum of **2e** (minor isomer).

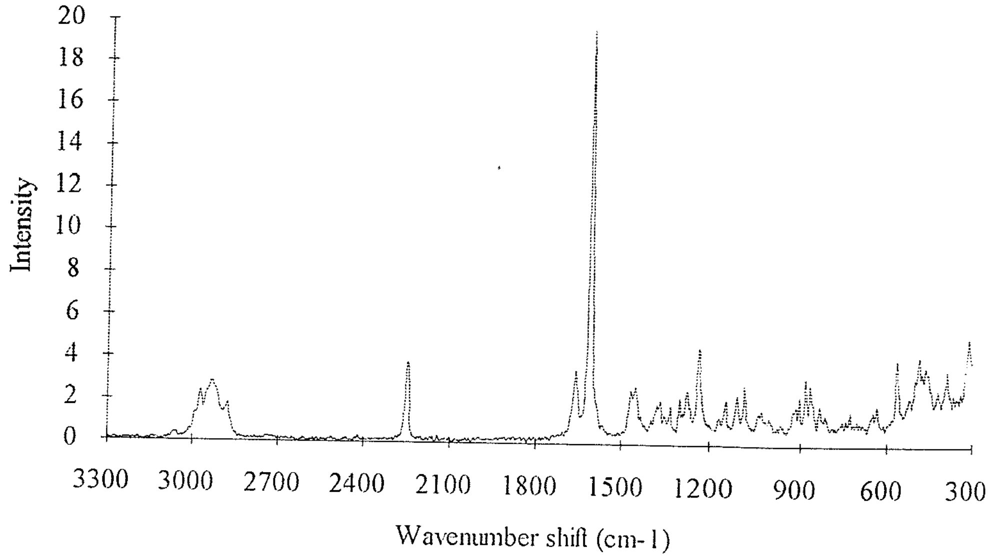

Figure 3.13a FT-Raman spectrum of **1f** (major isomer).

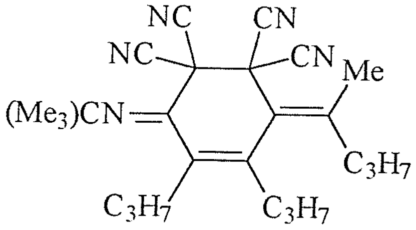

Figure 3.13b Structure of **1f**. C_3H_7 group at R_1 is 'syn' to CN in **2f** below.

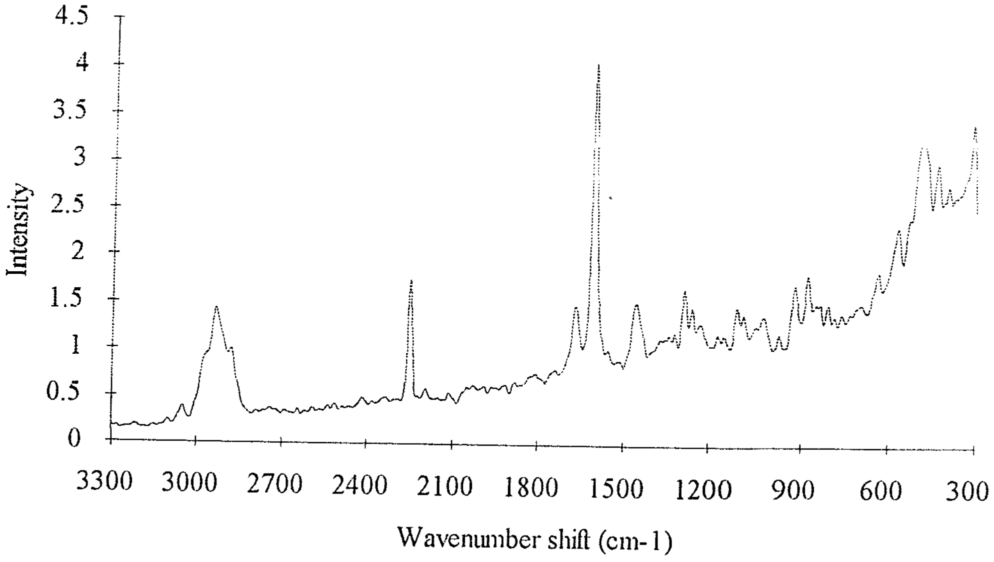

Figure 3.14 FT-Raman spectrum of **2f** (minor isomer).

All the Raman spectra are composed of sharp bands superimposed on either a flat or gently-sloping baseline. **2f** constitutes a special case, because the background can be attributed to fluorescence from the glass container used for this particular sample. In general, if the sample was pure enough to give good interference-free NMR spectra, that same sample gave good Raman spectra. Put another way, recrystallised products generally gave good spectra, whilst column-separated products generally resulted in still-higher quality spectra. The reason is the rigorous exclusion of by-products from synthetic work-up, known to be very problematical in conventional Raman spectroscopy.

3.4 Discussion

From the inspection of the FT-Raman spectra, several features stand out clearly. The first task is to identify features that are specific to the underlying "ring" cyclic structure, and to specific functional groups. Analysing the spectra from high to low Raman shift:

- The presence of **aliphatic** protons is shown by the broad **C-H stretch** band centred around **2930 cm^{-1}**, which appears as an asymmetric triplet in several of the adducts. When **aromatic** C-H is also present, a much narrower band is observed at ca. **3060-3070 cm^{-1}** shift. If **Me_3Si- groups** are present, they give rise to another strong C-H stretch at ca. **2910 cm^{-1}** shift.

- The sharp, medium-to-weak intensity band around **2250 cm^{-1}** shift, which in some cases displays splitting and/or asymmetry, must be due to the **nitrile (CN) stretch**.

- The sharp band close to **1670 cm^{-1}** shift, medium-to-weak in intensity, can be attributed to the **imino group C=N stretch**, and is in excellent agreement with previous studies[10,11]. This provides useful confirmation that the imine is not involved to any great extent in the π-system, since the C=N band shifts to lower frequency on conjugation. The assignment is confirmed by the appearance of an intense sharp absorption band in the IR spectra at almost exactly the same frequency - see figure 3.3.

- The most intense feature in all but one case (**1c**) is a sharp band around 1600 cm^{-1} shift. This is due to a **dienyl C=C stretch**, that of the backbone fragment.

Between 1600-1000 cm^{-1} shift a number of C-H bending and deformation modes occur, which results in a complex pattern of bands, a situation not simplified by the appearance of C-C skeletal stretching modes[7]. However, tentative assignments of certain bands may be made:

- A sharp band, albeit weak, near 1500 cm^{-1} shift, absent from some members of the series. This lies outside the usual region for aliphatic methyl or methylene deformation modes. It is most likely to be a phenyl ring-associated band, probably due to a complex ring-stretch plus deformation mode[13]; this assignment is supported by the absence of the band from the spectra of both the **f** isomers, which contain no phenyl groups.

- A weak, slightly broad band appears in all spectra near 1450 cm^{-1} shift. This is probably due to the interaction of methyl and methylene (CH_2-) in-plane deformation modes[12].

- The band near 1380 cm^{-1} shift is probably due to methyl symmetric deformation, although it is unexpectedly absent from the spectrum of **2d**.

- A medium-to-weak intensity band near 1033 cm^{-1} shift, present whether the species contains phenyl rings or not. The sharp band lies within a narrow range of values, from 1039 cm^{-1} shift in **1f** to 1024 cm^{-1} shift in **2d**. It is quite conceivable that this band is due to a C-C stretching mode, although it would not be appropriate to go further than stating this band is characteristic of the basic ring structure and not the side groups.

- Aromatic substituents (phenyl rings) are confirmed by the strong narrow band at approximately 1000 cm^{-1} shift. This is characteristic of the "ring-breathing" phenyl group mode, and serves to identify the group unambiguously[7,12]. The assignment is quite safe, since both isomers of **f**, which contain no Ph- rings, do not have these bands.

Interestingly, no band indicative of the Si-C moiety can be found in this region. Stretching modes of alkyl-Si species are strongly IR-active[14]; for instance, figure 3.4 shows the intense Si-C absorption band at 1264 cm^{-1} in **1b**.

However, the Raman spectra of **1b** and **1c** do show a pair of quite sharp bands - 1304 & 1287 cm^{-1} shift in **1b**, 1299 & 1283 cm^{-1} shift in **1c**. These may well be indicative of the $MeSi_3$- group. Four points support this argument:

- The separation (14 cm^{-1}) is the same in both cases
- Both pairs are medium to weak in intensity
- The higher-shift component is more intense than the lower.
- No such peaks are seen in any other member of the series.

1b may further be differentiated from **1c** simply by the presence of a narrow, medium-intensity band in the former (where R_2 = H) at 1331 cm^{-1} shift and not in the latter ($R_2 = C_2H_7$). Unfortunately, it is not possible to generalise this point to other R_2 = H members of the series, **d** and **f**.

Below 1000 cm^{-1} shift it becomes much more difficult to draw out bands characteristic of the ring structure. Bands in this region arise from modes coupled with other vibrations, reducing their usefulness as group frequencies:

- A sharp, medium-to-strong intensity band near 570 cm^{-1} in all spectra. This probably arises from a mode (or modes) of the tertiary butylimino group carbon skeleton. It falls near the accepted value for an internal quaternary carbon centre[14], although little data seems to be available for this particular vibration. The band itself is both strong in intensity and quite stable in position, falling between 555 cm^{-1} shift in **2d** and 578 cm^{-1} shift in **1a**. Thus assignment to the tertiary butylimino group seems reasonable, but is not proven.

- A similar medium-intensity narrow band occurs around 410 cm^{-1} shift, lying between 421 and 391 cm^{-1}; it is quite characteristic of the series, yet is difficult to assign to a specific functional group or structural feature.

- The same is true of a band near 630 cm^{-1} shift; the position ranges between 650 cm^{-1} for the high-shift doublet component in **1f**, to 607 cm^{-1} for the low-shift component in **2a**. This particular band is generally weak, can be quite broad, and may be an asymmetric doublet (**1d**) or a single peak (**1a**). The wide spread (± 20 cm^{-1}) from the average position (630 cm^{-1}) might be explained if the normal mode(s) which contribute to this band are sensitive to the exact nature of the substituents.

Some of the points made above require amplification. The first concerns the C=C stretching region, the second the CN-stretching.

3.4.1 The C=C stretching region

The strong band lying between 1615-1594 cm^{-1} shift is the frequency range expected from a conjugated diene. For instance, the Raman spectrum of liquid 1,3-butadiene exhibits a very strong band at 1637 cm^{-1} shift[7], which is due to the two C=C bonds vibrating in-phase. Given the environment of the dienyl C=C double bonds in the TCNE adducts, it is not unreasonable to propose that the 30 cm^{-1} downshift is due to mass effects of the groups attached to the dienyl fragment.

A further point concerns the intensity of the aromatic ring C=C mode. Since all the adducts except **f** contain phenyl groups, it is safe to assign the band near 1577 cm^{-1} shift (lying between 1581-1568 cm^{-1}) to the phenyl ring stretching mode which occurs in benzene at 1596 cm^{-1}. The intensity of this narrow band is quite unpredictable; no consistent explanation for the strength of this band can be reached from the data presented here. The very low intensity of the phenyl-associated 1581 cm^{-1} shift band in both isomers of **e**, an adduct with two Ph- groups, is still surprising. Again, the reason for this effect is unknown.

A second sharp band of appreciable intensity occurs in this region in the spectra of **1b** (1539 cm^{-1}), **1c** (1536 cm^{-1}), and both isomers of **e** (1556 cm^{-1} major, 1557 cm^{-1} minor). Again, it is difficult to correlate the intensity with any specific feature.

Two last points must be made about the C=C region for analytical purposes. The first is the splitting of the intense C=C band in **1c** into a doublet at 1601+1594 cm^{-1} shift, which is the only example of such splitting.

3.4.2 The nitrile (CN-) stretch

The nitrile stretching region around 2250 cm^{-1} shift provides many interesting points on which to comment. Experimental IR data is available on a wide range of nitrile environments[16-18] and the theoretical basis for the intensity variations and frequency shifts often observed in the IR absorption spectra is well-developed[19]. The broad features of the previous studies can be neatly summarised:

- Firstly, IR absorption intensities tend to be extremely unpredictable and vary widely.

- Secondly, the intensity can be correlated within certain series to the magnitude of the inductive effect operating on the nitrile groups, whilst the intensity is reasonably insensitive to the degree of conjugation in the system.

- Thirdly, it has been proposed that small changes in equilibrium CN bond length may cause significant change in the equilibrium value of the bond dipole moment, since in general dipole moment as a function of bond length is a steeply-curved function; this would give rise to large variations in the intensity of absorption for environments where the bond length had only changed slightly.

- Fourthly, in contrast to the intensity variability, the absorption frequency is remarkably stable, and depends on the electronic structure in the location of the nitrile group. Saturated nitriles absorb around 2250 cm^{-1}, whereas conjugated unsaturated nitriles absorb around 2220 cm^{-1}, with unsaturated unconjugated systems falling in between, along with aromatic systems, where the exact position depends on the nature of the side-groups appended to the cyclic system.

In addition to the experimental IR and Raman data, theoretical study[19] has shown that the frequency is remarkably unaffected by mechanical perturbations, and also that the CCN- moiety needs to be considered, not just the CN- in isolation because the CN- mode mixes significantly with the C-C bond adjacent. However, the CN- mixes strongly *only with this band*. This work also shows how the IR absorption strengths vary as a strong function of electronic environment.

Raman data for the intensity of the nitrile species is also available[20]. It confirms the narrow range of band position, and notes a similar trend in band position as a function of conjugation. However, the *intensity* of the nitrile band does not vary as widely, or as unpredictably, as the corresponding IR absorption bands. This has been attributed to the bond polarisability not being as steeply-curved a function of bond length as the dipole moment; hence large variations in equilibrium bond length, reflecting changes in CN environment, may have a small effect on the intensity of the Raman spectrum.

The very low intensity of the nitrile band in the IR spectra of the allenylketenimine-TCNE adducts was mentioned in the introduction and shown in figures 3.3 and 3.4. The extremely weak absorption of these compounds is clearly another example of the unpredictability in nitrile absorption strength.

The simplest model compound for the environment of the CN- groups in the adducts is malonitrile ($CH_2(CN)_2$). Jesson and Thomson reported a low value for the molar absorption intensity[16], which led them to the conclusion that dinitriles with CN- groups bonded to the same carbon atom have low IR intensity because of the inductive effect of one CN- group on the other. If this is the case, then the adducts under study here are good candidates for very low IR absorption intensities, because they have two more nitrile groups on the β-carbon. Figure 3.15 contrasts the two environments:

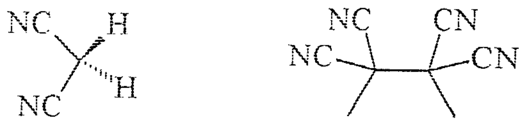

Figure 3.15 Malonitrile (left) and the -CN environment in the TCNE adducts.

In contrast, a great deal of information can be gained from the FT-Raman spectra in the CN- region, despite the apparent simplicity:

- In general there is one sharp band, around 20 cm^{-1} in width, with a definite shoulder or splitting, either to high or low shift. In the single case of the band being split appreciably (**1b**), the bandwidth of each component is reduced to 10 cm^{-1}.

- There are two different environments for the dinitrile groups; one has a C=N group on the β-carbon, whilst the other has a C=C. Each has the other dinitrile group as the other β-carbon substituent. A shift or splitting of the CN- band to reflect these two environments might be anticipated; the fact that no major splitting or large shifts are encountered is possibly a reflection that the two environments are not widely different in terms of electronic structure.

- The position of the band (ca. 2250 ± 5 cm^{-1}) is characteristic of a saturated nitrile group, and is unaffected by changes in the side groups. This confirms the small degree of mechanical coupling between the side groups and the CCN- bonds.

- The intensity of the band is, for the most members of the series, medium-to-weak in comparison to the C=C stretch. The intensity does not vary widely, and the band does not become unobservable in any of the series studied. The intensity and the band-position data agree, indicating a saturated nitrile environment.

Speaking from an analytical standpoint, it would be convenient to be able to distinguish between the major and minor isomers of the adducts by simply looking for a band (or bands) sensitive to the methyl group in the β-position to R_1 being 'syn' to the adjacent dinitrile group or not. It is quite plausible that the dinitrile grouping itself would be sensitive, since some steric interaction between the Me- and CN- groups is likely. This might explain the splitting in the nitrile region, since it would affect one dinitrile group and probably not the other.

However, the biggest splitting (resulting in well-resolved, separate bands) occurs in **1b**, where it is known that the very bulky Me_3Si- group at R_3 greatly perturbs the imino group. This may result in a "knock-on" effect, either sterically or through conjugation or both, which affects the dinitrile group in the β-position to the imino group; thus the imino-side dinitrile grouping may be affected whilst the other (C=C side) dinitrile group may not. **1c** provides another example of this, with the high asymmetry of the band leading to the conclusion that a second, weaker band is present at higher shift. Thus, isomerism is not necessarily the correct explanation for the nitrile band asymmetry and splitting.

It is quite plain after examining each pair of adduct isomers that no pair have identical band positions, or even the same band-structure in the nitrile stretching region band. Curve fitting would in principle yield more accurate estimates for the wavenumber position of the shoulders. However, without guidance on the number of functions to fit, the outcome may be of limited meaning. It is quite clear that the nitrile band may be used to differentiate between the two isomeric forms of a given adduct.

Adduct	Band position (cm^{-1})	Description
1a	2253 (2248)	Prominent shoulder to low shift.
2a	2247	Reasonably symmetric.
1b	2265, 2250	High-shift band weaker.
1c	2246, ?	Asymmetric (weaker band to high shift).
1d	2256 (2250)	Prominent shoulder to low shift.
2d	2250, ?	Slight asymmetry on low shift side.
1e	2251, ?	Very asymmetric; low shift shoulder.
2e	2253 (2248)	Prominent shoulder to low shift.
1f	2248	Symmetric; curious band shape.
2f	2249	Symmetric; simple line shape.

Table 3.2 Position and band shape of nitrile stretch

3.5 References

1. R.D. Dennehy, Ph.D. thesis, University of Southampton (1992)
2. E. Differding, and L. Ghosez, Tetrahedron Lett. 26, 1647 (1985)
3. R.D. Dennehy and R.J. Whitby, Chem. Commun. 35 (1992)
4. H. Bross, R. Schneider, and H. Hopf, Tetrahedron Lett. 23, 2129 (1979)
5. N.B. Colthup, L.H. Daly, and S.E. Wiberley, "Introduction to Infrared and Raman spectroscopy", 2nd Ed. (Academic Press, 1975)
6. G. Herzberg, "Molecular Structure and Molecular Spectra. II: Infrared and Raman spectra of polyatomic molecules" Ch. 2 Pt. 4 (Van Nostrand, 1944)
7. F.R. Dollish, W.G. Fateley, and F.F. Bentley, "Characteristic Raman Frequencies of Organic Compounds" (Wiley Interscience, 1974)

8. R.J. Whitby, M. Webster, and R.D. Dennehey, Acta Cryst. C48, 1252 (1992)
9. C.J. Petty, G.M. Warnes, P.J. Hendra, and M. Judkins, Spectrochim. Acta 47A, 1179 (1991)
10. A. Kirrmann and P. Laurent, Bull. Soc. Chim. Fr. 1499 (1956)
11. J. Fabian, M. Legrand, and P. Poirier, ibid, 1657 (1939)
12. R.G. Snyder and J.H. Schachtschneider, Spectrochim. Acta 21, 169 (1965)
13. E.B.Wilson Jnr., Phys. Rev. 45, 706 (1934)
14. G.Socrates, "Infrared characteristic group frequencies", Wiley-Interscience, J. Wiley & Sons, London (1980)
15. E.J. Rosenbaum, V. Grosse, and H.F. Jacobson, J. Am. Chem. Soc. 61, 689 (1939)
16. J.P .Jesson and H.W. Thompson, Spectrochim. Acta 13, 217 (1958)
17. R.E. Kitson and N.E. Griffiths, Anal. Chem. 24(2), 334 (1952)
18. M.F. Amr-Sayed and R.K. Sheline, J. Inorg. Nucl. Chem. 6, 187 (1958)
19. S. Besnainou, B. Thomas, and S. Bratoz, J. Mol. Spectrosc. 21, 113 (1966)
20. J.P. Jesson and H.W. Thompson, Proc. Roy. Soc. 268A, 159 (1962)

Chapter 4:

Hydration of the γ-Alumina surface

4.1 Introduction

Aluminium oxide (Al_2O_3) is one of the most important materials used in the modern chemical industry. It serves as a support in many heterogenous catalytic systems, whilst the γ-alumina surface has catalytic properties in its own right[1]. However, γ-alumina finds an important application in the electronic components industry - as it possesses excellent qualities as the dielectricium of electrolytic capacitors[2].

Typically, 100-800 nm thick films of γ-alumina are employed in capacitors; the films are generated by anodic oxidation of extremely pure aluminium foils, in proprietary electrolyte mixtures. The quality of the capacitor depends strongly on the homogeneity and thermodynamic stability of the film produced. It has been observed that treatment of the oxide film with phosphate greatly reduces the occurrence of surface reactions that lead to the formation of aluminium hydroxide $Al(OH)_3$. One of the most perplexing aspects of the surface stabilisation is the lack of definitive model concerning the structure of the phosphate-adsorbed alumina surface[3].

As part of a multidisciplinary research effort in the aqueous-phase chemistry of alumina, the Swedish universities of Umeå and Luleå have been jointly studying the reactions of the γ-alumina surface, as a function of pH, by extremely sophisticated potentiometric titration electrochemical experiments combined with theoretical modelling. This has led onto predictive thermodynamic calculations that in part reveal the surface speciation. The application of such titration techniques to mineral surfaces is new, and finding increasing application[4].

The application of vibrational spectroscopy to the hydrated γ-alumina surface, and to the phosphate-adsorbed surface, is extremely inviting. During a three-month exchange visit to Luleå in 1992, it was decided to apply FT-Raman techniques to the problem. This chapter presents the first results obtained from this application.

4.2 Experimental

The method used to prepare the hydrated γ-alumina samples was exactly the same as that used at Umeå, in order to maintain a direct comparison with the results obtained by titration.

Extremely well-characterised γ-alumina is required for the experiments, and was supplied by Mandoval AB. The purity was quoted as >99.99% with respect to trace metals, the mean particle size established as <0.1 μm diameter, whilst the surface area was determined (by the N_2 BET isotherm method) to be 145 m^2/g.

In the first series of experiments, 20 g/l suspensions of γ-alumina in deionised water (conductivity < 1μS/cm) were hydrated with stirring for 4-5 weeks without purging in air-tight vessels, thermostated at 25°C. The pH of the suspensions were monitored by glass electrode potential; after 3-4 weeks, a slow and steady drift to slightly alkaline (ca. pH 7.5-7) conditions began to stabilise.

After final equilibration of the glass electrode potentials at around 4-5 weeks, 20 cm^3 of the suspension was added to 30 cm^3 of 0.167 M NaCl(aq). If required, the pH was adjusted, then stirred for 12-24 hours, a final check on the pH made, then filtered under gravity, and dried under mild conditions (40-50°C). After 24 hours, the samples were ground in an agate pestle and mortar, and stored in a desiccator.

During the study, the hydration method changed slightly - such changes are outlined in detail where necessary in the coming sections. The changes made essentially involved hydrating at the desired pH rather than afterwards, changing the ratio of time spent hydrating to that equilibrating at different pH, and also changes in the hydration temperature, along with the use of a centrifuge for separation.

The first set of results gathered from the stirred samples highlighted a flaw in the experimental technique, which will be discussed in the next section. The outcome was that the stirring of the hydration suspension was ceased. Potentiometric studies in these systems indicated no change in equilibration time or in final pH, whilst spectroscopic studies revealed no apparent effects from the sodium or chloride ions introduced during pH adjustment, and no effect could be seen from leaving the systems to equilibrate in open, rather than sealed, vessels.

Unless otherwise noted, FT-IR/Raman spectra were collected on the Luleå instrument, a Perkin Elmer 1700 series equipped with a near-IR Raman bench. FT-Raman spectra were taken from samples pressed into the solid sampling accessory; 320 scans were co-added using 4 cm^{-1} resolution, with an incident power of ca. 600 mW, whilst cooling the InGaAs detector to 77K was always necessary, resulting in a maximum shift of ca. 2900 cm^{-1} being detectable. Mid-IR spectra were taken in diffuse reflectance, against a 2.5% dilution in dry KBr (refractive index 1.6, particle size 5-20 μm) against a pure KBr reference; typically 100 co-added scans at 4 cm^{-1} resolution were collected. Spectra were recorded in Kubelka Munk units, and transformed directly into absorbance units using the PE IRDM software. XRD was carried out on many of the samples, to attempt verification of any changes brought about by the surface reactions. The diffractometer was a Philips DCU PW 1710/00, using Cu $K_{\alpha 1}$ and $K_{\alpha 2}$ radiation at 1.54056 and 1.54435 Å respectively. Powder diffractograms from ca. 650 mg of sample were indexed by the JCPDS indexing service.

4.3 Results and discussion.

4.3.1 Hydrating γ-alumina

The attack of water upon the oxide surface is two-fold; hydroxylation, and hydration[5]. The first describes the attachment of $(OH)^-$. The reaction of water at the oxide surface proceeds by attachment of $(OH)^-$ to aluminium surface sites, whilst H^+ bonds to the oxide sites. The second step - hydration - is the adsorption of molecular water onto the hydrated layer formed in the first step.

Figure 4.1 shows the FT-Raman spectrum of γ-alumina powder before hydration. All that is seen from the bulk sample is a classic fluorescence background - sloping steeply towards the Rayleigh line, with no structure, and high intensity.

γ-alumina should be considered meta-stable, even at room temperature[6,7]; a small amount (ca. 0.02 mole per cent) of incorporated water seems required to stabilise the structure, although the exact role is still discussed.

Figure 4.2 shows the mid-IR spectrum of unhydrated γ-alumina, and clearly reveals broad hydroxyl bands around 3000 cm-1 and 1500 cm-1. Removing these bands requires dehydration around 900°C, at which temperature the structure reverts to α-alumina, known as corundum.

The catalytic activity of the γ-alumina surface is greatly improved by heat-treatment *in vacuo* to remove many of the hydroxide groups, which are readily readsorbed from the atmosphere to stabilise the structure. Such heat treatment causes the appearance of strained Al-O sites and vacancies[1,8].

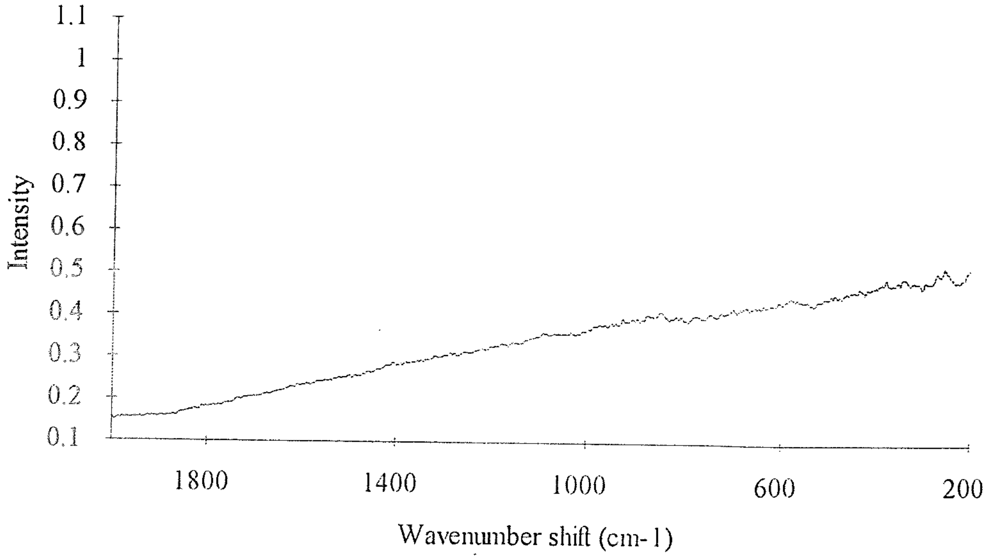

Figure 4.1 FT-Raman spectrum of unhydrated γ-alumina. NB: feature at near 260 cm^{-1} shift due to correction function artefact.

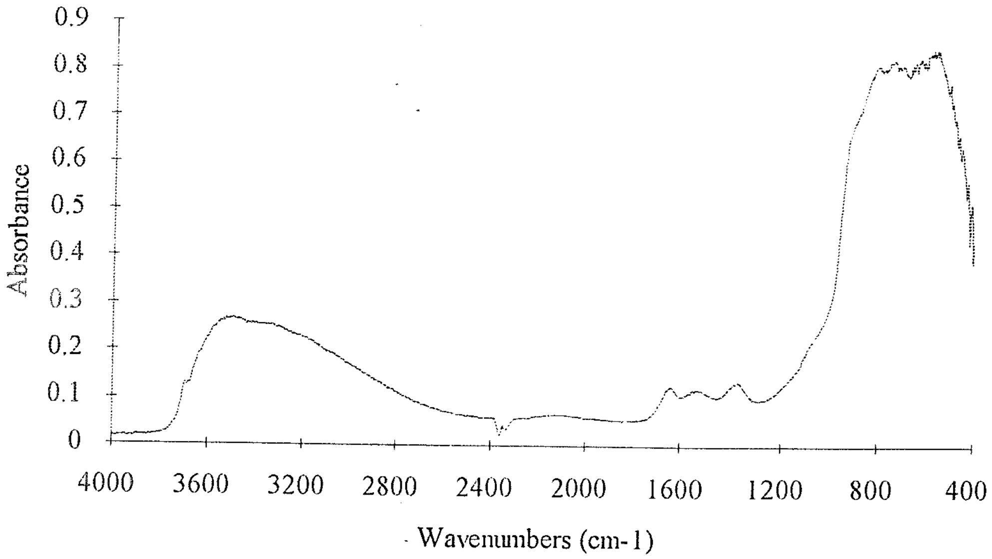

Figure 4.2 Mid-IR spectrum of unhydrated γ-alumina. NB: feature near 2400 cm^{-1} due to incomplete ratio of background.

A strong background has been noted in previous Raman studies of aluminas. This has generally been labelled fluorescence. Organic species present on the surface[9] and transition metal ions included in the bulk play a significant part. Other workers have identified a more fundamental process[10]. Although electronic transitions in perfectly-ordered alumina start to occur at around 6.8 eV (ca. 55, 000 cm^{-1}), disorder can cause the wavelength of these transitions to lengthen - to give an absorption at around 2 eV (ca. 16,200 cm^{-1}). This is the region around the most popular excitation wavelengths for visible Raman spectroscopy; when several wavelengths are used, it is plain that fluorescence intensity peaks in this region. Near-IR excitation at 1064 nm (<1.2 eV) may fall into the edge of this absorption - or may simply induce fluorescence due to transitions metal impurities. The purity of the γ-alumina used is high - although it has been shown in α-alumina that 20 ppm iron causes problems under near-IR excitation[11].

4.3.2 Initial hydration studies

Using the original synthetic method, major changes were definitely in evidence - figure 4.3 showing the changes manifest after 5 weeks hydration, followed by acidification.

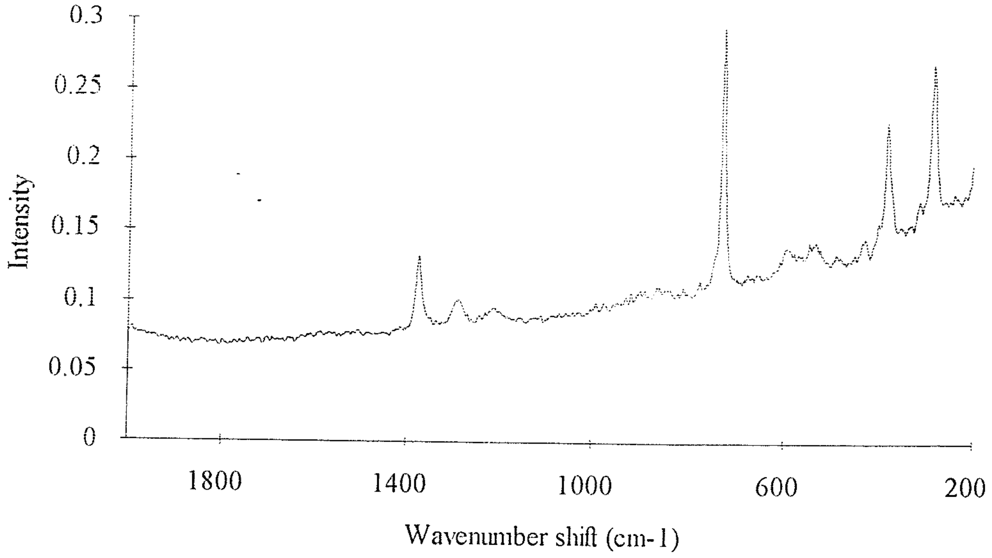

Figure 4.3 FT-Raman spectrum of the first hydrated γ-alumina sample.

On the previously-barren background, many low-shift peaks (<1400 cm^{-1}) are evident. Several of these are rather strong. This is a rather surprising result. According to the most accepted view of inorganic aluminate spectra-structure correlation[12], no bands above ca. 950 cm^{-1} shift corresponding to Al-O bonding should be evident. Either some mechanism is allowing the observation of other species (Al-O bridging bonds, or even O-H related modes) or the result is spurious.

It turned out (unfortunately) to be the latter. Figure 4.4 shows a quite different spectrum, from the very same batch of suspension - without the strong band near 725 cm^{-1} shift, or the characteristic progression near 1400 cm^{-1} shift. Instead, a band near 545 cm^{-1} appears.

The difference was only noticed when an alternative filtration method was tried. The sample was centrifuged, to separate the supernatant liquor from the suspended matter more thoroughly than by filtration. After this treatment, two distinct phases were in evidence. Figures 4.3 and 4.4 are in fact spectra from the two different phases.

It became clear that the contaminant was the Teflon (PTFE, or poly(tetrafluoroethene) coating on the stirring bar. Comparison against a spectrum of bulk Teflon confirmed this. Therefore, all subsequent hydrations were carried out without stirring.

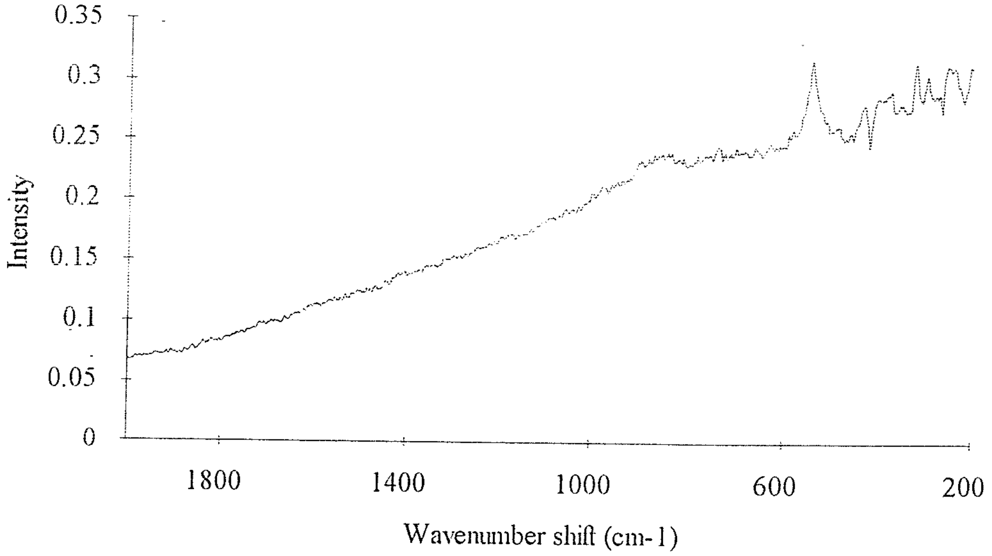

Figure 4.4 FT-Raman spectrum of second hydrated γ-alumina sample.

As mentioned above, no ill effects were noted - the equilibration times and the final solution pH were the same, with or without stirring. However, this result would not have come to light without the Raman study, and Teflon contamination would have gone unnoticed, perhaps with more serious impact. The change in experimental procedure is the first success for Raman spectroscopy in this study. In addition, centrifuging resulted in better separation of liquor and filtrate, whilst the solid phase also contained less water, reducing the required drying time.

An interesting feature arose during the filtration of PTFE-contaminated samples. Acidified batches took ca. 5-10 times longer to filter by gravity through the fine sinters used. Finely-divided alumina with a net positive surface charge due to proton attachment apparently traps the small easily-polarisable particles of PTFE, thereby increasing the effective particle size and clogging the sinter. Basic batches filtered normally. In support of this theory, the Raman spectra from the acidified samples were much stronger in PTFE bands than the basic, which showed hardly any at all - figure 4.5 shows the detail. PTFE completely obscured the 545 cm^{-1} band evident in the uncontaminated portion.

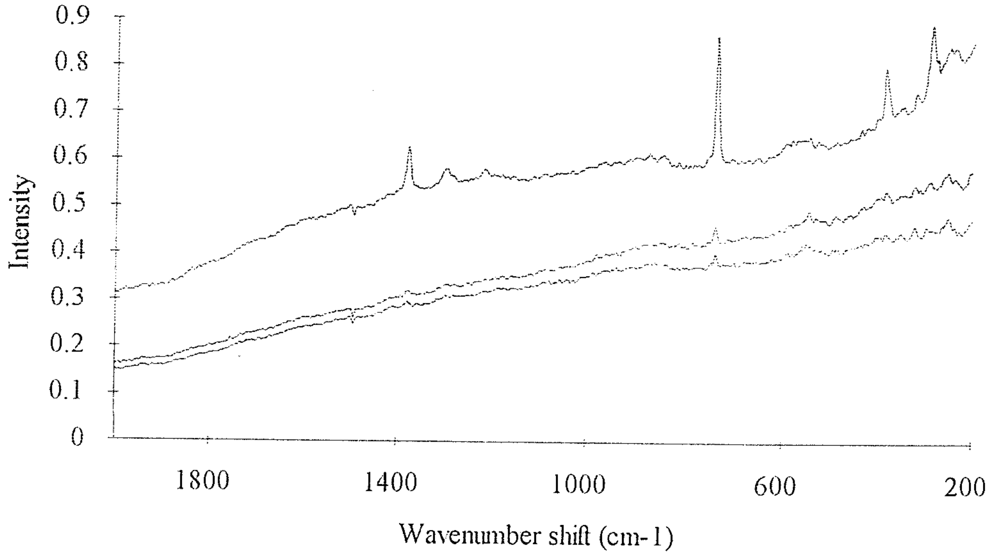

Figure 4.5 Raman spectra of Teflon-on-alumina. Top: acidic. Middle: neutral. Bottom: basic.

4.3.3 Changes on hydration

It is still quite obvious, comparing figures 4.1 and 4.4, that there are real changes as a result of hydration. When samples were taken for analysis throughout the course of a hydration at room temperature at pH neutral, no Raman or IR bands were detected for three weeks; after this time, they became very weakly visible - building up to be most intense after five weeks, by which time the glass electrode potential had stabilised. The bands indicate a new and stable chemical phase, correlated with the pH change in the aqueous suspension.

Powder X-ray diffraction of the hydrated sample revealed reference peaks due to Al powder superimposed with γ-alumina and $Al(OH)_3$ lines. These lines were from the bayerite polymorph. This is the first evidence that the stabilisation of the pH electrodes signifies the end of a reaction that forms a distinct new phase, and not just a meta-stable "buffer" state.

Figure 4.6 contrasts changes in the FT-Raman spectra, whilst figure 4.7 contrasts the mid-IR spectra in the 4000-3000 cm^{-1} region, before and after hydration.

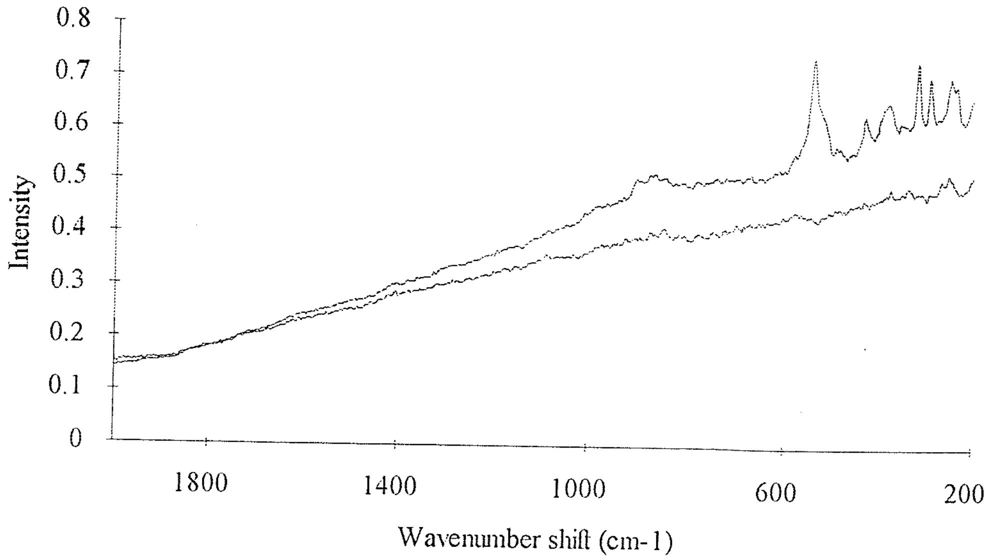

Figure 4.6 FT-Raman spectra before (lower) and after (upper) hydration.

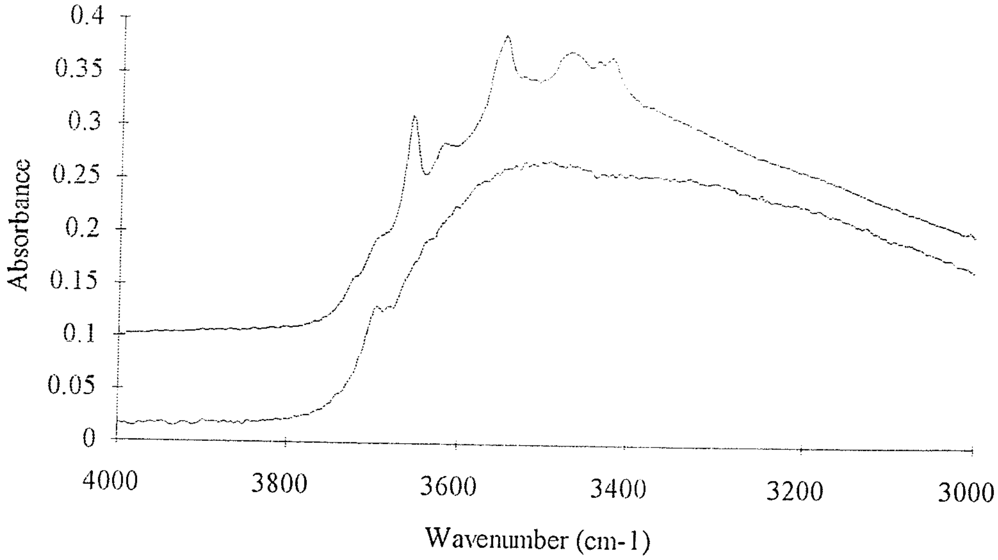

Figure 4.7 Mid-IR spectra before (lower) and after (upper) hydration. NB: 0.1 unit offset to upper trace.

The FT-Raman spectra showed a high degree of change. From the previously-discussed broad, intense and featureless background a series of medium-to-weak intensity, well-defined bands appeared below ca. 600 cm^{-1}, the strongest being at 545 cm^{-1} shift. Above this value, only one broad and weak band was discernible, near 900 cm^{-1} shift. These bands must be due to the hydroxide phase formed, and are tabulated in table 4.1.

Peak position (cm^{-1})	Relative intensity
902	Very weak and broad
870	As above
545	Strong slightly asymmetric
532 (?)	Shoulder to above
524 (?)	As above
434	Medium, sharp
323	Medium-to-strong, sharp
297	As above
280	Weak but sharp
251	Medium-intensity, broad -
241	- asymmetric doublet

Table 4.1 Raman band positions in hydrated γ-alumina (1000-200 cm^{-1} shift).

The IR data confirms this beautifully - the peak positions (given in table 4.2) unambiguously confirm that the spectra is that of bayerite, superimposed on that of γ-alumina[6].

Peak position (cm^{-1})	Relative intensity
3726	Weak shoulder
3695	As above
3657	Intense and sharp feature
3620	Broad, medium-intensity
3548	As above
3557	Weak shoulder on above
3470	Broad, medium-intensity
3439	Part of asymmetric doublet
3422	- broad, medium intensity

Table 4.2 IR band positions in hydrated γ-alumina (4000-3000 cm^{-1}).

Figure 4.8 shows the FT-Raman spectra of the same hydrated alumina sample run on the Southampton FT-Raman instrument. The O-H stretching vibrations above 3500 cm^{-1} were accessible on this instrument, since the detector did not require cooling to achieve an acceptable S:N ratio. The spectrum was recorded at lower excitation power with fewer scans co-added, compared to figure 4.4.

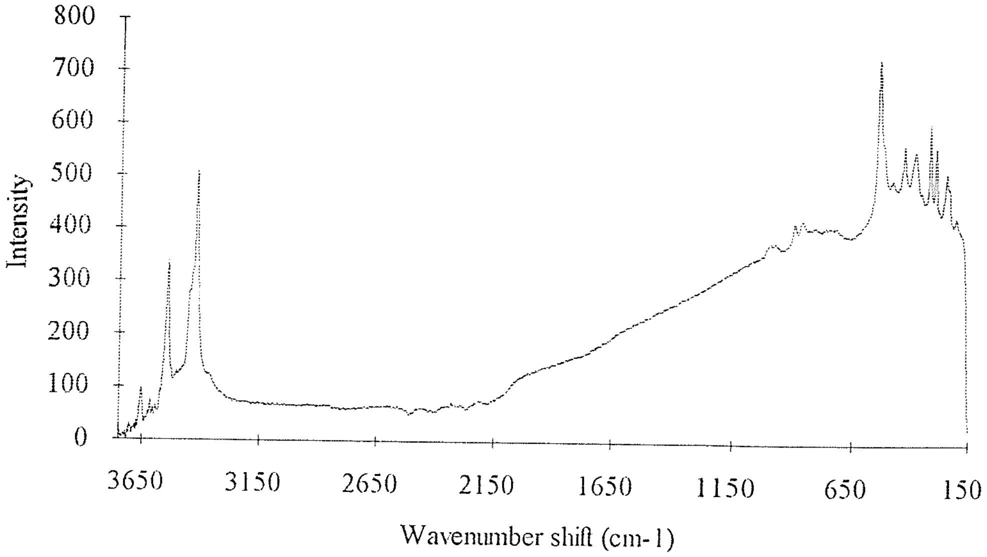

Figure 4.8 FT-Raman spectrum obtained with room-temperature high-impedance InGaAs photodiode.

The two bands very weak bands near 900 cm^{-1} in figure 4.4 are clearly resolved, at 869 and 903 cm^{-1} respectively, whilst another double peak is resolvable at 985 and 1006 cm^{-1}, probably Al-OH bending motions[13]. These would be expected to be weak in the Raman effect. The curious band shape of the background around 2000-2500 cm^{-1} shift is caused by -OH group overtone absorption.

The -OH stretching region vibrations occur at 3424 (with definite shoulders near 3439 and 3450), 3545, and 3657 cm^{-1}. This ability to record the Al-O region as well as the O-H region is extremely useful. The bands in this region are a prime example of the usefulness of correction for instrument response. Figure 4.9 shows the O-H stretching region for both corrected and uncorrected cases - normalised to the biggest peak. The "peak" around 3620 cm^{-1} would be dangerous to assign without correction, as the signal and noise levels are too similar.

The peak positions for these O-H vibrations are in good agreement with those derived by previous workers. Previous studies[14-16] used visible excitation, some employing microprobe techniques, on geological samples. The data from the micro-conventional spectroscopy seemed to required extensive smoothing, baseline correction, and zero-offset to even hope to record the low-shift region. Indeed, in the two earlier studies, no low-shift region could be recorded due to the extremely high fluorescence yield associated with visible excitation. Only the last study - a recent publication using top-flight expensive research equipment - succeeded; this is in marked contrast to the current FT-Raman study.

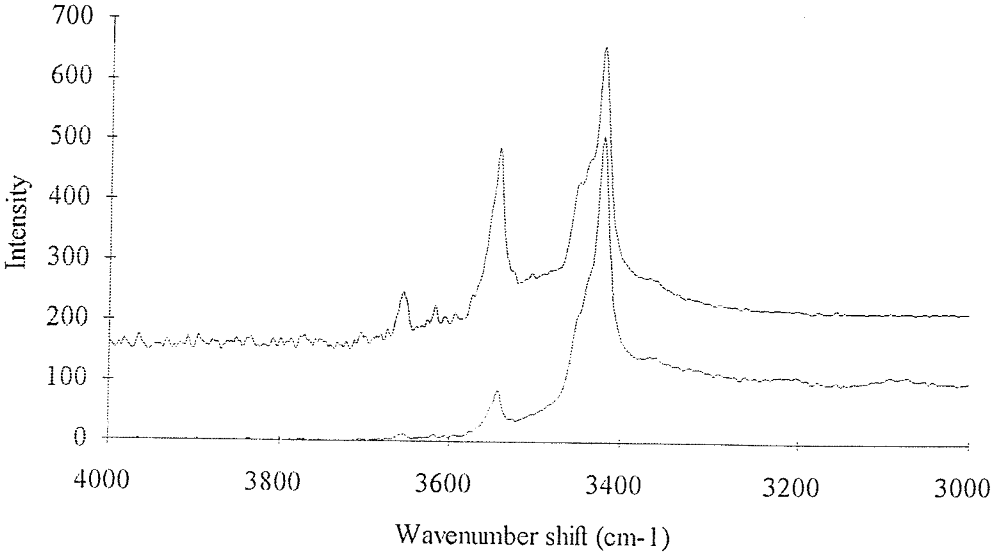

Figure 4.9 Corrected (upper) and uncorrected O-H stretching region of the Raman spectrum.

4.3.4 Elevated temperature hydration

Raman and IR spectra of samples hydrated and then adjusted in pH (in the manner described in the experimental section) showed few differences. Given that the hydration time is very long compared to the pH adjustment time (ca. 120:1) - to comply with the methods at Umeå used in the potentiometric titration - it is unsurprising.

Much more inspiring was the greatly enhanced rate of reaction found at 60°C. After 10 days at 60°C, the integrated band area under the Raman peaks had increased about 2-2.5 times compared to the sample at 20°C for 120 days - see figure 4.10.

The area under the background did not changed appreciably. In effect, changing the temperature by 40°C brought about a 100% increase in product in 10% of the time.

No additional bands are evident - implying the reaction products are the same at the higher temperature. This is in accord with the IR and XRD data, which show no additional lines or bands, and with phase diagram of the alumina-water system[7].

With this extra knowledge, the study of different hydration conditions is greatly facilitated. As an example of this, the effect of actually hydrating γ-alumina at different pHs - rather than adjusting afterwards - is shown in the FT-Raman spectra of figure 4.11.

The samples were hydrated at the desired pH for 21 days at 60°C, and the Raman spectra excited with 500 mW. It is clear that the amount of bayerite is highest in alkaline (pH 8.4) conditions and lowest in acidic (pH 6.0). No band-shifts were in evidence.

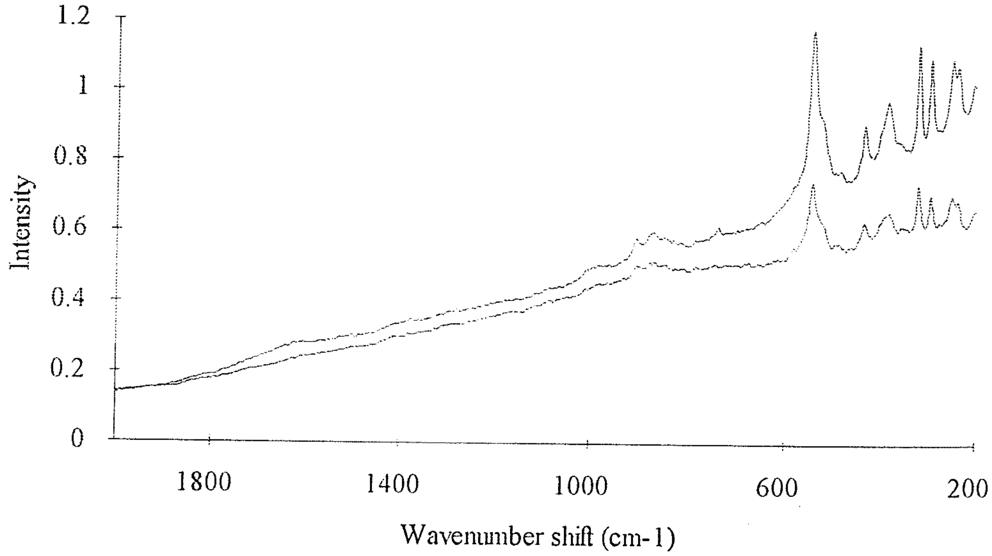

Figure 4.10 FT-Raman spectra of γ-alumina hydrated at 60°C for 10 days (upper trace) and at 20°C for 120 days (lower trace).

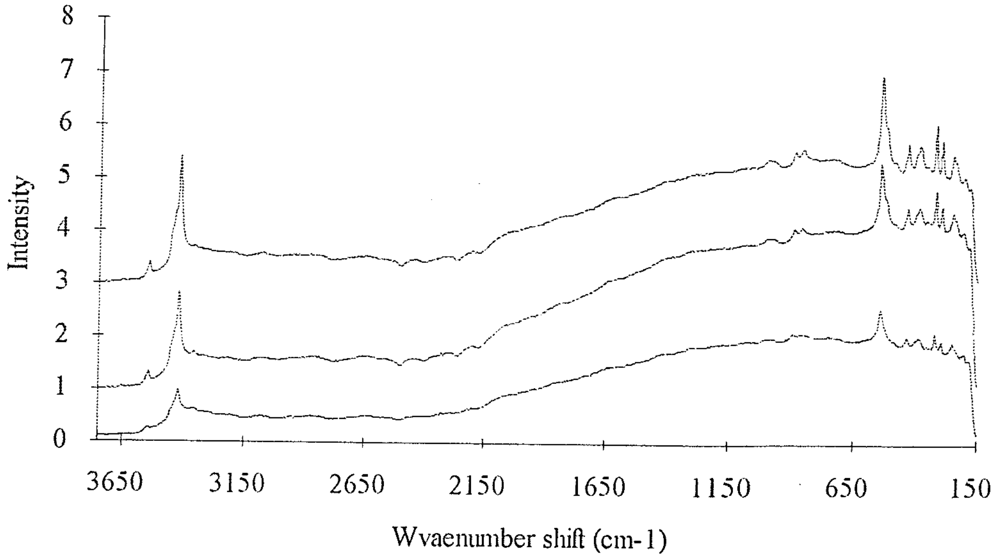

Figure 4.11 Formation of bayerite at various pH - upper trace: 8.4, middle trace: 7.6, lower trace: 6.0

4.3.5 Boehmite

Above 100°C the product likely from the γ-alumina/water system is boehmite, the α-AlO(OH) form of aluminium oxyhydroxide. The FT-Raman spectrum of boehmite is significantly different to that from γ-alumina, and therefore may be recognised easily.

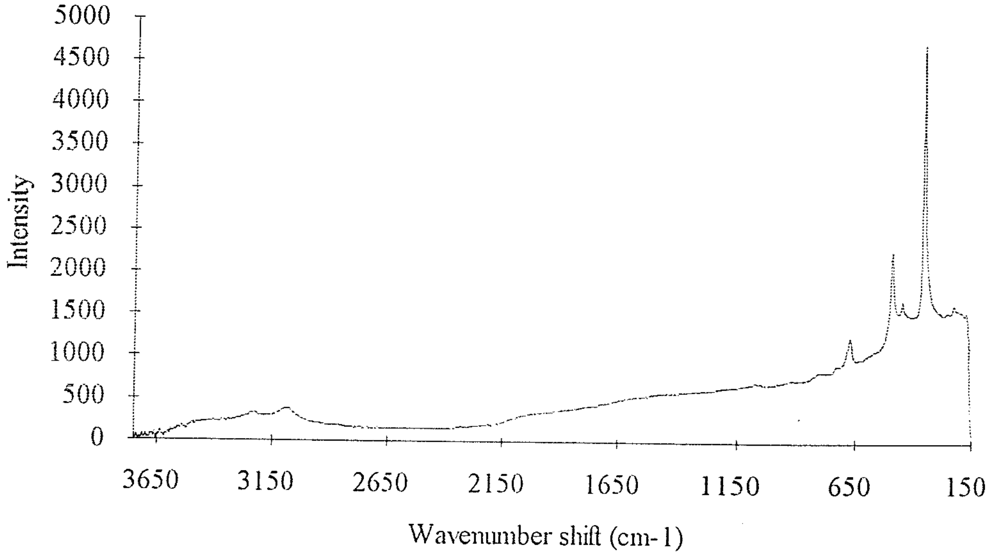

Figure 4.12 FT-Raman spectrum of boehmite, AlO(OH).

The background is much lower than γ-alumina. The major peak is a strong Al-O vibration at 363 cm^{-1}, much more intense than anything in a comparable γ-alumina spectrum, with three other bands to higher shift - weakest at 453 cm^{-1}, next at 678 cm^{-1}, with the second most-intense at 498 cm^{-1}. In the O-H region, there are two weak broad bands - compare to the three sharp bands of γ-alumina - at 3088 and 3278 cm^{-1}.

When hydrated under the same conditions as the γ-alumina samples, a similar lack of reactivity is noted as for α-alumina when hydrated. The boehmite spectrum only changed in one respect - a typical -OH absorption "inverse" band appeared around 2250 cm^{-1} shift, due to water incorporated in the sample.

4.3.6 Dehydroxylation

The degree to which the hydrated γ-alumina surface dehydroxylates, and the products formed on doing so, are also of interest to industry. Bayerite transforms most readily into either η-alumina or boehmite[6,17]. The heating of a small portion of hydrated γ-alumina to 200°C for 24 hours certainly removed all traces of bayerite - see figures 4.13 and 4.14 for the Raman and IR spectra.

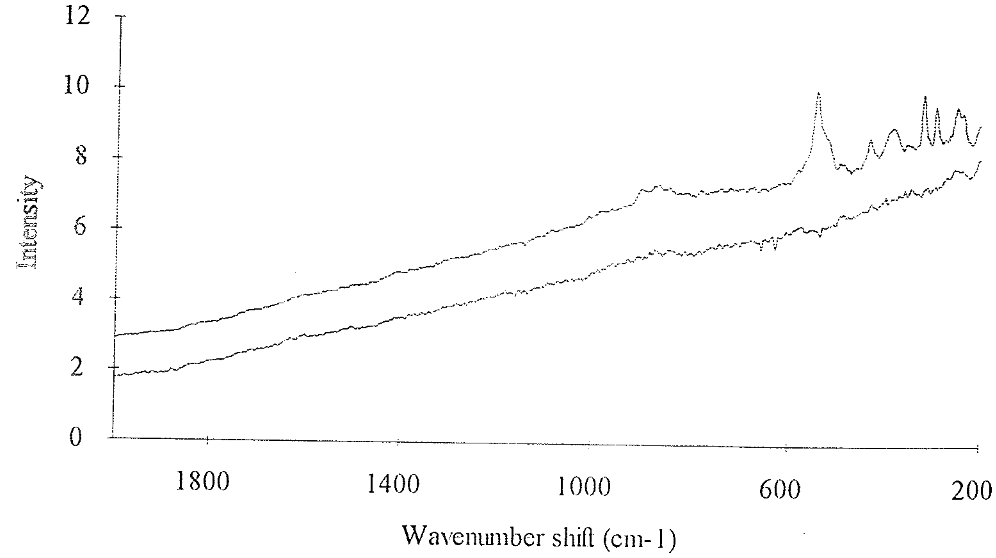

Figure 4.13 FT-Raman spectra of heat-treated (lower trace) and non-heat-treated (upper trace) materials.

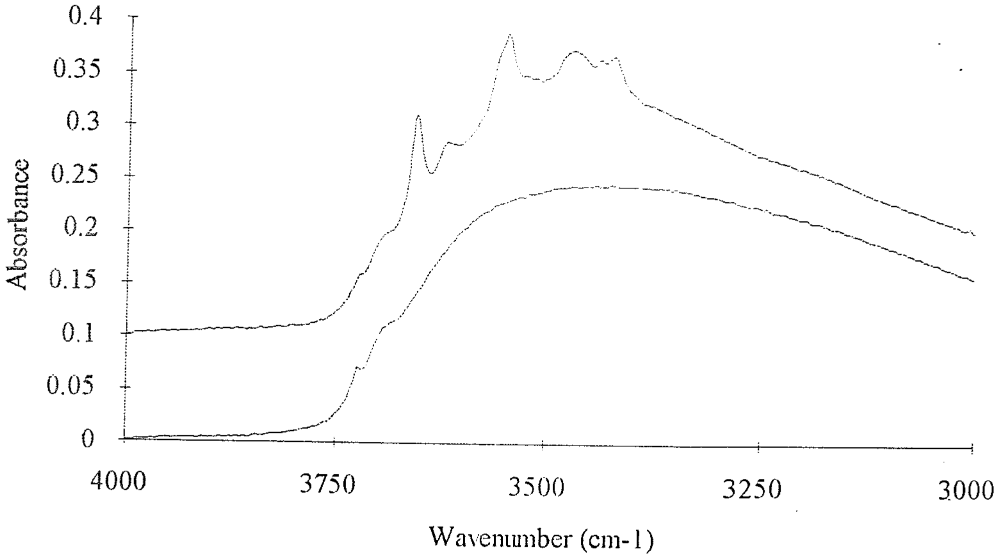

Figure 4.14 Mid-IR spectra of heat-treated (lower trace) and non-heat-treated (upper trace) materials.

Unfortunately, XRD could not discern any other form of alumina than γ-alumina. This is not all together surprising, as both transition aluminas have tetragonally-deformed spinel structures - the difference being in the nature of the deformation. One-dimensional disorder in the close-packed oxygen lattice is assumed to be caused by the stabilising hydroxyl groups in the η-alumina; whereas the distortion in γ-alumina is known to be due to strong cation disorder in the tetrahedral sites. The lattice constants of the structures are very similar (c-axis 7.80 A in γ-alumina, c-axis in η-alumina 7.90 A). The amount of the transformed material may be small, and the material poorly crystalline - XRD is known to be insensitive to the X-ray indifferent η-form. On this basis, it is difficult to say whether the spectra show anything more than simple dehydration of bayerite back to γ-alumina.

It is important to appreciate the effect of ultra-high vacuum (UHV) treatment on the hydrated materials; one of the newest methods for analysis of aluminium oxides and hydroxides is X-ray photoelectron spectroscopy[18] (XPS), a technique that involves partial pressures of 10^{-9} Torr.

Figures 4.15 and 4.16 show that the bayerite layer is reasonably stable under these conditions, even after a day under vacuum, except that a decrease in signal intensity is noticeable after removal from the XPS spectrometer.

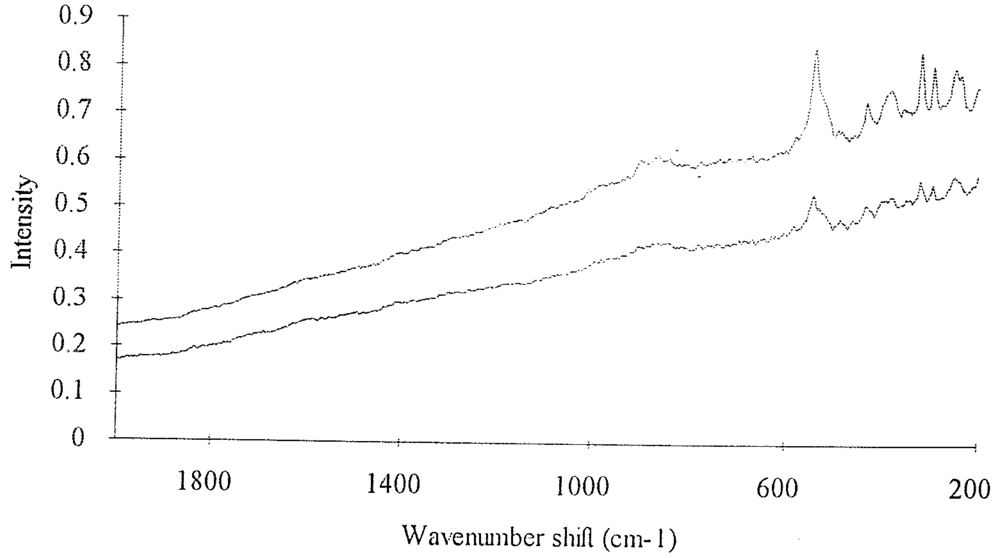

Figure 4.15 FT-Raman spectra of vacuum-treated (lower trace) and non-vacuum-treated (upper trace) materials.

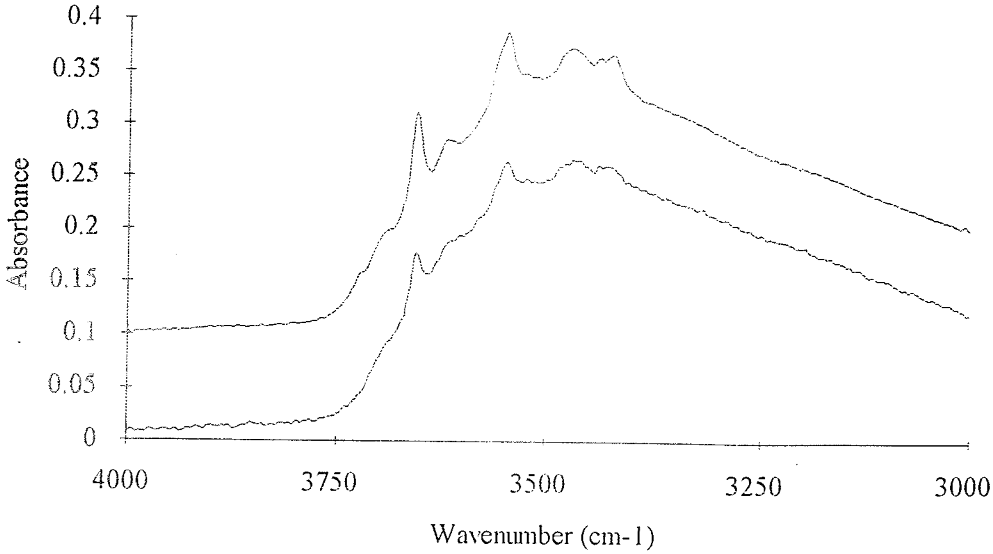

Figure 4.16 Mid-IR spectra of vacuum-treated (lower trace) and non-vacuum-treated (upper trace) materials.

4.3.7 Phenylphosphate adsorption.

Although many more experiments concerned with hydrating γ-alumina could have been carried out, it was decided that the effect of phenylphosphate di-anion adsorption upon the formation of bayerite should be monitored by Raman spectroscopy. Since phosphate adsorption is known to block the hydration, and since FT-Raman has been shown so far to be sensitive to the changes on hydration, this seemed likely to be successful.

Figure 4.17 shows an overlay of two spectra. The top trace was recorded from a simple dry mixture of sodium phenylphosphate and hydrated γ-alumina; the bottom trace was recorded from a sample of hydrated γ-alumina that had 1 ml of 70 mM phenylphosphate anion added to the 50 ml aliquot prior to pH-adjustment. The amount of sodium phenylphosphate added to the dry mix corresponded to the number of moles of anion added to the wet sample.

On the evidence of the bottom trace, phenylphosphate adsorption has apparently not stopped the hydration, which is in direct contradiction of many previous studies. However, by the time the phenylphosphate was added, the five-week-long equilibration had finished and the pH adjustment was being carried out. As stated before, this was to conform with the Umeå titration methods - their interests lie in the buffering capacity of hydrated as compared to unhydrated γ-alumina. Hence their interest in changing pH after hydration, rather than hydration at a given pH.

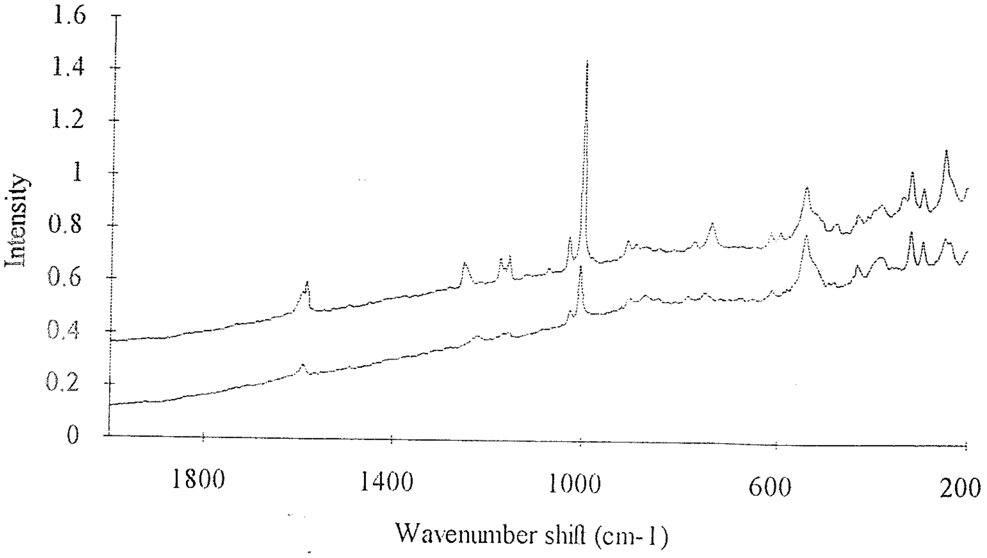

Figure 4.17 FT-Raman spectra of γ-alumina mixed with phenylphosphate (upper trace) and adsorbed with phenylphosphate (lower trace).

This result tallies well with the results presented earlier, where no apparent change was seen in the extent of bayerite transformation when the pH was altered after hydration.

Nevertheless, a surface reaction involving phenylphosphate had definitely occurred. On close comparison many phenylphosphate bands had shifted both in position and shape upon adsorption, the most important being a 30 cm^{-1} shift in band position of the characteristic P-O-(C_6H_5) group fingerprint[19] to be at 1222 cm^{-1} - to see a shift in this band must reflect a change brought about by bonding to the hydrated γ-alumina surface.

Other bands shift, too - the strongest band in the spectra, the phenyl "ring - breathing" mode at 1001 cm^{-1}, moves 4 cm^{-1} to higher shift upon adsorption. The companion "star-of-David" mode at 1029 cm^{-1}, although weak, perceptibly shifts down 3 cm^{-1} to 1026 cm^{-1}. These modes are known[20] to be substituent-sensitive, from the mono-substituted benzene spectra. However, the usually-insensitive doublet near 1597 cm^{-1}, due to ring stretching modes, is actually perturbed in these spectra - the well-resolved asymmetric bands at 1586 and 1596 cm $^{-1}$ blur and shift higher when adsorbed, to yield a broader band at 1594 cm^{-1} shift, with a weak sideband at 1604 cm^{-1}.

Perhaps the best evidence for a surface reaction having occurred is that given in figure 4.18, however. Here, the comparison of the Raman spectra of phosphate-treated γ-alumina and the very same sample after heat treatment at 200°C for 24 hours clearly shows that although all the bayerite has been destroyed, the phenylphosphate is still bonded to the surface - the strongest peak in the untreated spectrum being just visible in the treated, at 1006 cm^{-1} shift.

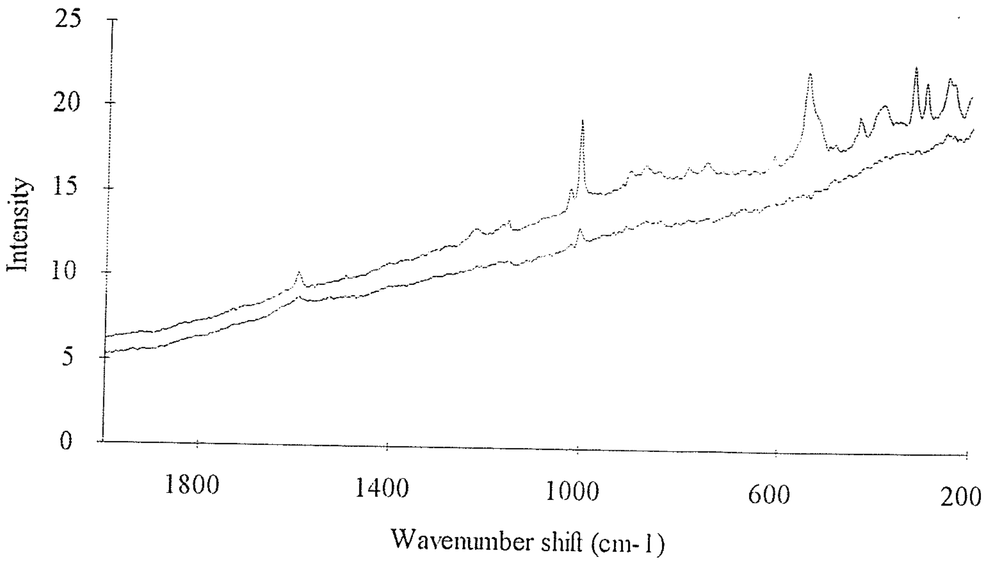

Figure 4.18 FT-Raman spectra of heat-treated (lower trace) and non-heat-treated (upper trace) γ-alumina adsorbed with phenylphosphate.

In order to study the effect of changes in pH and hydration temperature on the phosphate adsorption, it was necessary to change the synthetic procedure. A dispersion of 20 g/l of γ-alumina in water was made. Three 100 ml aliquots of this suspension were taken, 5 ml of sodium phenylphosphate was added (70 mM in the anion) to each, then the pH adjusted with 0.1 M NaOH or HCl to either 6.0, 7.6, or 8.4. After this, the samples were stood for 24 hours, before centrifuging, followed by dispersion once again in 100 ml of water. From each of these three samples, a further two samples - each of 30 ml - were drawn, to be hydrated for ca. 10 days at either 20 or 60°C. The remaining 40 ml in each case were centrifuged and dried immediately. After hydrating, all the other samples were centrifuged and dried at 50°C for 24 hours.

Thus a suite of nine samples is available, to show the effects of phenylphosphate adsorption as a function of pH and of hydration temperature. The spectra were collected at 4 cm^{-1} resolution, with 300 mW excitation power, with 300 scans co-added. The results are enlightening.

Taking the results of the unhydrated samples first - figure 4.19 shows that the acidified sample has the highest coverage of phosphate. As the conditions become more basic, the adsorption of phosphate seems to become suppressed.

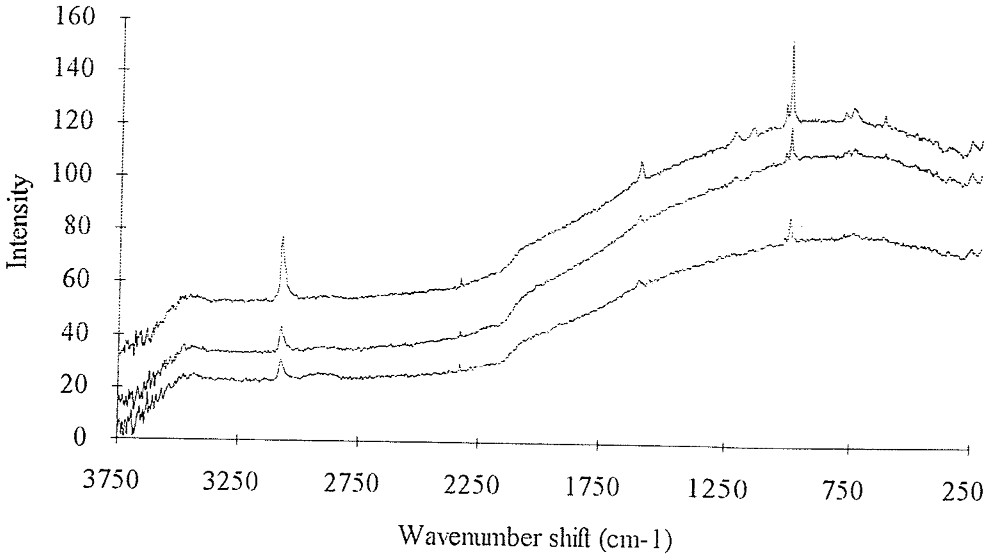

Figure 4.19 Effect of pH on phenylphosphate adsorption for unreacted γ-alumina. Upper: pH 6.0. Middle: pH 7.6. Lower: pH 8.4. Note the appearance of the gas-phase N_2 vibration at 2231 cm^{-1} shift.

These samples were not hydrated long enough to produce bayerite. However, the positions of the bands are those taken up on adsorption, with the strong band at 1005 cm^{-1} shift, rather than those of a simple physical mixture. Since the Southampton spectrometer can access the O-H and C-H stretching regions, the increase in coverage of phenylphosphate can be monitored by the higher intensity of the symmetric C-H stretching band at 3076 cm^{-1} shift in the acidified sample. Note that Teflon adhered to the surface most strongly in acidic conditions.

Upon hydrating at 20°C, there was little change. Whereas the overall signal level - scatter plus background - proved reasonably similar in the three unhydrated samples, the most pH basic hydration produced a much bigger scattering background than the other two samples. In common with the unhydrated samples, it also showed a much poorer coverage of phenylphosphate, as evidenced by reduced band intensities. Bayerite was not in evidence - no bands around 545 cm^{-1} shift, or around 3600 cm^{-1} - although this is not surprising, as earlier results showed three weeks hydration at room temperature did not appreciably convert any pH basic γ-alumina to bayerite.

The hydration at 60°C does show large changes, however. Previously, hydration at 60°C showed the production of bayerite at pHs 6.0, 7.6, and 8.4 - the amount increasing in that order. The conditions used here were identical, except for the addition of phenylphosphate anion during the pH adjustment, before hydration started. The effect is startling, and shown in figure 4.20.

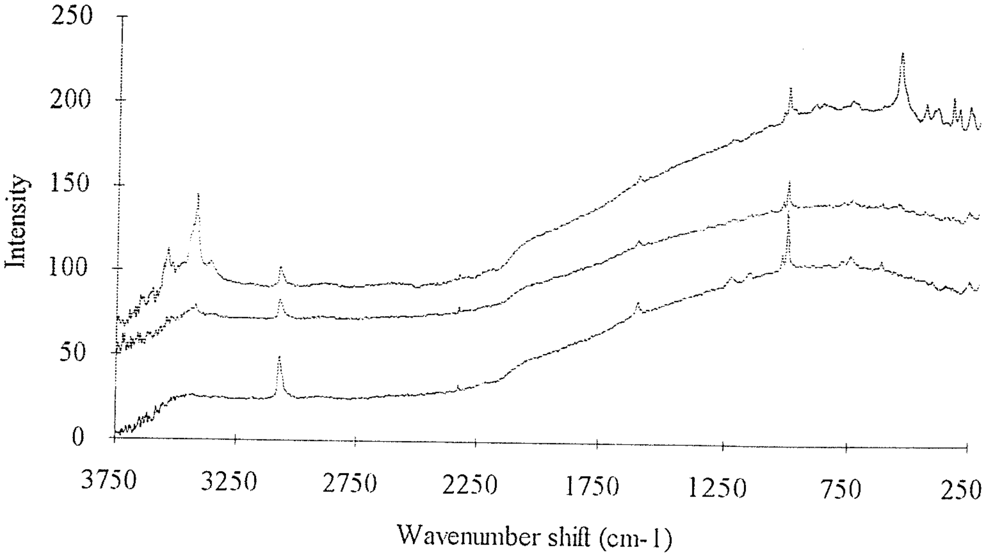

Figure 4.20 FT-Raman spectra of γ-alumina hydrated at 60°C in the presence of phenylphosphate. Upper: pH 8.4. Middle: pH 7.6. Lower: pH 6.0. Again, the weak 2331 cm^{-1} band from gaseous N_2 is visible.

The acidic sample still showed no sign of bayerite - in the O-H or the Al-O regions - and also showed the highest coverage of phosphate. Comparatively, the less basic sample shows a decrease in phosphate coverage, whilst also showing - very faintly - evidence of bayerite formation in the O-H region - by a band at 3423 cm^{-1} shift; this was the highest-intensity band of any of the bayerite peaks in this sample, and yet was barely visible.

However, the more-basic sample plainly shows a strong band at this position, a weaker band at 3541 cm^{-1} shift, a strong band at 545 cm^{-1} and all the others associated with bayerite. Although some of the phenylphosphate peaks are still quite easily seen, most are reduced significantly in intensity. It is clear that coating the surface with phosphate does not prevent formation of bayerite at basic pH. Also clear is that FT-Raman spectroscopy is an excellent method to determine the efficacy of phenylphosphate coatings.

4.4 References

1. H. Knözinger and P. Ratnasamy, Catal. Rev. Sci. Eng. 17(1), 31 (1978)
2. K.S. Chari and B. Mathur, Thin Solid Films 891, 271 (1981)

3. A.M. Ahern, P.R. Schwartz, and L.A. Schaffer, Appl. Spectrosc. 46(9), 1412 (1992)
4. L. Wu, W. Forsling, and P.W. Schindler, J. Colloid Interfac. Sci. 147, 148 (1991)
5. G.A. Parks, in "Mineral-water interface geochemistry", 23, (Ed. M.F.Hochella Jnr. and A.F.White) 133-176 (Bookcrafters, 1990).
6. R.S. Alwitt, in "Oxides and oxide films" (Ed. J.W.Diggle and A.K.Vijh) Ch.4 (Marcel-Dekker Inc., 1976)
7. K. Wefers and G.M. Bell, Alcoa technical paper 19, Alcoa research laboratories (1972)
8. J.B. Peri, J. Phys. Chem. 69(1), 220 (1965)
9. P.J. Hendra, J.D.M. Turner, E.J. Loader, and M. Stacey, J. Chem. Phys. 78, 300 (1974)
10. H. Jeziorowski and H. Knözinger, Chem. Phys. Lett. 42(1), 162 (1976)
11. A. Mortensen, D.H. Christensen, O.F. Nielsen, and E. Pedersen, J. Raman Spectrosc. 22, 47 (1991)
12. P. Tarte, Spectrochim. Acta 23, 2127 (1967)
13. G.A. Dorsey Jnr., J. Electrochem. Soc. 169 (1966)
14. J.T. Huneke, R.E. Cramer, R. Alvarez, and S.A. El-Swaify, J. Soil Sci. Soc. Am. 44, 131 (1980)
15. K.A. Rodgers, M.R. Gregory, and R.P. Cooney, Clay Minerals 24, 531 (1989)
16. K.A. Rodgers, Clay Minerals 28, 85 (1993)
17. T.H. Walter and E. Oldfield, J. Phys. Chem. 93, 6744 (1989)
18. S. Thomas and P.J. Sherwood, Anal. Chem. 64, 2488 (1992)
19. D.H. Williams and I. Fleming, "Spectroscopic Methods in Organic Chemistry" 4th edition (McGraw-Hill, 1987)
20. F.R. Dollish, W.G. Fateley, and F.F. Bentley, "Characteristic Raman Frequencies of organic compounds" (Wiley Interscience, 1974)

Chapter 5:

Raman spectroscopy of cement minerals and related species

5.1 Introduction

During the three month placement with Professor Willis Forsling at the University of Luleå, a project was undertaken to evaluate FT-Raman spectroscopy for studies of the structure and bonding of calcium silicates relevant to the cement industry[1,2]. Despite a century of careful research, the chemistry of cements is still not fully understood[3,4].

FT-Raman spectroscopy offers potential advantages* in many areas over the techniques traditionally used for cement characterisation and identification - which include X-ray diffraction and fluorescence (XRD/F), thermal analysis (DTA, TGA, DSC), polarised visible-light microscopies, and mid-IR absorption. FT Raman spectroscopy is known to be hazard-free, inexpensive, and non-destructive; and it offers unambiguous, easy-to-interpret results very rapidly on most systems. It is especially worth exploring in the light of the difficulties in fast, precise identification using existing methods.

5.2 Previous work

The prospects for Raman investigations were originally discussed by Bensted[6]. The twin problems of fluorescence and sample heating figured strongly in his appraisal. In a later publication[7], Bensted demonstrated that Raman spectra could be collected by classical scanning methods - using a double-grating additive-dispersion monochromator, PMT detection, macro sampling optics and visible excitation at either Ar^+ green or HeNe wavelengths.

The quality of spectra obtained even from pure white synthetic samples was not inspiring. Most displayed adequate S:N performance, whilst all showed an extremely large background, increasing rapidly past ca. 1000 cm^{-1}. This was quite

---

* In addition, a review of mineralogical applications of vibrational spectroscopy[5] had suggested that Raman spectroscopy using near-IR excitation might be useful in a number of mineralogical applications.

fortuitous, as nearly all the strong Raman-active bands of aluminate, silicate, sulphate, and carbonate species present occur below ca. 1200 cm^{-1} shift[8].

Use of a Raman microprobe[9] by Conjeaud and Boyer yielded excellent data, for much the same sort of sample. Their analysis of both synthetic cement minerals and their analogues found in the industrial blast furnace showed that the simple silicates were more amenable to study than aluminates or aluminoferrates, whilst the laboratory-prepared synthetic samples were again easier to study than industrially-prepared materials. This was attributed to the presence of ferrous iron (Fe^{3+}) in the industrial samples as an impurity causing fluorescence.

5.3 Comments on nomenclature, synthesis and sample identification

The chemical names of the synthetic cement minerals studied are given below in table 5.1, along with the designations used in the cement industry. The first set of samples used were supplied by Dr. Eric Hendersson of Euroc Research, via Dr. Vladimir Ronin. The second set were supplied directly by Mr. Roger Gollop of Blue Circle.

A distinction needs to be made between cement minerals and industrially-prepared cements, which are mixtures that include cement minerals. Certain cement mineral forms exist naturally, whilst others may be synthesised. Synthetic cement minerals are prepared by high-temperature reactions from specially-selected ore stocks or pure reagent-grade chemicals. On the scale of the industrial research laboratory, the minimum quantity of cement synthesised tends to be in the region of 10 kilograms.

Overall, the reaction is simple - heat calcium carbonate (or limestone) and silica (or sand) to around 1300-1600°C, calcining the carbonate to oxide, and reacting the oxide and silica in the solid state. In comparison, industrial cement manufacture tends to be a vast exercise. The products from industrial cement syntheses tend to be mixed, since the reaction conditions and exact chemical composition of the reactants in the kiln are difficult to control, given the nature of the feed stock and the amounts of reactant involved.

Species	**Formula**	**Designated**
Calcium silicate	$(CaSiO_3)$	CS
Dicalcium silicate	(Ca_2SiO_4)	C_2S
Tricalcium silicate	(Ca_3SiO_5)	C_3S
Tricalcium aluminate	$(Ca_3Al_2O_6)$	C_3A
Tetracalcium aluminoferrate	$(Ca_4Al_2Fe_2O_{10})$	C_4AF

Table 5.1 The list of abbreviations used to denote cement minerals.

It is important to understand the meaning of the abbreviations fully. Note that CS denotes $CaSiO_3$ - the material is not a mixture of CaO + SiO_2.

Confusion has arisen regarding labelling and naming many of the species involved, especially since the crystal habit of many of the minerals depends on the temperature and pressure of synthesis, which leads to several forms per mineral. Determining the exact stoichiometry and firing temperature required to produce a desired phase is non-trivial. The high-temperature phase behaviour of these systems is not straightforward to interpret, or to control[1-4].

5.4 Experimental

5.4.1 Analytical methods

Given the points discussed above, it was deemed very important to ascertain the polymorphic form of all samples by powder X-ray diffraction (XRD) whenever possible. In Luleå, these measurements were made using a Philips PW 1710/00 diffractometer, whilst in Southampton a Siemens D5000 diffractometer was employed. Both systems used Cu $K_{\alpha 1}$ and $K_{\alpha 2}$ lines, with Micro VAX data stations for processing. The spectra were indexed in accordance with the JCPDS powder file.

In some cases, elemental analyses were carried out using inductively-coupled plasma atomic emission spectrometry (ICP-AES), by either whole-rock ($LiBO_3$/HF dissolution) or standard ore (HF/HNO_3) analytical methods, by Svensk Grundämnesanalys AB (Sweden).

Conventional Raman spectra were recorded on scanning monochromators in the Department of Chemistry at the University of Stockholm, as well as in the

Department of Chemistry at the University of Southampton. Both instruments (Dilor in Stockholm, Coderg in Southampton) used Ar^+ laser excitation at 514.5 nm. Both were triple additive dispersion devices equipped with PMT detection used in the photon-counting mode.

In addition, Raman microspectroscopy using a single-grating based spectrograph employing CCD detection was carried out with Ar^+ green (514.5 nm), HeNe red (632.8 nm) and near-IR AlGaAs laser diode (792 nm) excitation sources on a Renishaw Raman microscope operated in the microprobe mode.

Near-IR reflectance absorption spectroscopy was carried out using a Perkin Elmer Lambda 19 spectrophotometer in Southampton and a NIR System 6500 spectrophotometer at the University of Umeå, Sweden. Both are fully near-IR-optimised scanning dual-beam grating instruments, equipped with diffuse reflectance integrating sphere accessories and PbS photodetectors.

Mid-IR transmission absorption spectra were recorded in Luleå and Southampton using Perkin Elmer 1700 series FT-IR spectrometers.

Near-IR FT-Raman spectra were recorded using Perkin Elmer 1700 series commercial FT-IR/Raman combined benches, both in Sweden and in Southampton. The Southampton instrument had a higher specification; it was equipped with sharper cut-off laser rejection filters, higher-throughput quartz substrate beamsplitter, gold-coated reflective optics and a hand-picked very sensitive InGaAs detector. In comparison, the Luleå instrument required cooling of the detector to yield acceptable S:N performance.

Near-IR diffuse reflectance measurements were also carried out on both the above-mentioned Perkin Elmer 1700 series interferometers. The first (based in Southampton) was used to study the Blue Circle cement samples, whilst the second (based in Sweden) was used for measurements on $Ca(OH)_2$. Spectra were recorded against spectrophotometric grade KBr. These spectrometers were not equipped with optimised near-IR detectors or sources for reflectance absorption spectroscopy, which lead to low sensitivity - therefore, the detection of trace impurities and/or defect sites was not attempted on these spectrometers.

5.4.2 Synthetic details

The feed stocks used were analytical grade reagents with very low metal ion and extraneous matter contents - iron less than 0.05% and alkali metals around 0.1% by mass, for typical analytical grade material. The apparatus available to carry out the syntheses was unfortunately not ideal. Furnaces capable of heating to ca. 1600°C and cooling back to ambient at a controlled and defined rate under closed atmospheres are neither common, nor easy to gain access to. Instead, only small low-temperature (<1500°C) open-atmosphere furnaces were available, of dubious heritage.

In Sweden, the syntheses of C_2S and C_3S were attempted using >99% pure $CaCO_3$ and SiO_2, in the stoichiometries 2:1 and 3:1. After dehydrating the silica at 950°C, the samples were ground in an agate pestle and mortar to pass a very fine (75 µm) nickel sieve, loaded into a carefully-cleaned (conc. HNO_3 / 70°C) platinum crucible, then covered. The furnace was reasonably clean, being used in the past to fire ceramic samples. After firing for an hour at 1350°C, the crucible was removed with nickel tongs, emptied into the pestle and mortar, and the reactants reground with 2-3 drops of water to improve the intimacy of the mixing for five minutes before re-firing.

After five such firings, the samples were allowed to cool to room temperature in a sealed desiccator. Cements and calcium silicates are highly hygroscopic, especially when freshly-prepared. Although the product could be ground to form a powder, after each successive firing it was found that the reactants were becoming increasingly more aggregated, and had to be persuaded from the crucible with a nickel spatula. Other than contact with the platinum crucible, the only other metal in contact with the reactants could have been in the slight residue of unknown origin present in the crucible before firing. Further syntheses were precluded, due to the limited time available.

In Southampton, several unavoidable changes were made. The oven could achieve 1500°C, although it was much less clean - it had previously been used for annealing steel engine parts. The platinum crucible was replaced with a proprietary brand of ceramic crucible ("Alcint" from Fisons Ltd.) based on an alumina ceramic. It was covered during use with another crucible. The stoichiometry 2:1 $CaCO_3$:SiO_2 was used, with no attempt to dehydrate the silica, or to account for the incomplete calcination of carbonate. In all other respects, the methods were the same. After the second firing, it was noticed that the sample had turned light green in colour. This was not noted during the Swedish syntheses. It probably reflects contamination - particles suspended on the roof of the furnace may have fallen into the crucible when the furnace was reloaded, since it proved impossible to load the furnace with the second crucible "lid" on top.

Furthermore, although the Alcint crucibles used can withstand 1600°C, they become permeable at 1500°C, which may result in impurities leeching through the base. After the fifth firing, the material was still light green, and was firmly stuck to the crucible - removal from the crucible was not possible other than by smashing the crucible apart. Hot calcium silicates are extremely corrosive - one of the reasons that several furnace-owners refused to allow the synthesis. The sample was a solid amorphous mass, from which Raman spectra - but not IR - could be collected quite simply.

5.5 Results

5.5.1 Euroc samples

Irrespective of choice of excitation wavelength, silicates generally have very poor Raman scattering cross-sections[6] - this results in very weak scattering, even when high excitation powers are used. Both the classical and quantum mechanical derivations of the expression for the intensity of vibrational Raman scattering[10] show a direct dependence on molecular polarisability[11] through the derived polarisability tensor, $\delta\alpha_{ij}/\delta Q$. Interpreted simply, silicon-oxygen (Si-O) bonds of low π-character and appreciable ionicity should be weakly Raman active[12]. Griffiths[13-15] commented on this point in his pioneering work on the Raman spectroscopy of minerals.* FT-Raman spectra of Euroc-supplied C_2S and C_3S are presented in figures 5.1 and 5.2 below.

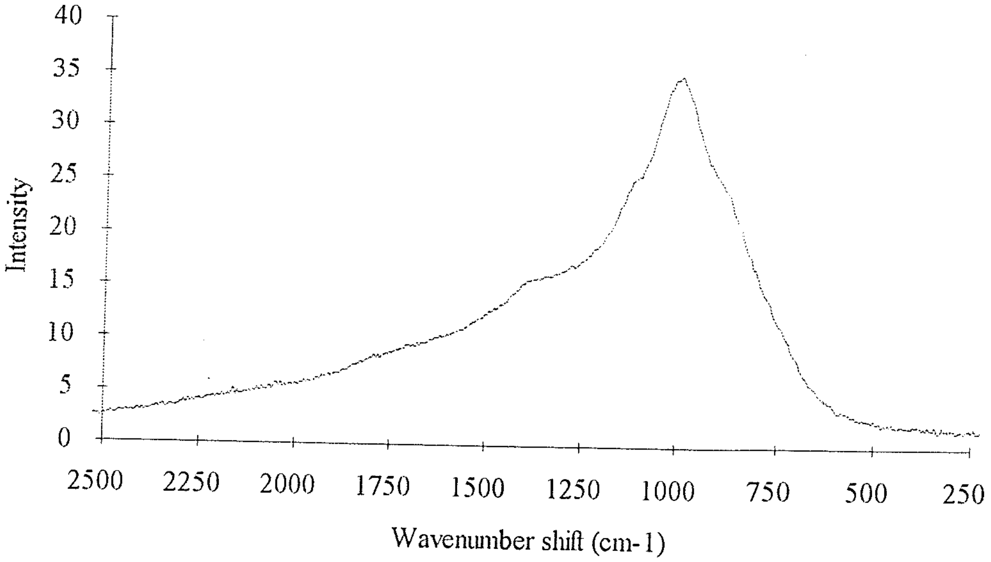

Figure 5.1 FT-Raman spectrum of Euroc C_2S.

---

* This point has been made again very recently[16].

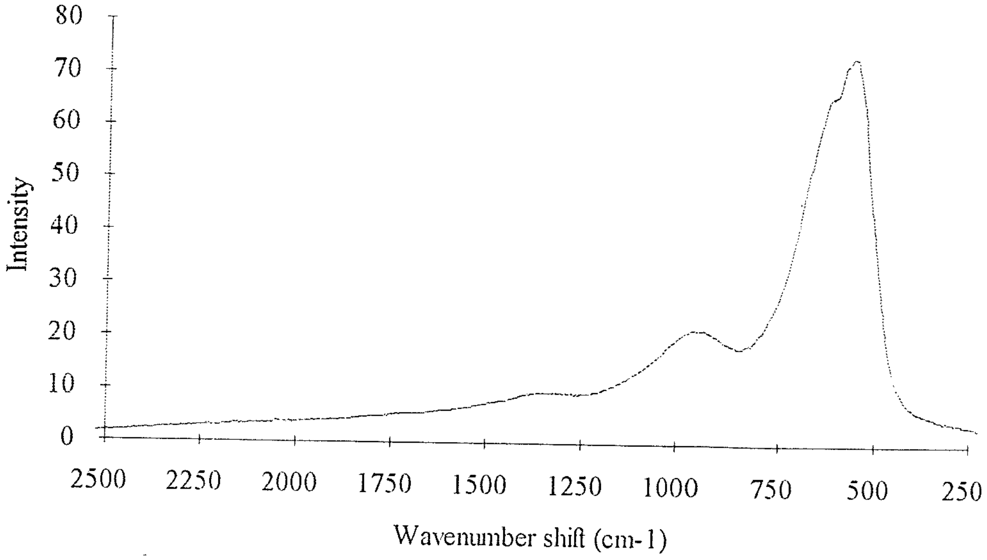

Figure 5.2 FT-Raman spectrum of Euroc C_3S.

The most striking features of the spectra are the curious shape of the background, and the lack of any obvious vibrational structure:

- C_2S has a maximum at 1023 cm^{-1} with a shoulder near 1105 cm^{-1}, then a weak feature at 1376 cm^{-1}, whilst the background continues to decay out past 2000 cm^{-1}.

- C_3S has a sharp band at 574 cm^{-1} shift with a shoulder at 626 cm^{-1}, a weak feature at 1007 cm^{-1}, and a further very weak broad peak at 1393 cm^{-1}, whilst the background decays more rapidly than in C_2S.

Since the FT-Raman spectra were carefully corrected for instrument response, the features seen are definitely not filter transmission artefacts*. Although the FT-Raman spectra presented above were recorded at 16 cm^{-1} resolution, very little change could be seen on comparison with 1 or 4 cm^{-1} resolution spectra.

Figures 5.3 and 5.4 show the obtained using visible excitation at 514.5 nm on the Dilor system in Stockholm.

---

* All FT-Raman spectra in this chapter have been corrected for instrumental response function[17].

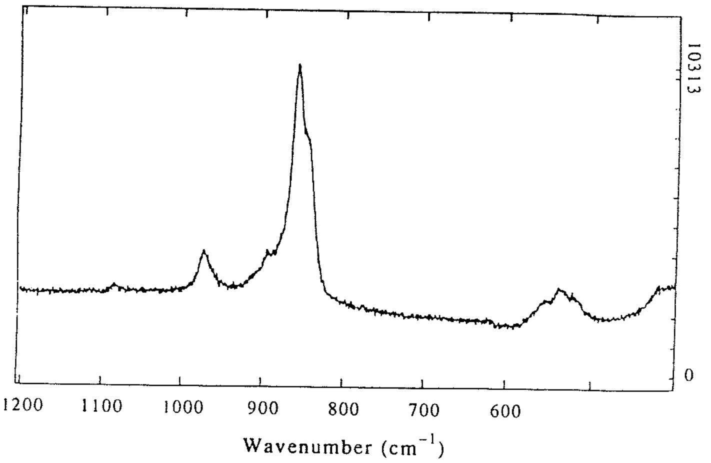

Figures 5.3 Conventional Raman spectrum of C_2S.

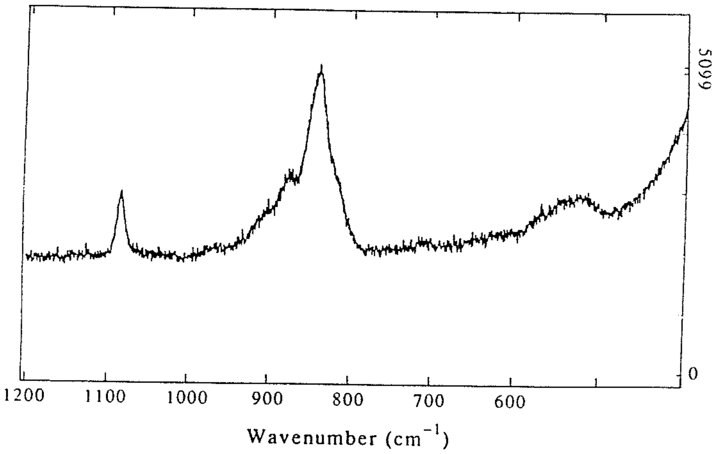

Figures 5.4 Conventional Raman spectrum of C_3S.

It is quite clear that near-IR excitation at 1064.1 nm does *not* give rise to the same spectra as expected from conventional studies. The true vibrational Raman spectra of calcium silicates is dominated by the symmetric stretching ("breathing") mode of the Si-O tetrahedron, situated near 800-900 cm^{-1} shift. It should be noted that the SiO_4^{4-} tetrahedra prevalent in silicate structures[3,4,18] produce a bigger contribution than the weakly-polarisable calcium-oxygen bonds that bind the structures together[13,16]. Plainly in evidence:

- C_2S has a major band at 856 cm^{-1}, a less-intense higher-shift band at 972 cm^{-1}, and a very weak band at 1084 cm^{-1}.

- C_3S has a broader, less-intense main feature at 842 cm^{-1}, no peak around 960 cm^{-1}, but a more noticeable 1084 cm^{-1} band.

The band at 1084 cm^{-1} is due to the symmetric stretch of the CO_3^{2-} anion of calcium carbonate, present as a carbonation product from the reaction of atmospheric CO_2 with the small amount of calcium silicate hydrate gel produced by adsorption of atmospheric moisture[19].

The most remarkable feature concerns the power required to excite the scattering. The conventional study required 1 Watt of Ar^+ excitation to record a reasonably weak spectrum - in sharp contrast, *5 mW* of near-IR excitation produced a signal strength high enough to saturate the detection system on the FT-Raman instrument.

The ratio of scattered to incident power developed by spontaneous Raman scattering excited far from resonance can be described classically[10-12] as:

$$I_{scattered} / I_{incident} \propto (\nu_{laser} - \nu_{vibration})^4$$

Here, I has the units of power, and ν is an absolute wavenumber. It can be seen that the above relationship predicts a *23-fold decrease* in scattered power on changing from 514.5 nm to 1064.1 nm excitation for a band at 850 cm^{-1} shift, for equal excitation powers.

Ignoring detector sensitivities and instrument response functions, and accepting difficulties in exact quantification because the spectrometers were operated at different spectral resolutions and have different etendué values[20,21] one fact should be obvious - *a true near-IR excited Raman spectrum should have been almost completely unobservable*.

When reviewed together with the differences in both band shape and position compared to previous work, this anomalous high intensity must be regarded as non-vibrational in origin, and probably due to fluorescence.

Although near-IR excitation is the preferred choice for many organic species, previous inorganic applications suggest a cautious* approach is wise[22,23]. Even if quite pure, certain inorganic species fluoresce or pyrolyse under near-IR excitation,

---

* This has very recently received support[24] - see later.

even at extremely low laser powers. Such compounds are not necessarily darkly-coloured, and can vary from simple binary salts to complex co-ordination compounds; the common factor is that all contain transition metals. None of the compounds in this study other than C_4AF were deeply-coloured at all - mostly off-white, cream, or very light blue/green.

It should be said that both C_3A and C_4AF supplied by Euroc behaved exactly as previous FT-Raman studies of aluminates and ferrates suggested - C_3A gave a broad and featureless background, whilst C_4AF simply pyrolised and gave a thermal emission spectrum, even at the lowest laser powers and after strong dilution in potassium bromide (KBr).

XRD showed the material supplied by Euroc to be quite pure, in cement chemistry terms; C_2S was identified in the β-polymorph (JCPDS 33-302), whilst C_3S was shown to contain a little pure triclinic C_3S (JCPDS 31-301), but mainly the form known as alite - $54CaO.16SiO_2.Al_2O_3.MgO$ (JCPDS 13-272). This is the usual form that C_3S takes up in industrial syntheses; the structure of $54CaO.18SiO_2$ is essentially built up of two unit cells each containing nine C_3S molecules, with two SiO_2 units being replaced by one MgO and one Al_2O_3.

ICP-AES revealed a different story. The Euroc samples were made by the reaction of selected limestone and silica sand deposits in a magnesia pot with calcium fluoride flux, and contain a huge range of metal ion impurities. Table 5.2 lists the constituents as revealed by ICP-AES.

Several of the metal listed are known to be incompatible with successful near-IR-excited Raman spectroscopy in certain environments. These species include Fe^{3+} (ca. 0.2% by mass) and Mn^{2+} (ca. 0.05% by mass), which are present in both samples; chromium, lead and tungsten are all present in the 25-55 parts per million (ppm) range.

The level of doping required for observable luminescence emission from minerals is of the order of 0.1%, or 1000 ppm[25] for iron and manganese. The sensitivity of near-IR FT-Raman spectrometers is such that 200 ppm iron impurity produced luminescence which completely obliterated any observable Raman features from a sample of alumina (Al_2O_3), whereas 20 ppm produced acceptable results[26].

Species	C_2S	C_3S
SiO_2	34.3 ± 0.1	25.3 ± 0.1
Al_2O_3	0.789 ± 0.001	0.351 ± 0.001
CaO	61.4 ± 0.3	68.9 ± 0.3
Fe_2O_3	0.217 ± 0.001	0.254 ± 0.001
K_2O	1.33 ± 0.001	0.0480 ± 0.0027
Na_2O	0.158 ± 0.001	0.0384 ± 0.0006
TiO_2	0.0168 ± 0.0002	0.0144 ± 0.0001
P_2O_5	0.0493 ± 0.0023	0.0480 ± 0.0011
MgO	0.484 ± 0.002	1.44 ± 0.01
MnO	0.0464 ± 0.0003	0.0528 ± 0.0002
Ba	18.4 ± 0.1	14.8 ± 0.1
Cr	28.1 ± 6.3	53.9 ± 1.9
La	<12.6	<11.8
Ni	<6.29	18.8 ± 1.3
Pb	40.7 ± 6.8	27.0 ± 8.2
Sr	698 ± 1	768 ± 1
W	34.9 ± 9.4	49.4 ± 5.5
Zn	44.5 ± 0.2	23.5 ± 0.3
Zr	18.4 ± 0.4	12.8 ± 0.1

Table 5.2 ICP-AES data on Euroc-supplied C_2S and C_3S. Species SiO_2-MnO quoted as % weight; thereafter, as parts per million (ppm) by weight. Limits bound 95% confidence (2σ level).

The prospects for the success do not seem high - fluorescence from one or more of the metal ions present therefore seems a good explanation for the appearance of the near-IR excited spectra, and rather damns FT-Raman as a method for analysis.

However, there were three good reasons to continue the study:

- No definite assignment had been made for the cause.
- The emission from the calcium silicates displayed rarely-seen structure.
- The failure of near-IR excitation on many inorganic species is a major concern for the technique, and should be investigated.

5.5.2 Synthetic calcium silicates

Proving impurity to be the cause of the structured emission relies upon being able to study truly pure and/or very well characterised samples, with strictly controlled and/or well-defined crystallographic phase - a very major undertaking. An attempt was made to synthesise chemically-pure material as a starting point. The FT-Raman spectra of the synthesised materials are shown below in figures 5.5-5.7.

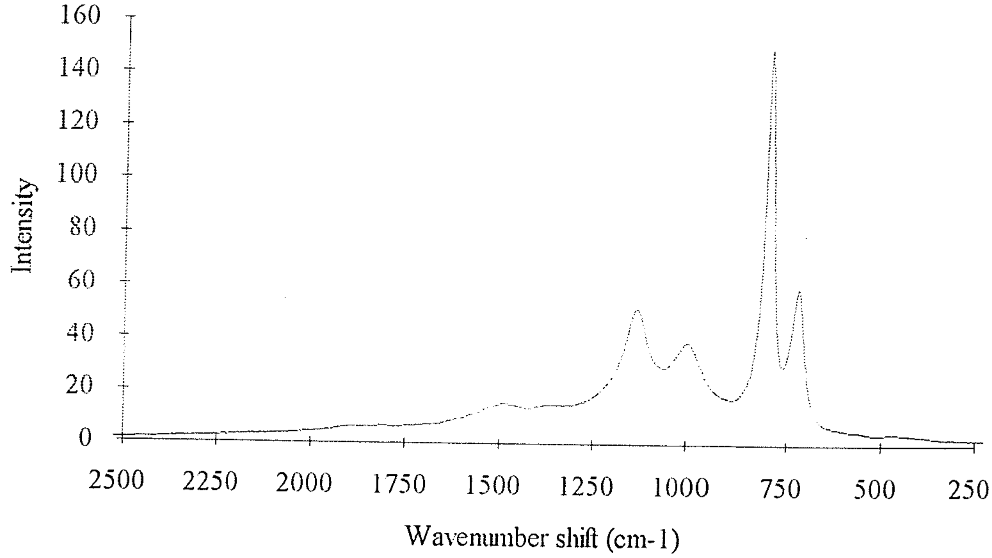

Figure 5.5 2:1 mix, Swedish synthesis.

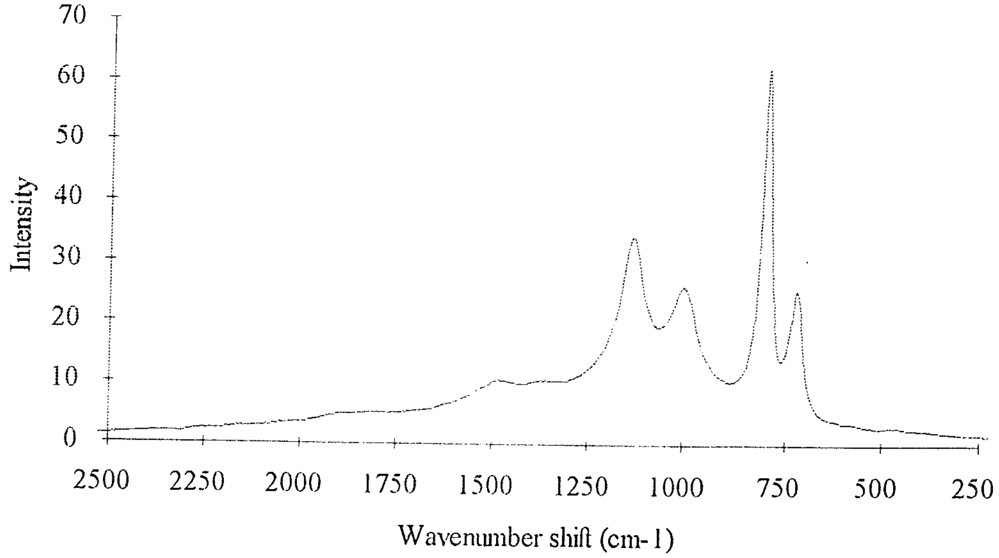

Figure 5.6 3:1 mix, Swedish synthesis.

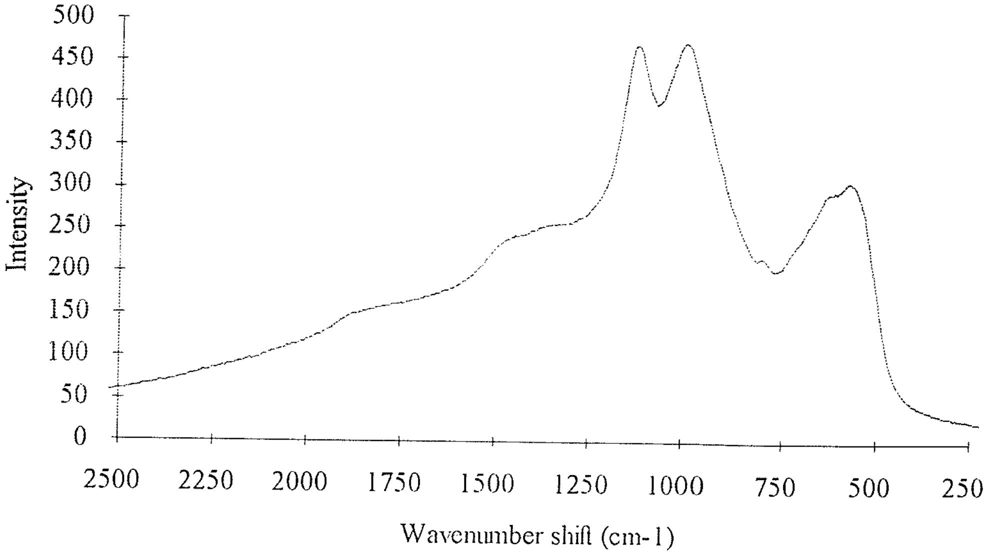

Figure 5.7 Southampton synthesis.

The heterogeneous nature of the Swedish products was revealed by powder XRD. Although not intended to be quantitative, both syntheses yielded mainly alite and pure C_3S, with a little γ-C_2S, CaO, γ-wollastonite (CS), and calcium carbonate. In common with the Euroc material, low laser power (<30 mW) produced huge signals, the spectra still showing broad peaks on a steep background. However, there are major differences in peak positions, the number of bands, and their width. One feature is quite plain - using pure chemicals apparently results in sharper spectral features than using selected mineral ore stocks.

The Southampton synthesis probably became contaminated - most likely with iron, given the previous usage of the furnace and the light green colouration. The FT-Raman spectrum in figure 5.7 is essentially a superposition of the major features of Euroc C_3S and C_2S, with the addition of the 1135 and 800 cm^{-1} bands from the Swedish syntheses. Unfortunately, XRD analysis was not available for this sample, and further syntheses were precluded by the unavailability of the furnace.

5.5.3 Blue Circle samples

Since the synthetic studies had to be curtailed the next most obvious source of data was from other cement suppliers. The samples supplied by Blue Circle were synthesised in a similar manner to those from Euroc in the mid- to late 1960s. In view of the age of the samples, it was decided to confirm the phase and the purity of samples by XRD and ICP-AES. Three of the samples were β-dicalcium silicates, one of which was stabilised with ca. 0.5% boron oxide (B_2O_3) during synthesis. The fourth was γ-dicalcium silicate, the fifth pure triclinic tricalcium silicate, and the sixth alite - monoclinic pseudo-C_3S, as discussed above.

Conventional Raman spectroscopy using the Southampton Coderg spectrometer with Ar^+ green excitation at 514.5 nm revealed no surprises - a high background, weak scattering, with sharp vibrational features due to Si-O bonding between 800-900 cm^{-1}. Subsequent re-examination using a far more sensitive and efficient spectrograph-based Raman microscope yielded similar data and the same conclusion.

The FT-Raman spectra of the β-C_2S samples without stabiliser are shown below in figures 5.8 and 5.9. The spectra are almost identical to that from the Euroc β -C_2S sample. XRD data confirmed unquestionably the phase of these samples (JCPDS 33-302).

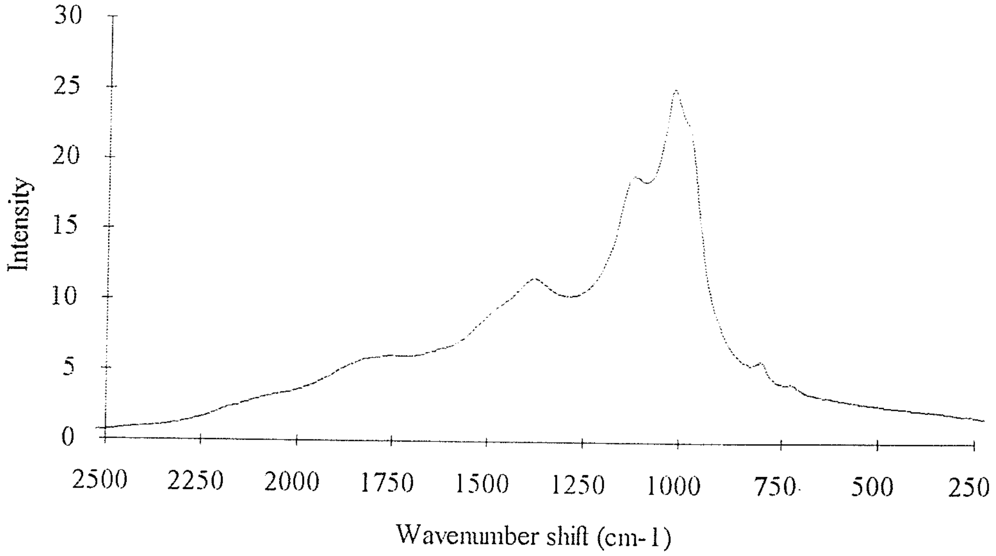

Figure 5.8 Blue Circle β-C_2S #1.

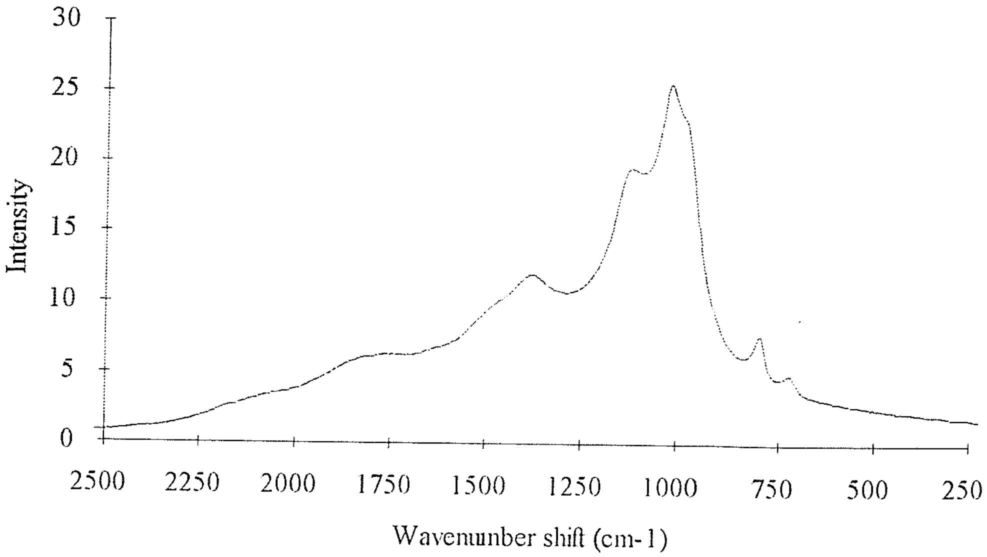

Figure 5.9 Blue Circle β-C_2S #2.

These two samples showed more structure on the large band at 1020 cm^{-1} than the Euroc C_2S sample - a definite shoulder to low shift at 989 cm^{-1}, and the sideband at 1122 cm^{-1} is much more pronounced. Furthermore, a broad weak feature is in evidence centred at 1377 cm^{-1}, with another much weaker and broader feature centred possibly at 1782 cm^{-1}. Also in evidence are two peaks on the low-shift slope of the main band, at 806 and 730 cm^{-1}.

The B_2O_3-stabilised sample gave a quite different spectrum:

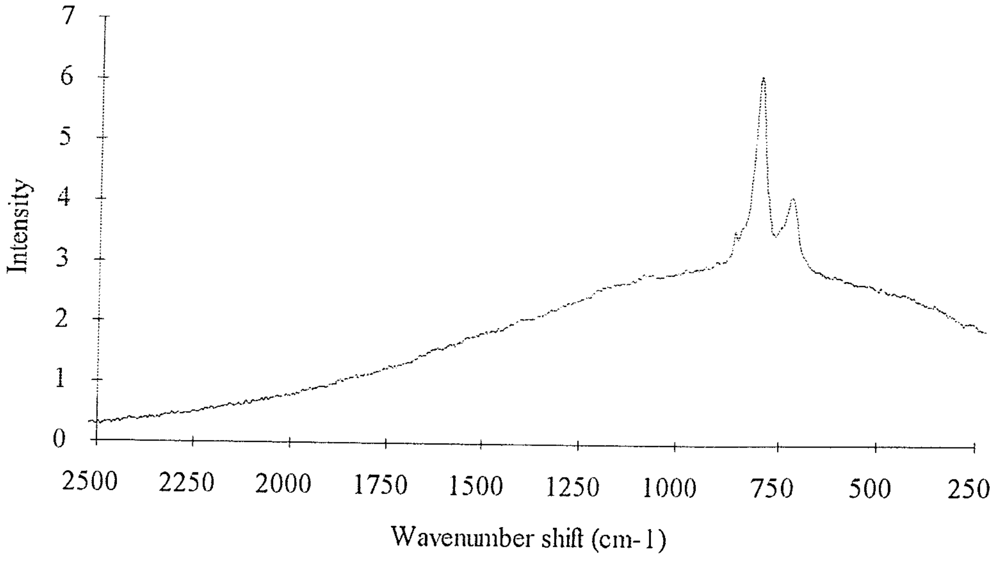

Figure 5.10 Blue Circle β-C_2S #3.

Three bands at 860, 802, and 725 cm^{-1} are clearly in evidence, but the background has markedly less structure and quite different profile. Since XRD confirmed the phase of the material, the changes compared to figures 5.8 and 5.9 must be due to the added B_2O_3. The addition of 0.5% B_2O_3 appears to quench the broad emission near 1000 cm^{-1} shift. XRD can not easily reveal the whereabouts of light atoms, since the scattering of X-rays is weak from such small areas of electron density, and the concentration of B_2O_3 in the silicate is low (1:200); perhaps the oxide perturbs the crystal structure and changes the fluorescence cross-section so that non-radiative decay may be favoured.

In order to check whether the added stabiliser gave an unusual Raman spectrum B_2O_3 was re-analysed with near-IR excitation. In accordance with the well-known hygroscopic conversion of boron oxide to hydroboric acid[18] a 25 year old sample of B_2O_3 gave an excellent fluorescence-free $B(OH)_3$ spectrum with a weak but definite band near 808 cm^{-1} shift confirming the presence of very little unconverted oxide - figure 5.11 shows the overlaid and offset spectra of new $B(OH)_3$ and old B_2O_3, in accordance with known Raman data[27].

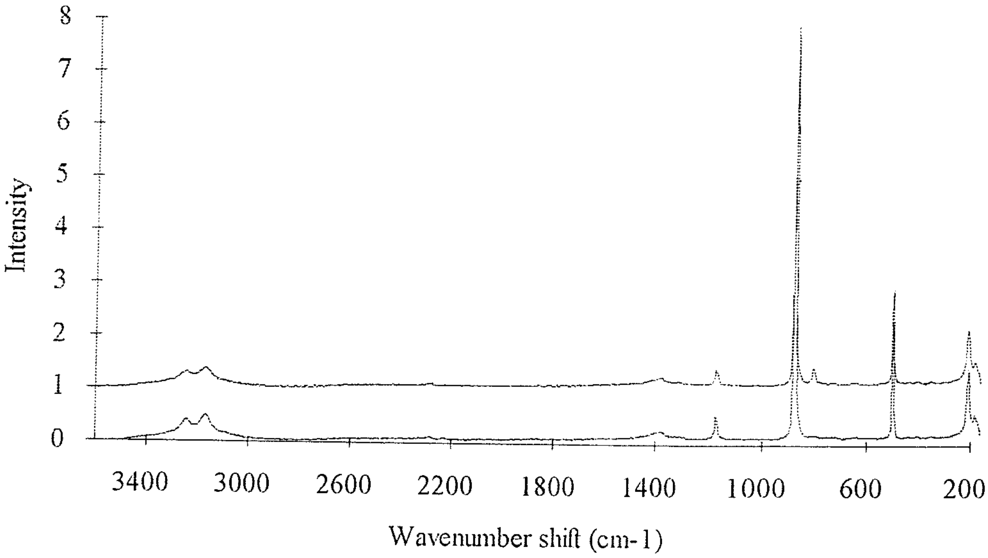

Figure 5.11 FT-Raman spectra of B_2O_3 (upper) and $B(OH)_3$ (lower).

Returning to the comparison of cement samples, the two bands near 800 cm^{-1} shift were apparent in all FT-Raman spectra from the synthetic materials as well as the Blue Circle β-C_2S samples. Since the Euroc samples have broadened features near 1000 cm^{-1} it is quite possible that these bands are weakly present in the Euroc materials too.

The band broadening possibly reflects a higher content of transition metals in the Euroc samples. ICP-AES data on Euroc β-C_2S reveals that level of iron in the sample (ca. 1500 ppm) is ca. 10 times greater than that in Blue Circle β-C_2S and both tricalcium silicate samples (ca. 80-125 ppm). Table 5.3 gives the analysis for these samples.

Species	β-C_2S	γ-C_2S	**Monoclinic** C_3S	**Triclinic** C_3S
Al	190 ± 1	890 ± 7	4600 ± 12	486 ± 1
Ca	439000 ± 614	451000 ± 1667	500000 ± 3901	477000 ± 1765
Fe	122 ± 1	665 ± 6	141 ± 1	81.7 ± 0.5
K	59.0 ± 16.2	<50	<50	101 ± 44
Mg	75.0 ± 2.9	1520 ± 14	7920 ± 23	53.8 ± 2.7
Na	234 ± 23	56.7 ± 10.3	<20	92.8 ± 33.6
Mn	2.46 ± 0.19	287 ± 2	1.94 ± 0.14	1.86 ± 0.08
As	<3.03	<2.85	<2.90	<2.92
Ba	6.13 ± 0.07	13.0 ± 0.3	47.1 ± 0.2	34.1 ± 0.1
Co	<1.01	<0.948	1.23 ± 0.19	<0.972
Cr	<3.03	8.14 ± 0.71	<2.90	<2.92
Cu	122 ± 1	58.1 ± 0.5	206 ± 1	<0.972
Mo	<5.05	<4.74	<4.83	<4.86
Ni	1.36 ± 0.78	1.05 ± 0.89	1.56 ± 1.13	13.7 ± 1.2
Pb	<10.1	<9.48	<9.67	<9.72
Sr	43.3 ± 0.2	586 ± 4	464 ± 1	370 ± 1
V	<1.01	<0.948	1.60 ± 0.17	1.24 ± 0.2

Table 5.3. ICP-AES data on Blue Circle-supplied β-C_2S, γ-C_2S, monoclinic C_3S, and triclinic C_3S. Species quoted as parts per million (ppm) by weight. Limits bound 95% confidence (2σ level).

Turning to the other samples, the structure of γ-C_2S was also confirmed by XRD (JCPDS 31-297). The FT-Raman spectrum is given in figure 5.12. This is surprisingly different from the β-C_2S samples. An extremely strong and sharp band appears at 802 cm^{-1}, whilst another sharp but weaker band lies to low shift at 724 cm^{-1}.

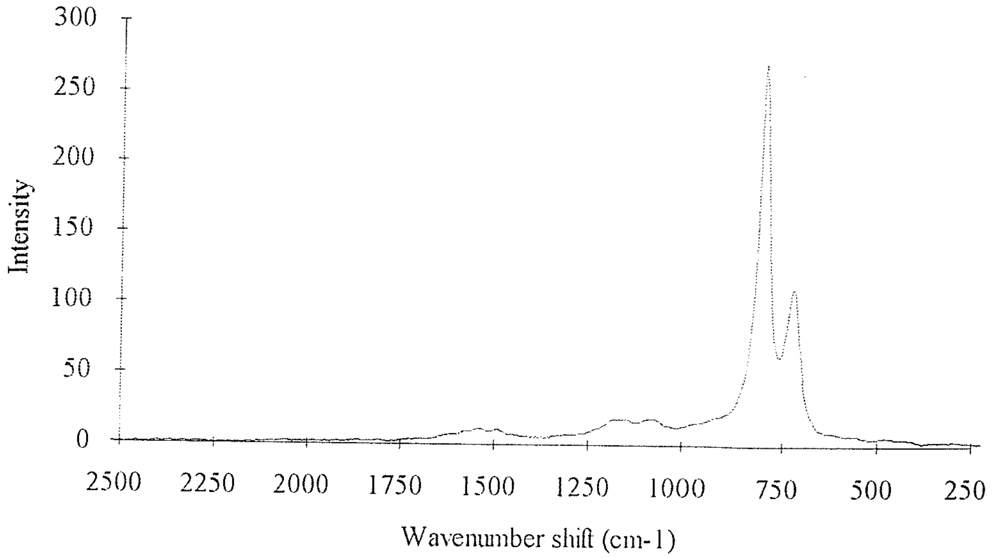

Figure 5.12 FT-Raman spectrum of Blue Circle γ-C_2S.

However - the curious point is that *the power required to excite spectra so intense that the detection electronics saturated for an hour was not measurable on the power meter normally used in the laboratory*. That is, *less than 5 mW.* This intensity is far higher even than the pre-resonance scattering of polydiacetylene polymers that saturate the detector near 3-4 mW, and proved absolutely repeatable.

Even more curiously, *the spectra could be repeated* (albeit less intense) *with the laser switched off and the beam path blocked*. This startling result lends great weight to the argument that the spectra are due to luminescence, not Raman scattering - the only explanation possible is that the "scattering" was caused by the very small amount of light from the HeNe reference laser that falls onto the sample in the Raman sample compartment, even on the commercial FT-Raman spectrometers. Although seemingly difficult to believe, this has been confirmed recently[24]. Excitation at 632.8 nm produces emission which is fixed in wavelength (unlike Raman scattering, where the shift is constant) and must be luminescence. Also surprising is the lack of a strong fluorescence background on the near-IR spectra.

In both monoclinic and triclinic C_3S the fluorescence background returns - see figures 5.13 and 5.14 respectively - although the two bands at 801 and 722 cm^{-1} are still in evidence. However, the monoclinic sample also has a broad band at 660 cm^{-1}, whilst the triclinic sample has this feature shifted to 545 cm^{-1}, revealing a shoulder to higher shift near 612 cm^{-1}.

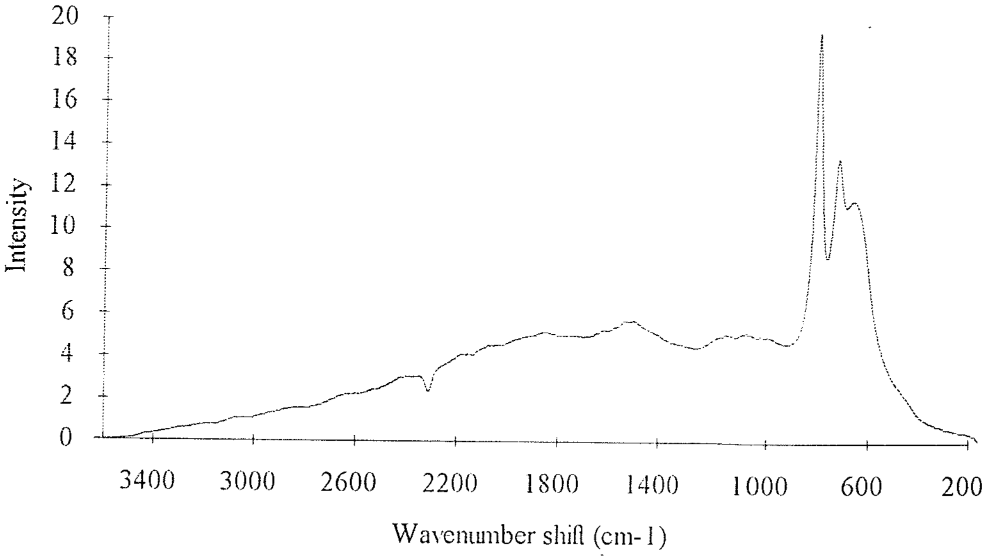

Figure 5.13 FT-Raman spectrum of Blue Circle monoclinic C_3S.

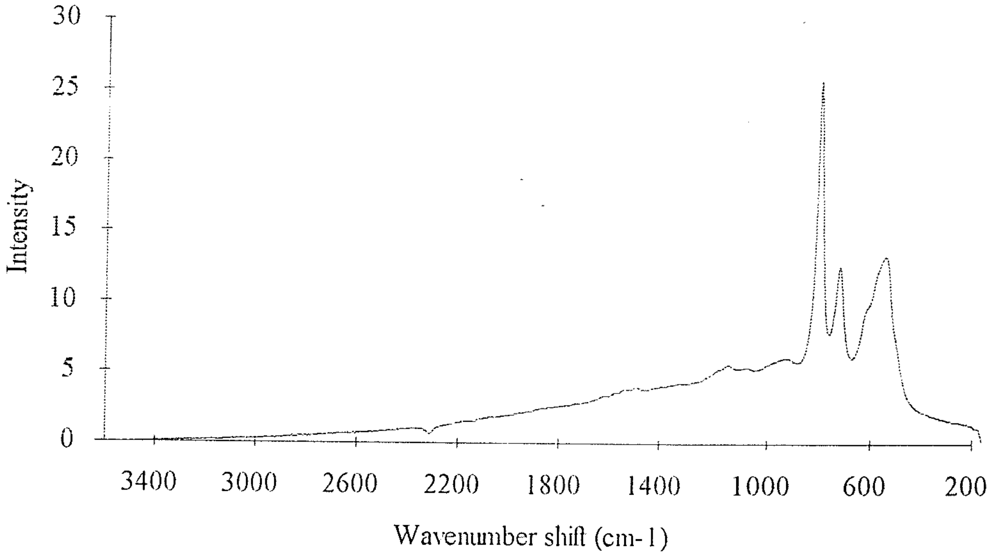

Figure 5.14 FT-Raman spectrum of Blue Circle triclinic C_3S.

Comparison with the Euroc C_3S sample - mainly alite with a little triclinic C_3S - shows a good correlation; however, the bands are not an exact fit. The ICP-AES data on the monoclinic Euroc sample indicates around 2000 ppm iron, rather than 100 ppm in the Blue Circle samples. The broadening of the peaks of the Euroc with respect to the Blue Circle samples may well be due to the higher level of metal ion impurities - which tallies with the results of the syntheses, where the Southampton synthesis showed far broader features than the Swedish syntheses.

Since the near-IR excitation of Raman scattering in the cement minerals is compromised by a strong and very unusual luminescence, and because absolutely no details could be found in the literature, further studies were carried out to investigate the problem.

5.5.4 Comparisons against simple systems

A survey of a range of simple species containing silicate and/or calcium cations was undertaken, to see whether these Raman spectra under near-IR excitation were also anomalous. The survey proved enlightening.

5.5.4.1 SiO_2, Al_2O_3, and Fe_2O_3

The FT-Raman spectrum of powdered silica shows a sharp band at 464 cm^{-1} shift, superimposed on a high background; the peak position is in good agreement with previous studies[28]. Also in good agreement with previous near-IR-excited Raman work is the broad and structureless fluorescence of α-alumina, centred at around 1800 cm^{-1} shift[29]. Ferrous oxide gave a strong fluorescence spectrum excited with <5 mW power to avoid burning and thermal emission. This is quite different from the case of visible excitation[30], where iron oxide spectra are possible to obtain under the correct conditions. The contrast between the extremely broad fluorescence and the structured fluorescence of the supplied and the synthesised cement minerals is quite obvious.

The effect of iron as an impurity in quartz is seen in the upper trace of figure 5.15. The FT-Raman spectrum here shows an intense background, with a broad peak near 583 cm^{-1} shift, with a weaker broad peak to higher shift at 974 cm^{-1}. Also in evidence is a much narrower band at 464 cm^{-1} shift, as a sideband to low shift side of the strongest peak. This is the "breathing" mode in the SiO_4^{4-} unit, as evident in spectra of powdered silica. All the other features are almost certainly due to fluorescence, due to the iron which gave this particular quartz sample its distinctive light yellow hue.

This was proven in the following manner. After pulverising a small section, grinding, and repeated washing with concentrated hydrochloric acid and distilled water to pH neutral, the FT-Raman spectrum was again obtained. The effect of the washing should have been to remove the iron as iron chloride - and the lower trace of figure 5.15 shows that this took place. The major feature in this spectrum is the 464

cm^{-1} silica band, and although the spectrum does have a background at least it is quite flat, and the other weaker silica features are visible.

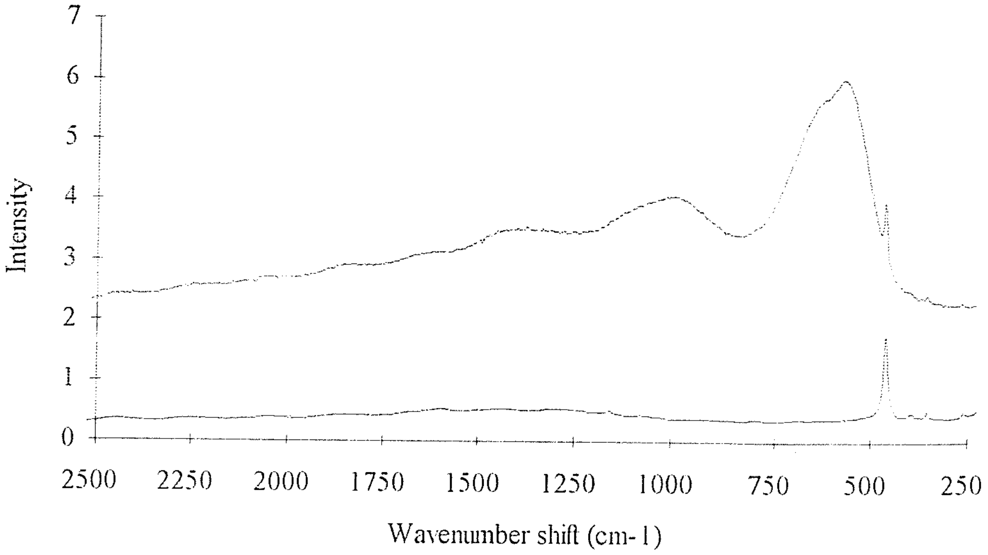

Figure 5.15 FT-Raman spectra of natural (upper) and washed (lower) quartz.

5.5.4.2 $CaSiO_3$

To augment the comparison with silicates, $CaSiO_3$ was obtained from the Aldrich Chemical Co. through Professor Ian Beattie. This sample of Wollastonite (designated CS) was fairly pure, and gave a good and recognisably vibrational FT-Raman spectrum - see figure 5.16. It is probably the first evidence that calcium silicates do have a vibrational spectrum that is amenable to FT-Raman study. Not only is this cause for hope, for near-IR Raman spectroscopy of calcium silicates as a group, but it also neatly displays the unpredictability of FT-Raman methods in solid-state inorganic chemistry.

The spectrum has a strong background, peaked near 1600 cm^{-1} shift, on which are grouped several sets of intense, sharp Raman bands. The three major bands are at 985, 578, and 371 cm^{-1}.

These positions do not agree well with the microprobe spectra of β-CS by Conjeaud and Boyer, who reported 971, 638 and 412 cm^{-1} shift for these bands[9]. The reason for this difference is not clear. It is known that β-CS exists in closely-related monoclinic and triclinic forms. Since no crystallographic data was available for the supplied sample, it is possible that the sample is actually not the same polymorph as studied by the previous authors. However, the bands are certainly vibrational, as opposed to the broad intense and featureless peak near 1600 cm^{-1}, which is much more reminiscent of a "classic" FT-Raman fluorescence background, like that in ferrous oxide.

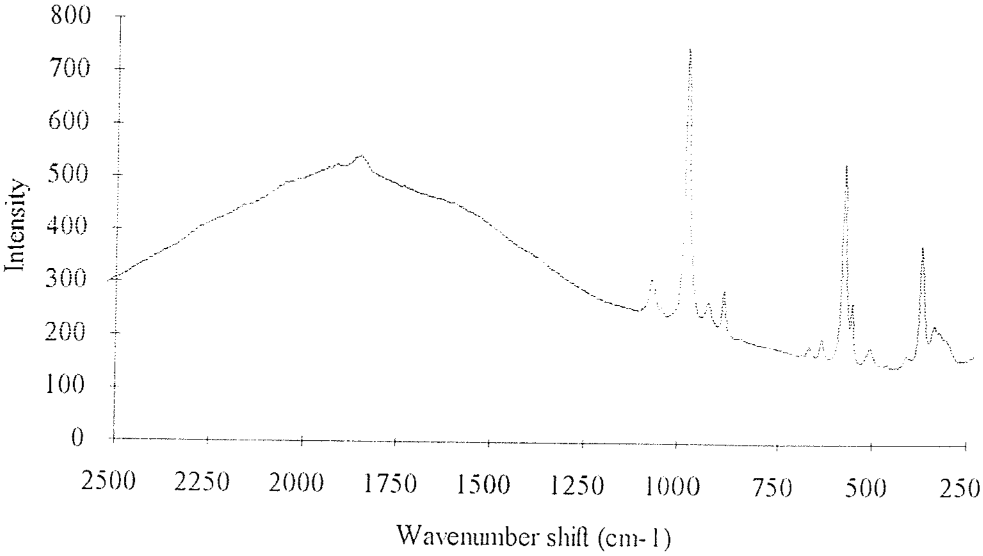

Figure 5.16 FT-Raman spectrum of Wollastonite.

5.5.4.3 CaO and $Ca(OH)_2$

CaO provided several very interesting results. Despite having no coloration at all[18] in the solid state, CaO has electronic states *in the gas-phase* just inside the UV and near-IR regions, at 385 nm and 865 nm respectively[31]. Most interestingly, it possesses a fully-allowed transition at 1162 nm - just 790 cm^{-1} to the red of the exciting line.

The FT-Raman spectrum of CaO shown below in figure 5.17 is composed of one strong and narrow band at 644 cm^{-1}, with three weaker and broader bands at around 770, 1025, and 1444 cm^{-1} shift. It has similar overall appearance to several of the luminescence spectra from the cement minerals. The laser power, however, was around 200 mW, far higher than for most of the calcium silicates, and far more characteristic of a Raman spectrum.

CaO crystallises in the rock salt (NaCl) face-centred cubic system[18] for which there should be[32-34] no first-order (fundamental) Raman bands - this has been commented on before in the literature[35]. On comparison with this reference, the closest match for the 644 cm^{-1} band in the FT-Raman spectrum is one of the features seen in polarised *second-order* (overtone/combination) spectra near 655 cm^{-1}. According to the literature, however, the second-order Raman spectrum was collected using a triple scanning monochromator using 1 W of Ar^+ 514.5 nm excitation, with photon-counting PMT detection.

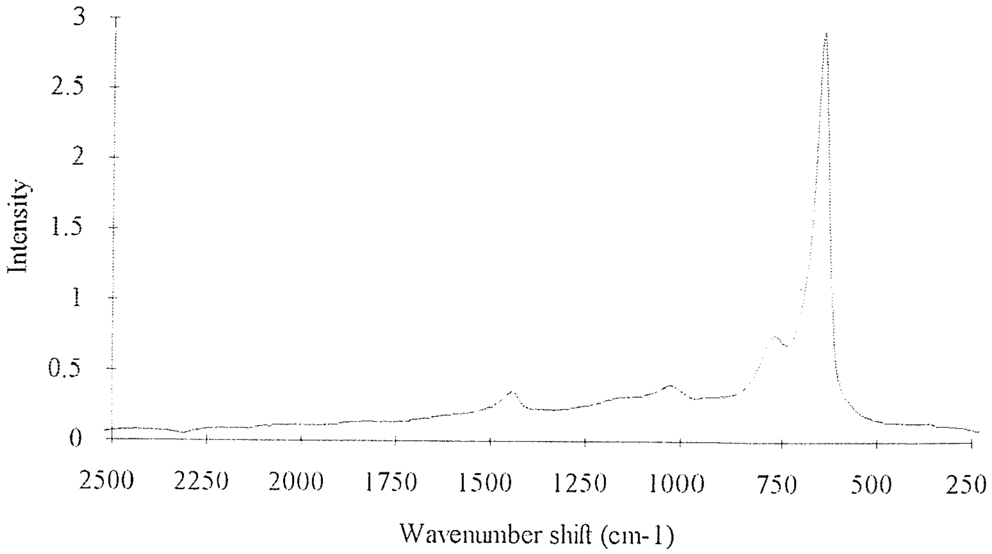

Figure 5.17 FT-Raman spectrum of CaO.

Taking all the evidence:

- Overtones and combinations are generally very weak in the Raman effect compared to fundamentals,
- The FT-Raman spectrum correlates poorly with the second-order spectrum,
- The overall appearance of the spectrum echoes that of the cement minerals, and
- CaO *in the gas-phase* has near-IR electronic states

it still seems more likely that the features are due to luminescence, despite the higher power needed to produce the spectrum.

Oddly, subsequent FT-Raman spectra *from the same batch* of reagent-grade CaO showed slight spectral differences. The lower trace in figure 5.18 was excited with 60 mW, and shows - at first sight - simply a lower-intensity, noisier spectrum, such that the weak bands can not be resolved. However, the strong band has *shifted* to 635 cm^{-1}. This is the position in which it is observed in the upper trace, the spectrum of the same sample of CaO dried at 1300°C for 90 minutes and excited with merely *10 mW*. Weak bands are again in evidence at 1435 and 1010 cm^{-1}. Such changes can only reflect heterogeneity in the sample, probably in impurity distribution, whilst excitation of a spectrum with 10 mW also seems to indicate fluorescence as the main cause.

Heat treatment was attempted for two reasons. Firstly, the appearance in the lower trace of a negative-going "peak" at 2316 cm^{-1} shift (7082 cm^{-1} absolute), which possibly indicates overtone absorption by hydroxyl (OH-) groups - see figure 5.19.

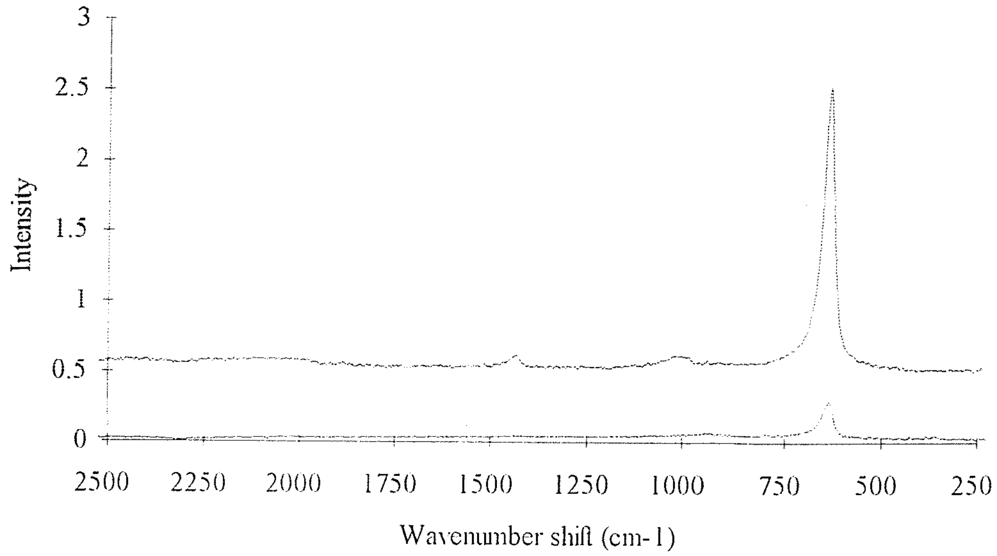

Figure 5.18 FT-Raman spectra of a second sample of CaO (lower) and a heat-treated sample of CaO (upper, offset 0.5 units).

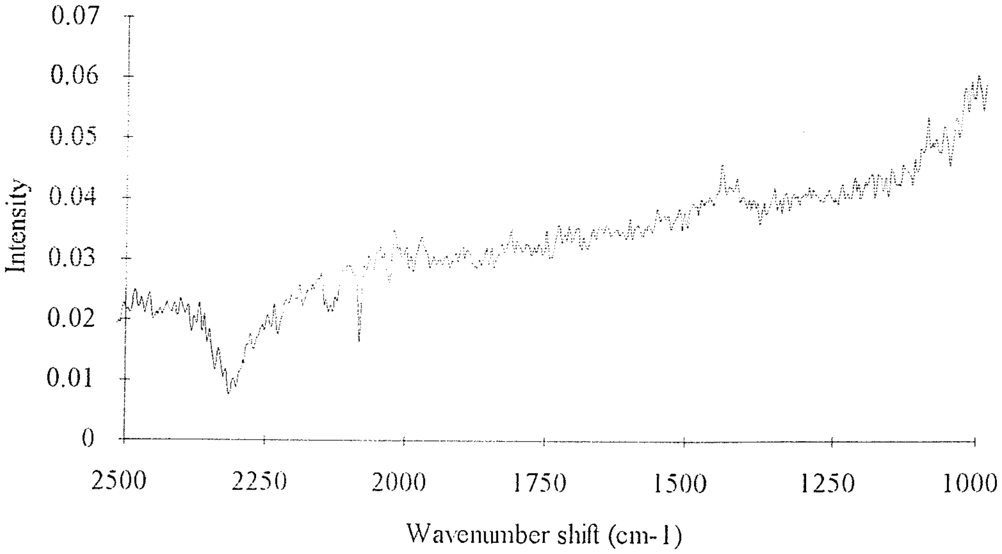

Figure 5.19 Absorption signature on high Raman background.

Calcium hydroxide, formed hygroscopically in low yield, would be distributed randomly throughout the CaO on mixing, which would confuse matters if $Ca(OH)_2$ proved to be fluorescent. Drying should reconvert hydroxide to oxide. Secondly, the spectra of the cement minerals might be explained in terms of fluorescence by inclusions of _non-reacted CaO_, which might react further if re-heated.

In fact, the fluorescence yield from the heat-treated CaO increased dramatically with time in the furnace, instead of decreasing, which dismissed the second theory. The first observation is correct, however - the absorption is not in evidence after heat-treatment. Combined TGA/DSC would be useful to clarify this point further.

$Ca(OH)_2$ was also investigated, and a huge variability found once again - but only in scattered intensity. Even in analytical-grade $Ca(OH)_2$, widely differing spectra were obtained from the same batch of sample. This can only reflect heterogeneity in the sample. Figure 5.20 shows spectra from two consecutive samplings.

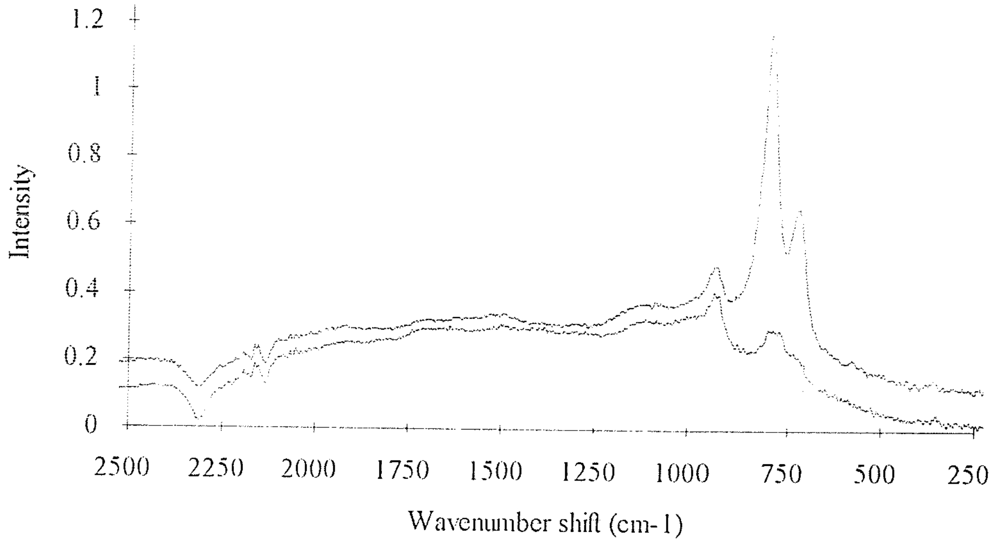

Figure 5.20 FT-Raman spectra of $Ca(OH)_2$.

Yet the most bizarre aspect concerned the form of the spectra - _the very same peaks as found in all the Blue Circle cements and the syntheses carried out in Sweden or in Southampton are plainly evident - near 802 and 726 cm^{-1}_. Furthermore, a peak at 933 cm^{-1} is visible, along with two inverse peaks at 2310 and 2134 cm^{-1}, reflecting hydroxyl absorption. In other spectra, an intense broad background, sometimes uniform but other times peaked near 1600 cm^{-1}, dwarfed the narrower features, whilst in others an additional band - weak, but sharp - near 630 cm^{-1} was visible.

In terms of intensity, the power required to excite the spectra without saturating the detector varied according to the amount of background present, but ranged from 50 mW to 1 W. Spectra from analytical grade material showed the same two peaks - with a reasonably broad band to low-shift, peaking around 644 cm^{-1}.

The possible causes are difficult to identify. *It is certain that the spectra are not vibrational in origin.* The Ca(OH)$_2$ crystal has structure analogous to that of CdI$_2$ - a crystal habit from which first-order Raman spectra may be, and have been, observed[37]. The Raman spectra should consist of one O-H mode at high shift around 3620 cm^{-1} (impossible to observe with the Luleå spectrometer, although not with that in Southampton) and three bands at low shift - 254, 357, and 680 cm^{-1} shift. This is most certainly not what is observed under near-IR excitation.

With excitation at 1064.1 nm, the peaks near 800 and 730 cm^{-1} are always seen to greater or lesser degree. When taken into consideration with the variable intensity of the spectra and the unusual shape of the bands, it seems likely - once again - that the spectrum is due to luminescence.

Calcium hydroxide displays a curious luminescence band after heat-treatment when excited by visible wavelengths[38,39]. It has been proposed that this is due to the formation of O_2^{2-} species as lattice defects, in combination with the low concentration of Mn^{2+} impurity centres discovered by electron spin resonance (ESR). It comes as no shock to find that the reagent grade and analytical grade Ca(OH)$_2$ samples used for spectroscopy were quite rich in manganese - as are the cement minerals.

One simple experiment to test this would be to heat the sample up to just above the dehydration temperature of Ca(OH)$_2$, and observe the increase in fluorescence intensity. This is a facile experiment, since the temperatures required are only around 150-250°C, and therefore thermal emission background is not a great problem. If necessary, a short wave pass filter could be used to cut the high-shift completely, thereby removing the excessive background with attendant saturation and shot noise problems, or pulsed/gated techniques used to discriminate against the background.

5.5.5 Near-IR absorption studies

"Inverse" re-absorption bands were evident in the FT-Raman spectra of Ca(OH)$_2$, and both the mono- and triclinic Blue Circle C$_3$S samples. This demands rationalisation.

The near-IR O-H absorption in calcium hydroxide can be seen at 7085 cm^{-1} in figure 5.21 - effectively 2312 cm^{-1} shift from 1064.1 nm excitation. This is in good agreement with the FT-Raman "inverse" peak position. Since the very strong IR fundamental absorption at 3643 cm^{-1} is also in evidence in the near-IR scan, it is likely that the absorption band near 7085 cm^{-1} is a combination with one of the lower-intensity IR absorption.

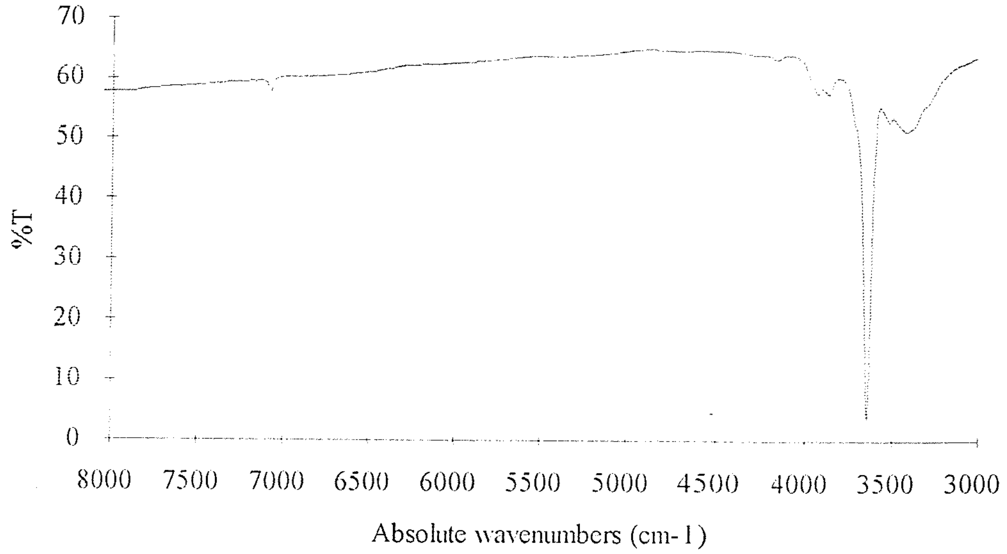

Figure 5.21 Transmission near-IR absorption spectrum of $Ca(OH)_2$.

Bands around 7100 cm^{-1} are not due to atmospheric water, because the spectrometer used for these experiments had a continual purge with parts-per-million (ppm) dry air to the IR sample compartment, and a dry nitrogen purge to the optics bench, whilst care was taken in recording background reference spectra to minimise residual water. Also, the $Ca(OH)_2$ and KBr used for pellets in the transmission study were dried for 24 hours at 175°C. In addition, the bands observed are also broad, and do not display the fine structure associated with gas-phase vibrotational bands.

However, the FT-Raman spectrometer that produced the Raman spectra from the Blue Circle cements with "inverse" bands was not purged; therefore, it was necessary to distinguish between a sample-based absorption and one due to atmospheric water. A simple experiment using the FT-Raman cold cell developed for the 1700 series spectrometer lead to the conclusion that the Raman "inverse" peaks were dominated by sample-based, and not atmospheric, absorption. On cooling a sample of the Blue Circle monoclinic C_3S to -145°C, the inverse peak shifted 10 cm^{-1} in position, from 2312 cm^{-1} in the room-temperature sample, to 2302 cm^{-1} in the cold sample. The region between 2000-2500 cm^{-1} shift is shown in figure 5.22.

Since the path length of air through the spectrometer is not affected by the change in temperature, *changes in the spectra on cooling must be sample based* - probably in lattice size.

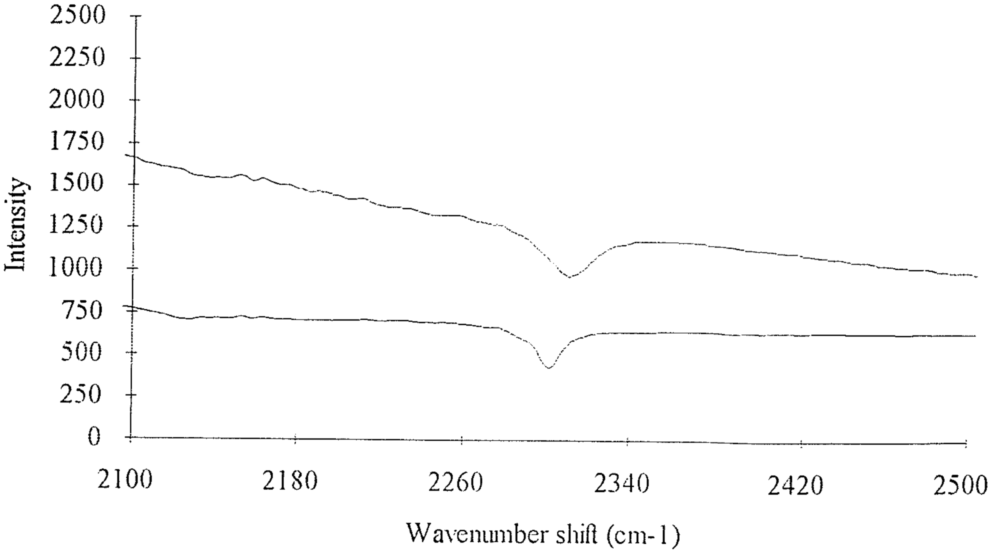

Figure 5.22 The "inverse" peak region of the Blue Circle monoclinic C_3S sample.

The near-IR absorption spectra of the Blue Circle samples are shown overlaid in figure 5.23. The band at 7083 cm^{-1} is possibly due to $Ca(OH)_2$.

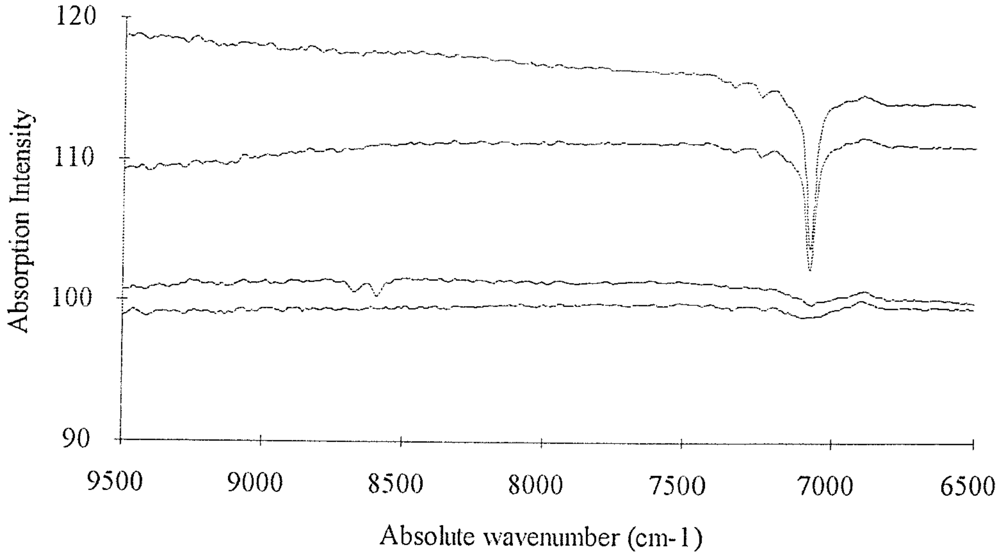

Figure 5.23 Overlaid near-IR diffuse reflectance spectra of the Blue Circle cements. Top→Bottom: Triclinic C_3S, Monoclinic C_3S, γ-C_2S, and β-C_2S.

The bands persisted even after drying the samples at 150°C, which implies that it is not due to weakly-bound water. The tricalcium silicate samples feature this band much more strongly than the dicalcium silicates.

The near-IR absorption spectra of γ-C_2S also contain a pair of very weak bands, at 8673 cm^{-1} and 8594 cm^{-1}. If these figures are subtracted from 9396 cm^{-1}, the reference wavenumber used as default for the Rayleigh line on the Southampton FT-Raman spectrometer, *the shift of these lines is 723 cm^{-1} and 802 cm^{-1}, respectively*.

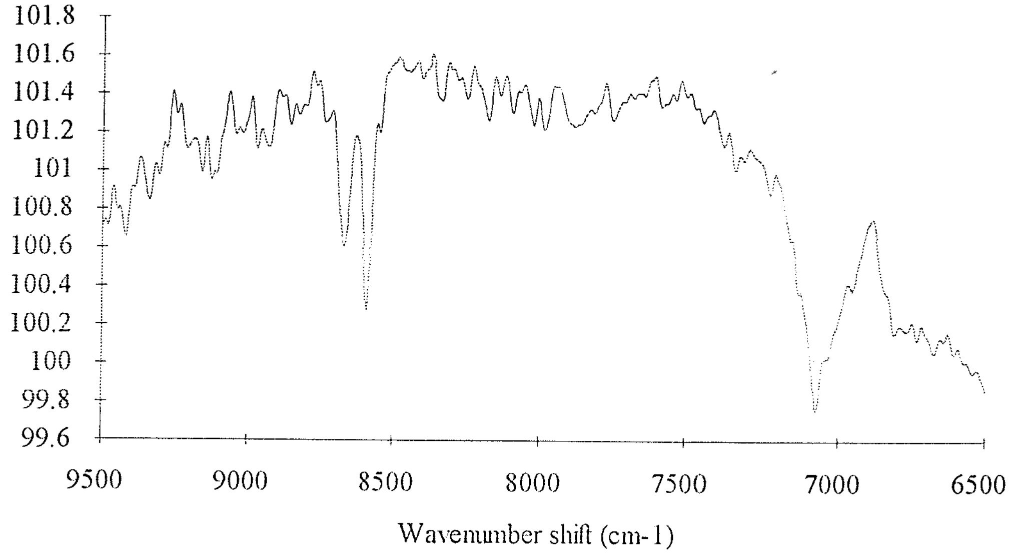

Figure 5.24 Expanded plot of γ-C_2S from figure 5.23.

Remember that *the FT-Raman spectrum γ-C_2S has two phenomenally strong lines at 724 cm^{-1} and 801 cm^{-1} shift*. It seems likely, therefore, that the cause of the two "Raman" features is actually luminescence emission at the wavelength corresponding to the near-IR absorption bands, as a result of pumping to the blue-shifted, shorter-wavelength side of these bands with 1064 nm excitation.

5.5.6 Low-temperature studies on line widths

The linewidth of the emission from the samples synthesised in Sweden (ca. 50 cm^{-1} FWHM for the broad peaks, ca. 25 cm^{-1} for the bands around 800 cm^{-1} shift) compared to the contaminated Southampton synthesis (ca. 100-200 cm^{-1}, exact measurement being difficult due to strong overlap) suggests impurity as a cause of the broadening of the spectral lines. This seems to be confirmed by the comparison of higher-purity Blue Circle samples to those of Euroc.

This may imply that the cause of the emission is but perturbed by changes in the lattice. Narrow spectral lines are often associated with long-lived, or meta-stable, excited states. Solid-state species usually have narrower line width at low temperature, because the suppression of external (lattice) vibrations means there is a lower probability of a lattice vibration interacting with an internal (molecular) vibration - or electronic excitation - as strongly, resulting in an increased lifetime for the intramolecular vibrations (as they are not destroyed by interaction) and a narrower line width results.

The low temperature FT-Raman experiment mentioned above provided the opportunity to reduce lattice vibrational perturbation, and resolve emission features more clearly. The effect on the near-IR-excited spectrum is profound, and is shown in figure 5.25 for Blue Circle monoclinic C_3S. The effect of cooling is partially to narrow and displace the two bands that are distinct at room temperature to lower shift, whilst the shoulder evident at room temperature disappears.

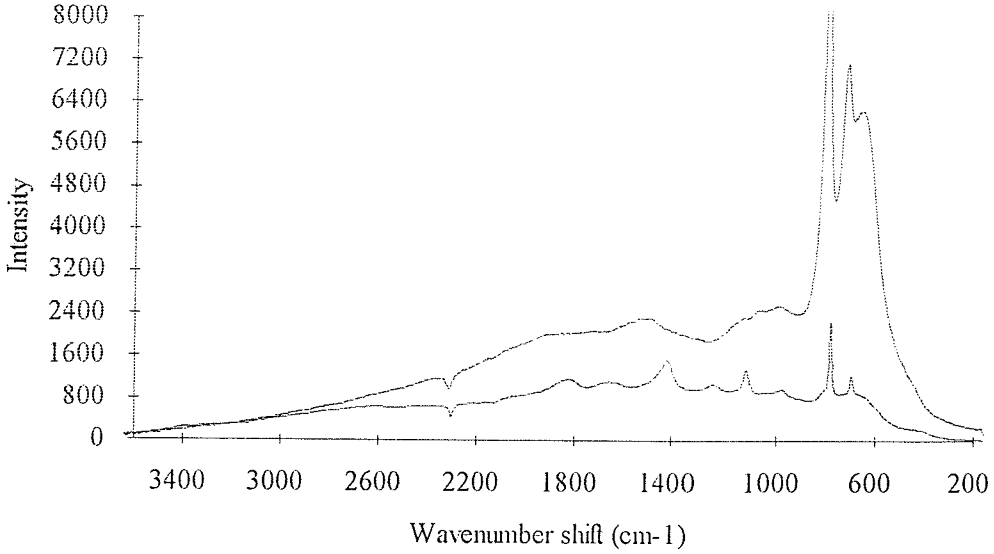

Figure 5.25 FT-Raman spectra of room-temperature and cooled monoclinic C_3S from Blue Circle.

Several new bands appear to higher shift. At first sight, there also seems to be a progression in the two strong peaks, although in fact no consistent pattern emerges. The position and relative intensity of these bands make it extremely unlikely that these are vibrational Raman features. In the absence of data on phase transitions - none is thought to occur[40] between ambient and -145°C - these are rather more likely to be luminescence bands that may only be resolved when the peaks are not broadened.

5.6 Discussion

The near-IR diffuse reflectance studies have shown that the -OH group is present in many of the cements, probably as $Ca(OH)_2$. From the results in this chapter, it seems that the appearance of two extremely strong "Raman" bands in γ-C_2S and in $Ca(OH)_2$ can be strongly correlated with the presence of $Ca(OH)_2$. This is not to say that the bands are caused by an electronic or vibrational process in pure $Ca(OH)_2$; just that the presence of calcium hydroxide seems required:

- $Ca(OH)_2$ shows the anomalous bands - the true vibrational (phonon) spectrum is known, and the anomalous bands are definitely *not* due to simple vibrational modes.

- The synthesised cement samples all show the bands - probably because they contained non-reacted CaO from the incomplete syntheses, subsequently hydrated in air to $Ca(OH)_2$.

- The supplied Blue Circle cements all show the two bands, and all show at least some $Ca(OH)_2$ absorption bands in the near-IR.

The Euroc-supplied samples did not show these features in near-IR absorption or in the FT-Raman experiment. However, the Raman bands are much broader (probably due to the higher metal ion content), which probably obscures the features of interest - and the near-IR FT spectrometer used was on the very lower limit of acceptability, in terms of sensitivity; it is designed for optimal use in the mid-IR. Thus the Euroc samples neither prove nor disprove the argument.

What is sure is simple - of all the samples that showed the anomalous two bands in the Raman spectrum, the biggest near-IR absorption and the largest Raman intensity was obtained from Blue Circle γ-C_2S. *This sample also contained the highest concentration of manganese (Mn^{2+}) by 2 orders of magnitude*.

Quite apart from being known as problematical under near-IR excitation, manganese has a "case history" of causing luminescence in $Ca(OH)_2$ under visible excitation. Previous workers also linked the luminescence to the formation of defect sites on heating.

Using the data from this chapter and the previous studies, it is tentatively proposed that the formation of calcium hydroxide on the surface of the cement grains due to the hygroscopic nature of the calcium silicates results in a disordered amorphous coating, with many structural defects, into which metal ions diffuse, become trapped at the defects, and form localised and highly luminescent electronic states.

Many further comparisons could be struck, between model compounds and the cement minerals. The danger is in becoming too simplistic in the approach, and whilst searching for simplifying comparisons branching into areas which deserve more in-depth coverage to interpret correctly. In passing, other alkali earth metal oxide and hydroxides have been observed to give erratic and bizarre Raman spectra under near-IR excitation; there is quite simply a whole area of "simple" systems which need to be re-explored to be understood.

The only real way forward in the study by FT-Raman spectroscopy of calcium silicates, and of the simpler calcium salts, lies in determining the cause of the strong and structured emission so often - but apparently unpredictably - encountered. A body of evidence has been assembled, much of it experimental, some argument by analogy, which leans heavily towards fluorescence. Given this is the most likely explanation, there are several outstanding questions.

The first question is by what mechanism does this luminescence arise - that is, is it due to intrinsic properties of the calcium silicates relating to electronic absorption in the solid state, or is it - more likely - due to impurities present in the form of one or many of the metal species revealed by analytical studies. There is evidence to suggest that it is connected with partial hydration, forming small amounts of oddly-behaved calcium hydroxide.

The second question is why does the luminescence emission have such a narrow line width, combined with a much greater amount of apparent structure, compared to the very broad and featureless fluorescence peaks most often observed in near-IR Raman spectroscopy - and why does it appear that the luminescence process is strongly affected by the level of impurity in the sample.

Although part of the answer may lie in crystal field theory and mineralogical spectroscopy, perhaps the best way to unravel the problem is by extremely pure synthesis, combined with accurate structural and compositional analysis, then to build up a body of spectroscopic data based not only on the pure calcium silicates, but also by doping these structures with the commonly-encountered impurity metals.

In order to do this requires a range of analytical methods. XRD - an often-used tool in cement analysis - provides little assistance in determining the chemical constituents, because the $Ca(OH)_2$ coating on silicate grains is thin, amorphous, and in small yield. Perhaps the best untried method for future application would be the use of calorimetric techniques DSC and TGA. These could, in principle, reveal the nature and amount of O-H present, by determining temperatures and heats of dehydration, along with mass loss on dehydration. Combined with a sensitive reflectance near-IR absorption technique, this could be a great help. The mid-IR spectra of cements contain broad and strong bands, well-overlapped in most instances - so a small signal from a small quantity of calcium hydroxide, whose bands lie in the same region, might be of little help.

On the other hand, if the current samples were to be employed in further work, determination of elemental content by X-ray fluorescence (XRF) would be a very useful additional tool, as might electron spin resonance (ESR) and magnetic susceptibility to determine the nature and number of paramagnetic cations present. As previously mentioned, DSC and TGA would be of benefit in determining degree and nature of hydration.

5.6.1 Alternative Raman techniques

The utility of FT-Raman spectroscopy is well-proven in many applications; yet the question must be asked whether near-IR FT-Raman the ideal method for solid-state inorganic species.

Data obtained using 792 nm excitation on a near-IR-optimised spectrograph (Renishaw development model System 1000) showed a combination spectrum, comprising the vibrational spectra, plus extra features seen at Raman shifts entirely unlikely to be vibrational. Figure 5.26 shows this very well for unstabilised Blue Circle β-C_2S. Contrast this with the FT-Raman data in figures 5.8 and 5.9. The Nd^{3+}:YAG-excited spectrum is almost useless, whereas the AlGaAs diode-excited spectrum has extremely clear luminescence features above 1000 cm^{-1} shift (seven Lorentzian bands) *plus* a weak but clear vibrational band near 850 cm^{-1} shift.

It should be noted that this spectrum has NOT been corrected for instrument response. This is extremely important to note, since the detector efficiency, as measured in units of quantum efficiency, is falling by *almost a factor 10* from low to high shift. This cut-off reflects the approach to the bandgap of the silicon CCD array detector used on the spectrograph. Indeed, the corrected spectrum would display a sharp *increase* in intensity at higher Raman shifts beyond 1000 nm. The luminescence bands being observed in this spectrum around 11,000 cm^{-1} (absolute) are the short-wavelength tail of the emission bands observed in the FT-Raman spectra at 8,500 cm^{-1} (absolute) - remember that emission bands alter position (with respect to the Raman shift scale) when different laser excitation sources are used for the Raman experiment.

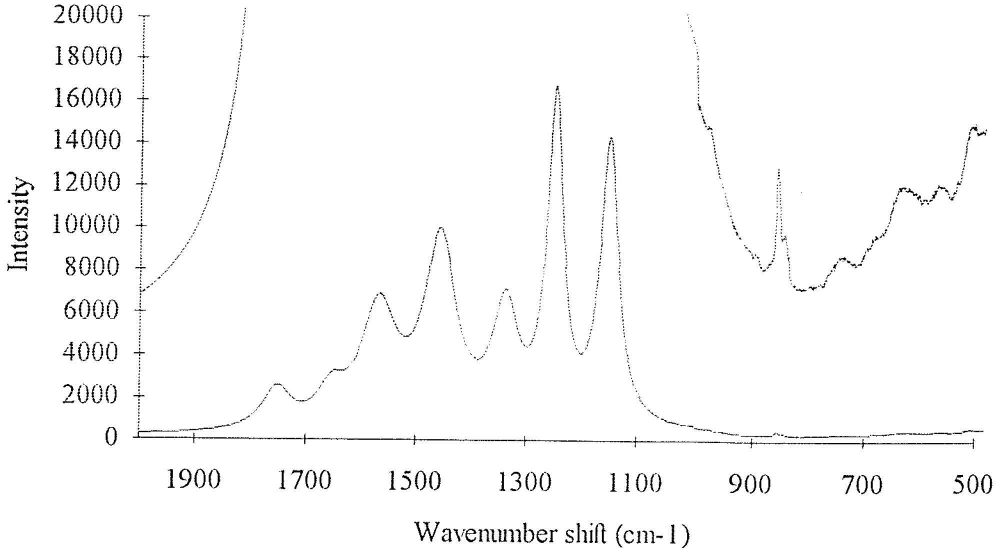

Figure 5.26 792 nm excitation of Blue Circle β-C_2S. Upper trace: x25 scale expansion. 10 seconds exposure time.

Moving back towards near-visible excitation (perhaps using 783 nm excitation from a titanium sapphire laser) is certainly possible on a FT-Raman spectrometer, providing the detector used is suitable for the scattered wavelength range (perhaps a silicon avalanche photodiode); the only questions worth debating are whether the superior performance of the CCD detector[41] renders the dispersive method more attractive, in terms of analysis time, whether the sharp cut-off in CCD performance renders the high-shift performance unattractive, and whether the redistributive effect of the FT process[42] would spread the noise from the strong luminescence bands over the weak Raman bands, making the FT technique less attractive.

From the above data, it seems that use of shorter-still wavelengths would avoid overlaying the fluorescence emission around 1 μm and the Raman spectrum. Although the "mixed" nature of the 792 nm data - Raman plus luminescence - might prove useful in identifying the luminescent centre, 792 nm was not ideal, as the luminescence was still too strong at 792 nm for some samples strongly luminescent at 1064 nm - for instance, γ-C_2S gave a very strong fluorescence background.

Two points about avoiding luminescence should be remembered. Even if luminescence occurs, it might be possible to record data close to the excitation wavelength if the *luminescence* is considerably red-shifted. The spectrum excited at Ar^+ green (514.5 nm) of the same unstabilised Blue Circle β-C_2S (figure 5.27) is a fine example. It shows that the emission at around 1000 nm is simply not detected when the excitation is near 19, 400 cm^{-1} and the Raman scattering falls out to about 18, 300 cm^{-1}, or about 550 nm.

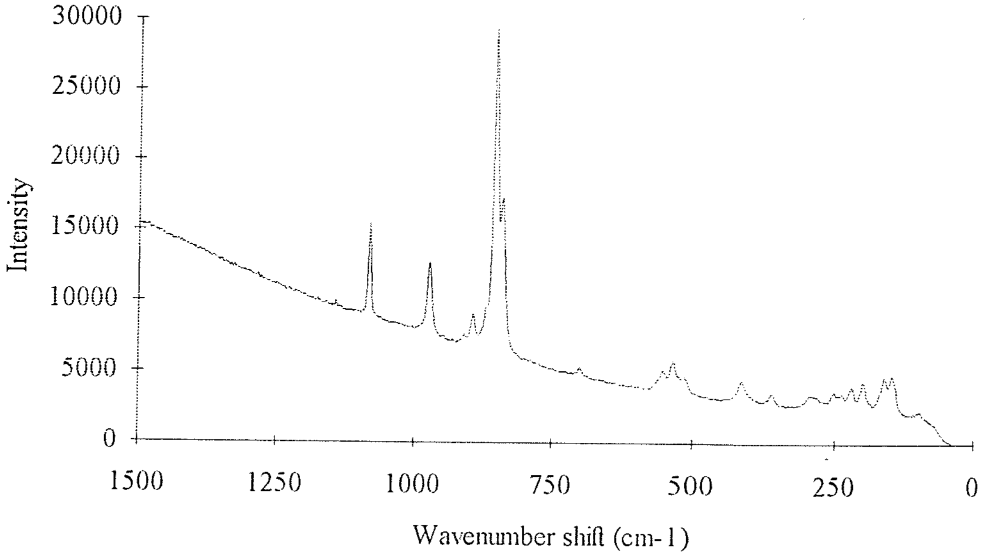

Figure 5.27 Ar$^+$ excitation of Blue Circle β-C_2S.

Luminescence may even be excited by "stray" light, as noticed during this study and confirmed by the recent literature[24]. Raman scattering from γ-C_2S excited with near-IR radiation was obliterated by luminescence caused by the HeNe reference laser; although well-shifted from the YAG laser (by nearly 6000 cm^{-1}), it still resulted in luminescence in the 1-2 μm region of interest to near-IR FT-Raman spectroscopy.

Figure 5.28 shows a conventional spectrum of Blue Circle β-C_2S recorded using HeNe (632.8 nm) excitation which reinforces the point. The spectrum presented here is a true vibrational spectrum; the luminescence occurs above 900 nm (see figure 5.26) and so does not obscure the Raman scattering, which occurs below 750 nm.

As an aside: it is always be possible in principle to record a Raman spectrum encompassing both the Stokes and anti-Stokes bands, to confirm that the observed spectra are indeed caused by Raman scattering. Band positions in luminescence are rarely "mirror-image" about the laser line.

In short, the spectral quality and information content could not be in greater contrast to the FT-Raman spectra. All the samples gave good vibrational spectra - and in further study, this was even true of industrially-prepared cements[43].

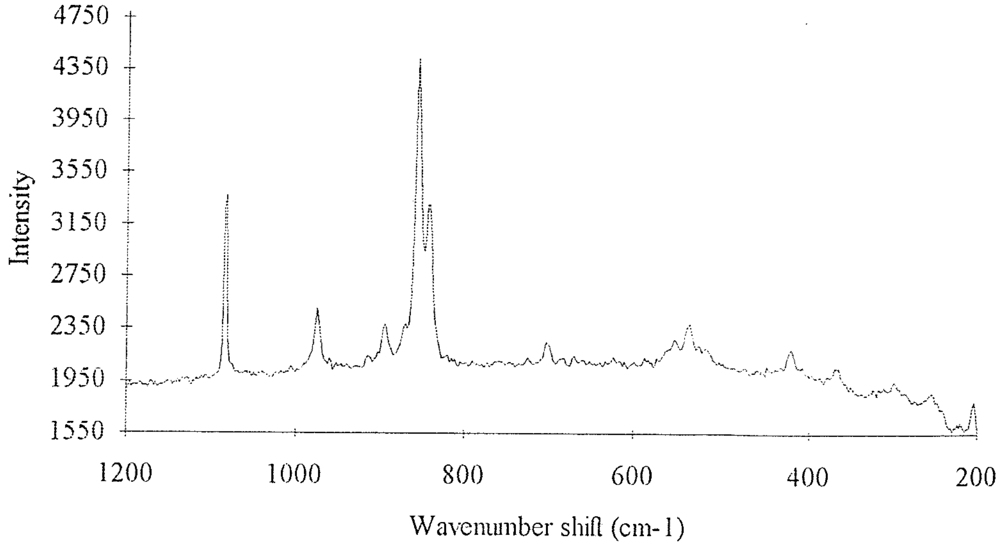

Figure 5.28 HeNe excitation of Blue Circle β-C_2S.

5.7 Postscript

As mentioned in the text, several researchers have recently endorsed the outcome of the findings in this chapter on the luminescence of certain calcium silicates[24]. However, Griffiths and co-workers have shown that FT-Raman spectroscopy has a new part to play, reporting excellent spectra from many deeply-coloured minerals[44]. It is clear that this particular field is ripe for further investigation.

5.8 References

1. F.M. Lea, "The chemistry of cement and concrete", Chemical Publishing Co. Inc., New York (1971)
2. R.H. Bogue, "The chemistry of Portland cements", 2nd edition, Reinland publishing Inc, NY (1955)
3. W. Eitel, "The physical chemistry of the silicates", University of Chicago press, (1954)
4. W. Eitel, "Silicate Science", Volumes 1-8 (Academic Press, 1964-1976)
5. P.F. McMillan and A.M. Hofmeister, Rev. Mineral. 18, 99 (1988)
6. J. Bensted, Cement Technology, page 161 ff, (Sept/Oct 1975)
7. J. Bensted, J. Am. Ceram. Soc. 59 (3-4), 140 (1976)

8. K. Nakamoto, "Infrared and Raman spectra of inorganic and coordination compounds", 4th Ed. (Wiley Interscience, 1986)
9. M. Conjeaud and H. Boyer, Cement and Concrete Research 10 (1), 61 (1980)
10. G. Placzek, "The Rayleigh and Raman scattering", UCRL Trans. No. 526 (L) (1959)
11. J.A. Koningstein, "Introduction to the theory of the Raman effect", (Reidel Publishing Co., 1972)
12. J. Tang and A.C. Albrecht, J. Chem. Phys. 49 (3), 1144 (1968)
13. W.P.Griffith, Nature, 224 264 (1969)
14. W.P. Griffith, J. Chem. Soc (A) 1372 (1969)
15. W.P. Griffith, Ch.8 in "The infrared spectra of minerals" Mineralogical Society monograph 4, Ed. V.C. Farmer, Mineralogical Society (1974)
16. A. Wang, J. Han, L. Guo, J. Yu, and P. Zeng, Appl. Spectrosc. 48(8), 959, (1994)
17. C.J. Petty, G.M. Warnes, P.J. Hendra and M. Judkins, Spectrochim. Acta 47A (9/10), 1179-1188 (1991)
18. F.A. Cotton and G. Wilkinson, "Advanced Inorganic Chemistry" 4th Ed., Wiley Interscience (1980).
19. J. Bensted, Cement and Concrete Research, 7, 161-164 (1977)
20. A. Crookell, P.J. Hendra, H.M. Mould, and A.J. Turner, J.Raman Spectrosc. 21, 85 (1990)
21. B. Schrader, Fres. J. Anal. Chem. 337, 824 (1990)
22. M.J. Almond, C.A. Yates, R.H. Orrin, and D.A. Rice, Spectrochim. Acta 46A (2) 177 (1990)
23. T.N. Day, P.J. Hendra, A.J. Rest, and A.J. Rowlands, Spectrochim. Acta 47A (9/10) 1251 (1991)
24. E.L. Varetti and E.J. Baran, Appl. Spectrosc. 48(8), 1028 (1994)
25. G. Walker, Ch.4 in "Bonding and Spectroscopy in mineral chemistry", Eds. F.J. Berry and D.J. Vaughan, Chapman and Hall
26. A. Mortensen, D.H. Christensen, O. Faurskov Nielsen, and E. Pedersen, J. Raman Spectrosc. 22, 47 (1991)
27. M.C. Tobin and T. Bååk, J. Opt. Soc. Am. 60, 368 (1970)
28. S.M. Shapiro, D.C. O'Shea, and H.Z. Cummins, Phys. Rev. Lett. 19, 361 (1967)
29. W. Forsling, private communication
30. A. Russell, private communication

31. J.B. Norman, K.J. Cross, H.S. Schweda, M. Polak, and R.W. Field, Mol. Phys. 66, 235 (1989)
32. S. Bhagavantam and T. Venkatarayudu, "Theory of groups and its application to physical problems", Academic Press (1969)
33. M.M. Sushchinskii, "Raman spectra of molecules and crystals" Israel Program for Scientific Translations (1972)
34. R. Loudon, Adv. Phys. 13, 423 (1964)
35. M. Voisin and J.P. Mon, Phys. Stat. Sol. B48, K185 (1971)
36. K.H. Rieder, B.A. Weinstein, M. Cardona, and H. Bilz, Phys. Rev. B8, 4780 (1973)
37. P. Dawson, C.D. Hadfield, and G.R. Wilkinson, J. Phys. Chem. Solids 34, 1217 (1973)
38. O. Chaix-Pluchery, J.C. Niepce, B. Jannot, and G. Martinez, J. Solid State Chem. 73, 563 (1988)
39. O. Chaix-Pluchery, J.C. Niepce, and G. Martinez, J. Mater. Sci. Lett. 6, 1231 (1987)
40. V. Ronin, private communication
41. J.E. Pemberton, R.L. Sobocinski, M.A. Bryant, and D.A. Carter, Spectroscopy 5 (3) 26 (1990).
42. a) J.W. Brault, Chapter 3 in "High resolution in astronomy" (Eds. Booth, Brault, and Labeyrie) 15th Advanced Course, SAAS-FEE (1985)
    b) J. Chamberlain, "The principles of interferometric spectroscopy" (Eds. Chantry and Stone) (Wiley, 1979)
43. Renishaw Application Note.
44. E.E. Coleyshaw, W.P. Griffith, and R.J. Bowell, Spectrochim. Acta 50A (11) 1909 (1994)

Chapter 6 :

Near-IR excited Raman scattering in the gas phase

6.1 Overview and historical introduction

Raman spectroscopy can play an important role in both fundamental and applied gas-phase research. The various techniques available provide methods to determine the identity and structure of gaseous species, as well as the composition of gas-phase mixtures. In certain cases, Raman spectroscopy is the only way to obtain vibrational or rovibrational information[1]; more usually, it helps build a more complete understanding of a gas-phase structure, when used in conjunction with other methods[2].

The intensity ratio of the Raman scattering to light at the laser wavelength (Rayleigh scattering, stray light, and reflection) in the gas phase tends to be ***higher*** (1:1000) than for liquid or solid samples, as suspended particulate matter and multiple reflections from the sample contribute far less to the Rayleigh component. This means in many cases that the gas-phase experiment can be carried out *without* triple-grating spectrometers (operating with additive dispersion) or triple-grating spectrographs (single spectrograph with double-grating subtractive-dispersion forestage). Double monochromators and single spectrographs are often adequate for the task, providing care is taken with stray light and providing low-wavenumber coverage (<100 cm^{-1}) is not required. The reduced optical complexity of these instruments allows straightforward accurate alignment, as well as offering fewer optical surfaces and therefore higher efficiency.

Significant advances were made during the 1930s with arc-lamp excitation and prism-based spectrometers[3]. However, the advent of the laser and the development of the scanning spectrometer with direct photoelectric recording made the technique much easier[4], and began a phase of renewed interest in gas-phase research. As improvements in instrumentation made higher-sensitivity measurements possible, so the partial pressure of the analyte mixtures decreased, whilst high resolution was also demanded[5,6].

The signal level in the gas phase experiment is very low. The intensity is directly proportional to the number of scattering species illuminated within the spectrometer field of view, so it is easy to appreciate that the experiment yields far lower signal levels than those due to liquids or solids, and that very sensitive detection is required. Scanning spectrometers often employ cooled photon-counting photomultiplier tubes (PMTs), whilst spectrographs (originally using photographic plates) moved on with the introduction of the intensified diode array (IDA) and more recently the charge-coupled device (CCD) camera array.

6.2 Aims and goals

It should be clear that the instrumentation used for gas-phase Raman research has to be of the highest quality and properly maintained. High-luminosity, low-loss spectrometers matched to sensitive detectors, with powerful excitation sources and carefully-designed high-efficiency sampling arrangements are pre-eminent. This accurately portrays the state of *gas-phase linear** Raman spectrometry at the present day. *Routine* Raman scattering experiments on gases should only be contemplated with conventional grating-based dispersive instruments using near-UV or visible excitation, and either photon-counting PMT or CCD detection.

Since 1987, FT-Raman spectroscopy has been ascendant for analytical Raman applications. Without exception, the major manufacturers of FT-IR spectrometers either offer near-IR Raman accessories or dedicated stand-alone FT-Raman systems. The majority of these instruments are being used primarily for analytical vibrational spectroscopy.

The owner of a FT-IR/Raman spectrometer may *occasionally* require to analyse gaseous samples. The aim of this work was simple - to demonstrate feasibility of a routine gas analysis cell in a commercial spectrometer for analytical purposes.

On a more fundamental level, there are a number of gases that have remained a challenge to visible Raman techniques. Chief amongst these is nitrogen dioxide (NO_2) as this species fluoresces very strongly under visible excitation as a result of strongly overlapped low-lying electronic absorption bands. Gas-phase Raman spectroscopy has proved extremely difficult; more frustratingly, the study of the dimer dinitrogen tetroxide (N_2O_4) in the gas-phase, close to dissociation, has been exceedingly difficult as well (no results published) due to fluorescence from the monomer NO_2 with which it exists in equilibrium. Near-IR excitation may offer the first results on the gas-phase Raman spectrum of the dimer.

---

* This discussion ignores the role of coherent Raman scattering, produced via higher-order terms in the molecular scattering tensor, which require quite different techniques.

6.3 Initial considerations

Several fundamental factors weigh heavily against the FT technique and should be discussed in relation to gas-phase methods, despite having been touched upon in earlier chapters:

- Most gases have well-defined (and well-documented) electronic structure. The majority lack broad absorption bands, and tend not to fluoresce - a notable exception being nitrogen dioxide, which is dark brown. This immediately neuters the argument that FT-Raman is the superior analytical Raman method on grounds of fluorescence-minimisation.
  Its also implies that even if the excitation wavelength inadvertently coincides with an absorption - remembering the linewidth of gaseous absorption spectra is very low - then the laser may (in principle) be tuned away from resonance in accordance with the literature.

- The intensity of the scattered radiation follows the well-known relationship that the total power radiated is proportional to $(\lambda_{scattered})^{-4}$. A *relative decrease* in overall scattered intensity of approximately *23-fold* occurs on lengthening the excitation wavelength from Ar^+ blue at 488 nm to Nd^{3+}:YAG at 1064 nm, for a rotational Raman line at $+100\ cm^{-1}$ shift.

- The detectivity of the two most commonly-used near-IR photodetector systems leave much to be desired when compared to the systems available in the visible. In the visible region PMTs, CCDs and IDAs provide detectivity that makes spectroscopy limited by the shot-noise* of the Raman signal routinely feasible. The same is simply not true of the Ge and InGaAs photoelements and arrays available for near-IR spectroscopy. This is partly a fundamental limitation of the materials, and partly the processing electronics. Devices based on these last two detector materials suffer in comparison because the signal powers required to generate a S:N ratio of 1:1 are at least 100 times *higher* than the comparable visible detection systems even for the highest quality near-IR detector elements with the best possible associated electronics[7].

---

* Shot noise occurs whenever the measured process involves measurement of the random, uncorrelated movement of quantised species (photons arriving at a detector, electrons moving across a transistor junction, etc.).

Counterbalancing in some part these severe disadvantages is Jacquinot advantage. Briefly restated:

- *"The throughput of an interferometric spectrometer-as measured by the product of limiting solid angle with limiting cross-sectional area-tends to be 30-300 times higher than for a grating spectrometer* ***of the same resolving power.****"*

In the near-IR it has been estimated[8] that this benefit is of the order of 200 times.

6.4 Previous work

Although limited, a small amount of interferometric gas-phase and near-IR-excited gas-phase work has been carried out.

- *Non-near-IR interferometric studies* - the most interesting pre-FT-Raman work was carried out using a stellar observation interferometer at the Kitts Peak National Observatory in the United States during the mid-1980s. This spectrometer is a purpose-designed visible Fourier transform spectrometer (FTS), employing a complex arrangement of "Cats Eyes" retroreflectors and multiple beamsplitters & recombiners[9]. It operates under vacuum, and utilises either one or two PMT detectors, dependant on whether the spectrometer is operated in double-output or double-passed mode. It is a fine example of a 1-meter optical path difference (OPD) Connes-type interferometer[10], and could never be described as well-suited to routine analytical methods.

  Sample pressures were typically just below atmospheric, whilst scan times were typically 3-6 hours for good (>150:1) S:N at 0.1 cm^{-1} resolution. The Raman spectra were excited using Ar^+ blue (488 nm) and green (514 nm) lines. Eight simple gases were studied[11] for both rotational and rovibrational detail, whilst higher-resolution data was also recorded[12] on D_2, as well as the rotational Raman spectra of H_2 and D_2 in flames[13]. The authors found little to dissuade them from the technique, apart from the difficulty in rejecting the light at the excitation wavelength without obscuring the Raman scattering. The authors were certainly more optimistic in their assessment of the possibilities for FT-Raman than were Schildkraut and Hirschfeld, in their original article on the method[14].

- *Fabry-Perot Interferometry* - an ingenious use of a Fabry-Perot interferometer (FPI) briefly saw cross-over from atomic vapour emission spectroscopy during the early 1970s[15-17]. This device may functions as a very narrow passband wavelength-recursive filter (etalon)[16], or as a high-throughput high-resolution interferometer (scanning FPI)[17]. The additional resolution (< 0.01 cm^{-1}) available by this method is greatly advantageous in resolving out the complexity of bands in the rotational spectrum of even the simplest gas mixture, and therefore has a greater claim as an analytical device. However, the scanning FPI is difficult to align and to stabilise, whilst the etalon requires following with a low-dispersion spectrograph to overcome the coalescence of the individual interference fringe patterns. It proved possible to achieve satisfactory laser line rejection without pre-filtering.

- *Near-IR non-interferometric studies* - one example of this area is available in the literature[18], where a double-grating additive-dispersion spectrometer was optimised for the near-IR, and equipped with a cooled Ge photodiode detector using a phase-sensitive "lock-in" detection technique. Excitation was provided by a Nd^{3+}:YAG laser at 1064 nm with prism pre-filtering. Good S:N data was acquired, albeit at the expense of very high (<10 W) excitation power and reasonably low (3 cm^{-1}) spectral resolution. However, bands close (20-30 cm^{-1}) to the Rayleigh line could be detected quite easily with this spectrometer, with both Stokes and anti-Stokes data available.

6.5 Results

Figure 6.1 shows the spectrum of air obtained on the prototype PE 1700 series FT-Raman spectrometer, simply observing the empty sample position.

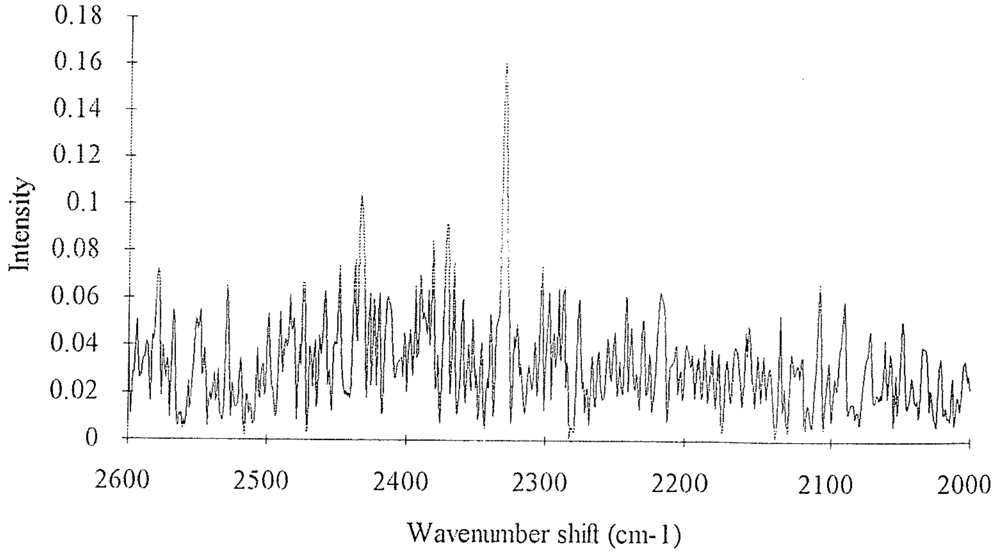

Figure 6.1 Spectrum of air with no cell.

This data (the N_2 vibrational line at 2331 cm^{-1}) was obtained after co-adding 400 spectra at 4 cm^{-1} resolution using 2.5 W excitation power. S:N is 3:1 at best, achieved in almost exactly 1 hour.

In order to realise better quality data it is patently obvious that it is necessary to collect more Raman scattered light. The simplest way to achieve this is to increase the effective power density at the focus of the spectrometer - and the most successful way of achieving this is to multipass the laser beam through the viewed spot. Simply increasing the laser power is often practical - the two methods are sometimes combined.

In conventional gas-phase experiments, increasing the brightness in the viewed patch is most often achieved in one of three ways. These arrangements are illustrated in figure 6.2, and several references serve as excellent introductions[19-24]:

- *The confocal-resonator or spherical-cavity cell.* The laser is injected off-axis into a confocal resonator, comprising (a)spheric reflecting surfaces or lens/mirror combinations, and subsequently traverses the centre focal spot a number of times determined by the exact geometry. A high-aperture collecting mirror focuses the scattered light back to the focal point; the spectrometer optics also view this point.

- *The intracavity cell.* This takes advantage of the much higher intensity inside the cavity, although problems in alignment and more fundamental issues involving which lasing transition(s) and mode(s) dominate often render the intra-cavity method difficult to optimise. Any misalignment drastically reduces the power available, as it directly affects the lasing of the device - the alignment is very critical.

- *The external resonator.* This is an arrangement which appears half way between the first two solutions. After the output-coupling (less reflective) front mirror of the laser cavity an anti-reflection coated lens is introduced to focus the beam into the gas cell, then a spherical mirror used to refocus the diverging beam. The gas cell windows need to be anti-reflection coated, or preferably Brewster-angled to minimise reflection. This results in a higher power than available directly after the output coupler, with consequential gain in power in the cell, because the effective end of the laser cavity is now the "return" spherical mirror. This set-up is much less difficult to align - and the laser still functions when the external cell is misaligned slightly.

The major problem is that all of these designs are optimised for the 90° scattering geometry, and are difficult to adapt to any other. For reasons involving the much greater ease of alignment inherent to "backscattering" (180°) collection, 90° collection is not used on most commercial FT-Raman spectrometers; since the laser and spectrometer are in theory focused at the same point in space for the backscattering method, three degrees of freedom and complexity are removed from the alignment. Some commercial FT-Raman spectrometers now include the 90° collection geometry for certain polarisation measurements.

Rather than try to adapt a multipass cell, it was decided to construct a multireflection cell especially for the backscattering experiment, to retain the ease of alignment. The solution was to use a "lightpipe" from a gas chromatograph (GC) IR spectrometer accessory as the basis for the cell design*. The cell would be aligned colinearly with the instrument optical axis, and the laser focused tightly into one end.

The lightpipe is essentially a glass tube of external diameter 1 cm and internal bore 1 mm that has been metallicised internally. The metal of choice in the near-IR is gold, as it has a high (>98 %) reflectivity over the 1-2 μm wavelength range.

One of the major problems associated with this approach is the development expense. Perkin Elmer (UK) Ltd kindly supplied free-of-charge several lightpipes from GC/IR spectrometers that had been damaged in transit.

---

* Bruker GmbH have patented a long pathlength liquid cell to similar design[25].

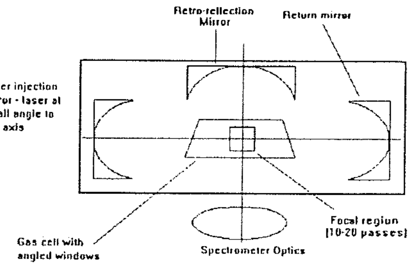

i) Confocal resonator.

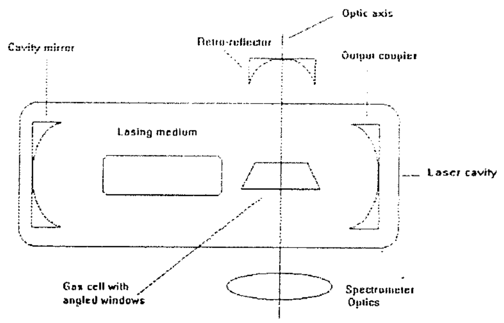

ii) Intracavity cell.

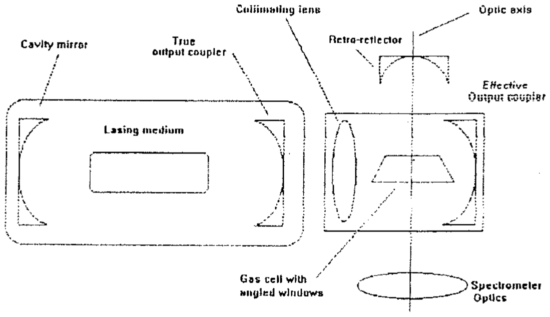

iii) External resonator.

Figure 6.2 Various classical gas cell geometries.

However, towards the end of the project Mr Mike Caplin of the Glassblowing workshop in Department of Chemistry discovered a method to produce lightpipes of essentially the same quality on a routine basis "in-house". This enabled a range of bore sizes to be examined, as well as for the optimum length to be determined. The plate thickness in these tubes was a little higher than the commercial tubing and estimated by Mr Caplin to be around 5 µm. The process used in producing the commercial tubing was not disclosed; however, it was probably similar to the method used for the "in-house" tubes, involving a "Bright Gold" colloidal emulsion from Johnson-Matthey PLC which is applied and then fired at 600 °C to drive off the organic material.

The use of standard silvering solution was tried and discarded, as the metallic coating is on the interfacial side - in other words, the exposed side of the tube had a thick layer of crystalline deposit, which fluoresced badly and reflected poorly.

Figure 6.3 shows the spectrum obtained under identical collection conditions to figure 6.1 - except that a 95 mm length 1.3 mm diameter lightpipe was used.

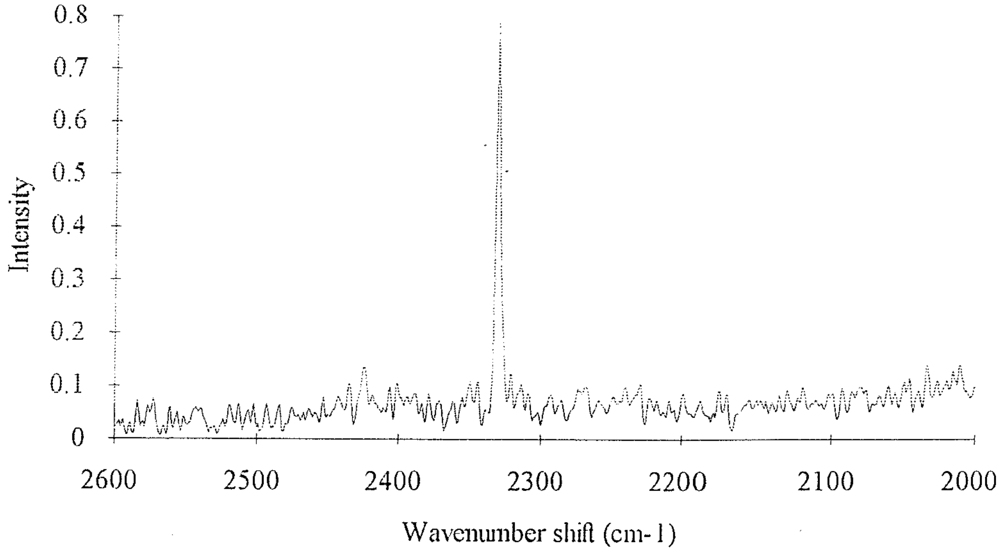

Figure 6.3 The enhancement of the signal by use of GC/IR lightpipe.

In terms of band area, *the increase in signal is x10*. Band area is a more reliable and less subjective estimate of relative performances than band height or S:N ratio where small signals are to be compared. An order of magnitude is an important gain in sensitivity.

The gas cell / spectrometer combinations used for each phase of the project were quite different. The first two gas cells were designed for use on the PE 1720 development prototype spectrometer. The first of these was designed to be demountable on a standard 3" x 2" accessory card. Although the second design was also demountable, it was held in a specially-designed baseplate/sample stage. The advantage of the standard accessory approach is that changeover from gas-phase to other studies remains an easy operation. However, the focusing reproducibility of the first approach was poor, and so results were very difficult to reproduce. In addition, filling required the use of a small vacuum line - the cell was be evacuated, then a flask containing either a gas or a liquid with high vapour pressure connected to the gas line and the cell opened to admit the gas.

The overall size of the cell and the bulky gas-handling facilities were perfectly acceptable for use in the laser laboratory, where open sampling arrangements did not contravene laser safety regulations, but for analytical systems the design was inappropriate. In order to satisfy the analytical requirements, a third system based upon a demountable cradle was designed. This cradle accepted a jig for alignment purposes as well as the cell itself. The gas handling fittings were more rudimentary on this cell, but demonstrated the feasibility of the cell. The cradle fitted directly to the much-improved sample area baseplate of the PE 1760X commercial spectrometer, and combined good reproducibility with ease of fitting. The only outstanding issue on this cell was the need to devise some method of adjusting the positioning of the cell with the sample area closed. The cell itself is shown below in figures 6.4 & 6.5 - notice that although this cell was simpler to fill directly from stock cylinders, no vacuum line fittings were incorporated.

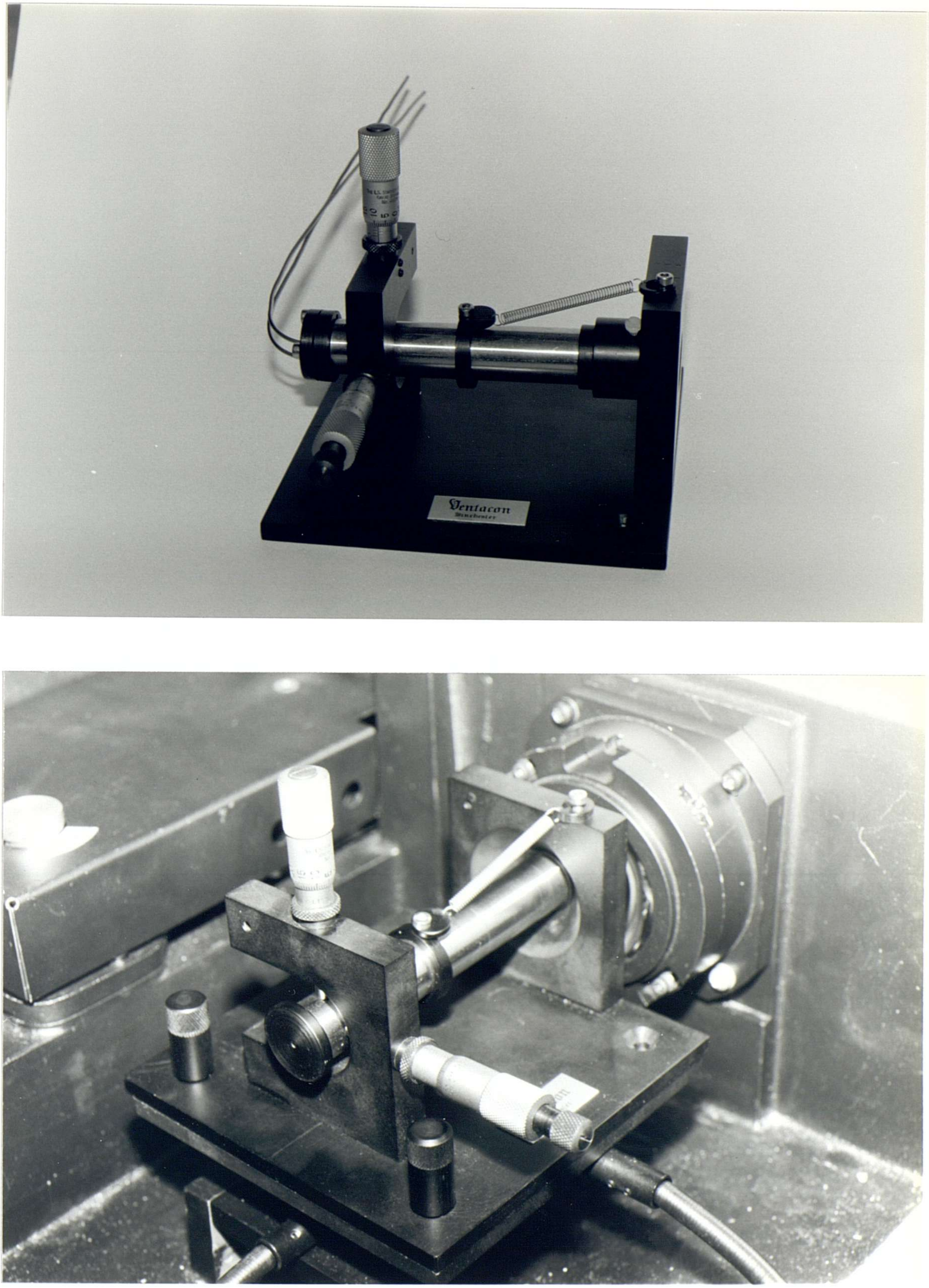

Figures 6.4 & 6.5 Final design of gas cell for commercial PE 1700 series spectrometer.

6.5.1 Studies using the prototype cells and spectrometer

6.5.1.1 Background reduction by spatial filtering

The first cell gave encouraging results, considering the crudity of the approach. The spectrum of N_2 shown in figure 6.6 indicates that reasonable S:N could be expected given an accumulation period a little under 4 hours and laser power 2.5-3.0 W.

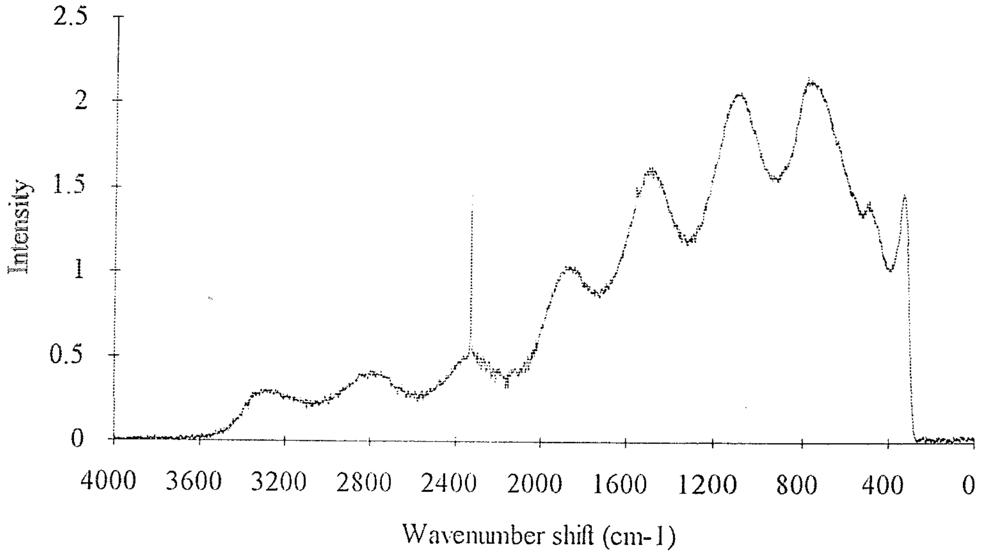

Figure 6.6 Spectrum of air collected using gas cell on prototype spectrometer.

The most obvious problem is that of a very strong non-Raman background. It obscures weak features, and raises the noise level over the entire spectrum, due to the shot noise associated with the background being distributed throughout the spectrum by the Fourier transformation process. When the total signal level (spectrum plus background) is very high then even FT-Raman spectrometers with "noisy" detectors become shot-noise limited - simply because the shot noise from such large signals is very high.

Since the background was not due to the gas, it must be from the cell. In this design of cell, the front window was a small piece of "swarf" glass approximately 100 μm thick. Such glass is left-over when pieces of equipment are blown in the glass shop, and this particular piece of swarf was part of the Young's tap assembly used to fill the cell on the gas line.

The window was the obvious first choice, being closest to the focal region and from a contaminated environment. Focusing onto the front window certainly gave a spectrum with background - although several orders of magnitude *less* than the spectrum in figure 6.6; this implies that the background is a function of the cell *body*, and not the window - either the gold coating, an adsorbed species, or the glass.

The latter turned out to be the case. Laser light was leaking through microscopic holes in the gold coating, and exciting fluorescence in the glass. The leakage of the laser light could be seen quite easily with the aid of a near-IR viewing camera; when a 5 mW HeNe laser was shone along the bore axis, the red (633 nm) light was clearly (albeit weakly) visible to the naked eye. The homogeneity of the layer was obviously questionable. The fluorescence was either escaping back through the holes and reflecting into the focal region, or reflecting along inside the body of the tube above the gold and emerging into the focal region through the front face.

To prevent this, several front face masks were evaluated. The simplest method (an iris) proved difficult to align reproducibly, whilst the idea of a cap was not feasible because the cell end was not flat; a pronounced ridge existed where the swarf had been stamped onto the lightpipe to form the window, preventing a stable fit. Even in the cases where a mask or iris could be positioned reasonably, alignment drifts invariably led to the laser clipping the mask with a resulting thermal emission background.

As an alternative, coating the front face seemed to present few problems. However, gold leaf simply peeled too quickly, and was difficult to size correctly; black enamel paint proved difficult to spread uniformly over the cell end without also impinging into the tube bore.

A more elegant method was devised. The development spectrometer foreoptics demagnify the image of the J-stop by a factor x6. So, if the J-stop were set to 8 mm diameter, the viewed patch at the sample from which light would be collected *and processed* would be 1.33 mm diameter. This is just fractionally greater than the bore diameter of the Perkin Elmer lightpipe, hence the J-stop size could be reduced *to only image the area of the bore itself.* Using a relationship derived from chapter 1:

$$\Delta\nu = \nu_{abs}\cdot(r_{stop})^2/2(f_{coll})^2$$

to relate resolution ($\Delta\nu$ in cm^{-1}), absolute wavenumber (ν_{abs} in cm^{-1}), J-stop radius (r_{stop} in mm) and focal length of collimating optic (f_{coll} in mm), spectral resolution at a Raman shift of 1400 cm^{-1} from 1064 nm would be of 0.5 cm^{-1} and give a viewed patch size of 0.48 mm if the J-stop were 2.8 mm in diameter.

More importantly - since the spectrometer would be sampling from the centre of the bore a reduction in fluorescence would be seen because the fluorescence escaping through the front face of the cell would be spatially filtered by the J-stop.

6.5.1.2 Methyl bromide spectra

This is shown spectacularly in figure 6.7 below. Both spectra are of methyl bromide (CH_3Br) at 760 Torr; the upper trace was recorded at 4 cm^{-1} instrumental resolution with a 4 mm diameter J-stop, whilst the lower used 0.5 cm^{-1} and 2.8 mm diameter J-stop. It must be emphasised that no spectral subtraction or manipulation of any sort has been carried out on these data.

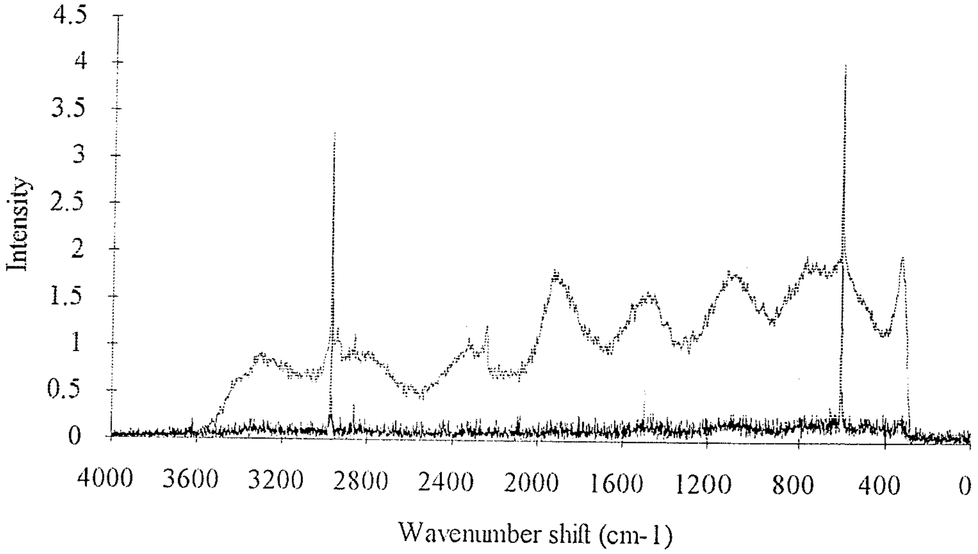

Figure 6.7 Effect of J-stop size on background level of methyl bromide spectra - upper trace, 4 mm J-stop, lower trace 2.8 mm.

Two problems potentially arise from this approach. The first is the laser spot size. It is conceivable that the sampled spot may be smaller than the illuminated region, which is quite straightforwardly inefficient. The relationship of spot diameter (d_{spot}) to focal length (f_{lens}) and laser wavelength (λ_{las}) is:

$$d_{spot} = 4.f_{lens}.\lambda_{las}/\pi.w_0$$

where w_0 is the original beam waist diameter. Since we also have

$$w_0=4.\lambda_{las}/\pi.\Theta_{full}$$

where Θ_{full} is the full divergence angle of the beam, we are lead to the most general expression applicable:

$$d_{spot} = f_{lens} \cdot \Theta_{full}$$

For our system $f_{lens} = 160$ mm, whilst $\Theta_{full} = 2$ mrad. Therefore, the laser spot size is 0.32 mm, well under the 0.48 mm viewed patch size.

The second problem is the reduction in throughput on closing down the entrance aperture. The background signal component was strongest with large J-stop - unsurprising if the edges of the 1.3 mm diameter lightpipe were "glowing". However, closing the J-stop resulted in useful signal from the bore also being discarded - as this was no longer admitted to the spectrometer. The ratio of the transmitted intensities is simply the ratio of the aperture areas, so we have $(d'/d)^2 = (\Delta v'/\Delta v)$. In other words, if we change from a 4 mm diameter aperture to a 2.8 mm aperture, we reduce the light throughput by x2. Put another way, we would have to collect x4 as many accumulations to generate equal S:N. The reduction in throughput can be verified by measuring the integrated band areas, with J-stop at 4 mm and 2.8 mm - the agreement with simple theory was good (18.2/9.7 = 1.9).

However, this last point neglects another effect on changing the J-stop size - the change in aspect ratio (the height:width ratio of the band) on increasing the resolution. Since S:N is generally a subjective assessment of peak-to-peak amplitude at a Raman band position versus peak-to-peak noise amplitude in a nearby region free from signal other than a baseline of similar magnitude, the apparent S:N remains approximately the same on changing resolution.

Two aspects of the spectra in figure 6.7 are of interest. The C-H stretch at 2973.5 cm^{-1} in the low-resolution shifts up to 2973 cm^{-1} in the high-resolution spectrum, as does the C-Br stretch at 611 and 612 cm^{-1} respectively. This is purely systematic J-stop error as discussed in chapter 1. The second point is that even at high resolution the effect of the 50.5:49.5 ^{79}Br:^{81}Br isotope splitting is not visible on the band. This could be due to a combination of large natural linewidth with mass effects. During the C-Br stretch, the Br- atom moves remarkably little in comparison to the CH_3- fragment, due to the six-fold higher mass of the Br- atom. It should be noted that the limiting resolution on a PE series 1700 spectrometer is 0.5 cm^{-1}, which results in these experiments being spectrometer-resolution limited, and not laser-linewidth limited*, since Spectron 301 and 501 series YAG lasers have a linewidth of around 0.05 cm^{-1}.

6.5.1.3 Chlorine isotopic splitting

Chlorine (Cl_2) gives a fine example of an isotopic splitting requiring relatively low resolution to observe. The spectrum shown in figure 6.8 required 800 accumulations at 1 cm^{-1} resolution with a 2.8 mm diameter J-stop and 3 Watts excitation. Despite the very high background, two bands at 555.5 and 548.0 cm^{-1} are clearly visible.

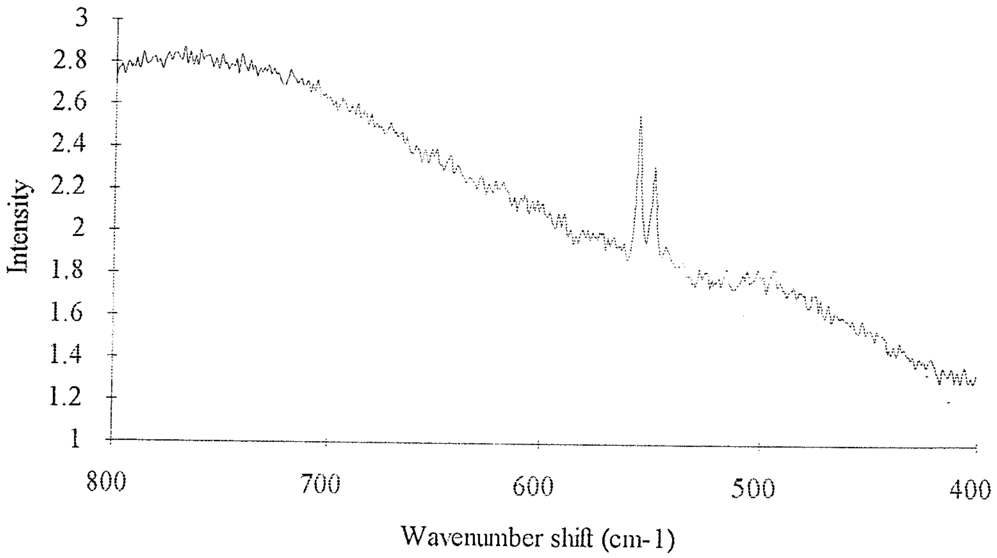

Figure 6.8 Chlorine isotopic splitting

If the simple theory of simple harmonic oscillators is to be believed, then the frequency difference between the $^{37}Cl^{37}Cl$, $^{37}Cl^{35}Cl$, and $^{35}Cl^{35}Cl$ should be simple to predict. The bond force constant k_{vib} should remain constant for all isotopomers of the diatomic species **A-B**, and then use the equation

$$\nu_{vib} = (k_{vib}/\mu)^{1/2}/2\pi$$

where

$$1/\mu = 1/RAM_A + 1/RAM_B$$

---

* NB: Our paper in The Analyst (Appendix 1) incorrectly stated the opposite to be true; this point has been confirmed with Spectron Ltd.

In this equation RAM stands for relative atomic mass, and has units Kg/mol. Using these equations, and knowing the two isotopes of Cl have relative atomic mass (in g/mol) 35 and 37 respectively:

$$\nu^{37:37}/\nu^{37:35} = \sqrt{70/72}$$
$$\nu^{37:35}/\nu^{35:35} = \sqrt{72/74}$$
$$\nu^{37:37}/\nu^{35:35} = \sqrt{70/74}$$

Since the relative abundance ^{35}Cl:^{37}Cl is 75.5:24.5, a 1:6:9 isotopic pattern for the intensities should be observed, assuming in the usual way that scattering efficiency is not influenced by isotopic mass.

It is clear that the two bands are due to the $^{37}Cl^{35}Cl$ and $^{35}Cl^{35}Cl$ isotopomers, and that the highest-mass, lowest-abundance species is unresolvable at this S:N level. The splitting of the bands (7.5 cm^{-1}) agrees with the predicted splitting (7.6 cm^{-1}) using the theory above and is in agreement with the value[26] for liquid Cl_2 (7.4 cm^{-1}) whilst the integrated band area ratio is 0.83 - predicted to be 0.67 by simple theory. The gas-phase band position for the fundamental transition is in good agreement with the literature value (554.9 cm^{-1})[27].

Alternate explanations that the weaker band is the "hot-band" transition of the most abundant isotopomer can be discounted, because the intensity ratio would be 0.05-0.10 at room temperature; a ratio of 0.67 would imply a sample temperature in excess of 700 °C by simple Boltzmann statistics. Also, previous work[26] on liquid Cl_2 shows that the "hot-band" transition is displaced by 5 cm^{-1} from the fundamental, not 7.5 cm^{-1} as witnessed above.

Despite using a small J-stop, the background on the Cl_2 spectrum is still very pronounced. This implies alignment is at fault - such problems can not be solved by closing the J-stop. The background merits comment for two further reasons.

Firstly, the periodicity is due to ripples in the passband of the multilayer dielectric filters used. Driven mainly by the surge in interest in FT-Raman methods, the quality of these filters has improved dramatically in the last five years. Figure 6.9 shows the improvement in performance achieved with modern filters over the development optics originally available*.

---

* NB: Our paper in The Analyst (Appendix 1) has these diagrams incorrectly labelled.

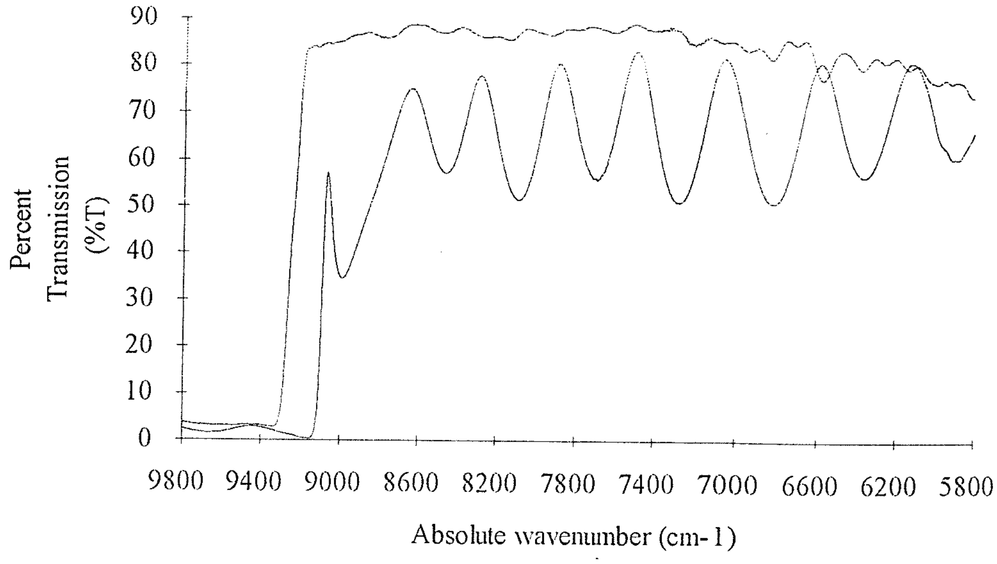

Figure 6.9 Comparison of filter profiles (upper trace PE commercial, lower trace Barr development).

The ripple may be smoothed out by multiplication with a suitable correction function for wavelength-dependant instrument response[28]. In cases where the S:N ratio low - such as for gas phase spectra - such a multiplication often degrades the S:N even further. This is because the experimentally-derived correction function also contains noise - which can not be smoothed out without degrading the quality of the correction function[29].

Secondly, even after evacuating the cell to 5 Torr for an hour the background still remained in evidence for the next set of spectra on N_2 and O_2. This implies that part of the cell background was caused by action of reactive species in the cell. The most likely cause is deposition onto the gold - or perhaps reaction with existing, less-fluorescent deposits. Cleaning with CS_2 did not help; the only method that came close to succeeding was heating whilst evacuating the cell on a gas line at around 10^{-4} Torr. After several such treatment a reduction in background was noticeable, although so was a reduction in cell efficiency. The reason for this became obvious upon viewing the cell with a near-IR camera - the defects in the tube coating had become more pronounced, implying degradation of the coating.

Since this cell could no longer be used optimally, the second cell type was constructed. The major advantages of this design were enhanced stability and greater reproducibility. The design was a great improvement, although the weight of the baseplate tended to alter the foreoptic alignment and require realignment for maximum signal. Rather than move the cell itself to align the system, the cell rested on four screws which could be independently raised or lowered to steer the cell coaxial with the optic axis.

The front window was affixed to the cell 2-3 mm forward of the front face to keep the window out of the focal region. The window itself needs to be highly-transmissive and low in fluorescence. The best material was 0.5 mm thickness fused quartz manufactured under the trade name "Spectrosil WF" as supplied by UQG Ltd. This material had very low (ppm) metal ion content, and gave a very weak Raman spectrum (of SiO_2) with almost no fluorescence. The window bonded cleanly to the brass cell with cyanoacrylate-based adhesive (Loctite "SuperGlue"), forming a gas-tight seal. At first problems were encountered with "fogging" of the cell window internally due to the vapours given off on curing; this was avoided by gently flowing N_2 up the cell interior with an extraction fan on the exterior.

Given that this design of cell and mounting proved more stable and the results were repeatable, it was possible to investigate the foreoptics more closely. Despite the improvements, the fluorescent background was still noticeable on a good number of spectra. The effect correlated not to sample, but to date of operation. The reason was quickly discovered, and concerned the method of alignment.

On the development prototype, the HeNe interferometer alignment/timing laser is not blocked after the J-stop. The collimated laser beam propagates along the optic axis, and focuses at the J-stop and the conjugate focus, in the IR sample compartment. This provides an ideal front-end alignment method, as the laser diverges out of the J-stop, is intercepted by the collection optics, and therefore focuses at the Raman sample position; since the collection optics are focused on the J-stop. Since the HeNe beam propagating out of the J-stop is split into three spots, the focus is established by noting where the weak red beams coalesces into one.

The problem with this method for very accurate alignment of small objects is that in reality the HeNe does *not* propagate exactly on-axis, and is arranged not to do so deliberately. This is to avoid potential external resonator effects in the HeNe laser, which would seriously disrupt the timing sequence and "crash" the interferometer. The laser is deliberately knocked 2 mm askew by placing a washer under one of its mountings. Obviously, this leads to a significant displacement of the focal spot for the HeNe beam with respect to the optic axis after the beam has traversed the collection optics.

Compounding this problem, the excitation laser was found to be non-axial with respect to the HeNe axis by ± 1 mm. The focal position was also determined to be incorrect, by about 1 mm. Such slight misalignments went essentially unnoticed before these studies because the large (± 2 mm) depth of field of the collection optics and the large viewed patch made these errors unimportant. Once the spectrometer foreoptics were realigned, the HeNe put back on-axis, and the exciting laser made coaxial, the incidence of high background diminished markedly. This could not have been achieved without a more stable cell design.

6.5.1.4 Carbon disulphide - higher order transitions

To demonstrate the improved performance, carbon disulphide (CS_2) at a pressure of 400 Torr was studied - the high and low resolution spectra shown in figure 6.10a.

The Fermi-enhanced first overtone of the Raman-inactive stretching mode can be seen quite clearly at 802 cm^{-1} in figure 6.10b. This is a classic and much-discussed example[30,31] of a weak Fermi resonance, in the sense that the unperturbed levels lie reasonably far apart, which shows in the comparatively small enhancement of the overtone band. Compare this with the Fermi resonance in carbon dioxide (CO_2) which is the best-known example of Fermi resonance to most Raman spectroscopists[32].

The bands at 659.1, 657.0, 651.8, and 649.9 cm^{-1} are assigned as "hot-bands" and isotopomers. The 657.0 and 649.9 cm^{-1} bands are included here even though they appear close to the noise level because they can been seen as shoulders on the lower-resolution spectrum; the band at 654.4 cm^{-1} is not included, despite being of similar intensity, because no evidence was seen in the lower-resolution spectrum.

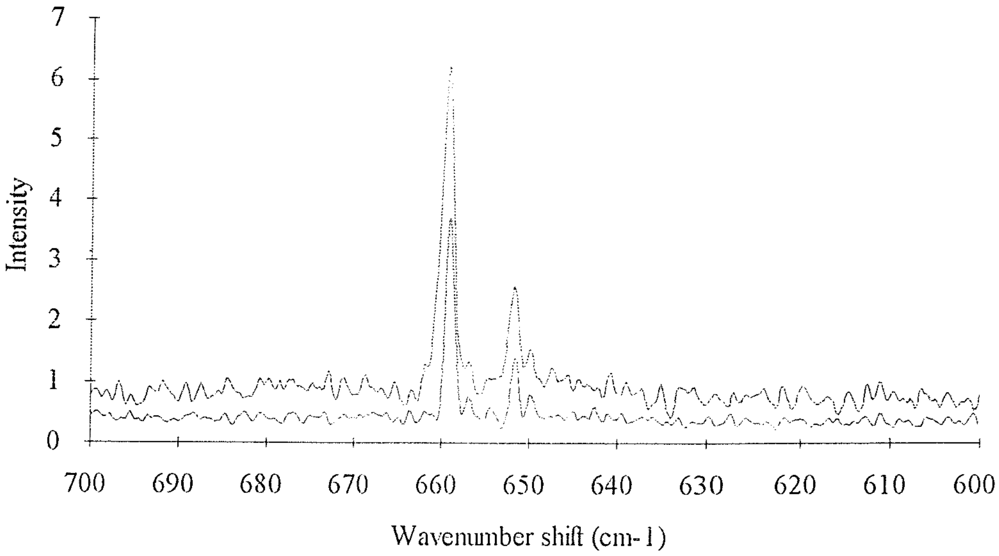

Figure 6.10a Carbon disulphide. Lower trace: higher resolution.

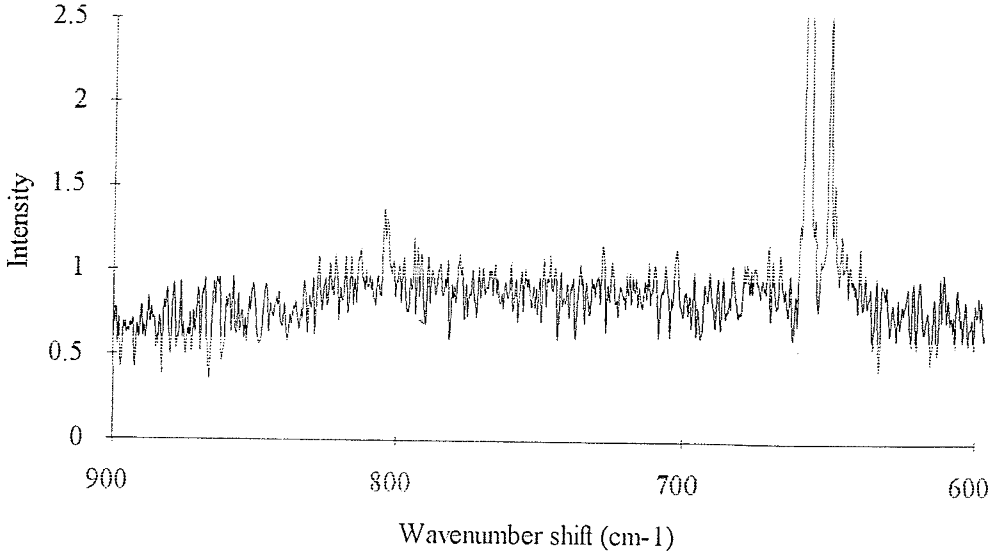

Figure 6.10b Fermi resonance in carbon disulphide.

Briefly, the 659.1 cm^{-1} feature is ascribed to the fundamental transition of the symmetric stretch in both the $^{32}S^{12}C^{32}S$ and $^{32}S^{13}C^{32}S$ ground-state species, whilst the 657 cm^{-1} band is attributed to the first "hot-band" of this transition in the $^{32}S^{12}C^{32}S$ isotopomer. The 651.8 cm^{-1} band is due to the fundamental excitation of the symmetric stretching mode of vibrationally-excited $^{32}S^{12}C^{32}S$ species with single excitation in both the antisymmetric stretch and bending modes. The 649.9 cm^{-1} feature is due to the fundamental symmetric stretch of the ground-state $^{34}S^{12}C^{32}S$ species and the first "hot-band" of the transition giving rise to the 651.8 cm^{-1} band.

6.5.2 Comparison of cell designs for the prototype Raman spectrometer

The obvious improvement of the second cell design is clearly seen in figure 6.11, comparing the C-H stretching region of two methane (CH_4) spectra. It should be noted that CH_4 is a rather good Raman scatterer - it has a normalised differential Raman scattering cross-section approximately 8 times higher[27] than that of N_2.

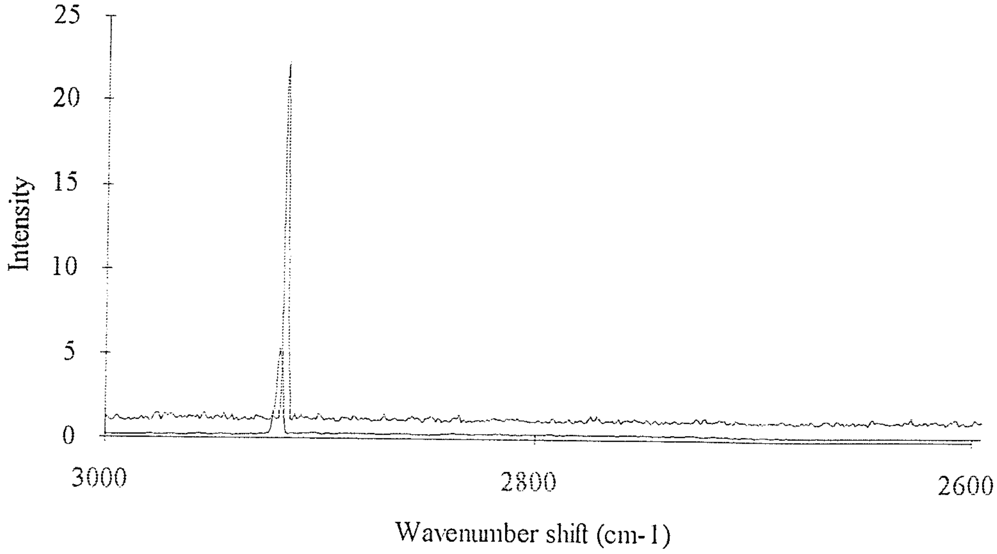

Figure 6.11 Overlaid spectra from the two cell designs - lower trace old design, upper trace new design, offset by one unit.

The spectra used almost-equal excitation powers (2.5-2.75 W) and tube lengths (100-110 mm); the old cell used 2 cm^{-1} resolution and a 5.6 mm J-stop, whilst the new cell used 1 cm^{-1} resolution and 4 mm J-stop. The band shift noticeable is partly J-stop error, partly due to a difference in laser reference wavenumber. The details are contained in the table 6.1 below:

Conditions:	**Old prototype cell**	**New prototype cell**
Instrumental resolution	2 cm^{-1}	1 cm^{-1}
J-stop diameter	5.6 mm	4.0 mm
Signal level (peak-peak, 2945-2880 cm^{-1})	5.21	24.8
Noise level (peak-peak, 2500-2100 cm^{-1})	0.09	0.47
S:N	57.9	52.8

Table 6.1 Comparison of gas cell efficiencies

The old cell appears marginally better in terms of S:N - yet this spectrum took 750 accumulations, compared to 25 for the new cell. In other words, a x30 reduction in scanning time.

This is quite startling, not least because the spectrum using the new cell was recorded at a mirror velocity of 0.2 cm/s - not the scan rate which gives optimum S:N on the prototype instrument. The issue was forced by the installation of two large cooling fans on top of the laboratory roof as part of the new computer suite. During the sudden "cut-on" of the cooling units the reference laser fringes were often lost, and the instrument "crashed" at low scan speeds. The only method around the problem for low scan-speeds was to collect short (10-20 scan) accumulations, unsuitable for this work. It was estimated that the loss in S:N was severe (x2) due to the use of a higher scan-speed.

One school of thought maintains that the accumulation of scans *ad infinitum* is useful when improvements in S:N are sought. Previous experience suggests that a law of diminishing returns applies after around 1,000 scans; that is, the graph of S:N ratio versus $(N_{scans})^{1/2}$ is no longer linear, but tends to a plateau around $N^{1/2} = 30$-35. The reason for this is open to debate although laser output "flicker", mechanical vibration, and acoustic noise certainly play a part*.

Spurious lines in the spectra presented a great problem. Random and pseudo-constant bands were imposed on the spectra by excessive vibration. Figure 6.12a shows a low-frequency spectrum _taken without any laser emission_.

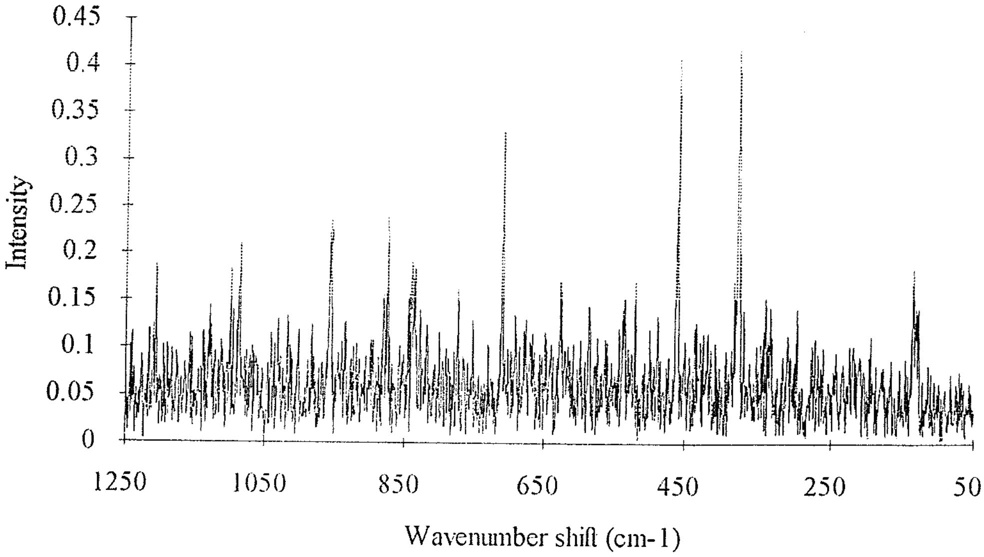

Figure 6.12a Typical "Spurious emission" spectrum.

---

* In the mid-IR, PE 1700 series spectrometers are stable up to ca. 32,000 scans; in the near-IR, the relationship holds up to ca. 10,000 scans.

A band near 1495 cm^{-1} was also noted in many spectra, seen in figure 6.12b below:

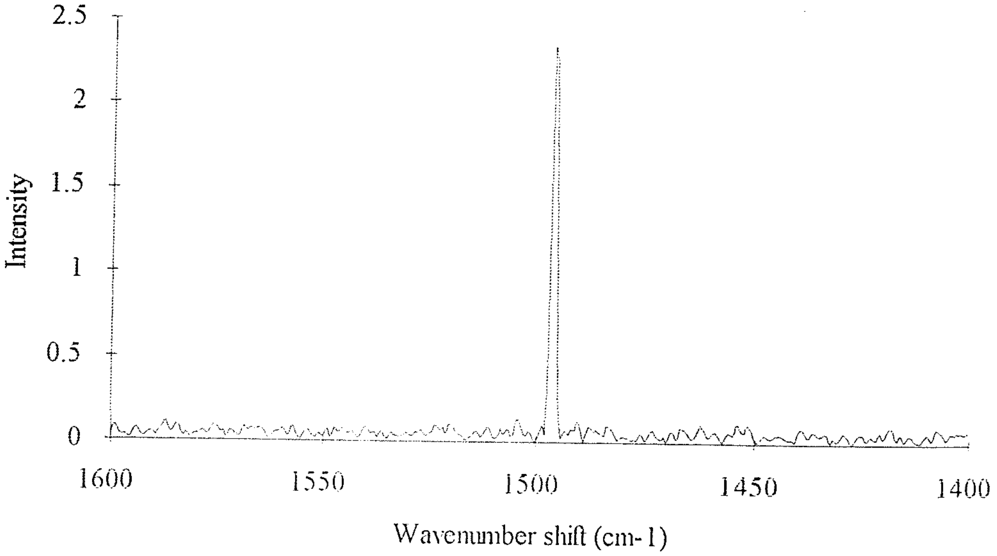

Figure 6.12b Reference HeNe laser-derived band.

This was not due to vibration or the room lighting, nor leakage through the laser plasma-line rejection filters, but appeared to be caused by the HeNe reference laser. In absolute wavenumbers, the band is at 7901 cm^{-1}; this is almost exactly half the HeNe laser wavenumber, 15803 cm^{-1}. Hence, this band may be put down to a problem with the electronic anti-aliasing filters, again not noticed until very high sensitivity was required.

If the excitation laser intensity is time-varying at around the same rate as the data collection rate (scan-speed dependant, usually around 1-3 KHz for near-IR wavelengths) then the interferogram may contain additional unwanted periodicities, because the actual intensity of the Raman scattering will not be constant at each data collection point - the FT process may interpret such periodic variations of the interferogram as "real" features, and generate unwanted spectral components. At the very least, a noisy laser output will degrade the S:N of the spectrum by increasing noise in the interferogram. For this reason, an active stabilisation circuit was added to the laser head, feeding a fraction of the power to a fast-response photodiode, with control loop to the 3-phase supply. This method stabilised the power output to 0.1% RMS of the maximum output intensity. The less-welcome outcome was that the maximum power available at the sample was restricted to 2-3 W to ensure stability.

In order to overcome low sensitivity, other methods of S:N improvement that were assessed, including retroreflection of the laser down the tube to create a two-pass cell, and cooling the detector. Retroreflection proved non-trivial, as plane mirrors channel an appreciable proportion of the diverging light into the glass of the cell even when the back face is coated in the same way as the front; this obviously causes increased fluorescence. Nevertheless, in favourable cases improvements between 20-80% were achieved, so the method has promise. The use of a curved mirror to focus the laser back into the tube was briefly investigated; the difficulty here was of alignment with little feedback to aid the optimisation. Cooling the detector should have led to a factor x2 improvement in S:N, after calculation using figures provided by the manufacturer. In the case of the development prototype spectrometer this was unattainable, due a fault in the Dewar design, which led to the InGaAs photodiode element vibrating excessively at 77 K against the strained gold electrical contacts to the photoelement.

6.5.2.1 Rotational Raman spectra

Rotational and rovibrational Raman spectroscopy is desirable for several reasons. Species without a permanent electric dipole moment or significant change in dipole moment during rotation may be studied, unlike with IR or microwave techniques; it is possible to deduce accurate values for bond lengths and centrifugal distortion coefficients from rotational spectra, as well as molecular symmetries[1].

Any attempt at rotational Raman spectroscopy requires very low stray light levels and very strong Rayleigh line rejection, because pure rotational bands nearly always lie in the 1-300 cm^{-1} shift region* . Only for the lightest of molecules do the rotational bands lie greatly outside this region. *Mixtures* present a great challenge. High resolution is needed to decongest the overlapping series of bands. This suggests the need for high-dispersion, low-stray-light triple grating devices.

Fortuitously, it has long been known that the *integrated* intensity of pure rotational Raman lines far exceeds the integrated intensity of rovibrational lines, by a factor of x100 in most cases[27]. Thus a strong rotational line is usually more intense than a pure vibrational line. It should be perfectly possible to collect rotational Raman spectra on an FT-Raman spectrometer, since this work has shown vibrational gas-phase spectroscopy to be viable.

To demonstrate this, the pure rotational spectra of N_2 and O_2 were studied using the second cell design. Given that CH_4 has eight times the relative normalised

---

* As a "ball-park" figure, reckon on the rotational line spacing being ca. 1/100th of the vibrational transition energy.

differential Raman scattering cross-section than either of these species[27], it seems strange at first glance not to use this instead. However, CH_4 is tetrahedral (T_d) in symmetry, and does not possess a pure rotational spectrum since it is a spherical top molecule - the polarisability is not modulated during rotation or any symmetric vibration[33,34].

The rotational spectra of N_2 and O_2 are shown below, displayed over the range 200-50 cm^{-1}. These spectra were recorded at 1 cm^{-1} resolution using 100 accumulations and 2 W excitation power at 760 Torr pressure. It should be noted that the total acquisition time was only one hour.

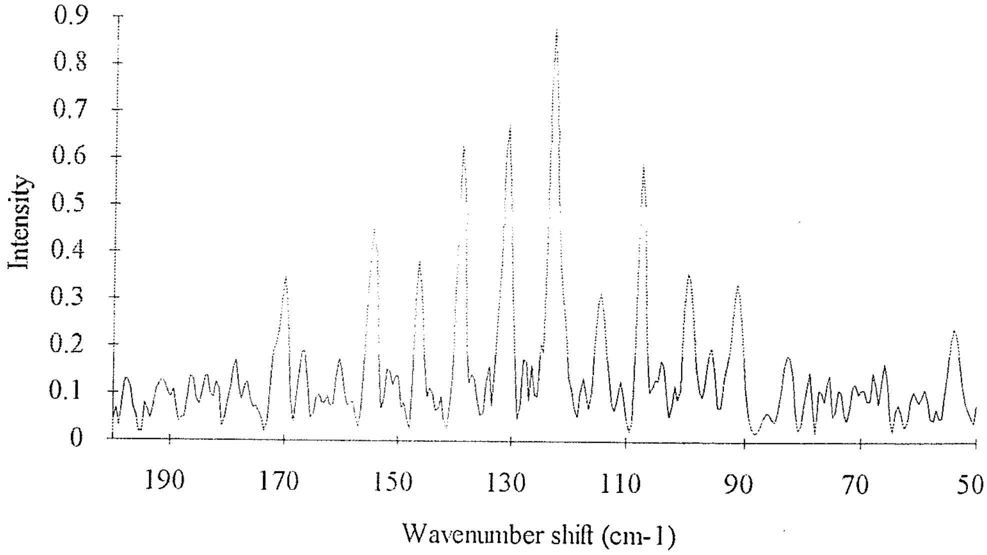

Figure 6.13 Pure rotational Raman spectrum of N_2.

Considering N_2 first (spectrum figure 6.13, data figure 6.14) it is clear that a line between 154.5 and 170.0 cm^{-1} is missing from the progression. This line should be near 162.0 cm^{-1}. This absence must be caused by a filter artefact. The major practical problem that arises with detection of low-frequency bands with the FT-Raman technique concerns the laser rejection filters. These exhibit large changes in transmissivity in the low-frequency region where the rotational lines appear, which obscures many lines and distorts the intensity "envelope".

It is, however, possible to angle-tune the band edge or blocked region over a short range to shorter wavelength, thus increasing the low-shift performance[29]. The problem is that the optical density (OD) - defined as equal to $-\log_{10}(\%T)$ - decreases as a strong function of tuning angle. With the filters supplied by Perkin Elmer, it proved possible to achieve a suitable balance at around 15°. Transmission data on these filters was not obtained at the working angle.

The band at 83.0 cm^{-1} looks as though it should be included in the series, although this is possibly dubious since the S:N is about 1:1 at this band. However, if the data is plotted as in figure 6.15 a straight line fit between the data points of slope 7.86 and correlation coefficient 0.9999 is obtained-the intercept at zero being 83.7 cm^{-1}. Therefore, the addition of the band at the 83 cm^{-1} position could be justified.

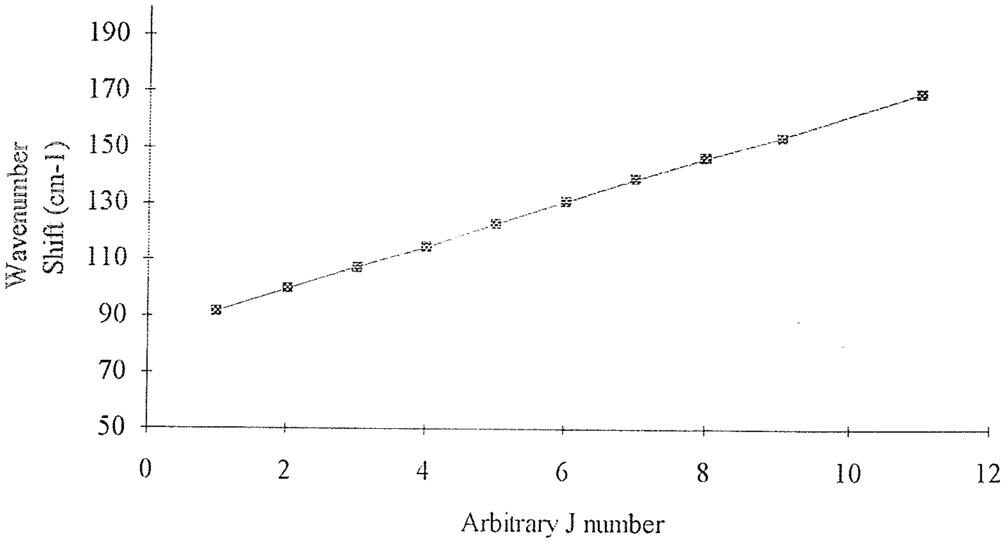

Figure 6.14 Plot of band position versus arbitrary J number for N_2.

Classically, the energy of a non-vibrating, non-translating diatomic molecule rotating in space about one of the two equivalent orthogonal axes perpendicular to the internuclear axis is given by:

$$E = \frac{1}{2} I \omega^2$$

Where I represents the moment of inertia of the system about the chosen axis, given by $I = \mu . r^2$. Here, μ (Kg) represents the reduced mass once again and r is the interatomic distance (m).

There is no moment of inertia for rotation about the internuclear axis - all the mass lies on this axis; there is no angular momentum generated by motion around this axis.

Re-writing the equation in terms of angular momentum about the axis, $P = I \omega$ proves useful:

$$E = P^2 / 2I$$

$$\therefore \; P = \sqrt{2EI}$$

The quantum-mechanical expression for the diatomic rigid rotator has solutions:

$$E_{rot} = BJ(J+1) \text{ cm-1}$$

where J is an integer (J= 0,1,2 ...) and $B = h/8.\pi.c'.I$ (cm^{-1}) is given by a collection of fundamental constants and I. Note that no zero-point energy exists for the rotor - E_{tot} may equal zero. Not only is total rotational energy quantised, but so too is the total angular momentum P:

$$P = \sqrt{}J(J + 1).h/2\pi$$

This can only have orientations about the rotational axis P_x such that:

$$P_x = n.\ h/2\pi,\ n = 0,1,2 \ldots.$$

For a given J value, P_x may therefore have (2J+1) components - the degeneracy of the rotation J is said to be (2J+1).

The rotational Raman selection rule is:

$$\Delta J = \pm 2$$

This can be understood as reflecting the fact that during rotation, the polarisability ellipsoid will be indistinguishable twice[33,34] - in other words, the polarisability goes through two cycles - hence $\Delta J = \pm 2$.

Considering only Stokes-shifted lines ($\Delta J = +2$), we have the general expression:

$$\Delta E = B(J+2)(J+3)-B(J)(J+1)$$

so that

$$\Delta E = B(4J+6)$$

In other words, the rotational Raman lines will be spaced 4B cm^{-1} apart, with the Rayleigh line 6B cm^{-1} from the first line. Plotting line position versus arbitrary J-number therefore gives us a slope of 4B cm^{-1}. Hence for N_2, B = 1.965 cm^{-1}, and r_{atomic} = 110.7 pm. This value is well within 1% of the accepted value[27], measured by sophisticated high-resolution methods. This simple approach has ignored centrifugal distortion (error 2 ppm) and isotopic substitution (^{14}N:^{15}N 99.6:0.4), as well as J-stop error in the band positions - however, this is about 2 cm^{-1} for the set resolution (1 cm^{-1}), and is approximately constant across the small range of absolute wavenumbers (variation in error is 0.03 cm^{-1} over the 90 cm^{-1} range).

Carrying out the same analysis on O_2 (spectrum in figure 6.15, details in figure 6.16) leads to the conclusion that the features at 122.0 and 125.5 cm^{-1} must be artefacts caused by vibration.

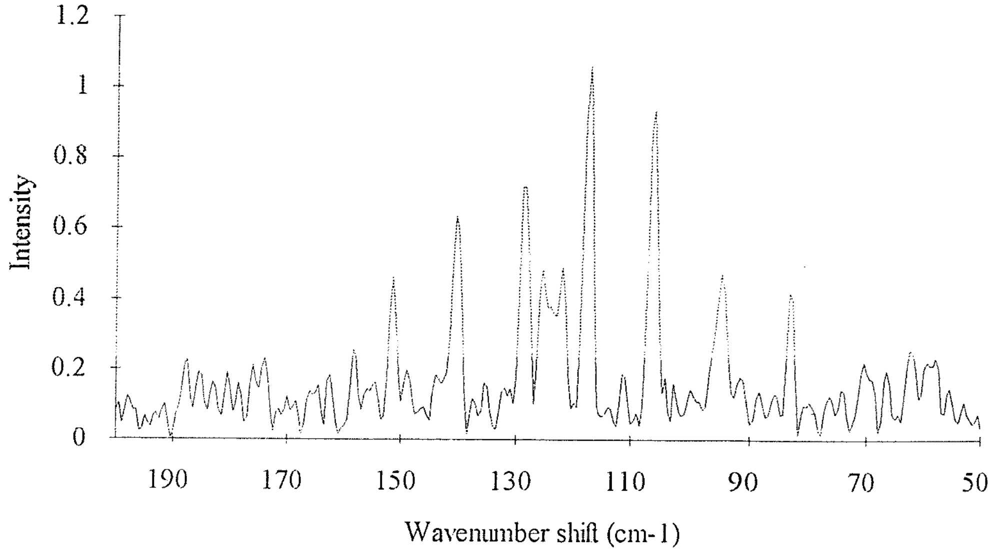

Figure 6.15 The pure rotational Raman spectrum of oxygen.

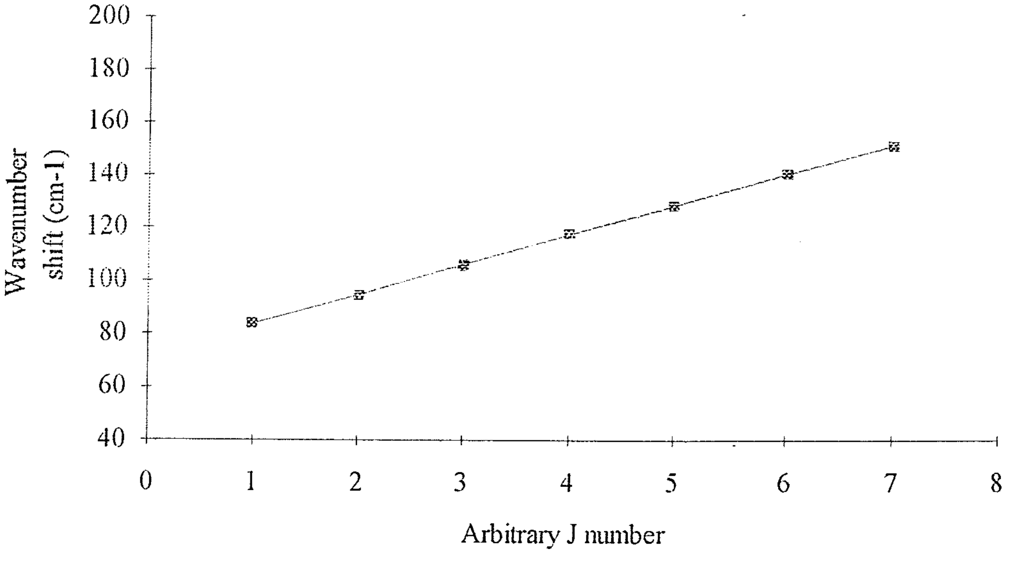

Figure 6.16 Plot of band position versus arbitrary J number for O_2.

The error in determining bond length by the method outlined above is more serious in this case. When the data is analysed, the slope of the line position versus arbitrary J-number is 11.38, with a correlation coefficient of 1.000 - an apparent B =

2.845 cm^{-1}. This would lead to an O_2 molecule of length 272.1 pm - which is approximately 124 % too large[27].

The error occurs in the assumption that every transition is allowed with equal intensity. In fact, for $^{16}O_2$ every rotational state with an even J-value remains unpopulated - thus every Raman transition from these states has a zero intensity[35]. Hence we only see half as many lines as in the case of N_2, so that the slope should be 8B cm^{-1} and B = 1.4225 cm^{-1}. This leads to an internuclear distance of 121.7 pm, again well within 1 % accuracy. The reason for the lack of population in every O_2 state with even J-number is to do with the overall symmetry that these states would possess - the symmetry of the product of the electronic, rotational, and nuclear spin wavefunctions; it transpires that these states have disallowed symmetries.

One further point need be considered. If the laser line is not blocked strongly enough by the rejection filters, the line can appear so intensely that "ringing" can be seen extending many tens of wavenumbers into the spectrum. This is as a result of incomplete apodisation, and should not be confused with rotational structure. The ringing bands are quite broad, and occur in an area where the comparatively weak Raman bands would still be strongly blocked by the rejection filters. The plasma filters used on the laser output should be of the highest quality for this application, since lamp-pumped YAG lasers have strong sharp emission bands in the frequency range that corresponds to the low shift region.

The method of rotational FT-Raman spectroscopy seems perfectly viable on the basis of these measurements. The S:N performance in the spectra above is modest; with higher laser powers, cooled detectors, longer scans, and optimised scan velocity values an increase in sensitivity of one order of magnitude should be quite attainable. This is encouraging, as it suggests that partial pressures in the 70-80 Torr region should be open to study.

Unfortunately, the rejection filters cut off too far from the laser line. This will always be the limiting feature of the FT-Raman approach, and will restrict the technique to analytical usage. This is the case even with the best currently-available alternative rejection filter technologies, some of which display band edges near 40 cm^{-1} Stokes/anti-Stokes. Also, the sensitivity of the technique requires that the spectrometer be perfectly optimised for every experiment, with the sample cell aligned very accurately for each experiment.

The last two points place high demands on the stability of the spectrometer, and the reproducibility of the sampling arrangement. Despite the great improvements made over the first cell, the problems still encountered on the development prototype spectrometer led to the development of the third cell design for the commercial instrument.

6.5.2.2 "Filterless" FT-Raman spectrometry ?

Before moving on to the design of the third cell, the last point on the development prototype concerns the possibility of doing away with Rayleigh filters all together. Two factors give this approach credence. Firstly, the ratio of Rayleigh to Raman scattering in the gas-phase is much lower when compared to solid or liquid-phase results, so that the ratio lies between 10^4-10^2:1; and secondly, the Rayleigh line should be highly polarised[21,36,37].

Because of these factors, it should be possible to use an efficient polariser to reject the Rayleigh line, whilst most of the rotational Raman intensity would be transmitted, because pure rotational lines (which exist for all molecules except spherical tops, such as CH_4 and SF_6) are *always* depolarised[34]. Hence the idea of removing the Rayleigh filters, and replacing them with a polariser set at the J-stop to pass linearly-polarised light orthogonal to the polarisation incident on the sample, the polarisation of which would be retained (to excellent approximation) by the Rayleigh scattering.

However, the success relied upon the spectrometer being isolated from stray light, and upon the Rayleigh line remaining strongly polarised. It proved impossible to satisfy these criteria on the development spectrometer - especially since the reflecting prism was only 99 % reflective at best, so that the prism "glow" could not be masked from the spectrometer effectively without obscuring >80 % of the collection volume. Because light at the laser wavelength comprised a mixture of scatter, reflection, and luminescence, the polarisation was not preserved - so that a significant amount of the residual signal passed through the polariser at the laser wavelength. Given that the LOT-Oriel linear near-IR polariser only had a 35 % transmission efficiency and 100:1 extinction coefficient at 1 μm, the experiment failed. Even the substitution of more efficient Perkin Elmer-supplied polarisers, additional spatial filtering, placing the polarisers in collimated light, and installing a gold-coated highly-reflective prism did not make the substantive gains required.

6.5.3 The commercial spectrometer

Although a great improvement, the second cell design/prototype spectrometer combination still did not present the stability and reproducibility required of a routine analytical method. The third design was constructed to fit the commercial PE 1760X spectrometer.

Since this spectrometer is laser safety-rated "Class 1" in normal operation, the HeNe alignment spots and the excitation laser may not ordinarily be used to align the cell. Therefore, alternative alignment methods needed to be devised.

As detailed above, the cell was based on a demountable cradle which locates with two bolts to the M5-drilled sample area baseplate of the spectrometer, after removing the 3" x 2" accessory card holder. The cell is aligned with the aid of a jig, which has removable end-caps. After rough alignment by eye, the rear end-cap is removed, an optical power meter placed on the sample stage behind the jig, and the "XYZ" sample stage positioners are adjusted to give maximum laser throughput. The positioners exhibit considerable backlash. After this, the rear end-cap is replaced, and the two micrometer positioners on the cell are adjusted to maximise the throughput. Although the "Chinese Lock" used to hold the jig and cell steady is stable, it does mean that any adjustment to the micrometers alters slightly the position of the cell front. Therefore, it is also necessary to make slight adjustments to the "XYZ" positioners. After this, the spectrometer is placed into "Monitor" mode, and the energy throughput noted. The idea is to make small adjustments to the alignment of the cell to minimise the figure-this figure is due to the fluorescence of the brass used to make the end-caps, and drops dramatically when the cell is properly aligned. The power meter is then removed, and the jig replaced with the gas cell.

The problem with this approach is quite obvious - since it requires many iterations, it requires that the sample compartment be opened very often. This means that the laser is switched to "Standby" (zero-emission) mode, with the subsequent need to wait a couple of minutes for the output power to restabilise, on every iteration. This is unduly time-consuming, so for much of the development work, the interlocks were defeated during the alignment phase. In a commercial design, the micrometer positioners would have longer barrels, so that the controls might be accessed via ports recessed into the sample compartment lid. The other advantage of this approach is that the constant raising and lowering of the lid, with attendant chance for misaligning the cell, is removed.

The cell itself had "Spectrosil WF" front and rear windows, with an "in-house" tube of 100 mm length and 1 mm bore. The front and rear faces were coated with gold paint, which proved an ideal mask material, to avoid severe fluorescence backgrounds where slight misalignments occurred.

Before choosing this tube it was necessary to check the performance against the Perkin Elmer-supplied tube. The spectra in figure 6.17 show quite clearly that the "in-house" tube gave almost identical results in terms of signal levels and fluorescence performance when similar tube lengths and bore sizes were compared at identical scan conditions (100 scans at 4 cm^{-1} resolution with 1 W excitation).

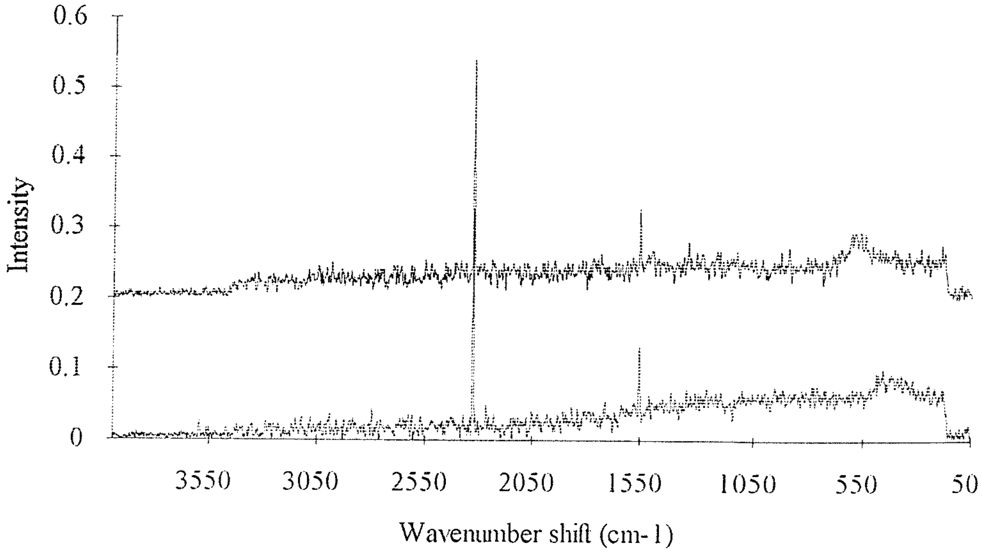

Figure 6.17 Comparison of PE and "In-house" tubes.

Slightly startling about this result is the fact that the Perkin Elmer tube had no gold paint on the end-face to blank out luminescence from the glass, yet the background is of a similar order of magnitude as the "in-house" tube with proven gold end-coat. This must imply that it was possible to align the cell to a remarkably high accuracy using the new cell holder.

This is borne out by a remarkable result, achieved quite by chance, *with just the jig in place.* Figure 6.18 was collected with 1 W excitation at 2 cm^{-1} resolution after 100 scans. The spectrum proved repeatable - if the cell was driven through the focal point and then re-positioned after taking up the backlash, the same spectrum resulted. However, after demounting and remounting the jig the spectrum could not be recovered. This conclusively shows the criticality of the alignment.

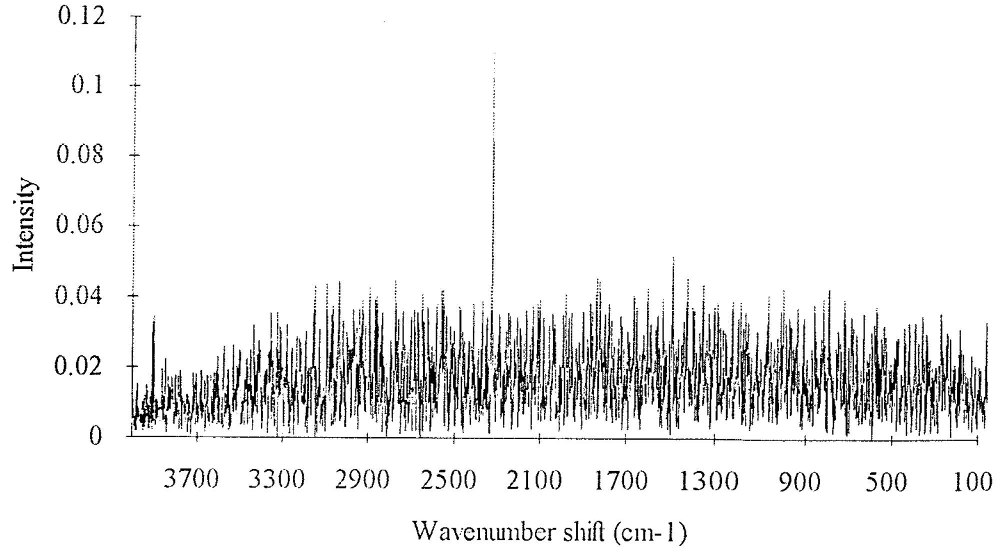

Figure 6.18 Air spectrum with jig only.

Figure 6.19 compares the first spectrum from the commercial system to a typical spectrum from the optimised prototype. The excitation power was approximately 2 W in both cases; for the development prototype, 425 accumulations at 1 cm^{-1} resolution (4 mm J-stop) using scan-speed 0.2 cm/s were co-added, whilst for the commercial spectrometer 200 accumulations using scan-speed 0.1 cm/s at 4 cm^{-1} resolution (8 mm J-stop). The band shift is due to the combined effect of J-stop error and difference in laser reference wavenumber.

As can clearly be seen from table 6.2, the S:N performance is quite similar. This is despite the superior detector of the commercial instrument. Part of the reason may lie in the conditions, as both spectrometers were operated at *non*-optimum scan-speed; the higher performance of the commercial system detector may be offset by the extra throughput of the prototype, due to the superiority of the gold-coated mirrors over the former's aluminium mirrors. Despite this, the commercial system spectra used half the number of scans of the development prototype; it should remembered that this spectrum is the first from the commercial spectrometer, without the benefit of several months development - for instance, notice the background attributable to poor alignment.

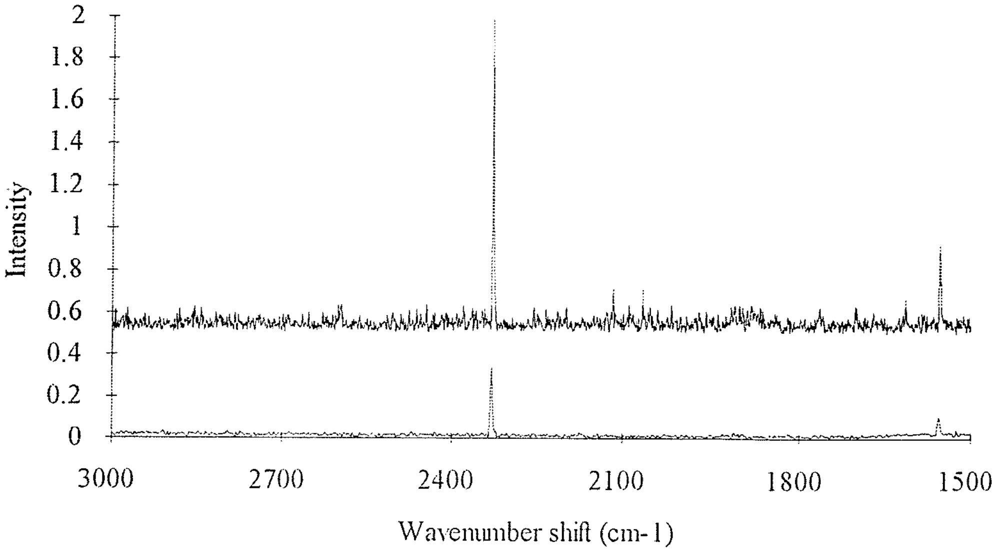

Figure 6.19 Comparison of prototype and commercial systems - lower trace is from commercial cell/spectrometer, upper trace from prototype systems - note 0.5 unit offset.

Conditions:	**Commercial**	**Prototype**
Signal (peak-peak, 2350-2300 cm^{-1})	0.337	1.48
Noise (peak-peak, 2800-2600 cm^{-1})	0.029	0.13
S:N	11.5	11.4

Table 6.2 Comparison of commercial and prototype spectrometers

The whole point of this development was to increase reproducibility to the stage where it is a viable analytical method. As previously mentioned, problems that were encountered with the prototype spectrometer itself engendered in part the move to the commercial system. To justify the move, several factors were investigated.

The first area concerned the reproducibility of the spectra themselves. The repeatability of measurement seems reasonable - figure 6.20 is a representative result. Each of the five spectra resulted from 50 co-additions at 4 cm^{-1} resolution, with 1 W excitation.

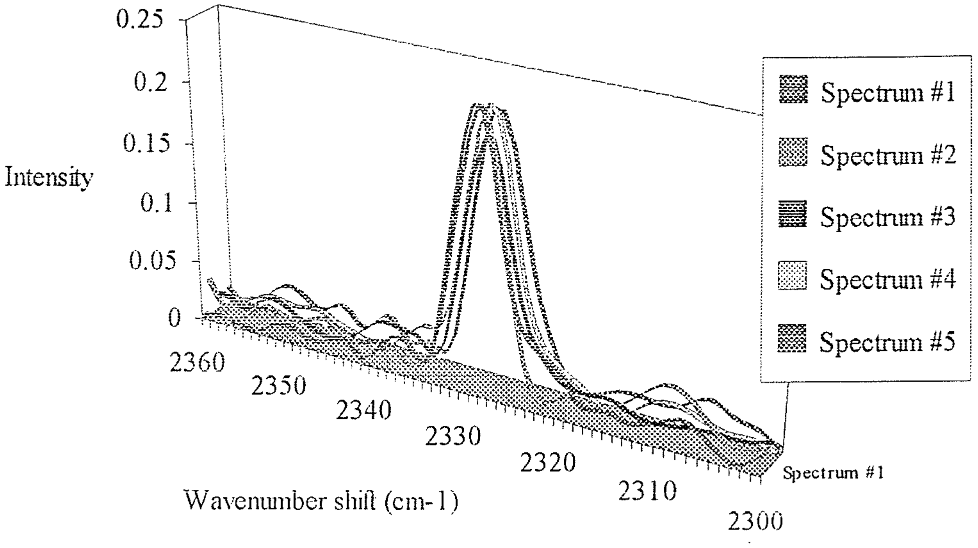

Figure 6.20 Reproducibility of collection.

The gain in S:N accrued by co-adding large numbers of scans was more problematic. In common with the development prototype, the commercial spectrometer seemed to plateau near 1,000 scans. The commercial instrumentation was fitted with the same active stabilisation as the development prototype - without stabilisation, the variation between individual spectra was more than ± 10 % in S:N. Also in common, vibration could not be fully isolated, but was far less problematical.

As expected, changing the spectral resolution altered the S:N performance. The spectra in figure 6.21 were collected at 1, 2, and 4 cm^{-1} resolution, with 1 W excitation, and 150 accumulations. Again, notice a slight band shift - due to the change in J-stop size.

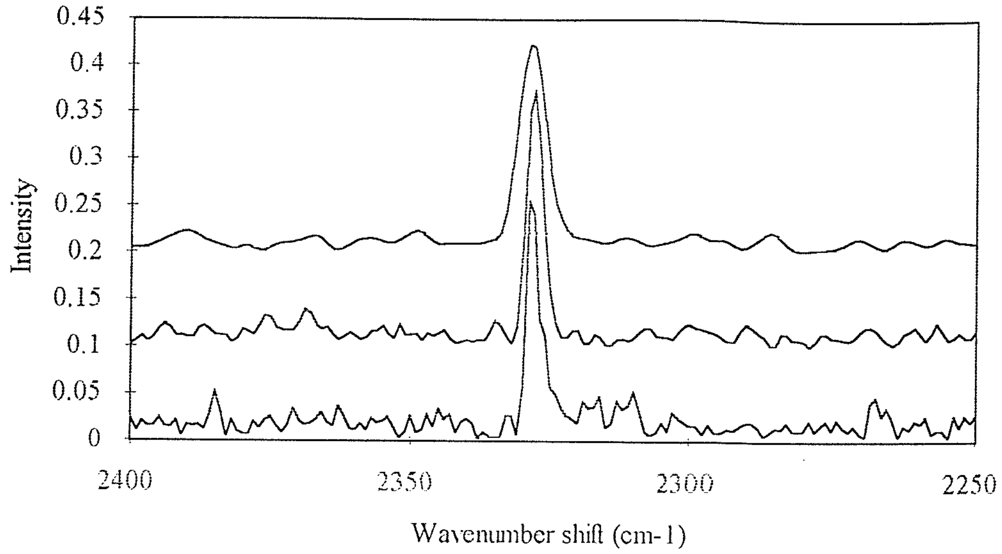

Figure 6.21 Change in S:N ratio with resolution. Upper plot: 4 cm^{-1}, centre plot: 2 cm^{-1}, lower plot: 1 cm^{-1}.

Given that the spectra are reproducible, the second area assessed was the ease of re-positioning. Whereas the prototype spectrometer had reasonably large depth of focus in the foreoptics (± 1 mm) the commercial system had much "tighter" (± 0.25 mm) focus. The actual focal point for maximum gas cell signal was fractionally less than 27 mm from the flat collecting lens surface; this result proved quite repeatable, although somewhat difficult to achieve in practice because of backlash in the "XYZ" stage and the fact that the three axes of motion were not fully decoupled.

Since the spectrometer was producing stable data and the cell focusing and re-positioning both proved to be repeatable, it was possible to evaluate different tube lengths and bore diameters. The optimum focus (27 mm) appeared to be invariant with respect to bore diameter.

As the results below clearly show for both the 1.0 mm (figure 6.22) and 1.5 mm (figure 6.23) bore sizes evaluated, the longest tubes gave the highest signal levels.

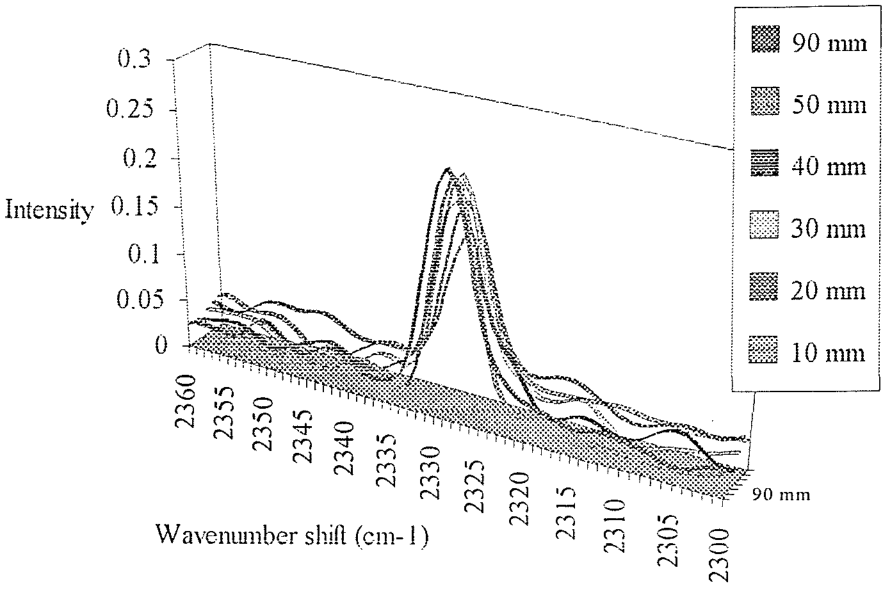

Figures 6.22 Dependency of signal on tube length for 1.0 mm diameter bore tubing.

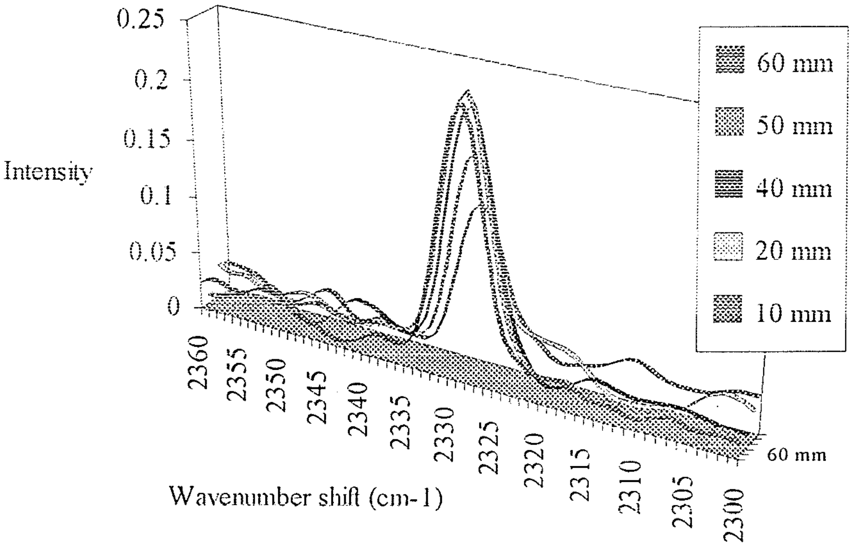

Figures 6.23 Dependency of signal on tube length for 1.5 mm diameter bore tubing.

These results proved quite repeatable, as did the fact that for a given tube length the bore diameter 1.0 mm made little difference, as shown below for 50 mm (figure 6.24) and 20 mm (figure 6.25) tube lengths.

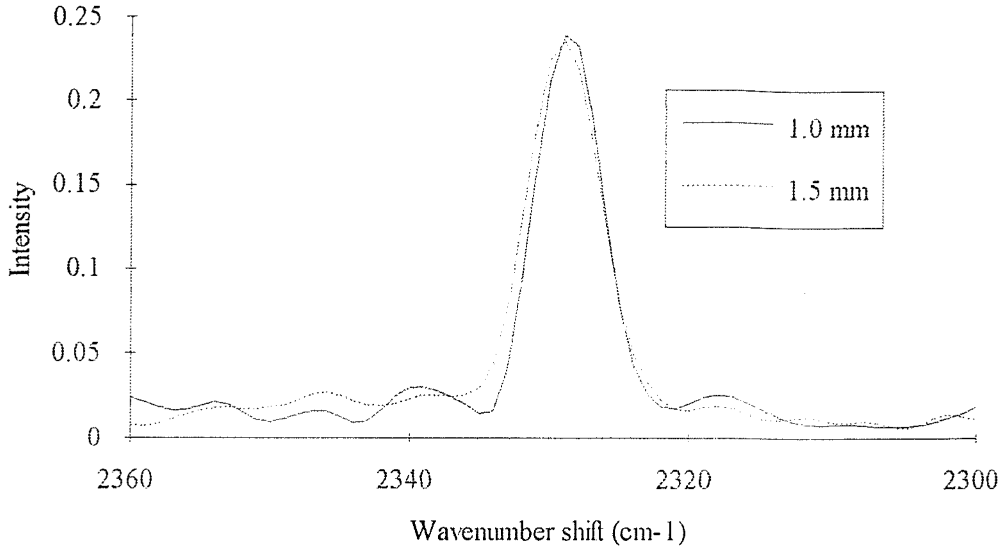

Figure 6.24 Dependency of signal on bore size for 50 mm tubing.

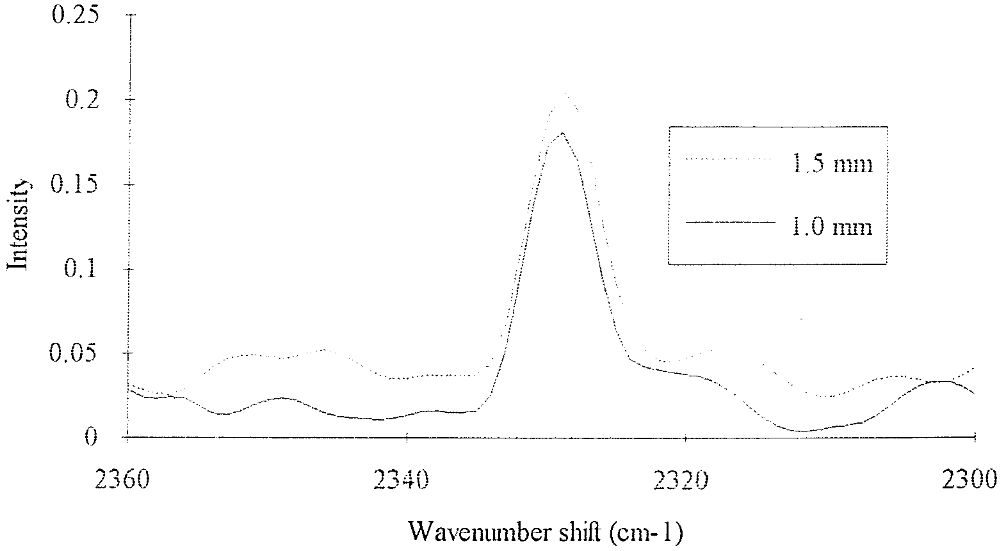

Figure 6.25 Dependency of signal on bore size for 20 mm tubing.

The larger bore size was preferable, as it proved easier to align.

Given that the stability of the experiment was very good, further investigations were made on retroreflectors. The results gained on the development instrument were vindicated-plane retroreflectors gave 20-80 % enhancements in signal, whilst often increasing backgrounds appreciably if the two end faces were un-coated, and were still remarkably difficult to align.

6.5.4 Results using the commercial spectrometer

Once the cell was developed, several areas of application presented themselves. The first was based on the analytical requirements of the Westinghouse-Hanford Corporation; the second was based upon a fundamental study of N_2O_4, a species never before studied in the gas phase, where near-IR excitation provided the prospect for success.

6.5.4.1 Westinghouse experiments

The studies carried out for Westinghouse were remarkably simple. Their concern is to prevent the storage facilities used for high-level nuclear waste from the Manhattan nuclear weapons project from exploding. This may seem unduly dramatic, but the gas pressure build-up generated by the various chemical, radiochemical and nuclear reactions inside the containers is serious and needs careful monitoring. At present this is a hazardous, time-consuming, and extremely expensive. Given the well-proven ability of fibre-optic Raman probes[38], it may prove possible in the long run to carry out *in-situ* on-line gas monitoring by Raman methods.

As a preliminary demonstration of the viability, two gases of interest to Westinghouse were recorded at highest possible S:N to indicate the likely trace detection capabilities with current macro cell designs. These gases were H_2 and D_2. Although somewhat uninspiring, the study of these species and their isotopomers has been the subject of feverish recent activity by several Japanese researchers[39].

The data for H_2 and D_2 is given below in table 6.3, along with the spectra themselves in figures 6.26 and 6.27. The spectra were recorded at 4 cm^{-1} resolution, with 1,000 accumulations, using 1 W excitation.

The most obvious thing to note is the very large spacing between the rotational lines. This is because the molecules are light and the moment of inertia is small. The study of pure rotation on the commercial instrument was limited to these species, as the filters are installed in non-tuneable mounts. In figure 6.27, the D_2 vibrational line is quite clear at 2989.0 cm^{-1}. The H_2 vibrational band lies at 4123 cm^{-1}; this corresponds to 4275 cm^{-1} absolute, well below the $In_{0.53}Ga_{0.47}As$ long-wavelength cut-off, determined by the bandgap threshold of the alloy[40].

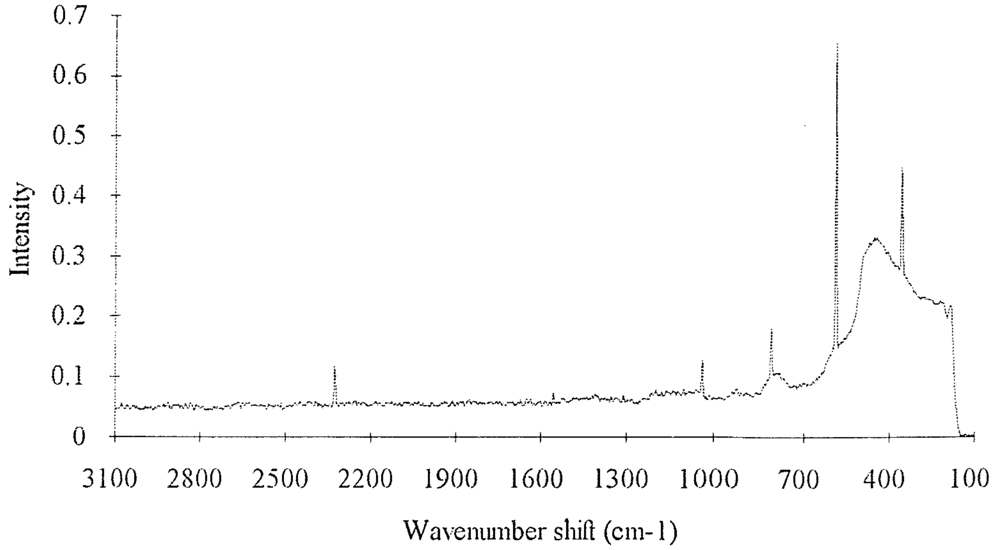

Figure 6.26 Rotational spectrum of ${}^1H_2$.

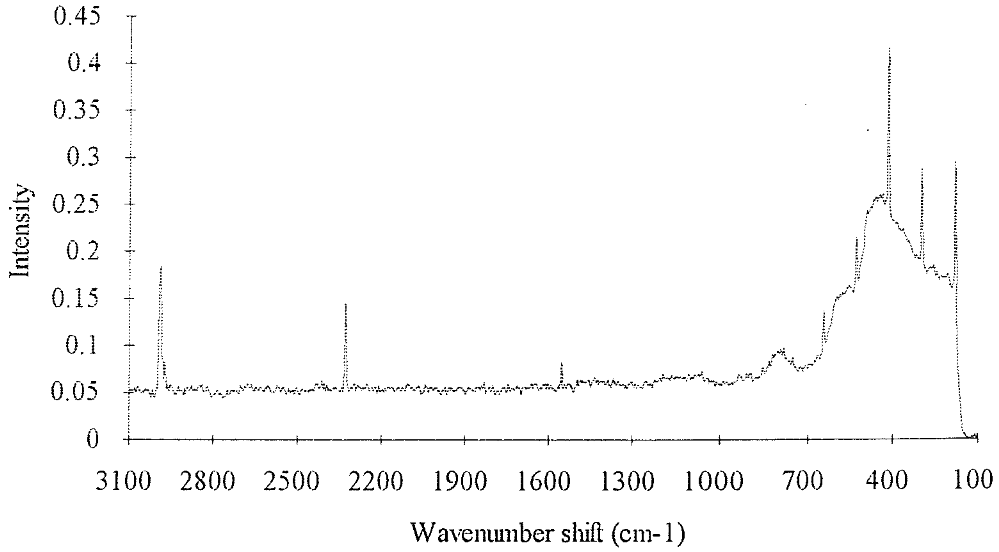

Figure 6.27 Rotational spectrum of ${}^2H_2$.

Interestingly, the derived values for the rotational constants and bond lengths of both species are in error with the accepted values[27] by 3-4 %. Contrast this with the accuracy (< 1 %) using N_2 and O_2. The magnitude of the error is almost certainly due to an insufficient number of lines in the fit giving an erroneous B-value.

Transition: **($J_{Upper} \leftarrow J_{Lower}$)**	**Hydrogen** **($^1H_2$)**	**Deuterium** **($^2H_2$)**
2-0	355.9 cm^{-1}	181.0 cm^{-1}
3-1	588.9 cm^{-1}	299.0 cm^{-1}
4-2	815.8 cm^{-1}	416.0 cm^{-1}
5-3	1035.7 cm^{-1}	531.0 cm^{-1}
6-4	– cm^{-1}	644.0 cm^{-1}
B_{Rot} (cm^{-1})	56.65	28.95
R_{Bond} (pm)	77.1	76.3

Table 6.3 Rotational parameters of H_2 and D_2.

The S:N performance is encouraging. Although only about 45:1 after 1000 scans, this means that without further improvement the study of species around 1/10th atmospheric pressure should be viable.

It should be noted that the background present resulted from a previous abortive attempt to study HOCl vapour, not due to alignment, and could not be removed. In addition the seal on the windows eroded slightly, hence the vibrational lines of air at 2331 cm^{-1} (N_2) and 1556 cm^{-1} (O_2) can be seen. Since air was obviously present in the cell, the partial pressure of H_2 or D_2 was necessarily sub-atmospheric, and therefore an additional gain in efficiency would be made by re-sealing the windows.

However, an estimate of the degree of leakage can be attempted. The relative band areas of D_2 and N_2 vibrational bands is about 2.8. Since the scattering cross-section of D_2 is reported[27] to be 2.5 times greater than that of N_2, this implies that the cell was only around half-full of D_2. This simple approach ignores the fact that the leakage would be dynamic (the D_2:N_2 ratio would decrease with time) and relies on the cross-section data being reliable in the near-IR.

Given that the laser power could easily be increased 3-fold, the detector cooled to decrease noise two-fold, and the retroreflector aligned to yield about 50 % higher signal, it should be possible to push S:N to 30-40:1 even at 1/10th atmospheric pressure. After optimising the scan-speed by reducing vibration, and fitting gold reflective optics rather than aluminium, a further two or threefold gain in signal could be attained - plus the ability to scan right up to 10,000 accumulations, in extreme cases.

The viability of analysing low partial pressures in gas mixtures seems proven. One last point of interest to Westinghouse - CH_4 is also of great importance to the nuclear industry, as a trace impurity in the process stream of tritium ($^3H_2$) in fusion reactors[41]. Since it is a three-times better vibrational Raman scatterer than any of the hydrogen isotopomers[27], the sensitivity of the optimised experiment to methane (and its isotopomers) should be very high indeed, and the study comparatively easy.

6.5.4.2 Dinitrogen tetroxide in the gas phase

The equilibrium $N_2O_4 \Leftrightarrow 2NO_2$ continues to present theoreticians and experimental spectroscopists alike with many challenges, in terms of the electronic structure and geometry of the ground and excited states. The driving force behind much of the research into nitrogen oxides is concern over the role played in severe atmospheric pollution caused by automobile exhaust emission[42].

Monomeric nitrogen dioxide (NO_2) is a stable paramagnetic free radical, possessing one unpaired electron, and exhibits a strong tendency to dimerize[43]. The dimeric species dinitrogen tetroxide (N_2O_4) has a rather long (178 pm) N-N bond[44], with both NO_2 groups showing geometry very little changed from those found in free NO_2[45]. The evidence of calculation supports the experimental view that the two NO_2 groups are held together by weak π-bonding, explaining the planarity of the species[44,45] although the role of the σ-bonding is still incompletely determined[46].

Interest exists in the nature of the bonding in the dimer for other reasons; the partial rotation about this bond (the torsional vibration) has been the object of quite intense study[47]. Unfortunately, it is neither IR nor Raman active, being of A_u character in the D_{2h} point group, and therefore its frequency must be inferred from combination band frequencies.

Gas-phase linear Raman spectroscopy of the dimer has previously proved impossible. Whilst the liquid phase at 20°C is approximately 99.9% N_2O_4, the gas phase[48] is almost 16% NO_2 - only at around 120 °C would the equilibrium be thrown completely to the monomer (100% NO_2). Since gaseous N_2O_4 can never be free entirely of NO_2 at atmospheric pressure, the strong resonantly-enhanced Raman scattering and structured fluorescence emission from the minority NO_2 gas-phase species have previously made observation of the much weaker unenhanced spontaneous scattering from the dimer impossible, with any wavelength chosen in the near-UV or visible.

The dense and strongly-overlapping rovibrational bands of NO_2 have been identified as belonging to no less than three low-lying electronic excited states of the same spin multiplicity, all transitions therefore being electric-dipole allowed; the rich structure of the near-IR absorption spectrum of NO_2 should be contrasted against the broad and featureless visible absorption spectrum of N_2O_4, which has its first resonance in the near-UV at around 340 nm (3.6 eV)[49].

The fact that NO_2 is absorbing around 1064.1 nm is confirmed beyond doubt by a simple experiment. The power incident on the front face and exiting the back face of the 150 mm cell was measured. With 2.75 W incident on the front of an empty cell, 90-95 % was transmitted; when measured after filling the cell to atmospheric pressure, this value dropped to around 35-40 %. It should be remembered that attenuation of the excitation beam and reabsorption of the Raman scattering both act to reduce the scattered signal level.

With a suitable method employing off-resonance excitation, it should be possible to directly probe the dimeric species. Near-IR excitation at around 1.064 μm provides such an opportunity - with the first gas-phase spectrum* of N_2O_4 being given in figure 6.28.

The strongest band in the spectrum occurs at 254 cm^{-1}, with a group of sharp but weak lines at 1304, 1322, and 1380 cm^{-1}. Also evident is a band at 1877 cm^{-1}, as well as a broad band at 806 cm^{-1}. Two rather weak bands near 407 and 355 cm^{-1} are probably due to the cell; the signal-to-noise (S:N) ratio of the present data does not justify a closer examination.

Referring to previous Raman data[50-53] on N_2O_4, it seems quite obvious that this spectrum contains the first gas-phase data on the dimeric species.

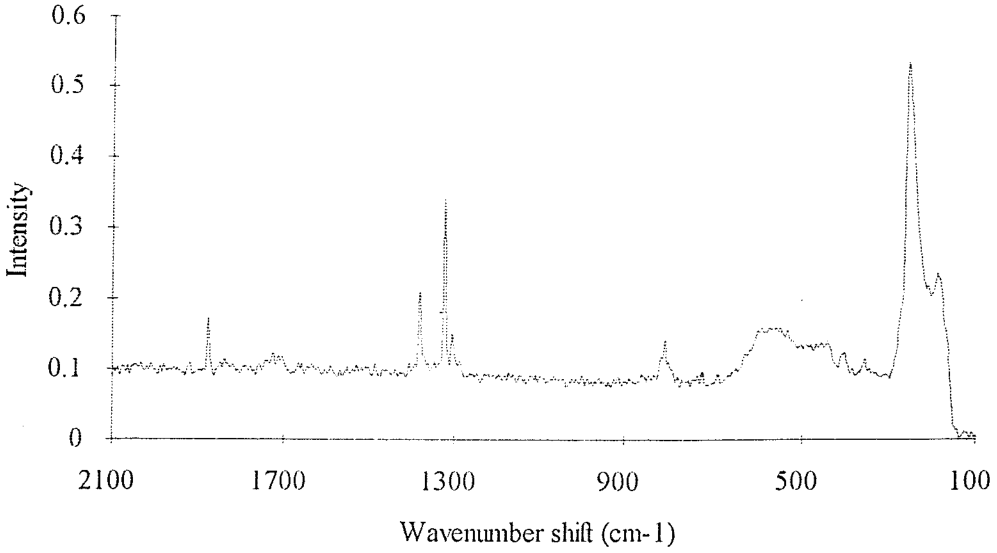

Figure 6.28 FT-Raman spectrum of NO_2/N_2O_4 in the gas phase.

---

* This work has recently been accepted for publication in Chemical Physics Letters.

The cell background is due to the presence of impurities from a previous experiment; the spectrum of air, taken over 100 accumulations, is shown as proof in figure 6.29.

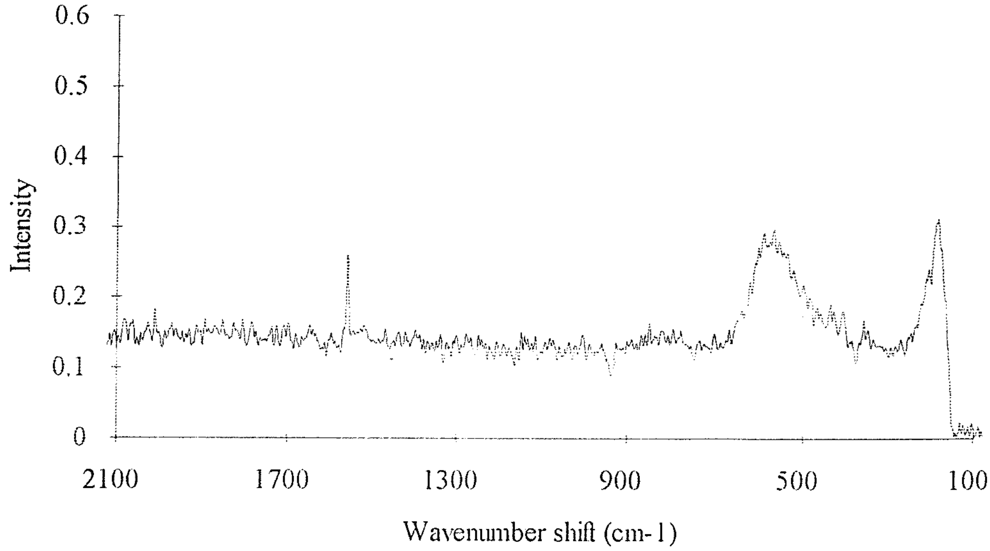

Figure 6.29 FT-Raman spectrum of air showing cell background (O_2 at 1556 cm^{-1}).

The bands correlate very well with the following previously-made observations:

- 1380 cm^{-1} (in-phase N-O symmetric stretch)
- 806 cm^{-1} (in-phase O-N-O bend)
- 254 cm^{-1} (N-N stretch)

These bands are the three totally-symmetric vibrations (symmetry species A_g), which are usually the strongest features in a Raman spectrum. The intensity pattern (with the 254 cm^{-1} band the strongest) shows the trend anticipated from the previous studies.

The N-N stretch at 254 cm^{-1} is shifted downwards by a significant amount from the reported liquid[52] and solid[53] values, by 10 cm^{-1} and 27 cm^{-1} respectively. The shift in N-N stretch band position possibly signifies a reduction in the force constant for the N-N bond in the gas phase, in anticipation of dissociation into the monomer. It should be remembered that band position (and shape) is usually perturbed by the physical phase of the sample - see section 6.5.1.3 in relation to Cl_2.

It is almost certain that dissociation is occurring during this experiment, as the band at 1322 cm^{-1} is probably due to the symmetric stretch of the monomer NO_2. The correlation with high-resolution dispersed fluorescence measurements[54] of the vibrational parameters is very good, and the similarity to the values derived from matrix-isolation resonance Raman studies using inert gas matrices make this assignment compelling. It should be noted that low-pressure gas-phase[55,56] and very dilute matrix-isolation[57] studies using resonantly-enhancing excitation wavelengths have been the only way to obtain gas-phase linear Raman data on NO_2 in the past.

The minority NO_2 monomer probably causes the absorption, via an overtone transition; the heated NO_2 then equilibrates with the rest of the sample, raising the overall temperature in the cell - causing dissociation of the dimer to ensure thermodynamic stability for the system at the new higher temperature.

Since it is difficult to accurately judge the concentration of the species under the conditions in the cell with the current apparatus, it is impossible to say what degree of resonance Raman enhancement to the NO_2 signal, if any, is being observed. Certainly at this S:N level, no characteristic overtone progressions are apparent. Despite the excitation wavenumber being close in value to the *predicted* energy difference to the first allowed electronic excited state, the most *probable* direct transition to this state lies at much higher wavenumber[44]. This may explain the apparent lack of strong enhancement.

The band at 1877 cm^{-1} is undoubtedly due to NO, by correlation with previous measurements on the species[27,58]. This raises the question how did such a reactive species come to be present in the cell so prominently. The possibilities include:

- through gas-phase chemical reaction (with water vapour)
- through reactions occurring on the gold surface (possibly catalysed by or including impurities)
- direct photochemical activation of the NO_2 species.

Given the high absorption noted for the laser radiation, it would be convenient to ascribe the presence of NO to direct photochemical activation, but without additional study it is impossible to comment on this further; the simplest of the photochemical pathways sees an electronically-excited NO_2 colliding with a ground-state molecule, producing 2NO and O_2.

The lack of evidence for O_2 should not be used to eliminate this possibility, as the oxygen may react further, or may be in low concentration. This would imply the

NO scattering to be surface- or resonance-enhanced. The reason is clear; NO and O_2 would be in similar concentration, and NO is less than 40 % as efficient a scatterer as O_2, extrapolating visible[27] data to the near-IR; hence some process whereby the NO species scattering dominates that from O_2 would need to be invoked.

Previous work involving very high resolution mid-IR absorption[59] studies on NO_2 has shown that NO will be present in the cell as a reaction product with atmospheric water, and that its concentration is very low. This would imply that the observed NO scattering is indeed strongly enhanced by some mechanism, or that the concentration in the cell is abnormally high, as a result of either photochemical dissociation or chemical reaction.

It is difficult to rule out the possibility that trace oxide species may be seeing a surface-enhanced Raman effect by bonding to the gold cell wall; certainly, this effect is known, and it was suggested earlier in this chapter that Cl_2 attacked the cell or contaminants corrosively. The possibility that trace species and contaminants were introduced into the cell on filling cannot be discounted, as no efforts were made to purify or check composition of the fill - the lack of vacuum line fittings was at fault.

The band at 1304 cm^{-1} raises slightly harder problems in its assignment. Fermi enhancement of an overtone band in the dimer would in principle produce a reasonable explanation. A weak interaction would produce the relatively small enhancement seen here; suitable pairs of bands need to be identified in further studies.

In fact, the solid and liquid phase dimer spectra do show Fermi effects[50] since the overtone of the 677 cm^{-1} IR-active band is enhanced by resonance with the 1382 cm^{-1} band to give a peak near 1325 cm^{-1}. No peak at this position is evident in the gas-phase spectrum of N_2O_4 presented here, as it is possibly covered by the wings of the strong band at 1322 cm^{-1}.

Less plausible assignments are worth exploring briefly. The band at 1304 cm^{-1} is possibly the first "hot-band" $(2 \leftarrow 1)$ transition of the NO_2 symmetric stretch, the band position being in good agreement with previous data. This would imply a Boltzmann temperature around 725 °C to achieve a significant population of the first vibrational excited state. This very high effective temperature could be due to the high absorption noted at the excitation wavelength, but is rather tenuous as an explanation without further investigation.

Isotopic shifts can be discounted straight away, as the relative abundance of the isotopes for oxygen and nitrogen are quite against an appreciable population of isotopomers. It is also unlikely that the band represents a fundamental vibrational transition in an excited electronic state; this would raise questions as to how this state became appreciably populated, and also why the scattered signal was so strong.

Following the discussion of the 1877 cm^{-1} feature, the band may also be due to resonance- or surface-enhanced trace species, or an impurity from the fill.

Another possibility which should be addressed is the possibility of overlap with spectral features from HNO_3. The presence of NO may be ascribed to gas-phase chemical reactions, which also form HNO_3; the effect of the Raman spectrum of this species on the current data is unknown at present, but seems unlikely from previous data[58].

6.6 References

1. P.J. Hendra and C.J. Vear, Spectrochim. Acta. 28A, 1949 (1972)
2. E.M. Nour, L.-H. Chen, and J. Laane, J. Phys. Chem. 87, 1113 (1983)
3. W.F. Murphy, W. Holzer, and H.J. Bernstein, Appl. Spectrosc. 23(3), 211 (1969)
4. J.J. Freeman, J. Heaviside, and P.J. Hendra, Appl. Spectrosc. 35(2), 196 (1981)
5. S. Broderson and J. Bendtsen, J. Raman Spectrosc. 1, 97 (1973)
6. M. D'Orazio and R. Hirschberger, Opt. Eng. 22(3), 308 (1983)
7. J.E. Pemberton, R.L. Sobocinski, M.A.Bryant, and D.A. Carter, Spectroscopy 5(2)
8. B.Schrader, Fresenius J. Anal. Chem. 337, 824 (1990)
9. D.E. Jennings, R. Hubbard, and J.W. Brault, Appl. Opt. 24(21), 3438 (1985)
10. G. Guelachvili, Appl. Opt. 16(8), 2097 (1977)
11. A. Weber, D.E. Jennings, and J.W. Brault, Proceedings of 4th ICORS Conference (Tokyo, 1984), page 58
12. D.E. Jennings, A. Weber, and J.W. Brault, Appl. Opt. 25(2), 284 (1986)
13. D.E. Jennings, A. Weber, and J.W. Brault, J. Mol. Spectrosc. 126, 19 (1987)
14. T. Hirschfeld and E.R. Schildkraut, in "Laser Raman Gas Diagnostics" (Eds. Lapp and Penney), page 379 (Plenum, New York, 1974)
15. W.J. Jones, Contemp. Phys. 13(5), 419 (1972)
16. R.J. Butcher, D.V. Willetts, and W.J. Jones, Proc. Roy. Soc. Lon. 324A, 231 (1971)
17. J.J. Barrett and S.A. Myers, J. Opt. Soc. Am. 61(9), 1246 (1961)
18. C. Engert, T. Michelis, and W. Kiefer, Appl. Spectrosc. 45(8), 1333 (1991)
19. A. Weber, S.P.S. Porto, L.E. Cheeseman, and J.J. Barrett, J. Opt. Soc. Am. 57(1), 19 (1967)
20. J.J. Barrett and N.I. Adams III, J. Opt. Soc. Am. 58(3), 311 (1968)

21. A. Weber and J. Schlupf, J. Opt. Soc. Am. 62(3), 428 (1972)
22. T.G. Matthews, Appl. Opt. 21(4), 577 (1982)
23. W.R. Trutna and R.L. Byer, Appl. Opt. 19(2), 301 (1980)
24. R.A. Hill, A.J. Mulac, and C.E. Hackett, Appl. Opt. 16(7), 2004 (1977)
25. J. Sawatzki and A. Simon, Proceedings of 12th ICORS Conference (South Carolina, 1990), poster reprint
26. H. Stammreich and R. Forneris, Spectrochim. Acta. 17, 775 (1961)
27. H.W. Schrötter, in NATO ASI Series C93 "Non-Linear Raman Spectroscopy and its Chemical Applications" (Eds. Kiefer and Long), page 19 (Reidel, Dordrecht, 1982)
28. C.J. Petty, G.M. Warnes, P.J. Hendra, and M. Judkins, Spectrochim. Acta. 47A(9/10), 1179 (1991)
29. C.J. Petty, Ph.D Thesis, University of Southampton (1991)
30. B.P. Stoicheff, Can. J. Phys. 36, 218 (1958)
31. S. Montero, C. Domingo, F. Wetzel, H. Finsterhölzl, and H.W. Schrötter, J. Raman Spectrosc. 15(8) 380 (1984)
32. E. Fermi, Z. Physik 71, 250 (1931)
33. J.M. Hollas, "Modern Spectroscopy" 2nd Ed. Chapter 5 (Wiley, 1992)
34. G.W. Chantry, in "The Raman Effect" Vol.1 (Ed. A. Anderson) Chapter 2 (Marcel Dekker, New York, 1971)
35. P.W. Atkins, "Molecular Quantum Mechanics" 2nd Ed. Chapter 11 (Oxford University Press, 1983)
36. E. Hecht, "Optics" 2nd Ed. Chapter 8 (Addison-Wesley, 1987)
37. N.J. Bridge and A.D. Buckingham, Proc. Roy. Soc. Lon. 295A, 334 (1966)
38. C.D. Newman, G.G. Bret, and R.L. McCreery, Appl. Spectrosc. 46(2), 262 (1992)
39. T. Uda, K. Okuno, and Y. Naruse, Radiochim. Acta. 56, 209 (1992)
40. V.S. Ban, G.H. Olsen, and A.M. Joshi, Spectroscopy, 6(3)
41. T. Uda, K. Okuno, S. O'Hira, and Y. Naruse, J. Nucl. Sci. Tech. 28(7), 618 (1991)
42. See, for instance, reference 1 in V.M. Donnelly, D.G. Keil, and F. Kaufman, J. Chem. Phys. 71, (1979) 659.
43. G.D. Gillispie, A.U. Khan, A.C. Wahl, R.P. Hosteny, and M. Krauss, J. Chem. Phys. 63, (1978) 3425.
44. R. Lui and X. Zhou, J. Phys. Chem. 97, (1993) 4413.
45. C.W. Bauschlicher Jr., A. Komornicki, and B. Roos, J. Am. Chem. Soc. 105, (1983) 745.

46. R.D. Harcourt, J. Chem. Soc. Farad. Trans. 87, (1991) 1089.

47. C.H. Bibart and G.E. Ewing, J. Chem. Phys. 61, (1974) 1284.

48. P. Gray and A.D. Yoffe, Chem. Rev. 55, (1955) 1069.

49. T.C. Hall Jr. and F.E. Blacet, J. Chem. Phys. 20, (1952) 1745.

50. G.M. Begun and W.H. Fletcher, J. Mol. Spectrosc. 4, (1960) 388.

51. D.E. Tevault and L. Andrews, Spectrochim. Acta 30A, (1974) 969.

52. T. Kato and H. Kato, Mol. Phys. 66, (1989) 1183.

53. A. Givan and A. Loewenschuss, J. Chem. Phys. 93, (1990) 7592.

54. A. Delon and R. Jost, J. Chem. Phys. 95, (1991) 5686.

55. M.J. Marsden and G.R. Bird, J. Chem. Phys. 59, (1973) 2766.

56. H.D. Bist, J.C.D. Brand, and R. Vasudev, J. Mol. Spectrosc. 66, (1977) 399.

57. F. Bolduan and H.J. Jodl, J. Mol. Spectrosc. 91, (1982) 404.

58. F. Melen and M. Herman, J. Chem. Phys. Ref. Data 21(4), 831 (1992)

59. A. Perrin, J-Y. Mandin, C. Camy-Peyret, J-M.Flaud, and J-P. Chevillard, J. Mol. Spectrosc. 103, (1994) 417

Chapter 7:

Conclusions

7.1 Introduction

Since 1987, the research group of Professor Patrick Hendra based in the Department of Chemistry at the University of Southampton has vigorously developed many aspects of the FT-Raman technique. Early in the program, the emphasis was biased towards instrumental development. However, the developments were inspired by the needs of chemists - the philosophy being to produce a routine analytical instrument to complement the more-prevalent mid-IR technique.

As the development progressed in conjunction with the Applied Research Group of Perkin Elmer Ltd, more emphasis was placed on exploiting the rapidly-improving performance. A wide range of previously-intractable chemical systems became open to study, due to the excellent suppression of fluorescence with excitation beyond 1 μm.

A wide range of collaborative projects were also undertaken with industrial partners. Although the benefits of Raman spectroscopy were well-known to a small community (essentially academic, along with some government and industrial research laboratories), major applicability of the technique in industry had never been shown - again, nearly always due to fluorescence.

The recent emphasis of the research in Professor Hendra's group has been directed towards novel chemical systems. As a part of this group between 1990-1993, I instigated and undertook several extended studies based on the evaluation of FT-Raman spectroscopy as a routine analysis method for a range of chemical systems.

This thesis comprises the results of the projects. In order of presentation, these chemical applications of FT-Raman spectroscopy have been critically appraised, and the conclusions presented below.

7.2 1,3-dithiole-2-thione and related compounds.

A series of highly-coloured thione-ring-based synthetic intermediates for the important tetrathiafulvalene (TTF) system have been investigated, and reported in chapter 2.

This study was undertaken to support the research of Dr Jeremy Kilburn. Mid-IR sampling techniques were not suitable for the thiones, and many were too deeply-coloured or impure to successfully employ conventional Raman spectroscopy. However, FT-Raman techniques have been successfully applied, yielding very good spectra in acceptable timescales.

Literature assignments of 1,3-dithiole-2-thione were found to be dubious. In an attempt to clarify the literature, Raman depolarisation studies and transmission IR spectroscopy have been undertaken on this simplest thione. These studies have resulted in a far more plausible assignment of those fundamentals of the thione ring system considered important in an analytical context.

The major features of the thiones have been deduced from group frequency argument, and the changes on conversion to oxones or coupling to form TTFs documented, with a view to laboratory analysis.

The original study did not envisage expansion. However, as more compounds became available, the Raman data obtained from these samples has been used to verify the claims made in the original study. With few exceptions, the claims have been vindicated. In areas of conflict, the original findings have been revised where necessary.

FT-Raman spectroscopy has been shown to be a good technique for identifying thiones, and to differentiate between them, on the basis of simple spectra-structure correlation. The method was not compromised by the fluorescence that was present quite strongly in some of the spectra. There are enough resolvable features in each spectrum to make the identification and differentiation possible even without all the spectrum being usable.

As a routine bench technique for the analytical spectroscopy of thione ring systems, FT-Raman has shown great promise, and furthermore provided data good enough to begin unravelling the underlying problems of the vibrational structure.

7.3 Allenylketenimine-TCNE derivatives

FT-Raman spectroscopy has been employed to probe the structure of a completely novel series of organic compounds, synthesised at Southampton by Dr Richard Whitby. As reported in chapter 3, the vibrational study of allenylketenimine-TCNE adducts with mid-IR methods was hampered by difficulties in sampling, and in the apparent variability of absorption by the -CN moiety.

In contrast, FT-Raman spectroscopy gave very good quality results. An assignment of the major functionalities of the structure has been made. It has been shown that allenylketenimine-TCNE adducts may be differentiated unambiguously by means of FT-Raman spectroscopy. In addition, structural data derived from XRD and

NMR studies has been confirmed where possible. The nitrile (CN-) stretch has been shown to be well-resolved and of reliable intensity.

From an analytical standpoint, there are features common to all spectra which allow assignment of the basic TCNE-allenylketenimine structural unit. Sufficient differences exist to be able to differentiate between individual adducts; and the exact shape of the nitrile band allows unambiguous determination of the isomeric form, once the adduct has been identified.

On the basis of this study, it is clear that FT-Raman is the method of choice for the vibrational analysis of allenylketenimine-TCNE adducts.

7.4 Hydration of the γ-alumina surface

The opportunity arose to take part in a Swedish exchange to the Department of Chemistry at Luleå University, to study with Professor Willis Forsling. One of the projects undertaken was a combined FT-IR/Raman study of the γ-alumina surface under various hydration conditions. The results are presented in chapter 4.

Changes to the oxide surface during hydration have been studied, as a function of pH, temperature, and hydrolysis period. The study conclusively and unambiguously shows that the bayerite polymorph of aluminium hydroxide is formed at the surface, after several weeks at room temperature, much faster at elevated temperatures, with larger conversions at alkaline pH.

The study has also indicated that phenylphosphate anion interacts with the surface, forming a reasonably strong bond. In addition, phenylphosphate adsorption was shown to be a good method to protect the γ-alumina surface from hydrothermal conversion to bayerite, providing the phenylphosphate was administered at the very start of any process likely to cause this reaction and providing the pH of the system did not drift too alkaline. Even at elevated temperatures, providing the pH was kept about neutral, the use of phenylphosphate as a coating agent was shown to be quite efficacious.

7.5 Cement minerals and some simple calcium-bearing inorganic compounds

Also as part of the Swedish exchange visit, a study was attempted of the structure of several calcium silicate-based cement mineral species. The results presented in chapter 5 clearly show that near-IR excitation at 1064 nm in many cases does not result in Raman scattering but a structured luminescence. It is proposed that this luminescence may involve transition metal impurities.

The study deviated from its original goal, in order to provide an introduction to this unexplored area. Synthetic studies have been undertaken, and results obtained from two independent sources of cement minerals. These results indicate a possible dependency of linewidth on impurity content, which is partially endorsed by low-temperature experiments on supplied material.

It has been shown that calcium hydroxide exhibits strong resemblance to several of the supplied calcium silicates' luminescence. After undertaking near-IR studies on this species and on several of the supplied minerals, it is proposed that the luminescence in the silicates might require both calcium hydroxide (formed on the surface of cement mineral grains) and manganese ions (present as impurity).

In addition, the study demonstrates the use of modern *visible excitation* Raman techniques for the study of cement minerals. A single-stage spectrograph with micro-sampling, Ar^+ green excitation and CCD detection seems preferable to the near-IR macro-FT-Raman method for the calcium silicates, on the basis of results presented here. This is at variance with some of the older work in the literature.

7.6 Near-IR-excited Raman scattering in the gas phase.

The viability of gas-phase FT-Raman spectroscopy with near-IR excitation has been demonstrated, for both vibrational and rotational spectroscopy, the details given in chapter 6.

A method for obtaining Raman spectra from gas-phase species using commercial instrumentation and a simple sampling accessory have been designed, developed, tested and implemented from first principles, necessitating critical evaluation of spectrometer performance and requiring several gas-cell redesigns.

The use of a multiple reflection cell has been shown to be vital, and the experimental technique for this method developed. The prospects for low-pressure studies or mixtures with low partial pressures have been discussed with reference to the sensitivity of the methods.

The application of the method developed to the NO_2/N_2O_4 system has led to a previously-intractable problem being solved - the study presented is the first success on the gas-phase dimer, and has provided quite fundamental data. The data also possibly reflects the first instance of a gas-phase NO_2 spectrum exhibiting *minimal* resonance Raman enhancement - and also possibly reflects strongly-enhanced scattering from the minority NO species.

All of the projects were successful to varying degree, delivering novel results on a diverse range of systems. For chemical applications, FT-Raman spectroscopy has been shown to be a powerful and versatile technique.

7.7 Further work

As discussed in chapter 2, a full vibrational analysis of the thione ring structure requires more data than is currently available, and a considerably improved model.

Modern *ab initio* methods show promise and have merit; much of the subjectivity and propagation of error may be eliminated when force constants are calculated from first principles, and not derived from previous studies. However, the methods commonly available are still too primitive and inaccurate to be of help in the nuances of the assignment.

The best way forward lies in collecting IR absorption data ranging from the near-IR (overtones) to the far-IR (low-frequency bands), along with Raman data over the widest possible shift range (from as close to the Rayleigh line as possible), and attempting to resolve as many combination and overtone modes as possible. Combined with polarisation measurements and isotopic substitution studies, this data should provide a normal co-ordinate analysis with enough parameters to at least predict fundamentals accurately.

In the case of the γ-alumina surface studies of chapter 4, the elucidation of the phenylphosphate bond to the hydrated surface, especially its geometry and the chemical nature of the bonding sites, would provide additional data to evaluate its efficacy as a prevention for hydration.

The study was not conceived to provide a quantitative method for analysing the distribution of species at the γ-alumina surface, but in view of the evident successes scored, further studies are on-going with a view to developing such a method. One of the aims of this further work is to determine the amount of surface coverage afforded by mM phenylphosphate concentration.

In the light of this study, the theoretical models of the hydrated surface may require revision, as they operate under the assumption that the proton adsorption/desorption reactions on which they are based occur at a "boundary" which is simply the oxide surface with hydroxylation and hydration mechanisms.

The study of the calcium silicates in chapter 5 has already provoked much discussion, with several researchers now active in the area. Calcium silicates are complex solid-state species, far more so than the simple binary salts (oxides and hydroxides) on which some of the arguments by analogy have been based in this study. However, few researchers in the near-IR FT-Raman community seem to have appreciated the complex nature of the fluorescence backgrounds apparent in simple inorganic species, let alone the more complex "real" mineral samples. There is plainly much work to do in determining what factor determine which inorganic species are suitable for analysis with near-IR excitation.

In addition, the results suggest that FT-Raman is best used in concert, and not in competition, with modern visible Raman methods.

In relation to the gas-phase work of chapter 6, several areas of instrumental importance have been identified. These correspond to the need for a well-maintained, high-specification, near-IR-optimised spectrometer, with special care to stabilise interferometer and laser; hence instrumental development, including detector performance improvements, should be continued.

In terms of the cell, a focusing retroreflector would be of great use, providing its alignment could be made as reproducible as that of the cell. In the long term, the cell and collection foreoptics should probably be modelled theoretically, to optimised collection and transfer efficiency. With these developments, perhaps the very weak rovibrational spectra would be open to study.

The study of the oxides of nitrogen should be expanded and consolidated. The non-resonance of NO_2, and the dependency of the N-N bond stretching frequency as a function of progress towards dissociation should be evaluated.

The most pressing needs are to correlate the absorption of the laser with path length, sample temperature, and species concentration - and to fully characterise the species flowing into the cell on fill, then present after irradiation. Of great help in this respect would be high-resolution *in-situ* near-IR absorption data in the 12,000-4,000 cm^{-1} spectral range, along with accurate instrument response correction and calibration functions for the Raman experiment.

These further studies require the construction of a cell which may be heated and cooled between 20-120 °C. The cell must also be able to be purged with dry, inert gas, as well as evacuated down to 1-2 Torr for low-pressure studies, and to hold vacuum for several hours during a long high-resolution experiment. Only in this way will it be possible to rigorously exclude O_2 and water vapour.

The reactivity of nitrogen oxides towards gold, the likely products, and their surface-enhanced Raman scattering efficiencies should be evaluated - as should the Raman spectra of NO and HNO_3 in the gas phase under these conditions.

A further intriguing experiment awaits: a high-quality set of holographic notch filters (HNFs) would allow coverage of low-frequency rotational structure and anti-

Stokes lines, facilitating the determination of effective temperature of the various species involved by measurement of intensity ratios and envelope profiles. Since N_2O_4 has no permanent electric dipole moment, the Raman spectrum is one of the few methods available to study the rotational spectrum. In a similar vein, the use of tuneable near-IR excitation with alkali metal vapour filters might provide useful low-frequency capability[1].

7.8 Other studies and published work

The projects in chapters 2 and 3 yielded published data, in collaboration with Drs Kilburn and Whitby, respectively. Chapter 4 has yielded one paper published, with a description of further studies in preparation. Chapter 5 has yielded, similarly, one paper published, with one further to be submitted. Chapter 6 yielded a study of the feasibility of near-IR FT-Raman gas-phase spectroscopy with initial results, whilst the nitrogen oxide work has recently been accepted for publication in Chemical Physics Letters.

Although not detailed in this thesis, a highly-successful project on the vibrational assignment, Fermi resonance, low-temperature spectroscopy, pre-resonance scattering, near-IR absorption, and previous Raman studies of a polydiacetylene conducting polymer was undertaken in collaboration with Dr Bill Maddams, who receives grateful and heartfelt thanks. This work is currently being collated and submitted.

7.9 References

1. M.J. Pelletier, Appl. Spectrosc. 47(1), 69 (1993)

Appendix 1:

Published work

Only work actually in print in refereed journals is reproduced here - the paper *"Raman spectroscopy of NO_2/N_2O_4 in the gas phase using near-infrared excitation"* by Chris Dyer and Patrick J. Hendra, accepted to Chemical Physics Letters December 1994, is omitted.

"Fourier transform Raman spectroscopy of 1,3-dithiole-2-thione and related compounds", C.D. Dyer, J.D. Kilburn, W.F. Maddams, and P.A. Walker, Spectrochim. Acta, 47A, 1225-1234 (1991)

"Fourier transform Raman spectroscopy of novel organic systems. The analysis of allenylketenimine-tetracyanoethylene Diels-Alder reaction products", R.D. Dennehy, C.D. Dyer, W.F. Maddams, and R.J. Whitby, Spectrochim. Acta, 50A, 819-831 (1994)

"Surface hydration of aqueous γ-Al_2O_3 studied by Fourier transform Raman and infrared spectroscopy - I. Initial results.", Chris Dyer, Patrick J. Hendra, Willis Forsling, and Maine Ranheimer, Spectrochim. Acta, 49A, 691-705 (1993)

"The Raman spectroscopy of cement minerals under 1064 nm excitation", Chris Dyer, Patrick J. Hendra, and Willis Forsling, Spectrochim. Acta, 49A, 715-722 (1993)

"Near-infrared Fourier transform Raman spectroscopy of gases", Chris D. Dyer and Patrick J. Hendra, Analyst, 117, 1393-1399 (1992)

The following published papers were included in the bound thesis. These have not been digitised due to copyright restrictions, but the links are provided.

C.D. Dyer, J.D. Kilburn, W.F. Maddams, P.A. Walker (1991)

Fourier Transform Raman Spectroscopy of 1,3-Dithiole-2-Thione and Related Compounds

Spectrochimica Acta Part A: Vol. 47, Nos. 9–10, pp.1225–1234

http://dx.doi.org/10.1016/0584-8539(91)80209-2

R.D. Dennehy, C.D. Dyer, W.F. Maddams, R.J. Whitby (1994)

Fourier transform Raman spectroscopy of novel organic systems. The analysis of allenylketenimine—tetracyanoethylene Diels—Alder reaction products

Spectrochimica Acta Part A: Vol. 50, No. 4, pp.819-831

http://dx.doi.org/10.1016/0584-8539(94)80018-9

Chris Dyer, Patrick J. Hendra, Willis Forsling, Maine Ranheimer (1994)

Surface hydration of aqueous γ-Al_2O_3 studied by Fourier transform Raman and infrared spectroscopy—I. Initial results

Spectrochimica Acta Part A: Vol. 49, Nos. 5-6, pp.691-705 http://dx.doi.org/10.1016/0584-8539(93)80092-O

Chris D. Dyer, Patrick J. Hendra, Willis Forsling (1993)

The Raman spectroscopy of cement minerals under 1064 nm excitation

Spectrochimica Acta Part A: Vol. 49, Nos. 5-6, pp.715-722

http://dx.doi.org/10.1016/0584-8539(93)80094-Q

Chris D. Dyer, Patrick J. Hendra

Near-infrared Fourier transform Raman spectroscopy of gases

The Analyst: Vol. 117, No. 9, pp.1393

https://doi.org/10.1039/an9921701393